

SEARCHING FOR NEW PHYSICS IN $b \rightarrow s\ell^+\ell^-$ TRANSITIONS AT THE LHCb EXPERIMENT

L. Pescatore

*Thesis submitted for the degree of
Doctor of Philosophy*



Particle Physics Group,
School of Physics and Astronomy,
University of Birmingham.

March 27, 2016

ABSTRACT

Flavour Changing Neutral Currents are transitions between different quarks with the same charge such as $b \rightarrow s$ processes. These are forbidden at tree level in the Standard Model (SM) but can happen through loop diagrams, which causes the branching ratio of this type of decays to be small, typically $\sim 10^{-6}$ or less. Particles beyond the SM can contribute in the loops enhancing the branching fractions of these decays, which are therefore very sensitive new physics. In this work two analysis of semileptonic $b \rightarrow s\ell^+\ell^-$ decays are presented. First, $\Lambda_b^0 \rightarrow \Lambda\mu^+\mu^-$ decays are analysed to measure their branching fraction as a function of the square of the dimuon invariant mass, q^2 . Furthermore, an angular analysis of these decays is performed for the first time. Secondly, $B^0 \rightarrow K^{*0}\ell^+\ell^-$ decays are analysed measuring the $R_{K^{*0}}$ ratio between the muon, $B^0 \rightarrow K^{*0}\mu^+\mu^-$, and electron, $B^0 \rightarrow K^{*0}e^+e^-$, channels, which is interesting as it is largely free from uncertainties due to the knowledge of the hadronic matrix elements. This thesis is organised in the following way. Chapter 1 introduces the Standard Model and the concept of flavour and explains how rare decays can help us in the quest for physics beyond the SM. Chapter 2 describes the LHCb detector, which was used to collect the data analysed in this thesis. This chapter also includes studies performed to validate the hadronic physics in LHCb simulation software. Chapter 3 deals with the measurement of the differential branching fraction of the $\Lambda_b^0 \rightarrow \Lambda\mu^+\mu^-$ decay, while Chapter 4 describes its angular analysis. Finally, Chapter 5 reports the measurement of the $R_{K^{*0}}$ ratio.

DECLARATION OF AUTHORS CONTRIBUTION

I am one of the main authors of the two analysis reported in Chapters 3, 4 and 5. For the analysis of $\Lambda_b^0 \rightarrow \Lambda\mu^+\mu^-$ decays I collaborated with Michal Kreps, who took care of implementing the decay model to re-weight the simulation and provided simulated samples. Furthermore, I want to thank him for the advice given throughout. The work on this analysis was published and can be found at Ref. [1]. For the $R_{K^{*0}}$ analysis, described in Ch. 5, I actively participated in most stages of the analysis collaborating with Simone Bifani. In particular I took care of the production of various simulated samples, participated in the definition of the selection, in the yields extraction and I provided a fit and data-reduction framework. Finally, as a service work for the LHCb experiment, I developed the tools used to perform the validation studies described in Sections 2.11–2.13.

ACKNOWLEDGEMENTS

First of all I would like to thank Nigel, who always supported me in these years and granted me many good opportunities. I think I could not hope for a better supervisor. A big ‘thank you’ also to Simone, I think we’ve had a good collaboration for the $R_{K^{*0}}$ analysis and he taught me a lot. Thanks also to the people of the Birmingham LHCb group: Cristina, Jimmy and the new students and a ‘thank you’ also to Michal, who adopted us, Birmingham students, for a while. A special ‘thank you’ goes to Pete, who shared with me this three years experience. I think it would have been a very different and less interesting experience without him. A ‘thank you’ also goes to the members of the LHCb collaboration and in particular of the Rare Decays Working Group.; in particular to the working group conveners Gaia, Tom and Marco and to Gloria, who patiently guided me through the depths of the LHCb software. Finally, I’m grateful to Vincenzo and the LHCb Bologna group, who kindly hosted me for a few months and in particular to Umberto for all the wisdom he shared. I want also to thank the LTA folks, who were with me during the long period I spent at CERN and especially Mark and Lewis, adventure companions. And speaking about CERN people a great ‘thank you’ to Lorenzo and Federico, because when it’s 1pm I always feel that I should be in front of the trays. Going now to who is always waiting for me in Italy when I go back, a big ‘thank you’ to my family: my dad Orazio, my mum Paola and my sisters Giulia and Silvia, for all their support and all the Italian food they brought me while I was living abroad. A big ‘thank you’ also to my friends Ivan, Enrico, Martina, Federico, Valentina, Letizia and all the others. And finally, last but not least, a giant thank you to Lucia, who is the engine of my life and to whom this thesis is dedicated.

*A Lucia,
perché quando tutto perde di senso
tu sei il mio piccolo mondo felice.*

*Nec per se quemquam tempus sentire fatendumst
semotum ab rerum motu placidaque quiete.
(Lucretius, De rerum natura, vv. 462-463)*

Contents

1	Introduction	1
1.1	The electroweak interaction	4
1.2	Flavour and the CKM matrix	5
1.3	The puzzles of the SM	9
1.3.1	The flavour problem	10
1.4	Beyond the Standard Model	11
1.4.1	Flavour and BSM theories	12
1.5	Rare decays: a tool to search for new physics	13
1.5.1	Theoretical framework: the effective Hamiltonian	14
1.5.2	Operators	16
1.5.3	Phenomenology of $b \rightarrow s\ell^+\ell^-$ decays	18
1.5.4	Observables in $b \rightarrow s\ell^+\ell^-$ decays	19
1.6	Experimental status	20
1.6.1	Dimuon decays of b hadrons	20
1.6.2	Semileptonic $b \rightarrow s\ell^+\ell^-$ decays of b hadrons	22
1.6.3	Lepton Flavour Violation searches	24
2	The LHCb detector at the Large Hadron Collider	25
2.1	The Large Hadron Collider	25
2.2	The LHCb detector	27
2.3	The magnet	29
2.4	Tracking system	29
2.5	Calorimeters	32
2.5.1	Bremsstrahlung recovery for electrons	34
2.6	RICH	35
2.7	The muon system	36
2.8	Particle identification	37
2.8.1	PID calibration	39
2.9	Trigger and software	39
2.10	Constrained kinematic fits	41
2.11	Validation of hadronic processes in the simulation	42
2.11.1	Geometry and interaction probability	44
2.11.2	PDG prediction	45
2.11.3	Validation results	46
2.12	Material budget studies	49
2.13	Validation and material budget studies conclusions	49

3 Differential branching fraction of $\Lambda_b^0 \rightarrow \Lambda\mu^+\mu^-$	51
3.1 Analysis strategy and q^2 regions	53
3.2 Candidate types	54
3.3 Simulation	55
3.3.1 Decay Model	56
3.3.2 Kinematic re-weighting	57
3.3.3 Event type	58
3.4 Selection	59
3.4.1 Pre-selection	59
3.4.2 Neural Networks	60
3.4.3 MVA optimisation	63
3.4.4 Trigger	65
3.4.5 Background from specific decays	66
3.5 Yield extraction	68
3.5.1 Fit description	69
3.5.2 Fit results	73
3.6 Efficiency	79
3.6.1 Geometric acceptance	79
3.6.2 Reconstruction and neural network efficiencies	80
3.6.3 Trigger efficiency	80
3.6.4 PID efficiency	81
3.6.5 Relative efficiencies	82
3.7 Systematic uncertainties	85
3.7.1 Systematic uncertainty on the yields	85
3.7.2 Systematic uncertainties on the efficiency determination	87
3.7.2.1 Effect of new physics on the decay model	87
3.7.2.2 Simulation statistics	87
3.7.2.3 Production polarisation and decay structure	88
3.7.2.4 Λ_b^0 lifetime	89
3.7.2.5 Downstream candidates reconstruction efficiency	89
3.7.2.6 Data-simulation discrepancies	90
3.8 Differential branching fraction extraction	90
4 Angular analysis of $\Lambda_b^0 \rightarrow \Lambda\mu^+\mu^-$ decays	95
4.1 One-dimensional angular distributions	96
4.2 Multi-dimensional angular distributions	98
4.3 Angular resolution	100
4.4 Fit strategy	102
4.4.1 Feldman-cousins plug-in method	103
4.4.2 Modelling the angular distributions	104
4.4.3 Angular acceptance	105
4.4.4 Studies on a three-dimensional fit	107
4.5 Systematics uncertainties on angular observables	108
4.5.1 Angular correlations	108
4.5.2 Resolution	109
4.5.3 Efficiency description	110

4.5.4	Background parameterisation	110
4.5.5	Polarisation	111
4.6	J/ψ cross-check	112
4.7	Results	113
5	Testing lepton flavour universality with $R_{K^{*0}}$	117
5.1	Combining ratios	120
5.2	Experimental status	121
5.3	Analysis strategy	122
5.4	Dilepton invariant mass intervals	123
5.4.1	Control channels	124
5.5	Data samples and simulation	124
5.5.1	Data-simulation corrections	124
5.6	Selection	127
5.6.1	Trigger and Stripping	128
5.6.2	PID	132
5.6.3	Peaking backgrounds	133
5.6.3.1	Charmonium vetoes	134
5.6.3.2	ϕ veto	134
5.6.3.3	$B^+ \rightarrow K^+ \ell^+ \ell^-$ plus a random pion	135
5.6.3.4	Λ_b decays	135
5.6.3.5	$B^0 \rightarrow (D^- \rightarrow K e^- \bar{\nu}) e^+ \nu$	136
5.6.3.6	$B^0 \rightarrow K^{*0} (\gamma \rightarrow e^+ e^-)$	136
5.6.3.7	Other peaking backgrounds	137
5.6.4	Partially-reconstructed background	138
5.6.5	Bremsstrahlung corrected mass	139
5.6.6	Multivariate analysis	140
5.6.7	Optimisation	143
5.7	Selection summary	147
5.8	Mass fits	148
5.8.1	Muon channels	148
5.8.1.1	$B^0 \rightarrow K^{*0} (J/\psi \rightarrow \mu^+ \mu^-)$ PDF	149
5.8.1.2	$B^0 \rightarrow K^{*0} \mu^+ \mu^-$ PDF	150
5.8.1.3	Summary	151
5.8.2	Electron channels	153
5.8.2.1	Signal PDFs for the electron channels	154
5.8.2.2	Background PDFs for the electron channels	157
5.8.2.3	Summary of the fit to the electron samples	160
5.8.3	Event yields	162
5.9	Efficiency	166
5.9.1	Geometric efficiency	168
5.9.2	Reconstruction efficiency and bin migration	168
5.9.2.1	Bin migration	168
5.9.3	PID efficiency	170
5.9.4	Trigger efficiency	170
5.9.4.1	Electron triggers	171

5.9.4.2	TISTOS cross-check	173
5.9.5	Neural networks and BCM efficiencies	175
5.10	Systematic uncertainties	176
5.10.1	Choice of signal and background PDFs	176
5.10.2	Efficiency determinations	178
5.10.3	Bin migration	178
5.11	Result extraction	179
5.11.1	$R_{J/\psi}$ sanity check	180
5.11.2	$R_{K^{*0}}$	180
6	Conclusions	181
A	Decay models	193
A.1	$\Lambda_b^0 \rightarrow \Lambda \mu^+ \mu^-$ distribution	193
A.2	Two-dimensional angular distribution parameters	196
A.3	$\Lambda_b^0 \rightarrow J/\psi \Lambda$ distribution	196
B	Data-simulation comparison	198
C	Systematic uncertainties on the efficiency calculation for the $\Lambda_b^0 \rightarrow \Lambda \mu^+ \mu^-$ branching fraction analysis.	201
D	Improved predictions for $\Lambda_b^0 \rightarrow \Lambda \mu^+ \mu^-$ observables.	204
E	Invariant mass fits to $B^0 \rightarrow K^{*0} \ell^+ \ell^-$ simulated candidates	207
F	Invariant mass fits to $B^0 \rightarrow K^{*0} e^+ e^-$ candidates divided in trigger categories	212

1

CHAPTER 1

2

3

Introduction

4

5 The Standard Model of particle physics (SM) is a Quantum Field Theory (QFT)
6 describing strong and electroweak (EW) interactions. It was formulated in its cur-
7 rent form in the mid-70s and has been an extremely successful predictive theory
8 since then. Almost all known phenomena from 1 eV up to several hundred GeV are
9 described well by the SM and experiments at the Large Hadron Collider (LHC) are
10 now probing the SM up to and above the TeV scale. As an example of the level
11 of accuracy of the SM, Tab. 1.1 reports the predicted and measured values of the
12 widths of the Z and W bosons [2]. Finally, in 2012 the Higgs boson, which is one
13 of the fundamental building blocks of the theory, was observed [3, 4]. This is a
14 critical ingredient of the SM as it introduces a mechanism that produces particles'
15 masses [5]. Despite the success of the SM, experimentally well-established effects,
16 like neutrino oscillations and the presence of dark matter, remain outside the reach
17 of this theory. Furthermore, the model does not include the description of gravity,
18 which can be neglected at the EW energy scale. This motivates the search for New

Physics (NP).

Table 1.1: Predicted and measured values of the decay widths of the Z^0 and W bosons [2].

Quantity	Predicted	Measured
Γ_{Z^0}	2.4960 ± 0.0002 GeV	2.4952 ± 0.0023 GeV
Γ_W	2.0915 ± 0.0005 GeV	2.085 ± 0.042 GeV

¹⁹

The SM is based on the symmetry groups of strong, $SU(3)_C$, and electroweak, $SU(2)_W \times U(1)_Y$, interactions. The subscripts C, W and Y stand for colour charge, weak isospin and hyper-charge respectively. The Lagrangian describing the SM results from the application of the principle of invariance of the wave function under the unitary group transformations given by the product $SU(3)_C \otimes SU(2)_W \otimes U(1)_Y$, and leads to conservation laws such as the conservation of electric and strong charge. The model has then 26 free parameters, which have to be experimentally measured.

Particles included in the SM can be grouped into a few categories depending on their properties and ability to interact with each other. The first distinction is between fermions, half-integer spin particles, and bosons, integer spin particles. Fermions constitute the basic building blocks of matter, while bosons are the mediators of the interactions. Since the concept of bosonic mediators of interactions arises because of local gauge symmetry [6], they are called “gauge bosons”. The list of the known interactions with their force carrier and properties is reported in Tab. 1.2. The matter of which we are made of is mainly composed of electrons and protons, which have spin 1/2; protons are in turn composed of u and d quarks, which again

Table 1.2: Fundamental forces of nature together with their gauge bosons, ranges and relative strengths, as they act on a pair of protons in an atomic nucleus [2]. Gravity is not included in the SM and the graviton is hypothetical at the current time.

Interaction	Mediator	Strength	Range (m)	Mediator mass
Strong	g	1	∞	0
EM	γ	10^{-3}	∞	0
Weak	Z^0, W^\pm	10^{-16}	10^{-18}	$W^\pm = 80.399 \text{ GeV}/c^2$ $Z^0 = 91.188 \text{ GeV}/c^2$
Gravity	g^0 (graviton?)	10^{-41}	∞	0

³⁶ have spin 1/2. Among fermions one can then consider two smaller groups: quarks
³⁷ and leptons. Quarks carry colour charge and therefore can interact through the
³⁸ so-called strong interaction, while leptons, which do not carry colour charge, are
³⁹ insensitive to it. For each particle a corresponding anti-particle exists with opposite
⁴⁰ quantum numbers. Finally, fermions are divided into three families having similar
⁴¹ properties but different masses. This last classification embedded in the SM is also
⁴² called “flavour structure” and it will be the main tool used in this thesis; a more
⁴³ detailed description of it is given in the following sections. A schematic view of the
fundamental particles in the SM is shown in Fig. 1.1.

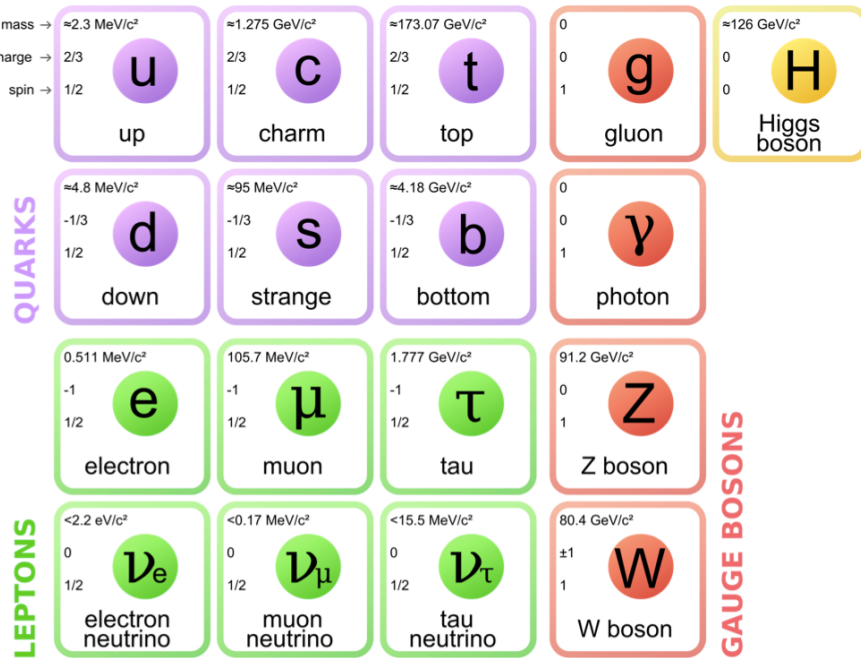


Figure 1.1: A scheme of the fundamental particles in the SM with their properties [7].

44

⁴⁵ Due to the asymptotic freedom of the strong interaction quarks cannot be observed
⁴⁶ alone but are always combined with other quarks to form color singlets [8]. Non-
⁴⁷ fundamental particles composed of quarks are called hadrons and are classified into
⁴⁸ two groups: mesons, where the color singlet is achieved by the combination of a
⁴⁹ quark and an antiquark ($q \bar{q}$), and baryons formed from three quarks ($q q q$) of
⁵⁰ different colours. Recently, in 2014 and 2015 evidence for new states, formed by
⁵¹ four and five quarks, was found [9, 10].

52 1.1 The electroweak interaction

53 The electromagnetic interaction is responsible for binding electrons and nuclei to
54 gether to form atoms and its mediator is the photon. The weak interaction is
55 responsible for the β decay of nuclei and is mediated by the exchange of W^\pm and
56 Z^0 bosons. Unlike the electromagnetic force, that affects only charged particles, all
57 known fermions interact through the weak interaction. The weak interaction is also
58 the only one that violates the parity symmetry, which states that interactions are
59 invariant under an inversion of spatial coordinates. This symmetry breaking arises
60 from the fact that only left-handed fermions interact through the weak interaction
61 as discovered by Wu in 1957 [11]. Similarly, the weak interaction is the only one that
62 also breaks the CP symmetry, which combines parity transformations and charge
63 conjugation. This is particularly interesting because all interactions are believed to
64 be invariant under the CPT transformation, which combines the CP transformation
65 and time reversal. Hence, breaking CP the weak interaction implies that the process
66 is also not invariant under time reversal transformations.

67 In 1968 Salam, Glashow and Weinberg unified the weak and electromagnetic forces
68 into a single theory, where the coupling constants of the electromagnetic, e , and
69 weak, g , interactions are related through the weak mixing angle, θ_W by the rela-
70 tion $g \sin \theta_W = e$ [2]. The electroweak symmetry is spontaneously broken by the
71 Higgs mechanism [12] and this causes the W^\pm and Z bosons to become massive (see
72 Tab. 1.2) and consequently the weak force has a very short range. In fact, using
73 Heisenberg's Principle, $\Delta E \Delta t > \hbar$, together with Einstein's formula $\Delta E = mc^2$,
74 which relates mass and energy, and knowing that the maximum space that a parti-
75 cle can cover in a time Δt is $r \sim c\Delta t$, qualitatively $r \sim \hbar/mc$. In this picture the
76 carriers of the weak force can travel $r \sim 2 \cdot 10^{-3}$ fm. In contrast, the photon must
77 be massless in the theory, which accounts for the long range of the electromagnetic
78 force. The EW interactions are divided into Charged Currents (CC) and Neutral
79 Currents (NC). In the first group, quarks and leptons interact with the W^\pm bosons,
80 producing decays such as $\mu^+(\mu^-) \rightarrow e^+ \nu_e \bar{\nu}_\mu (e^- \bar{\nu}_e \nu_\mu)$ and $n(\bar{n}) \rightarrow p e^- \bar{\nu}_e (\bar{p} e^+ \nu_e)$. The

study of these processes confirmed that only the left-handed (right-handed) component of fermions (anti-fermions) takes part in weak processes. The CC interactions have a peculiarity: they are the only interactions in the SM that violate flavour conservation at tree level, while any other interaction not conserving flavour has to proceed through higher order processes. The second group of EW interactions, NC, corresponds to diagrams mediated by a photon or a Z boson interacting with a fermion and its anti-fermion.

1.2 Flavour and the CKM matrix

“Flavour” in particle physics refers to the quark-lepton composition of a particle. The introduction of flavour quantum numbers was motivated in order to explain why some decays, although kinematically allowed, had never been observed. All leptons are assigned a quantum number $L_\ell = 1$ (where $\ell = e, \mu, \tau$), which in the SM is conserved by all interactions. This conservation is experimentally well established; for example decays like $\mu^- \rightarrow e^- \gamma$ have never been observed. In the hadronic sector particles carry flavour numbers described as:

- *Isospin*: $I_3 = 1/2$ for the up quark and $I_3 = -1/2$ for the down quark;
- *Strangeness*: $S = -(n_s - \bar{n}_s)$, where n_s and \bar{n}_s are the numbers of strange and anti-strange quarks respectively;
- *charmness, bottomness, topness*: in analogy to strangeness they are respectively defined as $C = -(n_c - \bar{n}_c)$, $B = -(n_b - \bar{n}_b)$, $T = -(n_t - \bar{n}_t)$.

As mentioned previously, in the SM the only interaction violating flavour conservation is the weak interaction when mediated by W^\pm bosons.

Measuring branching fractions of weak decays like $\pi \rightarrow \mu\nu_\mu$ and $K \rightarrow \mu\nu_\mu$, corresponding respectively to $ud \rightarrow \mu\nu_\mu$ and $us \rightarrow \mu\nu_\mu$ processes, suggested the existence of more than one coupling constant for different quarks. Nicola Cabibbo, in order to

106 preserve the universality of weak interactions, suggested that the differences could
 107 arise from the fact that the doublets participating in the weak interactions are an
 108 admixture of the mass eigenstates [2, 13]. He therefore introduced the Cabibbo an-
 109 gle, θ_c , proposing that eigenstates participating to the weak interaction are rotated
 110 with respect to the flavour eigenstates.

$$\begin{pmatrix} d_W \\ s_W \end{pmatrix} = \begin{pmatrix} \cos \theta_c & \sin \theta_c \\ -\sin \theta_c & \cos \theta_c \end{pmatrix} \begin{pmatrix} d \\ s \end{pmatrix} = \begin{pmatrix} \cos \theta_c \cdot d + \sin \theta_c \cdot s \\ \cos \theta_c \cdot s - \sin \theta_c \cdot d \end{pmatrix} \quad (1.1)$$

111 In a six quark system one angle is not sufficient to describe a rotation but the mixing
 112 can be generalised using a 3×3 unitary matrix, called the CKM matrix, from the
 113 names of Cabibbo, Kobayashi and Maskawa [13, 14]. The unitarity of the matrix
 114 is required to preserve the universality of the weak interaction. Theoretically, a
 115 $N \times N$ complex matrix depends on $2 \cdot N^2$ real parameters. Requiring unitarity
 116 ($AA^\dagger = A(A^*)^T = I$), the number of independent parameters left is

$$(N-1)^2 = \underbrace{\frac{1}{2}N(N-1)}_{\text{Number of mixing angles}} + \underbrace{\frac{1}{2}(N-1)(N-2)}_{\text{Number of complex phases}} . \quad (1.2)$$

117 Therefore a 3×3 matrix depends then on 4 real parameters: three real constants and
 118 one imaginary phase. The imaginary phase generates the CP-violation which was
 119 observed in weak interactions. Figure 1.2 displays examples of CC processes together
 with the CKM elements associated with their vertices. Equation 1.3 reports the most

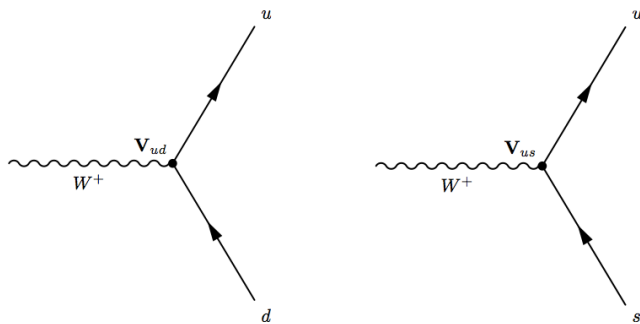


Figure 1.2: Feynman diagrams with CKM weights on weak interaction vertices as defined in Eq. 1.3.

recent measured values of its elements [2] together with the widely used Wolfenstein parametrisation which highlights the hierarchical structure of the matrix. In fact, elements on the diagonal, corresponding to transitions between quarks of the same generation, are approximately 1 and become smaller and smaller going farther from the diagonal. In the formula ρ , A , and λ are the real constants and η the imaginary phase and Eq. 1.4 shows how they are related to the three mixing angles; terms further from the diagonal are proportional to higher powers of λ .

$$V = \begin{pmatrix} V_{ud} & V_{us} & V_{ub} \\ V_{cd} & V_{cs} & V_{cb} \\ V_{td} & V_{ts} & V_{tb} \end{pmatrix} = \begin{pmatrix} 0.9743 \pm 0.0002 & 0.2253 \pm 0.0007 & 0.0035^{+0.0002}_{-0.001} \\ 0.2252 \pm 0.0007 & 0.9734 \pm 0.0002 & 0.00412^{+0.0011}_{-0.0005} \\ 0.0087 \pm 0.0003 & 0.0404^{+0.0011}_{-0.0005} & 0.99915^{+0.00002}_{-0.00004} \end{pmatrix}$$

$$= \begin{pmatrix} 1 - \lambda^2/2 & \lambda & A\lambda^3(\rho - i\eta) \\ -\lambda & 1 - \lambda^2/2 & A\lambda^2 \\ A\lambda^3(1 - \rho - i\eta) & A\lambda^2 & 1 \end{pmatrix} + O(\lambda^4) \quad (1.3)$$

128

$$\begin{aligned} \lambda &= \sin(\theta_{12}) = \sin(\theta_c) \\ A\lambda^2 &= \sin(\theta_{23}) \\ A\lambda^3(\rho - i\eta) &= \sin(\theta_{13})e^{i\delta} \end{aligned} \quad (1.4)$$

129 The unitarity of the CKM matrix imposes constraints to its elements of the form:

$$\sum_i |V_{ik}|^2 = 1 \text{ and } \sum_k V_{ik} V_{jk}^* = 0. \quad (1.5)$$

130 These correspond to constraints on three complex numbers, which can be viewed
131 as the sides of triangles in the (ρ, η) plane; these are called “unitarity triangles”.
132 The most commonly used unitarity triangle arises from $V_{ud}V_{ub}^* + V_{cd}V_{cb}^* + V_{td}V_{tb}^* = 0$.
133 Figure 1.3 shows a representation of such triangle together with a plot summarising
134 the most up-to-date experimental constraints to its parameters [15]. Due to these
135 unitarity constraints flavour-changing neutral currents are forbidden at tree level in
136 the SM.

137 The precise measurement of the parameters of the CKM matrix is a powerful sta-

¹³⁸ bility test of the SM and sets a solid basis for new physics searches in the flavour
¹³⁹ sector. One of the main goals of the LHCb experiment is to measure precisely the angle γ , which is currently the least constrained by measurements.

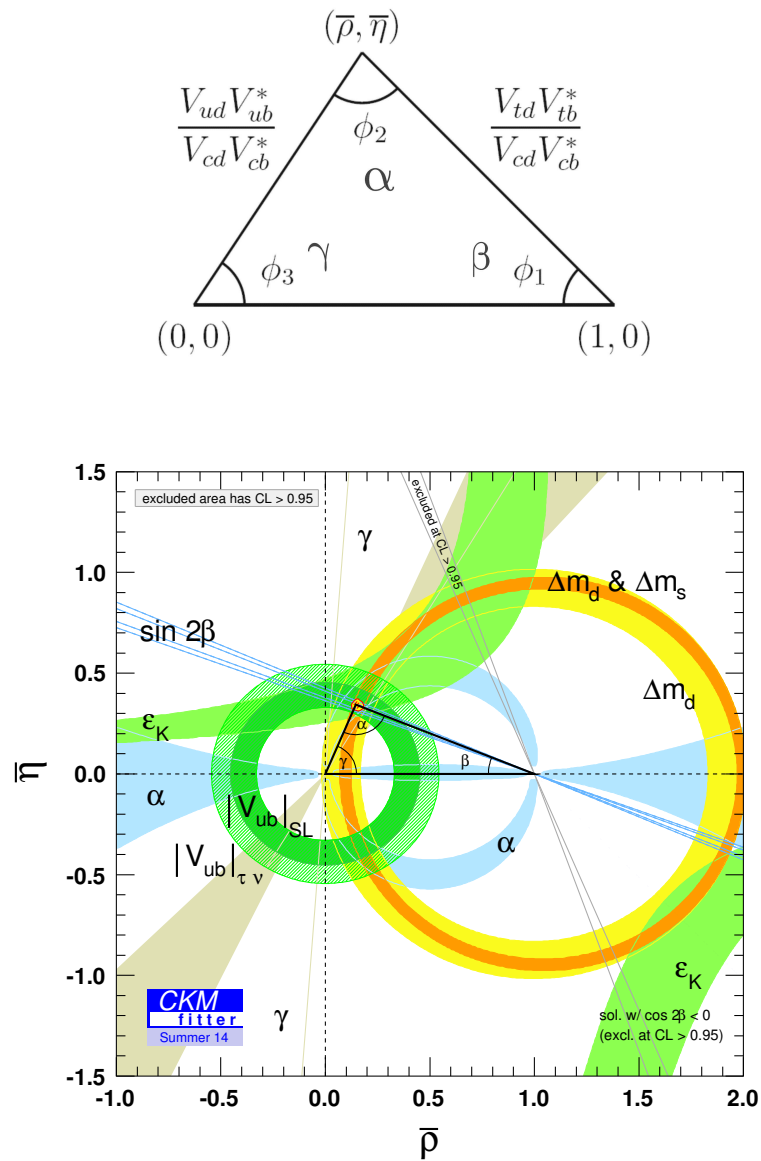


Figure 1.3: (top) A representation of the unitarity triangle and its parameters. (bottom) A summary of the most up-to-date measurements of the unitarity triangle parameters [15].

₁₄₁ 1.3 The puzzles of the SM

₁₄₂ Despite the experimental confirmation of many predictions of the SM, the theory has
₁₄₃ several limitations and is unable to account for some well-established experimental
₁₄₄ facts:

- ₁₄₅ • *Dark matter*: experimental evidence tells us that the content of visible matter
₁₄₆ in the universe is not sufficient to account for the observed rotation of galaxies [16]. The most natural way to solve the problem is the hypothesis of a form
₁₄₇ of matter that interacts with the gravitational field but not with the other SM
₁₄₈ interactions.
- ₁₅₀ • *Matter-antimatter asymmetry*: a large asymmetry is observed between the
₁₅₁ quantity of matter and antimatter in the universe, $O(10^{-9})$. Assuming that
₁₅₂ both were equally created in the initial state of the universe, a condition such
₁₅₃ as the violation of the CP symmetry is necessary to account for the observed
₁₅₄ imbalance. However, the magnitude of CP violation predicted by the SM,
₁₅₅ $O(10^{-20})$, is not sufficient to account for the observed asymmetry [17].
- ₁₅₆ • *Gravity*: even though the gravitational force was the first to be discovered
₁₅₇ this is not included in the SM. When introducing gravity in the framework of
₁₅₈ QFT the theory diverges. On the other hand gravity becomes irrelevant for
₁₅₉ the small masses of particles and can be neglected to a good approximation at
₁₆₀ the EW energy scale. Many attempts have been made but there is not yet a
₁₆₁ consistent theoretical framework through which gravity can be introduced in
₁₆₂ the SM [18].
- ₁₆₃ • *Neutrino oscillation*: measurements of solar and atmospheric neutrinos, as
₁₆₄ well as neutrinos from nuclear reactors, have established that neutrinos can
₁₆₅ change flavour while propagating in space. This is not predicted in the SM, in
₁₆₆ fact in the SM neutrinos are massless, while an oscillation requires a non-zero
₁₆₇ mass [19, 20, 21, 22].

- 168 • *The hierarchy problem*: the mass of a scalar (spin 0) particle, such as the
169 Higgs boson, suffers from quantum corrections due to the physics at high
170 energy scales. As new physics can appear anywhere up to the Planck scale,
171 $\sim 10^{19}$ GeV, at which gravity cannot be neglected any more, these corrections
172 can be very large and it would require a high level of fine-tuning for them to
173 cancel out and give such a small value as the one measured for the Higgs Mass,
174 ~ 126 GeV/ c^2 [23, 3].

175 In conclusion, even though the SM has been very successful in describing the prop-
176 erties of the observed particles and their interactions so far, because of its many
177 puzzles, it is believed only to be part of a more general theory or only to be valid
178 up to a certain energy scale.

179 1.3.1 The flavour problem

180 Flavour Changing Charged Currents (FCCC) that are mediated by the W^\pm bosons
181 are the only sources of flavour changing interaction in the SM and, in particular, of
182 generation changing interactions, where a quark or a lepton of a family transforms
183 into one of another family. Another class of processes is the Flavour Changing
184 Neutral Currents (FCNCs), e.g. transitions from a b quark with a charge of -1/3 to
185 a s or d quark with the same charge. Examples of FCNC transitions in the quark
186 and lepton sector are shown in Fig. 1.4. FCNCs are experimentally observed to be
187 highly suppressed which derives from the unitarity of the CKM matrix, however
188 there is no fundamental reason why there cannot be FCNCs at tree level. In fact
189 the CKM matrix could be part of a larger matrix involving for example quark-
190 lepton terms. This would introduce new sources of FCNCs but could also allow for
191 natural explanations of the equality of the proton and electron charges. Furthermore,
192 the observation of neutrino oscillation proves that flavour is not always conserved
193 suggesting flavour structures beyond the SM. Finally, the values of the terms of the
194 CKM matrix and the PMNS matrix [24, 25], which is the mixing-matrix equivalent to
195 the CKM in the lepton sector, are not explained in the SM but have to be measured

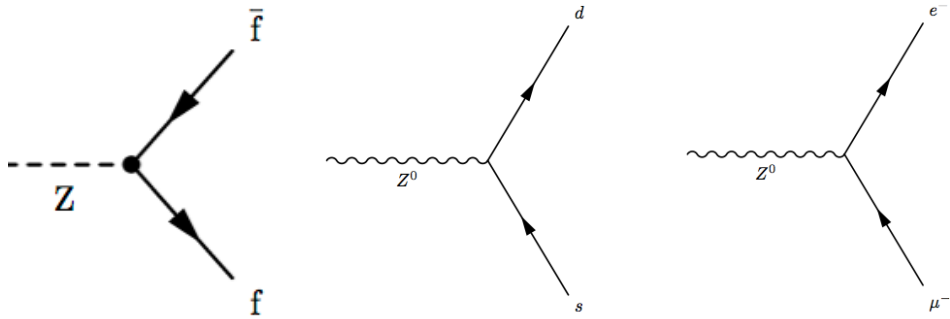


Figure 1.4: Feynman diagrams of a neutral current allowed in the SM (left), where f represents any fermion, and FCNCs processes forbidden in the SM (center-right).

¹⁹⁶ experimentally. These open problems motivate searches for flavour symmetries and
¹⁹⁷ deeper motivations for flavour conservation.

¹⁹⁸ 1.4 Beyond the Standard Model

¹⁹⁹ From the previous sections it is evident that, despite the great success of the SM,
²⁰⁰ there is a need to explore theories Beyond the SM (BSM). Among the most promis-
²⁰¹ ing approaches there are those involving Super-Symmetry (SUSY) [26] and extra-
²⁰² dimensions [27]. In SUSY new degrees of freedom are introduced to suppress the
²⁰³ diverging terms of the Higgs mass. This theory assumes that for each fermion there
²⁰⁴ is a corresponding boson and, since bosons and fermions contribute with opposite
²⁰⁵ sign to the mass term, these would naturally cancel out. Supersymmetry also pro-
²⁰⁶ vides a candidate for dark matter. In fact the lightest Super-Symmetric particle, the
²⁰⁷ neutralino, which in R-parity [28] conserving variants of the theory must be stable,
²⁰⁸ is a weakly interacting potentially heavy particle. The idea to introduce extra
²⁰⁹ dimensions was triggered by the fact that gravity is not relevant in particle physics
²¹⁰ but it would be natural if all forces had similar strength. By adding extra dimen-
²¹¹ sions to the normal three spatial dimensions, one can restore the strength of gravity,
²¹² as this could be dispersed by the wider space available. In all these approaches con-
²¹³ straints to masses and couplings must be imposed to maintain compatibility with
²¹⁴ the SM at the electroweak scale and the existing experimental observations.

²¹⁵ 1.4.1 Flavour and BSM theories

²¹⁶ Most BSM theories predict processes violating flavour conservation. Therefore, the
²¹⁷ observation or non-observation of these processes can give important information
²¹⁸ about new physics. BSM theories can be classified according to the amount of
²¹⁹ flavour violation they introduce. The first class of models to consider is that with
²²⁰ Minimal Flavour Violation (MFV). These are models in which the only sources of
²²¹ flavour changing transitions are governed by the CKM matrix and the CKM phase
²²² is the only source of CP violation. This definition is driven by the fact that usually
²²³ a solution of the hierarchy problem is expected at the TeV scale, while the very
²²⁴ small amount of flavour violation observed in measurements seems to indicate that
²²⁵ the SM would remain valid up to much higher energy scales. It is therefore assumed
²²⁶ that new physics must respect flavour symmetry principles, which also makes these
²²⁷ types of models naturally compatible with the SM. Examples of such models include
²²⁸ the MSSM with minimal flavour violation and the SM with one extra-dimension.
²²⁹ Reviews of MFV models are presented in Refs. [29, 30]. A powerful test of MFV
²³⁰ is provided by the study of ratios between $b \rightarrow d$ and $b \rightarrow s$ transitions, because
²³¹ their hamiltonians share the same structure. One particularly important example
²³² is the ratio between the decay rates of B^0 and B_s^0 into dimuons [31], as this is a
²³³ purely leptonic decay free from hadronic uncertainties. In the SM such ratios are
²³⁴ approximately equal to $|V_{td}/V_{ts}| \sim 1/25$, only modified by phase space and hadronic
²³⁵ matrix elements, while they can take very different values in non-MFV models.

²³⁶ In the quest for new physics an important role is also played by simplified models
²³⁷ as an intermediate model building step. Instead of constructing theories valid up
²³⁸ to the GUT scale one can consider simplified models, where the SM is extended by
²³⁹ the addition of new degrees of freedom with a limited number of parameters. Such
²⁴⁰ models are easier to constrain but can nevertheless point in the right direction to
²⁴¹ build more complete theories. The choice of the new sector to add can be driven
²⁴² by the need to explain existing tensions between measurements and SM predictions
²⁴³ or by theoretical prejudice. Two models especially relevant when studying rare

244 decays, which are the main topic of this thesis, are Z' -penguins and leptoquarks.
245 A Z' -penguin is a FCNC process involving a neutral field arising from an extra
246 $U(1)$ gauge symmetry, for example $U(1)_{B-L}$, where B and L are the baryon and
247 lepton numbers. As for the SM penguins, the Z' field contributes in loops causing
248 modifications of the effective couplings with respect to the SM. A survey of Z' models
249 can be found in Ref. [32]. Leptoquarks are bosonic particles that carry both quark
250 and lepton flavour quantum numbers, which for simplicity are assumed to be scalar.
251 A tree level exchange of a leptoquark induces processes such as $b \rightarrow (s, d)\ell^+\ell^-$,
252 and therefore can result in an enhancement of their decay rates with respect to the
253 SM [33]. Leptoquarks would also provide a natural explanation for non-universal
254 couplings to leptons.

255 1.5 Rare decays: a tool to search for new physics

256 In the Standard Model FCNC processes are forbidden at tree level but can occur
257 through loop diagrams such as penguin or W box diagrams (see Fig. 1.5). The
258 branching fractions of decays going through these processes are small, typically
259 $\sim 10^{-6}$ or lower, and therefore they are called “rare decays”. Additional contribu-
260 tions to the virtual loops are not necessarily suppressed with respect to the SM
261 component which makes these decays very sensitive to new physics. This approach
262 to new physics searches is interesting as new particles could be at high mass scales
263 that are not accessible via direct production at colliders but their effect could be
264 observed in loops. Radiative and penguin decays are particularly interesting because
265 they are theoretically well understood, which allows precise comparisons with mea-
266 surements. Furthermore, they provide a large quantity of observables that can be
267 affected by new physics, not only decay rates, but also CP asymmetries and angular
268 observables such as forward-backward asymmetries. The joint analysis of different
269 observables can help to build a consistent picture and rule out specific models.

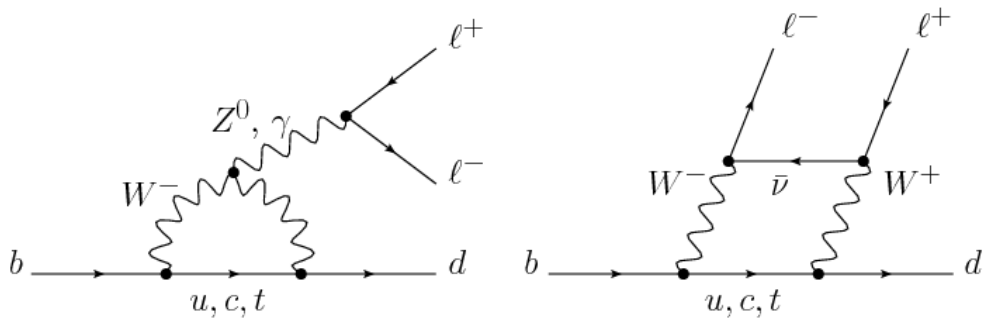


Figure 1.5: Loop Feynmann diagrams allowing $b \rightarrow d$ FCNC processes: penguin diagram (left) and W box (right).

270 1.5.1 Theoretical framework: the effective Hamiltonian

271 Rare decays of b hadrons are governed by an interplay between weak and strong
272 interactions. The large masses of the W^\pm and Z^0 bosons and top quark compared
273 to that of the b quark allow the construction of an effective theory that divides the
274 problem of calculating weak decay amplitudes into two parts: “short-distance” and
275 “long-distance” effects separated at an energy scale μ . The first part, dealing with
276 short distance physics, handles perturbative contributions due to energy scales above
277 the b mass. The second part typically deals with non-perturbative contributions.
278 A classic example of an effective theory is the Fermi theory of weak interactions
279 which describes the β decay in terms of a four-fermion interaction, where the short
 distance physics is hidden into a point-like vertex as illustrated in Fig. 1.6.

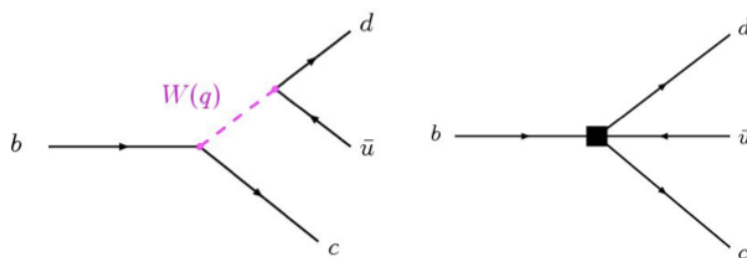


Figure 1.6: Example of a Fermi theory in which the full theory (left) is divided into (right) a short distance contribution, hidden in the vertex, and a long distance contribution.

281 The effective hamiltonian [34] relevant to $b \rightarrow s/d\gamma$ and $b \rightarrow s/d\ell^+\ell^-$ transitions
282 can be written as:

$$\mathcal{H}_{eff} = \frac{-4G_F}{\sqrt{2}} \left[\lambda_q^t \sum C_i(\mu, M) \mathcal{O}_i(\mu) + \lambda_q^u \sum C_i(\mu, M) (\mathcal{O}_i(\mu) - \mathcal{O}_i^u(\mu)) \right], \quad (1.6)$$

283 where G_F denotes the Fermi coupling constant and the λ constants are the CKM
284 factors, $\lambda_q^t = V_{tb}V_{tq}^*$ and $\lambda_q^u = V_{ub}V_{uq}^*$. In $b \rightarrow s$ quark transitions, which are the main
285 topic of this thesis, the doubly Cabibbo-suppressed contributions can be neglected
286 as $\lambda_s^u \ll \lambda_s^t$. To obtain this formula the Operator Product Expansion (OPE) [35]
287 method is used, which implements a summation over all contributing operators
288 weighted by corresponding constants called Wilson coefficients. In this Hamiltonian
289 the long-distance contributions are described by the operators, \mathcal{O}_i , while the short-
290 distance physics is encoded in the Wilson Coefficients, C_i . Operators and coefficients
291 are evaluated at the renormalisation scale μ . Any particle that contributes to the
292 decay and has a mass greater than the scale μ will affect the value of at least one of
293 the Wilson coefficients, including SM particles as the top quark.

294 In order to describe SM processes the effective theory must be matched with the
295 SM by requiring the equality between each term in effective theory and the full the-
296 oretical calculation at a matching scale, typically the EW scale (μ_W). Then, using
297 the scale independence of the effective Hamiltonian, one can derive a renormalisa-
298 tion group equation for the Wilson Coefficients [36]. Taking into account only SM
299 contributions and using $\mu_W = m_b$, the Wilson Coefficients have values:

$$C_7^{SM} = -0.3, \quad C_9^{SM} = 4.2, \quad C_{10}^{SM} = -4.2 \quad (1.7)$$

300 and new physics contributions appear in the Wilson Coefficients in the form of
301 additive factors:

$$C_i = C_i^{NP} + C_i^{SM}. \quad (1.8)$$

302 The amplitudes of exclusive hadronic decays can be calculated as the expectation
303 values of the effective Hamiltonian. Given an initial state I and a final state F

³⁰⁴ (e.g. $I = B^0$ and $F = K^{*0}\mu^+\mu^-$) the decay amplitude can be calculated as

$$A(I \rightarrow F) = \langle I | \mathcal{H}_{eff} | F \rangle = \\ = \frac{G_F}{\sqrt{2}} \sum V_{CKM}^i \underbrace{C_i(\mu)}_{\substack{\text{Perturbative} \\ \text{Includes new physics}}} \cdot \underbrace{\langle I | \mathcal{O}_i(\mu) | F \rangle}_{\substack{\text{Non-perturbative} \\ \text{Known physics}}}, \quad (1.9)$$

³⁰⁵ where $\langle I | \mathcal{O}_i(\mu) | F \rangle$ are the hadronic matrix elements also called “form factors”.
³⁰⁶ These can be evaluated using non perturbative methods such as lattice calculations.
³⁰⁷ However, due to the limitations of these methods, they represent the dominant
³⁰⁸ source of uncertainty in theoretical calculations.

³⁰⁹ 1.5.2 Operators

³¹⁰ Separating the left- and right-handed components the effective Hamiltonian is

$$\mathcal{H}_{eff} = \frac{4G_F}{\sqrt{2}} V_{tb} V_{ts}^* \frac{\alpha_e}{4\pi} \sum_{i=1}^{10} [C_i \mathcal{O}_i + C'_i \mathcal{O}'_i]. \quad (1.10)$$

³¹¹ A complete basis is given by a set of 10 operators, where $\mathcal{O}_{1,2}$ are the tree level
³¹² W operators; $\mathcal{O}_{3-6,8}$ are penguin diagrams mediated by gluons; and $\mathcal{O}_{7,9,10}$, which
³¹³ are the operators that are relevant for radiative and leptonic penguin processes are
³¹⁴ defined as [31]:

$$\begin{aligned} \mathcal{O}_7 &= \frac{m_b}{e} (\bar{s}\sigma^{\mu\nu} P_R b) F_{\mu\nu}, & \mathcal{O}'_7 &= \frac{m_b}{e} (\bar{s}\sigma^{\mu\nu} P_L b) F_{\mu\nu}, \\ \mathcal{O}_9 &= (\bar{s}\gamma_\mu P_L b)(\bar{\ell}\gamma^\mu \ell), & \mathcal{O}'_9 &= (\bar{s}\gamma_\mu P_R b)(\bar{\ell}\gamma^\mu \ell), \\ \mathcal{O}_{10} &= (\bar{s}\gamma_\mu P_L b)(\bar{\ell}\gamma^\mu \gamma_5 \ell), & \mathcal{O}'_{10} &= (\bar{s}\gamma_\mu P_R b)(\bar{\ell}\gamma^\mu \gamma_5 \ell), \end{aligned} \quad (1.11)$$

³¹⁵ where $P_{L/R} = (1 \mp \gamma_5)/2$ denote the left- and right-handed chiral projections and
³¹⁶ $F_{\mu\nu}$ is the electromagnetic field tensor. The \mathcal{O}' operators correspond to right-handed
³¹⁷ coupling obtained by swapping P_R and P_L in the equations. In the SM, as well as
³¹⁸ in MFV models where the flavour violation is entirely ruled by the CKM matrix,
³¹⁹ the C' Wilson Coefficients are suppressed by the strange coupling, $C'_i \sim (m_s/m_b)C_i$.

320 The operator \mathcal{O}_7 relates to penguin diagrams that are mediated via a photon. It
321 represents the dominant contribution to the radiative $b \rightarrow s\gamma$ transition and con-
322 tributes to $b \rightarrow s\ell^+\ell^-$ processes when the virtual photon decays into a dilepton
323 pair. The semileptonic \mathcal{O}_9 and \mathcal{O}_{10} correspond to penguin diagrams mediated by
324 a Z^0 boson and W mediated box diagrams. These are the dominant contributions
325 in semileptonic $b \rightarrow s\ell^+\ell^-$ decays. The vertices corresponding to the radiative and
semileptonic operators are illustrated in Fig. 1.7

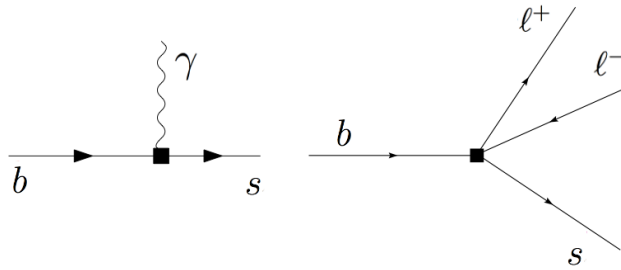


Figure 1.7: Interaction vertices corresponding to the radiative (left) and semileptonic (right) operators.

326

327 It is also common to express the semileptonic operators in a basis with left and right
328 projected leptons

$$\begin{aligned} \mathcal{O}_{LL} &= (\mathcal{O}_9 - \mathcal{O}_{10})/2 & \mathcal{O}_{LR} &= (\mathcal{O}_9 + \mathcal{O}_{10})/2 \\ \mathcal{O}_{RR} &= (\mathcal{O}'_9 - \mathcal{O}'_{10})/2 & \mathcal{O}'_{RL} &= (\mathcal{O}'_9 + \mathcal{O}'_{10})/2 \end{aligned} \quad (1.12)$$

329 where the Wilson Coefficients are redefined as

$$\begin{aligned} C_{LL} &= C_9 - C_{10}, & C_{LR} &= C_9 + C_{10}, \\ C_{RR} &= C'_9 - C'_{10}, & C'_{RL} &= C'_9 + C_{10}. \end{aligned} \quad (1.13)$$

330 This basis is particularly useful in frameworks where BSM physics at a high mass
331 scale respects the $SU(2)_W$ part of the SM gauge symmetry group. Finally, in the
332 picture presented in this section all operators were considered as universal with
333 respect of the flavour of the involved leptons. However, BSM models often contain
334 sources of lepton universality violation leading to a split of the same operators
335 depending on the lepton considered: $C_i \rightarrow C_i^e, C_i^\mu, C_i^\tau$ and $\mathcal{O}_i \rightarrow \mathcal{O}_i^e, \mathcal{O}_i^\mu, \mathcal{O}_i^\tau$.

336 1.5.3 Phenomenology of $b \rightarrow s\ell^+\ell^-$ decays

337 Semileptonic b hadron decays are characterised by two kinematic regimes which are
 338 treated theoretically in different ways; Table 1.3 shows a scheme of the q^2 spec-
 339 trum. The ‘high q^2 ’ is the region of low hadron recoil, $q^2 > 15 \text{ GeV}^2/c^4$, and is
 340 characterised by the energy of the hadron being less than the energy scale of QCD in-
 341 teractions within the meson, $\Lambda_{QCD} \sim 1 \text{ GeV}$. In this region theoretical calculations
 342 of B meson decays can be simplified by working in the heavy quark limit, $m_b \rightarrow \infty$.
 343 In this limit a Heavy Quark Effective Theory (HQET) [37] can be constructed in
 344 which the heavy quark interacts only via ‘soft’ hadronic processes and an OPE in
 345 $1/m_b$ is valid. The ‘low q^2 ’ region is where the light spectator quark is energetic
 346 and cannot be neglected. Furthermore, the light quark interacts not only via ‘soft’
 347 hadronic processes, as in HQET, but also via the so-called ‘collinear’ hadronic pro-
 348 cesses. The boundary of this region can be set at $\sim 7 \text{ GeV}^2/c^4$ which corresponds
 349 to the threshold for $c\bar{c}$ production, $(2m_c)^2$. In this region the hadronic interactions
 350 are handled by expanding in terms of the energy of the emitted energetic hadron,
 351 $1/E_h$, forming the so-called Soft-Collinear Effective Theory (SCET) [38]. In both
 352 regions decay rates can be predicted using the different methods and the biggest un-
 353 certainties come from the limited knowledge of hadronic transition matrix elements.
 354 The intermediate region is characterised by the presence of charmonium resonances,
 355 produced though tree level $b \rightarrow \bar{c}cs$ transitions and no precise theoretical calculation
 356 is available [39].

357 As can be seen in Fig. 1.8 the very low q^2 region is characterised by a peak due to
 358 the virtual photon contribution, associated with C_7 . In the region $1 - 6 \text{ GeV}^2/c^4$ the

Table 1.3: A scheme of the q^2 spectrum.

q^2	$E_{K^{*0}}$	Regime	Valid theory
$\sim 0 \text{ GeV}^2/c^4$	$\sim m_B$	Max. recoil	SCET
$< 6 \text{ GeV}^2/c^4$	$>> \Lambda_{QCD}$	Large recoil	
$q^2 \sim m_{J/\psi, \psi(2S)}^2$	$\sim 3 \text{ GeV}$	$c\bar{c}$ resonances	–
$q^2 > 15 \text{ GeV}^2/c^4$	$E_{K^{*0}} \sim \Lambda_{QCD}$	Low recoil	HQET
$q^2 = (m_B - m_K^{*0})^2$	$E_{K^{*0}} \sim 0$	Zero recoil	

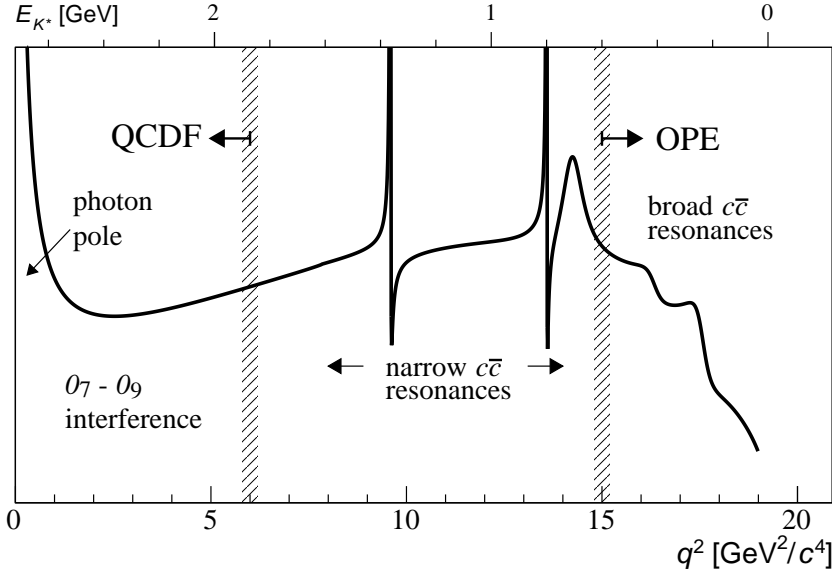


Figure 1.8: A typical q^2 spectrum of $b \rightarrow s\ell^+\ell^-$ processes characterised by the photon pole at low q^2 , charmonium resonances at central q^2 and broad resonances at high q^2 [31].

359 interference between C_7 and C_9 becomes large, yielding sensitivity to new physics in
 360 C_9 . The $7 - 15$ GeV^2/c^4 interval is dominated by the charmonium resonances, J/ψ
 361 and $\psi(2S)$. Although these decays can be experimentally vetoed in principle char-
 362 monia affect the entire q^2 space. Finally, at high q^2 broad charmonium resonances
 363 can contribute, like those observed by LHCb in $B^+ \rightarrow K^+\mu^+\mu^-$ decays [40].

364 1.5.4 Observables in $b \rightarrow s\ell^+\ell^-$ decays

365 Rare decays and especially semileptonic $b \rightarrow s\ell^+\ell^-$ processes offer a number of ob-
 366 servables which can be used to study BSM models. The most direct effects appear
 367 in decay rates that can be enhanced by new physics but the precision on these
 368 measurements is often limited by uncertainties on the non-perturbative part of the
 369 calculations. Therefore, it is important to also look for different observables. One
 370 important class of observables are angular quantities that can often carry comple-
 371 mentary information with respect to branching ratio measurements. The most basic
 372 of these observable are forward-backward asymmetries that characterise the angular

³⁷³ distribution of final particles. For the $B^0 \rightarrow K^* \mu^+ \mu^-$ decay combinations of ob-
³⁷⁴ servables have been proposed that are independent of form factor uncertainties at
³⁷⁵ leading order order [31].

³⁷⁶ Another way to build safe observables is to construct ratios between similar decays,
³⁷⁷ in which uncertainties due to the hadronisation process cancel out. These observ-
³⁷⁸ ables include the R_H ratios, between B^0 decays into electrons and muons, that are
³⁷⁹ described in detail in Ch. 5. It is also interesting to compare decays which proceed
³⁸⁰ via the same fundamental process but where the spectator quark has a different
³⁸¹ flavour. This is the case of $B^+ \rightarrow K^+ \mu^+ \mu^-$ and $B^0 \rightarrow K_s^0 \mu^+ \mu^-$ decays, which are
³⁸² both $b \rightarrow s$ transitions where the spectator quark is an u quark in the first case
³⁸³ and a d quark in the second. The normalised difference of the branching fractions
³⁸⁴ of these decays is called isospin asymmetry.

³⁸⁵ 1.6 Experimental status

³⁸⁶ To set the background for the analyses described in this thesis, this section reports a
³⁸⁷ brief review of recent results of new physics searches involving rare decays or lepton
³⁸⁸ flavour violation. Among these, results recently obtained by the LHCb experiment
³⁸⁹ show a series of anomalies with respect to the SM that have the potential to yield
³⁹⁰ to BSM scenarios.

³⁹¹ 1.6.1 Dimuon decays of b hadrons

Decays of B mesons into a pair of muons are two-body decays where the two muons are back to back in the hadron rest frame. The simple signatures of these decays makes them easy to study and the fact that they are unaffected by hadronic physics in the final state makes predictions very clean and precise. Therefore these are essential tests of the SM. The $B^0 \rightarrow \mu^+ \mu^-$ and $B_s^0 \rightarrow \mu^+ \mu^-$ decays are FCNCs that can only happen via loops and furthermore they are CKM-suppressed, which makes

them particularly rare. In addition to that the decay of a pseudo-scalar B meson into two muons has a significant helicity suppression. The latest SM predictions for these decay rates are [41]:

$$\mathcal{B}(B_s^0 \rightarrow \mu^+ \mu^-) = (3.65 \pm 0.23) \times 10^{-9} \text{ and} \quad (1.14)$$

$$\mathcal{B}(B^0 \rightarrow \mu^+ \mu^-) = (1.06 \pm 0.09) \times 10^{-10}. \quad (1.15)$$

The uncertainties on these values are dominated by the knowledge of the decay constants and CKM-elements. BSM models can produce significant enhancement to these decay rates and the measurement of their ratio is a stringent test of the MFV hypothesis. A combination of the LHCb and CMS results measured the values [42]:

$$\mathcal{B}(B_s^0 \rightarrow \mu^+ \mu^-) = (2.8^{+0.7}_{-0.6}) \times 10^{-9} \text{ and} \quad (1.16)$$

$$\mathcal{B}(B^0 \rightarrow \mu^+ \mu^-) = (3.9^{+1.6}_{-1.4}) \times 10^{-10}. \quad (1.17)$$

Neither decay had been previously observed, while now the B_s^0 decay is observed with a significance of 6σ and evidence for the B^0 decay is found at 3σ significance level. The measured branching fractions are compatible with SM predictions within 2σ and put strong constraints on the available parameter-space for BSM theories. Figure 1.9 shows the fit the dimuon invariant mass of B meson candidates where the peaks of the two decays are visible.

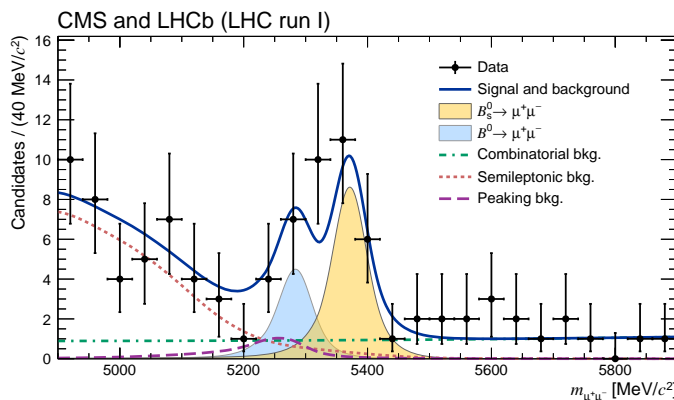


Figure 1.9: Dimuon invariant mass of B candidates showing peaks corresponding $B_s^0 \rightarrow \mu^+ \mu^-$ and $B^0 \rightarrow \mu^+ \mu^-$ decays [42].

³⁹⁸ 1.6.2 Semileptonic $b \rightarrow s\ell^+\ell^-$ decays of b hadrons

³⁹⁹ At the LHC it is possible to collect large data samples of semileptonic decays, es-
⁴⁰⁰ pecially those with muons in the final state. Many branching fractions of semilep-
⁴⁰¹ tonic B meson decays were recently measured at the LHCb experiment, including
⁴⁰² $B \rightarrow K\mu^+\mu^-$, $B \rightarrow K^{*0}\mu^+\mu^-$ and $B_s^0 \rightarrow \phi\mu^+\mu^-$ [43, 44, 45]. Baryon decays were
⁴⁰³ also studied at LHCb: including the rare $\Lambda_b \rightarrow \Lambda\mu^+\mu^-$ decay [1], whose analysis is
⁴⁰⁴ described in this thesis. In contrast to purely leptonic decays, SM predictions for
⁴⁰⁵ semileptonic decays are affected by the knowledge of hadronic form factors, which
⁴⁰⁶ results in relatively large uncertainties, $\mathcal{O}(30\%)$. As a result measurements are now
⁴⁰⁷ typically more precise than predictions.

⁴⁰⁸ Among the measurements of angular observables that can be affected by new physics,
⁴⁰⁹ particular interest was raised by the measurement of a set of observables in $B^0 \rightarrow$
⁴¹⁰ $K^{*0}\mu^+\mu^-$ decays, free from form factors uncertainties at leading order [46]. Most
⁴¹¹ of the measurements are found to be in agreement with SM predictions with the
⁴¹² exception of the P'_5 observable, shown in Fig. 1.10, which presents a local 3.7σ de-
⁴¹³ viation confirmed by a recent analysis with higher statistics [47]. Attempts to build
⁴¹⁴ a consistent picture point to a new physics contribution to the Wilson Coefficient
⁴¹⁵ C_9 [48]. An angular analysis of $B^+ \rightarrow K^+\mu^+\mu^-$ decays was also performed, where
observables are found to be compatible with SM predictions [49]. Other observables

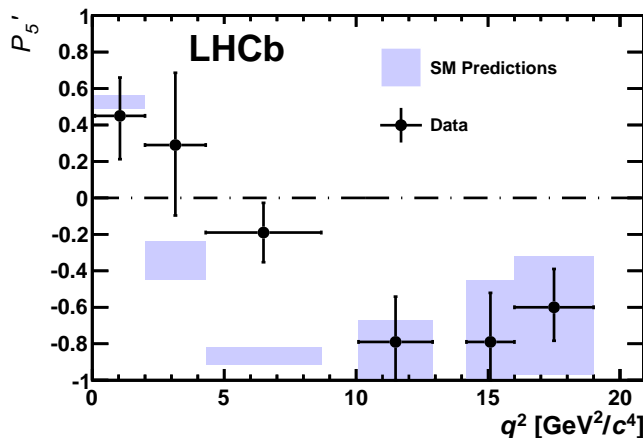


Figure 1.10: Measurement of the P'_5 observable as a function of q^2 , showing a tension with SM predictions in the 2–6 GeV^2/c^4 region [46].

	$B^0 \rightarrow K^+ \mu^+ \mu^-$		$B^0 \rightarrow K^{*0} \mu^+ \mu^-$	
	1.1–6 [GeV $^2/c^4$]	15.0–22.0 [GeV $^2/c^4$]	1.1–6 [GeV $^2/c^4$]	15.0–19.0 [GeV $^2/c^4$]
\mathcal{A}_{CP}	0.004 \pm 0.028	-0.005 \pm 0.030	0.094 \pm 0.047	-0.074 \pm 0.044
\mathcal{A}_I	-0.10 $^{+0.08}_{-0.09}$ \pm 0.02	-0.09 \pm 0.08 \pm 0.02	0.00 $^{+0.12}_{-0.10}$ \pm 0.02	0.06 $^{+0.10}_{-0.09}$ \pm 0.02

Table 1.4: Measurement of CP and isospin asymmetry in $B^0 \rightarrow K^{*0} \mu^+ \mu^-$ decays from the LHCb experiment [31].

for which the sensitivity to form factors effects is reduced are the CP asymmetry between B and \bar{B} decays, \mathcal{A}_{CP} , and the isospin asymmetry between B^0 and B^+ decays, \mathcal{A}_I . Due to the small size of the corresponding CKM elements, CP asymmetries of $B^0 \rightarrow K^{(*)} \mu^+ \mu^-$ decays are tiny in the SM, $O(10^{-3})$. In BSM models new sources of CP violation can arise and therefore \mathcal{A}_{CP} measurements are a powerful test of the SM. The isospin asymmetry is not zero in the SM due to isospin breaking effects in the form factors. This is expected to be $\sim 1\%$ at low q^2 and increase to $\sim 10\%$ as q^2 tends to zero. The LHCb experiment, using the full dataset collected in Run I, corresponding to an integrated luminosity of 3 fb $^{-1}$ and $\sim 10^9$ B decays, measured both of these asymmetries to be consistent with zero [43, 50], as reported in Tab. 1.4. Recently, progress was made measuring also electron channels. The branching fraction of the $B^0 \rightarrow K^{*0} e^+ e^-$ decay was measured to be $(3.1 \pm 1.3) \times 10^{-7}$ in the dilepton mass interval 30–1000 MeV/ c^2 [51]. Furthermore, for the first time angular observables were measured for this decay and found to be consistent with SM predictions [52].

Given the wide set of available measurements, theorists have implemented global fits including results from rare decays analyses, as well as inputs from B_s^0 mixing and Higgs measurements, in order to understand if the existing anomalies could be caused by a common factor. The results of such global fits agree that there is a tension with respect to the SM at the level of 3–4 standard deviations, depending on the set of assumptions made. In particular they favour a shift $C^{NP} \sim -1$ to the C_9 Wilson Coefficient, related with the penguin diagram mediated by a Z^0 boson [53, 48, 54].

439 1.6.3 Lepton Flavour Violation searches

440 Several Lepton Flavour Violation (LFV) searches are linked to rare decays as they
 441 involve small branching ratios in the SM that can be enhanced by BSM physics. Lep-
 442 ton flavour conservation is experimentally well-established measuring the branching
 443 ratios of decays of muons into electrons and no neutrinos, but has no strong the-
 444 oretical explanation in the context of the SM. In fact it is already observed that
 445 flavour is not conserved in neutrino oscillations. The best-studied decays violating
 446 lepton flavour are rare muon decays including $\mu^+ \rightarrow e^+ \gamma$ and $\mu^+ \rightarrow e^+ e^- e^+$. Since
 447 muons can be abundantly produced and the final states are simple, these decays
 448 provide the best constraints to LFV. The present best upper limits are 1.2×10^{-11}
 449 for the radiative decay and 1.0×10^{-12} for $\mu^+ \rightarrow e^+ e^- e^+$ obtained respectively by
 450 the MEGA [55] and SINDRUM [56] experiments. Several LFV searches in the B
 451 sector have recently been performed at the LHCb experiment including decays such
 452 as $B^0 \rightarrow e\mu$ [57] and τ decays such as $\tau \rightarrow \mu^+ \mu^- \mu$ [58]. None of these searches has
 453 found evidence of new physics so far and therefore they set limits, constraining the
 454 parameter space available for BSM models. Figure 1.11 shows a summary of the
 455 best limits set at different times on LFV searches [59].

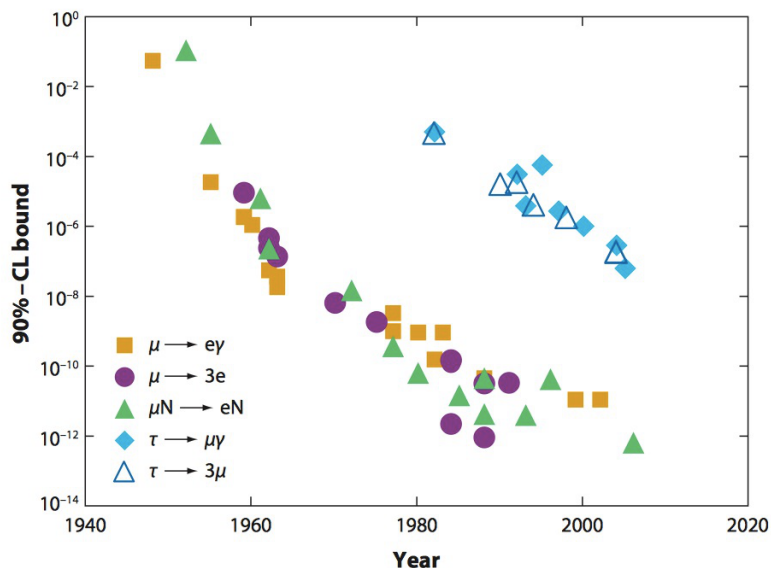


Figure 1.11: Summary of limits set in LFV searches as a function of time [59].

456

CHAPTER 2

457

458

The LHCb detector at the Large Hadron Collider

459

460

2.1 The Large Hadron Collider

461 The Large Hadron Collider (LHC) [60] is a synchrotron particle accelerator with a
462 circumference of 27 km located about 100 m underground at CERN in the surround-
463 ings of Geneva, Switzerland. Two proton beams circulate in opposite directions
464 around the ring and cross each other in four points, in which particle detectors are
465 placed. These include two general-purpose detectors, ATLAS and CMS, sitting on
466 opposites sides of the ring and two smaller detectors, ALICE and LHCb that are
467 designed to study specific topics (see Fig. 2.1).

468 Each beam consists of a series of proton bunches, up to a maximum of 2835. Each
469 bunch consists of about 10^{11} protons and the bunch spacing is such that the nominal
470 bunch crossing rate is 40 MHz. The beams are injected into pre-accelerators and
471 then pass into the LHC through the CERN acceleration system shown in Fig. 2.1.

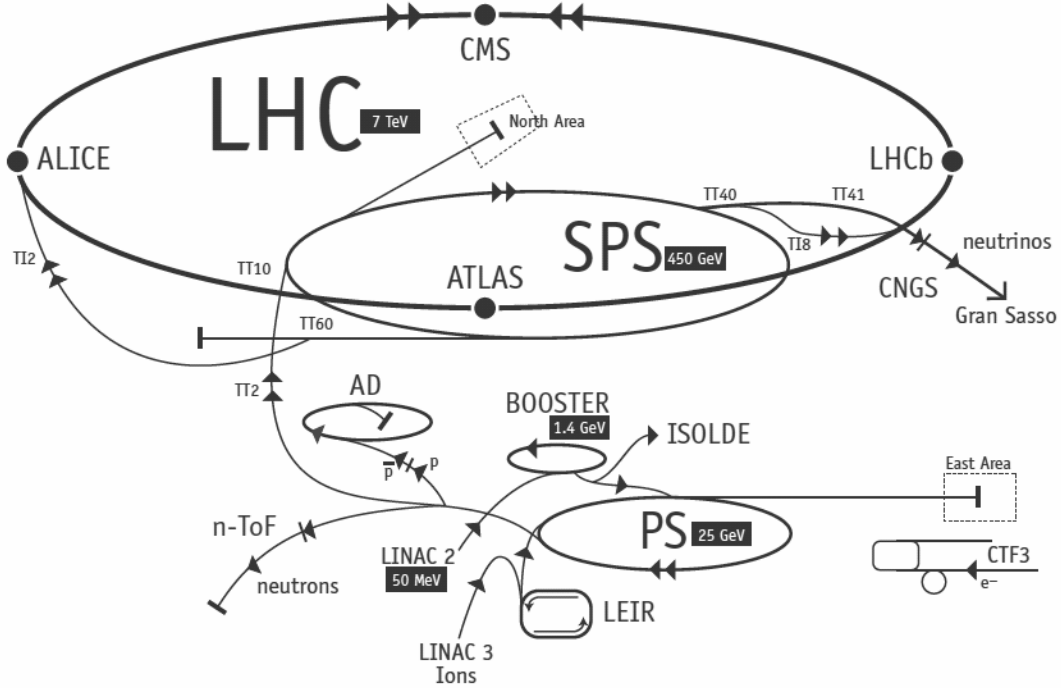


Figure 2.1: Schematic of CERN accelerators [61].

472 Protons are produced from hydrogen gas and are initially accelerated to an energy
 473 of 50 MeV in a linear accelerator (LINAC). Then they are injected into the Proton
 474 Synchrotron Booster (PSB), where they are boosted to an energy of 1.4 GeV, into
 475 the Proton Synchrotron (PS) to 25 GeV and into the Super Proton Synchrotron
 476 (SPS) to 450 GeV. Finally, protons enter into the LHC storage ring, where they are
 477 accelerated from injection energy to the final one by radio frequency (RF) cavities.
 478 The beams are steered around the ring by 8 T magnetic fields produced by 15 m
 479 long superconducting niobium-titanium dipole magnets and focused by quadrupole
 480 magnets. The LHC magnets use a design in which both proton beam pipes are
 481 contained in the same housing, allowing a common liquid helium cooling system to
 482 be used. The LHC began colliding proton beams in “physics mode” in 2009 at a
 483 centre of mass energy of $\sqrt{s} = 900$ GeV and from April 2010 to November 2011
 484 accelerated beams at $\sqrt{s} = 7$ TeV (3.5 TeV per proton beam) with a maximum
 485 instantaneous luminosity of $3 \cdot 10^{33} \text{ cm}^{-2}\text{s}^{-1}$, while in 2012 the energy was increased
 486 to 8 TeV. The LHC maximum design energy is 14 TeV, and its design luminosity is
 487 $10^{34} \text{ cm}^{-2}\text{s}^{-1}$. After a long shut down to upgrade and maintain the machine, a new

488 run started in June 2015, in which protons are collided at a centre of mass energy
489 of $\sqrt{s} = 13$ TeV. At this energy the total proton-proton cross-section is expected to
490 be roughly 100 mb.

491

2.2 The LHCb detector

492 The LHCb detector [62] was designed to study decays of B and D mesons, mainly
493 looking for CP-violating processes. In 2011, running at a centre of mass energy of 7
494 TeV, the cross-section for $b\bar{b}$ production was measured to be $284 \pm 53 \mu\text{b}$ [63], while
495 it will be $\sim 500 \mu\text{b}$ at the current LHC energy, 13 TeV. At these high energies,
496 proton-proton interactions produce highly boosted virtual gluons which produce $b\bar{b}$
497 pairs at small angles, close to the beam pipe. For this reason the LHCb detector is
498 designed to have a very forward angular coverage. The detector is fully instrumented
499 from 10 mrad to 300 mrad, corresponding to an interval $2 < \eta < 5$, where η is the
500 “pseudorapidity”, a quantity defined as:

$$\eta = -\ln(\tan(\theta/2)), \quad (2.1)$$

501 where θ is the angle between a particle’s momentum and the beam direction¹.

502 At LHCb’s collision point the luminosity can be adjusted by displacing the beams
503 from head on collisions while keeping the same crossing angle. This allows the exper-
504 iment to keep an approximately constant instantaneous luminosity, compensating
505 for the reduction in beam intensity due to extended operation periods. This also
506 means that the average number of interactions per bunch crossing can be regulated,
507 which is important because the detector efficiency, especially in detecting secondary
508 vertices, decreases for events with an high number of primary vertices (PV). Reduc-
509 ing the particle occupancy through the detector also keeps radiation damage to a

¹LHCb’s reference system has the z axis in the direction of the beam, the x axis directed to the centre of the accelerator and y is directed upward. Then we define θ as the angle with the beam direction and ϕ as the position around the beam in the xy plane, taking $\phi = 0$ on the x axis. The origin, $(x, y, z) = (0, 0, 0)$, corresponds to the centre of the interaction area.

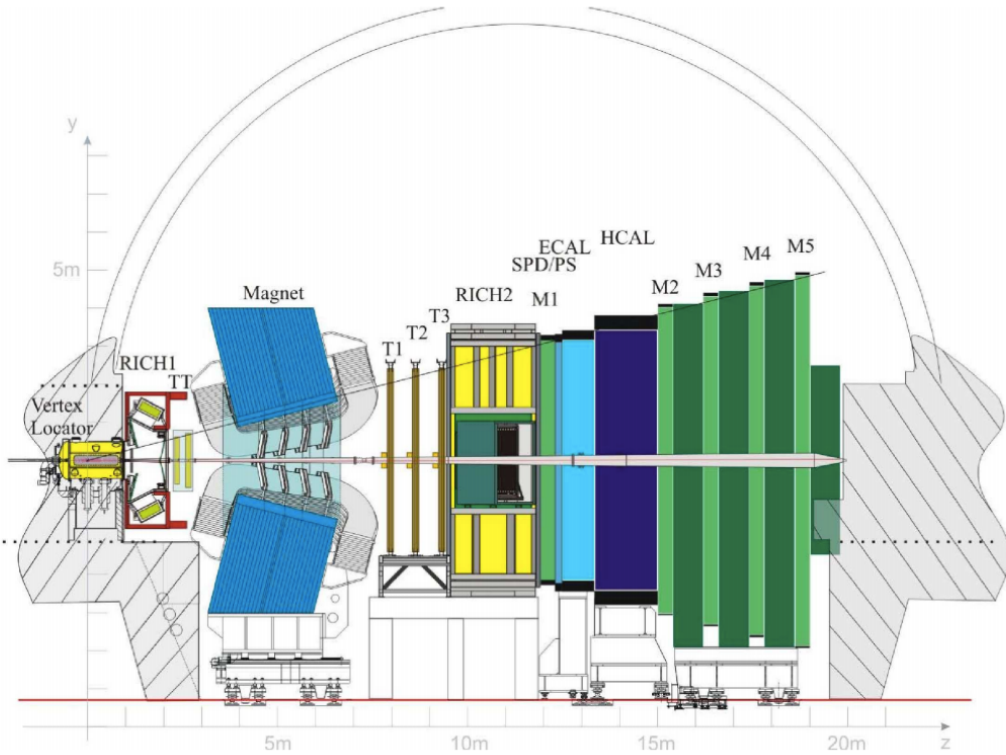


Figure 2.2: A side view of the LHCb detector [62].

minimum. Until the end of 2011 the instantaneous luminosity was $3 \cdot 10^{32} \text{ cm}^{-2}\text{s}^{-1}$, corresponding to an average number of 1.5 PVs per bunch crossing and at the end of 2011 LHCb had collected an integrated luminosity of 1 fb^{-1} . In 2012 the luminosity was increased and a further 2 fb^{-1} of data were collected.

Experiments like BaBar at the Stanford Linear Accelerator (SLAC), Belle at KEK at J-PARC (Japan) and the Tevatron experiments at Fermilab have made measurements in heavy flavour physics which have so far been found to be consistent with the SM predictions. However, some of the deviations from the SM are expected to be very small. Therefore LHCb was designed to make the most precise measurements in heavy flavour physics to test the consistency of the SM and look for new physics.

The LHCb detector comprises a high-precision tracking system consisting of a silicon-strip vertex detector surrounding the pp collision point, and larger silicon-strip and drift tubes detectors located on both sides of a dipole magnet with a bending power of about 4 Tm. Charged hadrons are identified using information from two Ring-

524 Imaging Cherenkov detectors (RICH) [64]. Photon, electron and hadron candidates
525 are identified by a calorimeter system and muons by a system composed of alter-
526 nating layers of iron and multi-wire proportional chambers [65]. A schematic view
527 of the detector is shown in Fig. 2.2 and more details on each sub-detector are given
528 in the following sections.

529 2.3 The magnet

530 Charged particle trajectories are deflected horizontally in the magnetic field so that
531 their momentum can be measured from the radius of curvature. The LHCb dipole
532 magnet is composed of two coils supported by an iron yoke and is shaped to fit
533 the LHCb angular acceptance. Unlike the other LHC experiments, LHCb uses a
534 warm magnet which can be easily ramped allowing the field polarity to be inverted
535 periodically. When the polarity is flipped, particles of a given sign are bent in
536 the opposite direction. This method is used to limit systematic uncertainties that
537 arise due to performance variations in different areas of the detector, which average
538 out using data taken in both polarities. A current of 5.85 kA flows in the magnet
539 generating an integrated magnetic field of 4 Tm for 10 m long tracks. In order to
540 achieve the required momentum precision the magnetic field must be mapped with
541 a 10^{-4} precision. For this reason a grid of 60 sensors is positioned inside the magnet
542 and provides real time magnetic field maps.

543 2.4 Tracking system

544 B mesons have lifetimes of approximately 1.5 ps. At the LHC energies, this means
545 that they travel about 1 cm before decaying to form a displaced vertex. To study
546 specific decays, it is therefore important to be able to separate the particles pro-
547 duced at the primary pp vertex and at the B decay secondary vertex (SV). The
548 tracking system consists of the Vertex Locator (VeLo), and four tracking stations:

the Tracker Turicensis (TT), which are located before the magnet and the T1, T2 and T3 stations, located after the magnet. The latter three stations are in turn formed by two subsystems: the Inner Tracker (IT) close to the beam-line, where the particle density is greatest, and the Outer Tracker (OT) covering the rest of the acceptance.

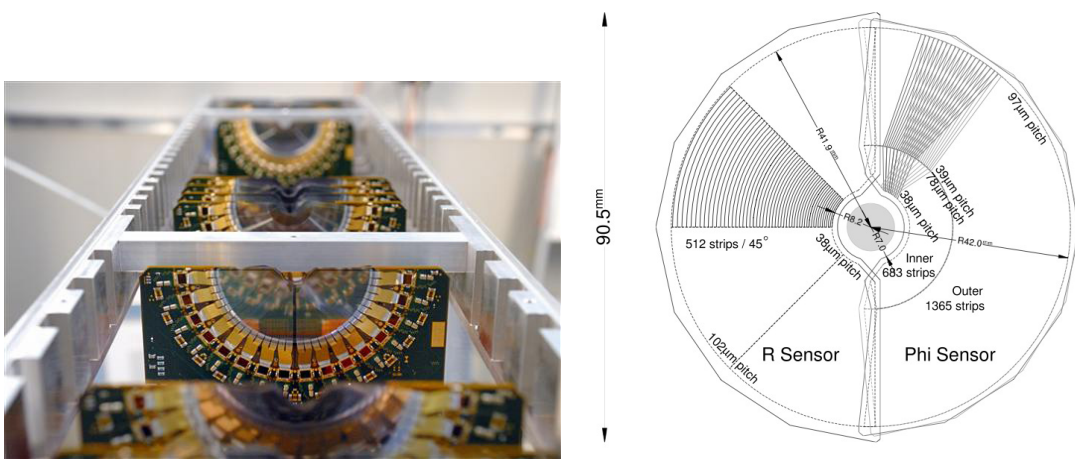


Figure 2.3: On the left VeLo sensors mounted in line and on the right a schematic view of one sensor [62].

554

The VeLo accurately measures positions of tracks close to the interaction point which is essential to reconstruct production and decay vertices of bottom and charm hadrons. The VeLo is composed by 21 silicon modules that surround the beam axis and are positioned from $z = -18$ cm to $+80$ cm. The sensitive region of the VeLo starts at an inner diameter of only 8 mm from the beam axis and it is able to detect particles within a pseudorapidity range $1.6 < \eta < 4.9$. The VeLo is housed in its own vacuum vessel of thin aluminium foil, which protects the vacuum of the beam pipe from any outgassing. The silicon layers composing the VeLo consist of two modules each including two types of sensors: the ϕ -sensor, which measures the azimuthal position around the beam, and the R-sensor, which measures the radial distance from the beam axis. A sketch of the VeLo sensors is shown in Fig. 2.3. The sensors are $300 \mu\text{m}$ thick and to ensure that they cover the full azimuthal angle the right-side module is placed 1.5 cm behind the left-side module on the z -axis and

568 they overlap. There are two modules which cover the backward direction and are
 569 used as a veto for multiple interactions; this is called the pileup system.

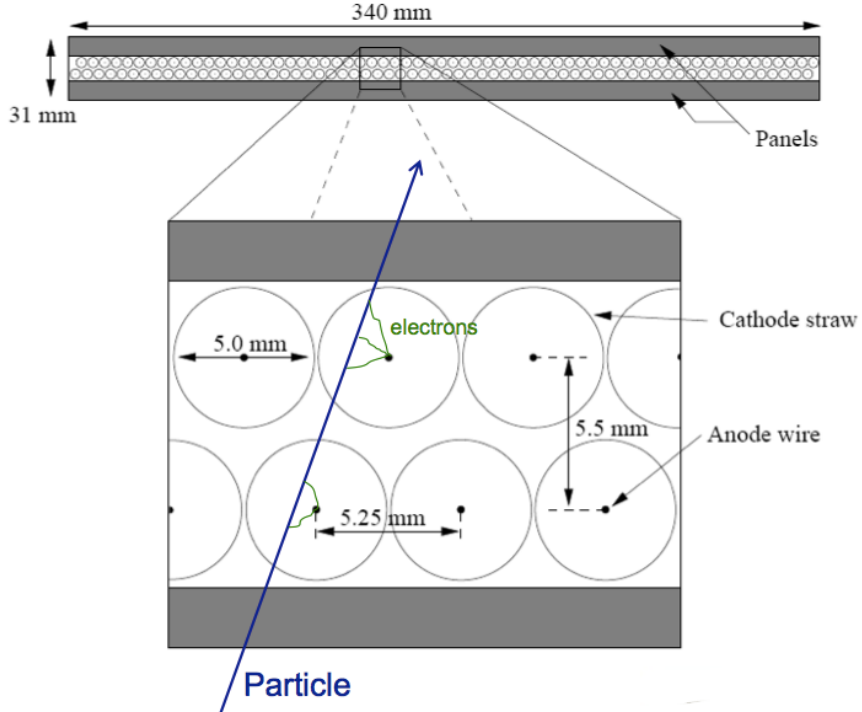


Figure 2.4: A sketch of the straw tubes which constitute the OT layers [62].

570

571 The IT and TT both use silicon strips and together constitute the Silicon Tracker
 572 (ST). Straw tubes are instead used in the OT, of which a sketch is shown in Fig. 2.4.
 573 The IT requires a higher inner granularity because of the greater flux of particles
 574 close to the beam pipe. In fact, it covers only 1.3% of the total area of IT plus
 575 OT but it contains about 20% of the tracks. Each ST station has four detection
 576 layers: the first and last are vertical, measuring the track position in x , while the
 577 second and third layers are rotated by an angle of +5 and -5 degrees, which allows
 578 the measurement of the y coordinate. The TT is placed upstream of the magnet to
 579 allow the reconstruction of tracks from low-momentum particles, which are bent out
 580 of the downstream acceptance. Overall the tracking system provides a measurement
 581 of momentum, p , with a relative uncertainty that varies from 0.4% at 5 GeV/ c to
 582 1.0% at 200 GeV/ c . The impact parameter (IP), namely the minimum distance of a

track to a primary vertex, is measured with a resolution of $(15 + 29/p_T) \mu\text{m}$, where p_T is the component of the momentum transverse to the beam, in GeV/c . The z -axis position of a PV reconstructed with 35–40 tracks can be measured with a precision of roughly 50–60 μm . The decay products of B mesons tend to have high IP values because the B decay imparts transverse momentum to them. Therefore, accurate IP and vertex displacement measurements allow LHCb to distinguish effectively between B meson decays and background processes.

2.5 Calorimeters

In general the main purpose of a calorimeter system is to determine the energy of particles but in LHCb it is mostly used to help the identification electrons and hadrons. Sampling calorimeters, as those used in LHCb, are composed of layers of absorber and active material. Particles interact with the absorber layers and produce a cascade of secondaries, that multiply quickly and are detected by the active part, which is usually composed of scintillating layers. The light produced is detected by photo-multipliers (PMTs) and it is approximately proportional to the energy of the deposited particles. Calibration is then used to translate the signal into an energy measurement. The LHCb’s calorimeter system consists of the Scintillator Pad Detector (SPD), the Pre-Shower Detector (PS) as well as the Electromagnetic Calorimeter (ECAL) and the Hadronic Calorimeter (HCAL). A sketch of the LHCb calorimeters is shown in Fig. 2.5. The SPD/PS cells are read out with PMTs located outside the LHCb acceptance, while the ECAL and HCAL have individual PMTs located on the modules. All four detectors are segmented, which allows the energy deposits to be associated to the tracks detected by the tracking system. The segmentation of the cells varies according to the distance from the beam pipe due to the different track density.

The most difficult identification in LHCb is that of electrons. The rejection of a high background of charged pions is achieved using a longitudinal segmentation of the

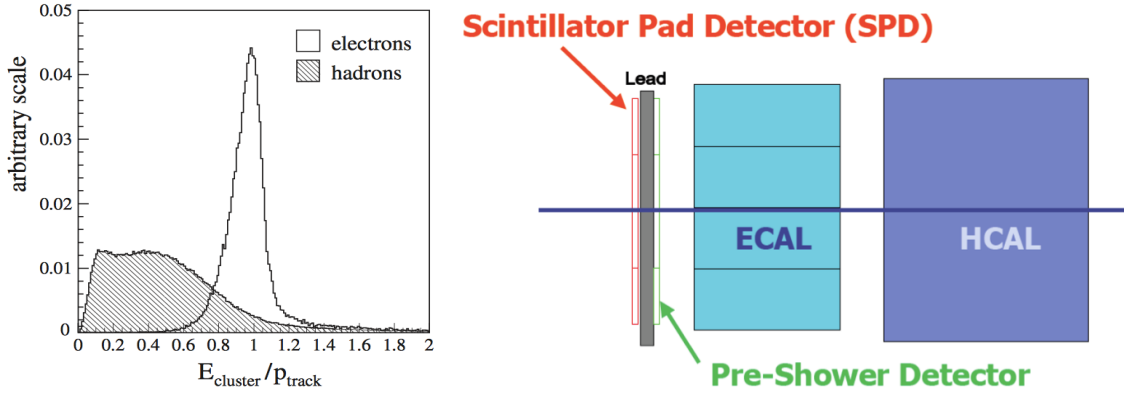


Figure 2.5: (left) The ratio of the energy deposited in the ECAL and the particle momentum, which allows the separation between electrons and hadrons [62]. (right) A schematic of the LHCb’s calorimeter system.

610 electromagnetic calorimeter which is provided by the PS detector added in front of
 611 the main electromagnetic calorimeter, ECAL. Electrons also have to be distinguished
 612 from high energy π^0 s and photons. For this purpose the SPD calorimeter, detecting
 613 charged particles, is located in front of the PS and ECAL detectors. Figure 2.5
 614 illustrates how the ratio between the energy detected in the ECAL and a particle’s
 615 momentum allows the separation of electrons and hadrons.

616 The ECAL is formed by 66 lead layers (2 mm thick) separated by 4 mm thick plastic
 617 scintillator layers. In order to obtain the highest energy resolution the showers
 618 from high energy photons must be fully absorbed. For this reason the ECAL has a
 619 thickness of 25 radiation lengths and its resolution is measured to be $\sigma_{\text{ECAL}}(E)/E =$
 620 $10\%/\sqrt{E(\text{ GeV})} + 1\%$ [62], which results in a mass resolution of $\sim 70 \text{ MeV}/c^2$ for
 621 B mesons and $\sim 8 \text{ MeV}/c^2$ for π^0 . The HCAL is mainly used for triggering and
 622 it is similar to the ECAL but with 4 mm thick scintillator layers and 16 mm thick
 623 absorber layers. The trigger requirements on the HCAL resolution do not depend
 624 on the containment of the hadron showers as much as for the ECAL, therefore, due
 625 to space limits, its thickness is only 5.6 interaction lengths and its resolution is given
 626 by $\sigma_{\text{HCAL}}(E)/E = 69\%/\sqrt{E(\text{ GeV})} + 9\%$.

627 2.5.1 Bremsstrahlung recovery for electrons

628 Bremsstrahlung is an electromagnetic radiation produced by charged particles that
 629 undergo an acceleration. Typically electrons produce Bremsstrahlung when de-
 630 flected by atomic nuclei. The probability of emitting bremsstrahlung radiation is
 631 proportional to the inverse of the squared mass of the particle ($1/m^2$) and therefore
 it is most relevant for electrons. At LHC energies, if electrons radiate after the mag-

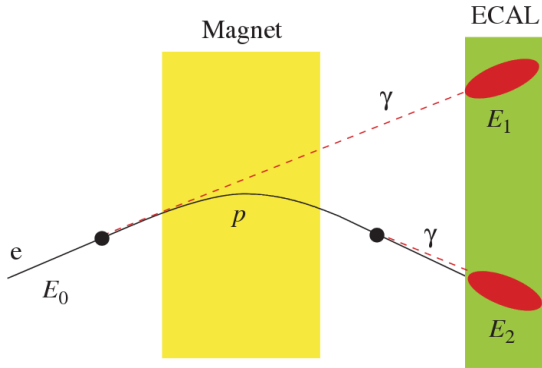


Figure 2.6: Schematic view of the bremsstrahlung recovery [62].

632
 633 net, the photon will hit the same calorimeter cell as the electron and the energy will
 634 be automatically recovered, as illustrated in Fig. 2.6. However, if the photon is emit-
 635 ted before the magnet, the electron will be deflected by the magnetic field whereas
 636 the photon will continue on its initial trajectory, with its energy being deposited in
 637 a different part of the calorimeter. Missing this energy results in a poorer recon-
 638 structed invariant mass resolution, so it is desirable to recover these bremsstrahlung
 639 photons. A tool for bremsstrahlung recovery is available in the LHCb analysis soft-
 640 ware. This tool looks for other clusters in the calorimeter and, reconstructing the
 641 trajectory of the electron, checks if they may be associated with emitted photons.
 642 The photon energy is then added to the electron and its momentum is recalculated.
 643 For more information see Ref. [66].

644 2.6 RICH

645 The two RICH detectors are a special feature of LHCb, as it is the only experiment
 646 at LHC using them. These detectors take advantage of the Cherenkov radiation
 647 produced by particles passing through a medium with speed higher than the speed
 648 of light in the medium. The Cherenkov light, as shown in Fig. 2.7, is produced in
 649 cones with a specific opening angle depending on the velocity of the particle. The
 650 relation between the angle and the particle velocity can be written as

$$\cos \theta = \frac{1}{\beta n}, \quad (2.2)$$

where $\beta = v/c$ and n is the refraction index of the medium.

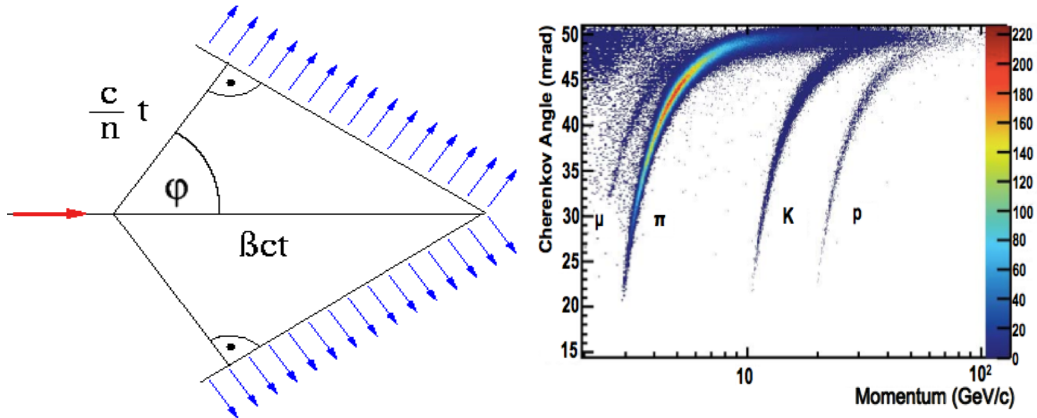


Figure 2.7: (left) A sketch of Cherenkov light emission [67]. (right) Measured Cherenkov angle as a function of particle momentum [62], where one can see that the study of the Cherenkov angle allows to distinguish particles' identities.

651

652 RICH 1 is located before the magnet in order to cover a larger angular accep-
 653 tance. Its purpose is to ensure particle identification over the momentum range
 654 $1 < p < 70 \text{ GeV}/c$. It uses two radiators: C_4F_{10} that covers the momentum range
 655 $5 - 70 \text{ GeV}/c$ and silica aerogel which covers $1 - 10 \text{ GeV}/c$. RICH 2 is positioned
 656 after the magnet and tracking stations and it identifies higher momentum particles
 657 from approximately $20 \text{ GeV}/c$ up to beyond $100 \text{ GeV}/c$ using CF_4 as a radiator.
 658 The Cherenkov light produced when charged particles travel through the radiators,
 659 is reflected and focussed using mirrors, which are tilted so that a ring image is re-

flected onto arrays of PMTs. The radius of the ring can be used to measure the opening angle of the Cherenkov cone because of the known geometry. The photo-detectors are located outside of the LHCb acceptance in order to reduce the amount of material that the particles have to traverse. Pattern recognition algorithms are then used to reconstruct the Cherenkov rings.

2.7 The muon system

It is essential for many of the key physics analyses in LHCb to be able to identify muons in decay final states. Muons are the most penetrating particles that can be detected at LHC experiments, so the muon chambers are the farthest sub-detectors from the interaction point. The muon system consists of five stations (M1 - M5), the first one being located before the calorimeters in order to improve p_T measurements. The remaining four stations are behind the HCAL and are separated from each other by 80 cm thick iron blocks, which absorb hadrons, electrons and photons to ensure that only muons reach the final muon station. A schematic of the muon system is shown in Fig. 2.8. Only muons with a minimum momentum of 10 GeV/c traverse all of the five stations and, for positive identification of a muon, the trigger requires a signal in each of them. Each station has a detection efficiency of at least 95% and the detectors also provide position measurements. Since there is a larger particle flux close to the beam pipe, the stations are divided into four concentric rectangular regions (R1-R4) with increasing cell size, which results in a similar occupancy over the four regions. All of the muon stations use Multi Wire Proportional Chambers (MWPC) except for the inner region of M1, where the particle flux is too high. In this region triple-GEM (Gas Electron Multiplier) detectors are used because of their better ageing properties as they have to withstand a rate up to 500 kHz cm⁻² of charged particles. These detectors consist of three gas electron multiplier foils sandwiched between an anode and a cathode.

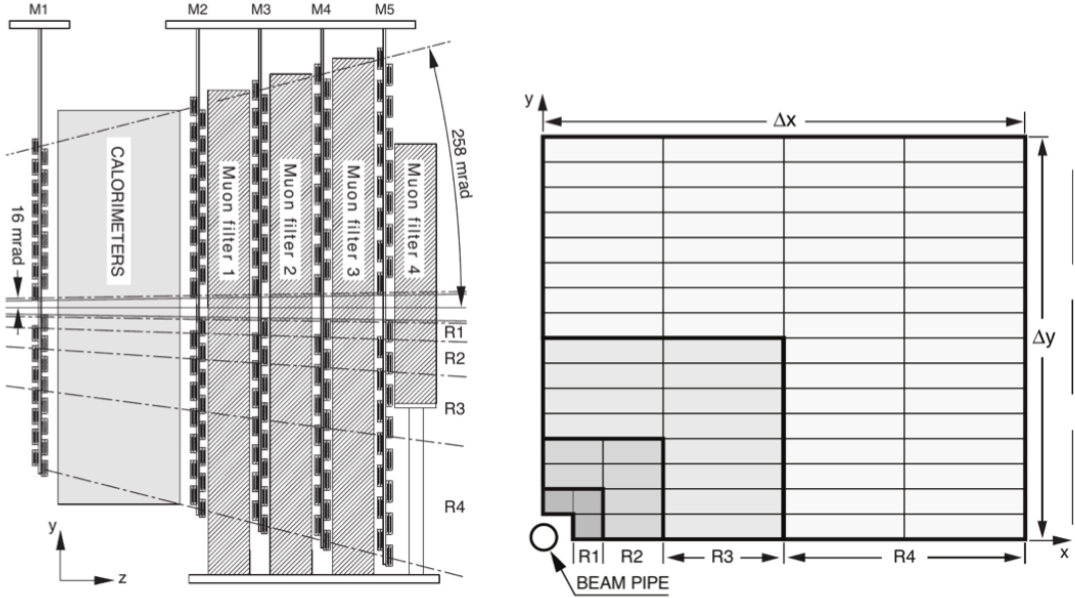


Figure 2.8: The LHCb muon system [62].

686 2.8 Particle identification

687 Particle identification (PID) is an important feature in LHCb and it is performed in
 688 various ways. The electromagnetic calorimeters can distinguish between pions and
 689 electron, the muon chambers identify muons and the RICH detectors can be used
 690 to identify heavier charged particles such as protons and kaons.

691 The RICH assigns an ID to a track calculating the global likelihood for the observed
 692 distribution of hits being consistent with the expected distribution from various
 693 ID hypotheses. The algorithm iterates through each track and recalculates the
 694 likelihood when the track PID hypothesis is changed to that of an electron, muon,
 695 kaon or proton. For electrons and muons additional information from the calorimeter
 696 and muon systems is also used. The hypothesis which maximises the likelihood is
 697 assigned to the track.

698 To quantify the quality of the ID the pion hypothesis is used as a reference point
 699 and the probability of a specific ID is given in terms of Log-Likelihood difference
 700 between the given ID hypothesis and the pion one. This variable is called Delta

⁷⁰¹ Log-Likelihood (DLL) and denoted with ‘‘PID’’. For example,

$$\text{PID}_K = \text{DLL}_{K-\pi} = \log(\mathcal{L}_K) - \log(\mathcal{L}_\pi) \quad (2.3)$$

⁷⁰² quantifies the probability of a particle being a kaon rather than a pion. Figure 2.9
⁷⁰³ shows the efficiency for correctly identifying and mis-identifying kaons and protons as
⁷⁰⁴ a function of the measured momentum of the particle. For kaons the efficiency drops
⁷⁰⁵ at momenta below 10 GeV, where they fall below threshold for the gas radiators.
⁷⁰⁶ The DLL cuts enable LHCb physics analyses to distinguish between kinematically
⁷⁰⁷ similar decays with different final states. For example, Fig 2.10 illustrates the power
⁷⁰⁸ of particle identification, showing how the application of DLL cuts can be used to
isolate $B^0 \rightarrow \pi^+\pi^-$ decays from other two-body B decays. The identification of

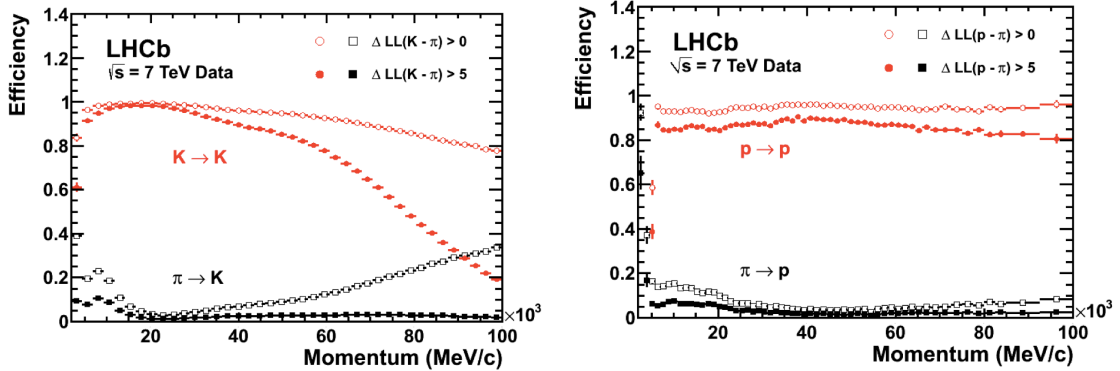


Figure 2.9: Particle identification performances for kaons (left) and protons (right) as a function of the measured momentum of the particles [62].

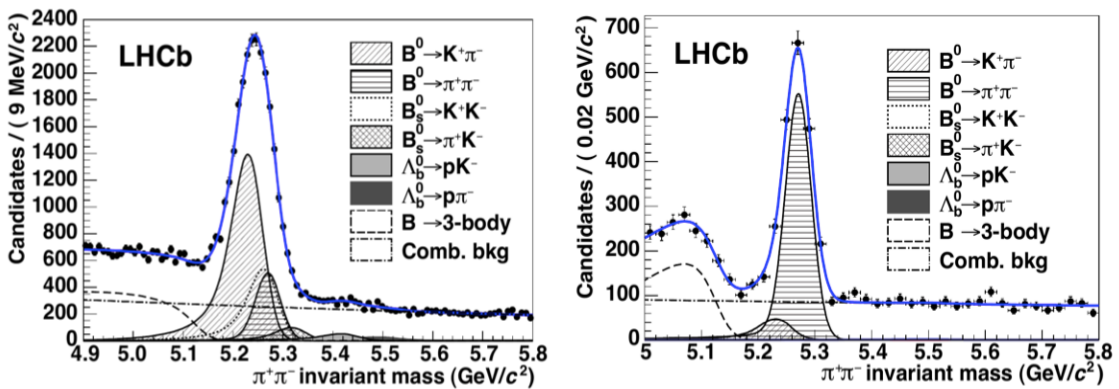


Figure 2.10: Invariant mass peak of the $B^0 \rightarrow \pi^+\pi^-$ decay before (left) and after (right) the application of PID requirements [68].

709

710 muons is particularly important in LHCb and it is quantified using two variables:
711 the `DLLμ` and the `isMuon` variable. The latter is a boolean variable determined
712 by defining a ‘field of interest’ around a track trajectory extrapolated through the
713 muon chambers. The variable is set to true if hits in multiple muon stations are
714 found in the field of interest.

715 2.8.1 PID calibration

716 In order to be able to calculate detection efficiencies, a “data-driven” method was
717 developed. The calibration software is referred to as `PIDCalib` package [68]. This
718 tool uses decays where final particles can be identified thanks to their kinematic
719 properties. For example the $K_s^0 \rightarrow \pi^+\pi^-$ decay has a clear signature with a displaced
720 vertex and can be easily singled out from other decays and used to test pion ID
721 efficiency. The narrow peaks of the $J/\psi \rightarrow \mu^+\mu^-$ and $J/\psi \rightarrow e^+e^-$ decays allow
722 muon and electron efficiencies to be calibrated. A “tag-and-probe” method is used
723 in this case, where only one of the two leptonic tracks is reconstructed requiring
724 the correct identity and the other one is used to probe the PID efficiency. Finally,
725 $\phi \rightarrow KK$ samples and $D^{*+} \rightarrow D(\rightarrow K^-\pi^+)\pi^+$ decays, where the D^{*+} is used to tag
726 the decay, are used to test the kaon efficiency. In all cases the residual background
727 is subtracted using the `sPlot` technique [69].

728 2.9 Trigger and software

729 The LHCb trigger system [70] consists of a hardware stage, L0, based on information
730 from the calorimeters and muon system, followed by a software stage, the High-
731 Level Trigger (HLT), which applies a full reconstruction of the events. To increase
732 performance, the HLT is further split into two stages, HLT1 and HLT2. The HLT1
733 phase happens in real time and saves data to local disks while the HLT2 phase uses

the resources available during periods with no beam. The event selected by the HLT2 stage are then saved for offline analysis. Figure 2.11 shows a schematic of the trigger system. The bunch crossing frequency is 40 MHz, which corresponds to an instantaneous luminosity of $2 \cdot 10^{32} \text{ cm}^{-2}\text{s}^{-1}$ for LHCb. About 15% of the total number of $b\bar{b}$ pairs produced will contain at least one B meson with all of its decay products within the detector acceptance. This rate needs to be reduced to about 2 kHz at which the events can be written to disk.

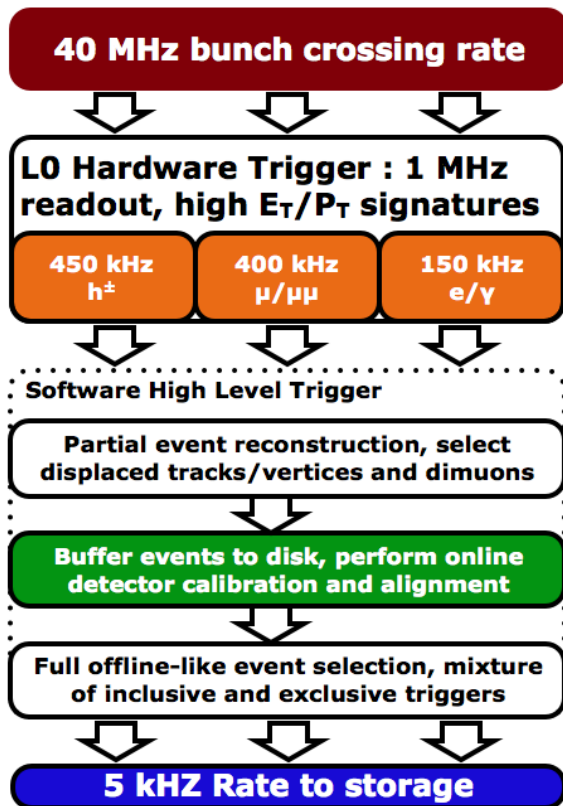


Figure 2.11: A schematic of the LHCb trigger system [62].

740

The L0 trigger reduces the rate of visible interactions from 10 MHz to 1 MHz. Due to the heavy mass of B mesons, they often produce particles with high energy and momentum. Therefore the trigger selects events with large deposits in the calorimeter or high p_T muons. The event is classified as L0Muon if it was triggered due to information from the muon detector, while the information from the calorimeters is used to divide the events into five categories: L0Photon, L0Electron, L0LocalPion, L0GlobalPion, L0Hadron. The PS detector information is converted to a photon

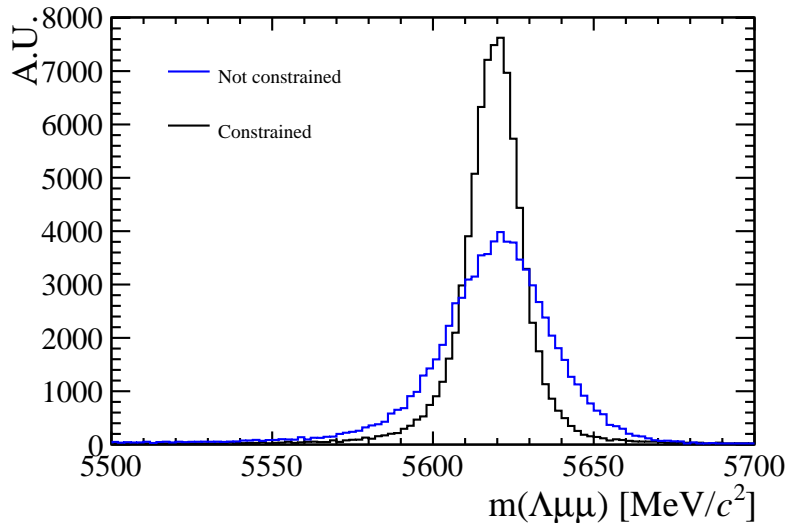
748 flag (`PS && !SPD`) or an electron flag (`PS && SPD`). The “local” label of the `L0Pion`
749 trigger refers to π^0 reconstructed through their $\gamma\gamma$ decay, where the two photons fall
750 in the same ECAL element, they are labelled “global” otherwise. The first four
751 calorimeter triggers require energy clusters in the ECAL, while `L0Hadron` requires
752 clusters also in the HCAL. The `HLT1` uses information from the VELO and trackers
753 performing a partial reconstruction of the event and reduces the rate to 2 kHz by
754 adding requirements on the IP and χ^2 of tracks. Finally, the `HLT2` involves a full
755 reconstruction of the event and includes many “lines” designed to select specific
756 decay structures.

757 LHCb also developed an extended simulation software in order to reconstruct ef-
758 ficiencies and signal shapes. In the simulation, pp collisions are generated using
759 `PYTHIA8` [71, 72] with a specific LHCb configuration [73]. Decays of hadronic par-
760 ticles are described by `EVTGEN` [74], and final state radiation is generated using
761 `PHOTOS` [75]. Finally, the interaction of the generated particles with the detec-
762 tor and its response are implemented using the `GEANT4` toolkit [76] as described
763 in Ref. [77]. For this analysis in this thesis, the `ROOT` framework [78] is used to
764 analyse data and the `RooFit` package to perform maximum likelihood fits. A multi-
765 variate analysis is also performed based on the `NeuroBayes` package [79, 80], which
766 provides a framework for neural network training.

767 2.10 Constrained kinematic fits

768 The resolution of key variables, such as the measured invariant mass of decaying
769 particles, can be improved by imposing constraints on the measured quantities to
770 remove redundant degrees of freedom. The four-momentum conservation can be
771 ensured at each vertex and the origin and decay vertices of a particle are related via
772 the momentum of the particle. Furthermore, additional constraints can be imposed
773 due to a particular decay hypothesis such as the known invariant masses of final and
774 intermediate particles. In order to do this the `DecayTreeFitter` tool was developed

775 by the BaBar experiment and later used by LHCb [81]. The algorithm takes a com-
 776 plete decay chain and parametrises it in terms of vertex positions, decay lengths
 777 and momentum parameters. These parameters are then fit simultaneously, taking
 778 into account the relevant constraints, including the information from photons. Fig-
 779 ure 2.12 illustrates the effect of the application of the kinematical fit on the 4-body
 780 invariant mass of the final daughters of the $\Lambda_b^0 \rightarrow J/\psi \Lambda$ decay. The resolution in this
 781 case improves by over a factor of 2. Furthermore, the χ^2 from the kinematic fit can
 782 be used to quantify the compatibility with a specific decay structure, which helps to
 783 separate candidates where random particles from the event have been added to the
 decay tree, or where one or more particles is not reconstructed or mis-identified.



784 Figure 2.12: Invariant mass of the final daughters of simulated $\Lambda_b^0 \rightarrow J/\psi \Lambda$ decays
 calculated with and without constraints using the `DecayTreeFitter` tool.

785

2.11 Validation of hadronic processes in the simulation

786 Particle-antiparticle asymmetries are of major interest for LHCb and detection ef-
 787 ficiencies are usually obtained from simulation. It is therefore important, in order
 788 to limit systematic uncertainties, to have a model that parametrises correctly the
 789 cross-sections of particles and antiparticles or at least their ratio.

790 The LHCb simulation software propagates particles through the detector using the
791 GEANT4 toolkit [62]. This offers a variety of models for physics processes over a
792 wide range of energies for both electromagnetic and strong interactions. Given a
793 combination of projectile, target and energy there can be several models applicable
794 with different reliability and computational costs. GEANT4 provides a number of
795 pre-packaged physics lists each representing complete and consistent sets of models
796 chosen to be appropriate for a given use case. In LHCb mainly two hadronic physics
797 lists are considered:

798 • **LHEP** (Low and High Energy Parametrisation): based on a parametrised
799 modelling of all hadronic interactions for all particles. This list combines
800 the High Energy Parametrised model (HEP) and the low energy one (LEP).

801 There is a sharp switch from the low to the high energy model at 25 GeV.
802 The modelling of elastic scattering off a nucleus and of nuclear capture also
803 proceeds via parametrised models.

804 • **FTFP_BERT**: includes the following models:

805 – Bertini cascade model (BERT) [82], which simulates the intra-nuclear cas-
806 cade, followed by pre-equilibrium and evaporation phases of the residual
807 nucleus, for protons, neutrons, pions and kaons interaction with nuclei
808 at kinetic energies below 9.9 GeV. The Bertini model produces more
809 secondary neutrons and protons than the LEP model, yielding a better
810 agreement with experiment data.

811 – FTFP model, which implements high energy inelastic scattering of hadrons
812 by nuclei using the FRITIOF model [83].

813 The change between the two models happens with a linear shift from BERT
814 to FTFP that starts at 4 GeV and ends at 5 GeV.

815 Figure 2.13 summarises the composition of the different models.

When two models overlap in an energy interval the choice of the model for each interaction is made using a random number: the probability to select each model varies linearly from 0 to 100% over the overlap range. Because of the differences of the two models in the overlap region, unphysical discontinuities can be produced as a function of energy.

2.11.1 Geometry and interaction probability

The results presented in the following sections are produced using the version v45r0 of the full LHCb framework for simulation, **GAUSS** [77], which is interfaced to **GEANT4** v95r2p1. A simple geometry setup is used in order to be able to calculate in a clean way the interaction cross-sections in a specific material. This is constituted by a series of rectangular boxes filled with the most relevant materials for LHCb: Aluminium, Silicon and Beryllium. For each material three boxes are defined with different thicknesses (1mm, 10mm, 50mm). These values are chosen to be indicative of the amount of material present in the LHCb detector.

The simplest quantity available to extract the cross-section is the interaction probability, P_{int} , defined as:

$$P_{int} = \frac{N_{int}}{N_{tot}}, \quad (2.4)$$

where N_{int} is the number of particles which interacted in the material and N_{tot} is the number of generated particles. As **GEANT4** provides an ID for the end process

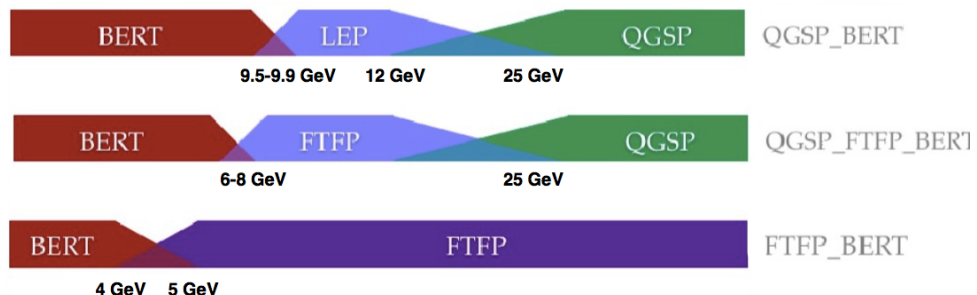


Figure 2.13: Diagram of LHEP, FTFP_BERT and QGSP_BERT models' composition as a function of energy.

835 of a particle (e.g. 121 for inelastic interaction, 111 for elastic, 201 for decay) it
836 is possible to distinguish the inelastic and elastic probabilities of interaction and
837 therefore cross-sections.

838 To compare simulation and data the cross-section and P_{int} are related through the
839 following formula valid for thin layers:

$$\sigma_{int} = \frac{A}{\rho N_A \Delta x} \cdot P_{int}, \quad (2.5)$$

840 where ρ is the density of the material and A is its mass number, Δx is the thickness
841 of the considered layer and N_A is the Avogadro number.

842 2.11.2 PDG prediction

In the Review of Particle Physics (PDG) [2] cross-sections of protons and neutrons
are parametrised as:

$$\sigma_{tot}^{ab} = Z^{ab} + B^{ab} \log^2(s/s_M) + Y_1^{ab}(s_M/s)^{\eta_1} - Y_2^{ab}(s_M/s)^{\eta_2}, \quad (2.6)$$

$$\sigma_{tot}^{\bar{a}\bar{b}} = Z^{ab} + B^{ab} \log^2(s/s_M) + Y_1^{ab}(s_M/s)^{\eta_1} + Y_2^{ab}(s_M/s)^{\eta_2}, \quad (2.7)$$

843 where $s_M = (m_a + m_b + M)^2$ and $B^{ab} = \lambda \pi (\frac{\hbar c}{M})^2$. Some of the constants in these
844 equations are universal and valid for any kind of collision: $M = 2.15$, $\eta_1 = 0.462$, η_2
845 = 0.551, $\lambda = 1$ (for p, n and γ) and 1.63 (for d). The other ones are characteristic
846 of each type of collision and are listed in Tab. 2.11.2. In these formulae the particle-
847 antiparticle asymmetry arises from the last term which has opposite sign in the
848 two equations. This term becomes less and less important with increasing energies.
849 Therefore a net asymmetry is found at low energies, while the cross-sections tend
850 to a common point at high energy and continue increasing logarithmically.

2.11.3 Validation results

This section reports particle and antiparticle cross-sections and their ratios compared, where available, with predictions and with data from the COMPASS experiment [84]. Figure 2.14 shows the probability of interaction for protons and anti-protons in 10 mm of Aluminium using the FTFP_BERT and LHEP models compared with COMPASS data and Fig. 2.15 shows the ratios of $\sigma_{\bar{p}}^{tot}/\sigma_p^{tot}$ together with the PDG prediction. A difference of 40% is found between the two considered models for 1 GeV incoming anti-protons. This difference becomes negligible at higher energies. The discrepancies between the two physics lists for kaons and pions are of a few percents (2–3%) and usually constant with the energy. From the comparison with data and PDG predictions it can be qualitatively concluded that the FTFP_BERT model gives a better description of hadronic interactions at low energies, while both models give good results at high energy, above ~ 10 GeV.

The tool developed for these studies is not limited to cross-sections but can also give information on other simulated quantities. As an example, Fig. 2.11.3 shows a comparison between the types of particles generated in inelastic collisions of protons and anti-protons onto Aluminium using different models. Physics lists can give very different results, for example the LHEP model does not produce photons in inelastic collisions. However, it is difficult to use these quantities for validation as there is no data available for a comparison.

872

Proj / Targ	Z^{ab}	Y_1^{ab}	Y_2^{ab}
$\bar{p}, p / p$	34.71	12.72	7.35
π^\pm / p	19.02	9.22	1.75
K^\pm / p	16.56	4.02	3.39
K^\pm / n	16.49	3.44	1.82
$\bar{p}, p / n$	35.00	12.19	6.62

Table 2.1: Values for the constants Z^{ab} , Y_1^{ab} and Y_2^{ab} [2], which parametrise hadronic cross-sections.

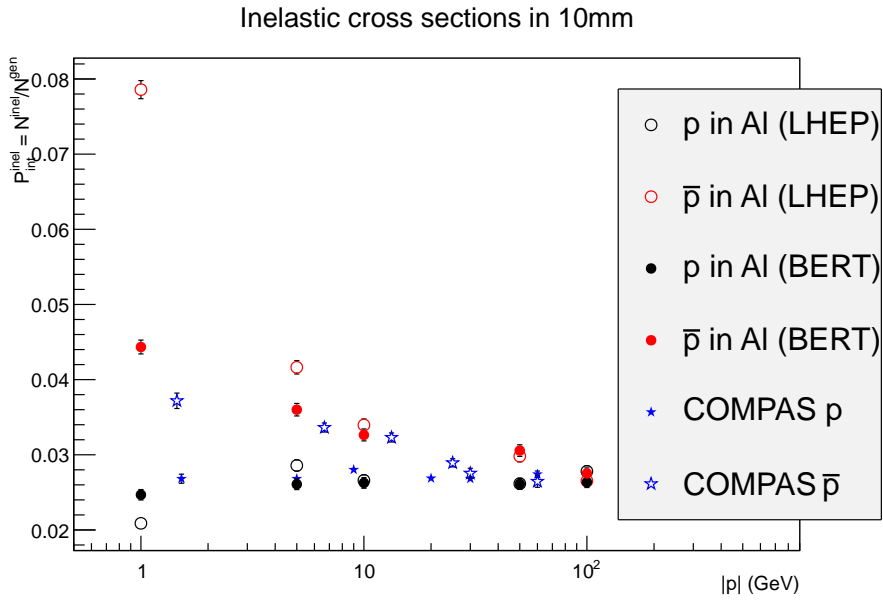


Figure 2.14: Probability of interaction for protons and anti-protons in Aluminium as a function of the projectile momentum. Two physics lists are used to generate events that can be compared with data from the COMPASS experiment.

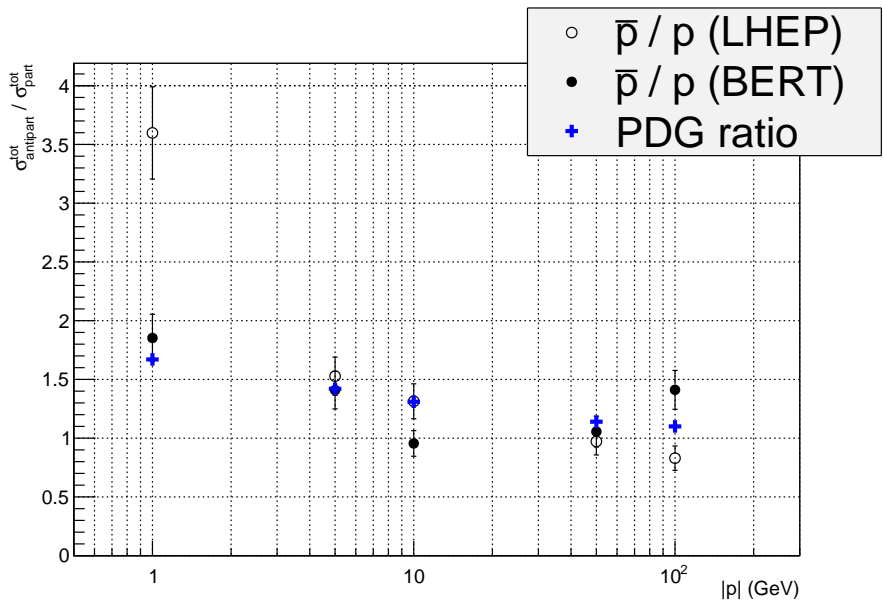


Figure 2.15: Ratio of antiproton over proton total interaction cross-section as a function of energy compared with PDG predictions.

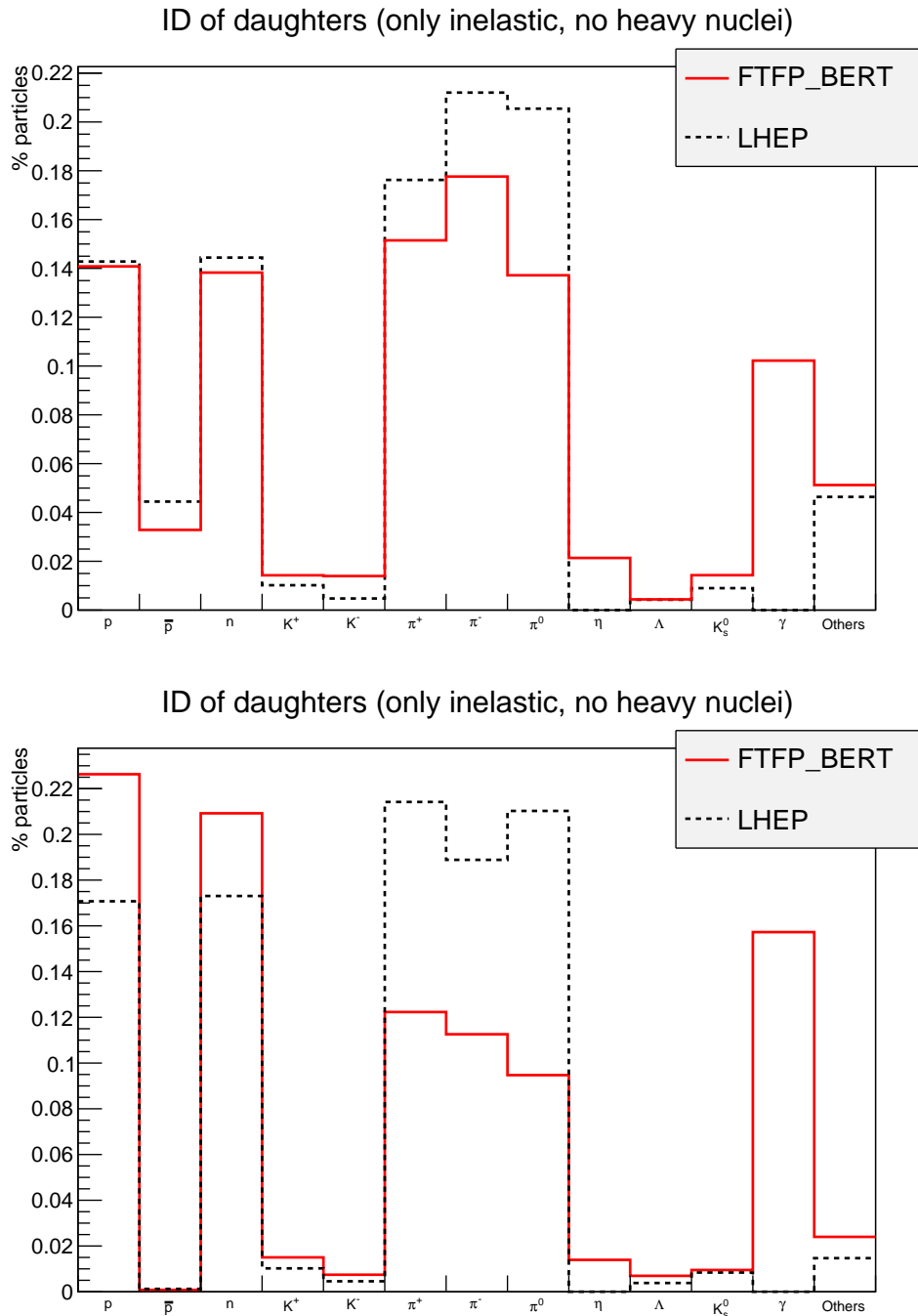


Figure 2.16: Composition of secondary particles produced in 100 GeV protons (top) and anti-protons (bottom) collisions in 1 mm Aluminium.

873 2.12 Material budget studies

874 It is important for many analysis to quantify the amount of material present in the
875 detector, for example to estimate the amount of multiple scattering. In GEANT4
876 particles are propagated in steps through the detector and for each step the frame-
877 work analyses the geometry to understand in what material the particle is and
878 modifies its trajectory accordingly. A tool was developed where neutrinos are used
879 as probes to scan the detector summing the radiation length seen at each step up
880 to a certain point. Neutrinos are used as they do not bend in magnetic field and
881 do not interact with the detector to any appreciable extent. Thin air planes are
882 inserted after each sub-detector. When these are traversed by the neutrinos, the
883 information about the accumulated radiation and interaction length is saved. In
884 this way it is possible to obtain maps of the detector, such as the one shown in
885 Fig. 2.17. Using the tool developed for this study it is also possible to obtain the
886 cumulative interaction length. As an example Fig. 2.18 shows the average radiation
887 length as a function of the distance from the interaction point. Furthermore, it is
888 possible to displace the primary vertex from its position, normally set at the origin,
889 in order to study how this translates into the amount of material traversed.

890 2.13 Validation and material budget studies conclusions

891 The studies outlined in the previous two sections are based on tools which are
892 now officially part of the LHCb simulation framework. These tools were used to
893 validate the framework when passing from GEANT4 version 9.5 to version 9.6. In
894 particular a patch was provided by the GEANT4 team including improved kaon cross
895 sections and it was verified these go into the right direction. The tool will continue
896 to be used in the future, in particular to validate the upgrade to GEANT4 10, in
897 2016. Furthermore, the tools can be used by analyses sensitive to the quality of the
898 simulation of particle and antiparticles cross-sections in order to study systematic
899 effects and uncertainties.

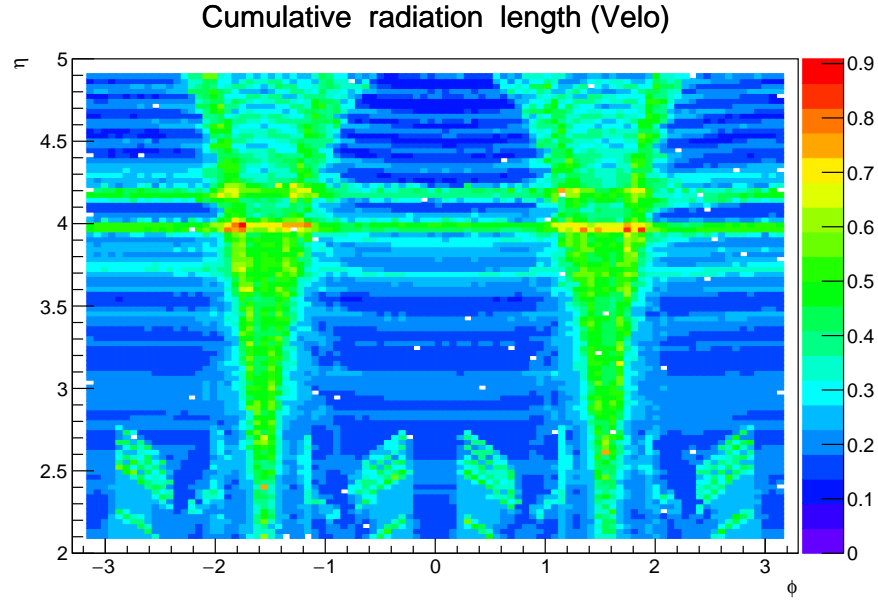


Figure 2.17: Map of cumulative radiation length seen by a particle starting from the interaction point up to the end of the VeLo.

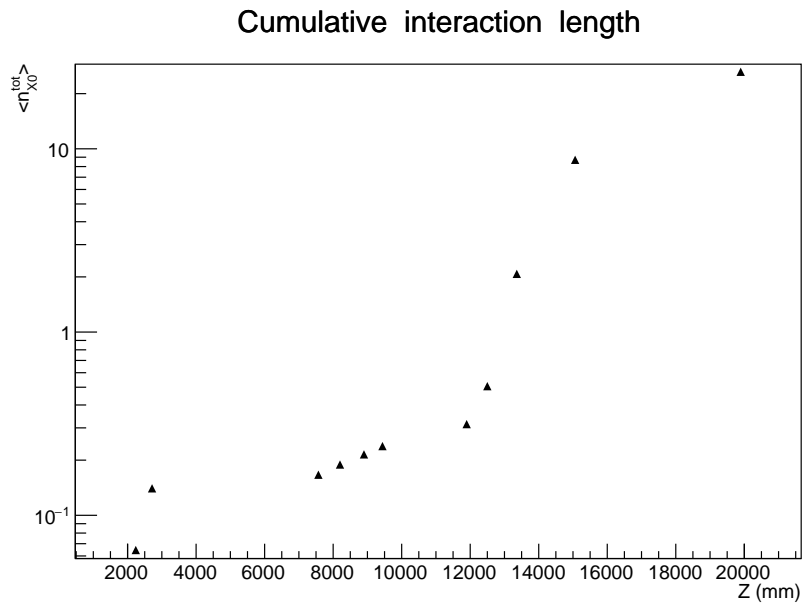


Figure 2.18: Average cumulative radiation length as a function of the horizontal distance from the interaction point. Each considered point corresponds to the end of a sub-detector: VeLo, RICH1, RICH2, tracking stations, ECAL and HCAL and muon detector.

900

CHAPTER 3

901

902

Differential branching fraction of $\Lambda_b^0 \rightarrow \Lambda\mu^+\mu^-$

903

The $\Lambda_b^0 \rightarrow \Lambda\mu^+\mu^-$ decay is a FCNC process governed by the $b \rightarrow s\mu^+\mu^-$ quark level transition which, in the SM, proceeds only through loop diagrams (electroweak penguin or W box) as discussed in Sec. 1.5, and therefore it is highly sensitive to new particles entering the loops. Interest in Λ_b^0 baryon decays arises, first of all, from the fact that the Λ_b^0 has non-zero initial spin, which allows to extract information about the helicity structure of the underlying Hamiltonian that cannot be obtained from meson decays [85, 86]. Secondly, the Λ_b^0 baryon can be considered to a first approximation as composed of a heavy quark and a light di-quark, therefore the hadronic physics differs significantly from B meson decays. This provides the possibility to better understand and test the hadronic physics in the theory, which could yield an improved understanding relevant also for the meson case.

With respect to B^0 decays going though the same transitions, such as $B^0 \rightarrow K^{*0}\mu^+\mu^-$, Λ_b^0 decays can provide independent confirmations of the results as they involve the same operators but different hadronic matrix elements. Furthermore, Λ baryons

918 decay weakly, which results in complementary constraints with respect to B^0 de-
 919 cays. Finally, the narrow width approximation, used in theoretical calculations, is
 920 fully applicable in the Λ_b^0 case, which has $\Gamma_{\Lambda_b^0} \sim 2.5 \cdot 10^{-6}$ eV. This is not the case
 921 for $B^0 \rightarrow K^{*0} \mu^+ \mu^-$ decays because the contribution from the non-resonant channel
 922 $B^0 \rightarrow K \pi \mu^+ \mu^-$ is unconstrained.

923 The theory of $\Lambda_b^0 \rightarrow \Lambda \mu^+ \mu^-$ decays was widely investigated both in the context of
 924 the SM and in various BSM scenarios [87, 88, 89, 90, 91, 92, 93, 94, 95, 96, 97]. All
 925 authors start from the effective Hamiltonian outlined in Sec. 1.5.1. However, form
 926 factors, describing hadronic physics are not as well-developed as for the meson case
 927 because there are fewer experimental constraints, which leads to a relatively large
 928 spread in predicted branching fractions. For these reasons an interesting quantity
 929 to study is the differential branching fraction as a function of q^2 . This still suffers
 930 from the limited knowledge of form factors but, as different approaches to form
 931 factors calculations are applicable in different q^2 regions, it allows a more meaningful
 932 comparison with theory.

Experimentally, the $\Lambda_b^0 \rightarrow \Lambda \mu^+ \mu^-$ decay was observed for the first time in 2011 by
 the CDF collaboration [98] and later updated in preliminary form using their full
 statistics [99]. The latter measurement yields $\mathcal{B}(\Lambda_b^0 \rightarrow \Lambda \mu^+ \mu^-) = [1.95 \pm 0.34(\text{stat}) \pm$
 $0.61(\text{syst})] \times 10^{-6}$ and the signal was observed only in the q^2 region above the square
 of the $\psi(2S)$ mass. Recently, the decay was also observed at LHCb [100] with a yield
 of 78 ± 12 signal events using 1 fb^{-1} of integrated luminosity collected in 2011. The
 signal was also found only in the high q^2 region, above $m_{\psi(2S)}^2$. The LHCb result for
 the branching fraction relative to the $J/\psi \Lambda$ decay, which is used as a normalisation
 channel, is

$$\frac{\mathcal{B}(\Lambda_b^0 \rightarrow \Lambda \mu^+ \mu^-)}{\mathcal{B}(\Lambda_b^0 \rightarrow J/\psi \Lambda)} = [1.54 \pm 0.30 \text{ (stat)} \pm 0.20 \text{ (syst)} \pm 0.02 \text{ (norm)}] \times 10^{-3}$$

and for the absolute branching fraction,

$$\mathcal{B}(\Lambda_b^0 \rightarrow \Lambda \mu^+ \mu^-) = [0.96 \pm 0.16 \text{ (stat)} \pm 0.13 \text{ (syst)} \pm 0.21 \text{ (norm)}] \times 10^{-6}.$$

933 This chapter describes the measurement of the differential branching fraction of the
 934 $\Lambda_b^0 \rightarrow \Lambda\mu^+\mu^-$ decay using 3 fb^{-1} of pp collisions collected by the LHCb experiment
 935 in 2011 and 2012.

936 3.1 Analysis strategy and q^2 regions

937 A typical q^2 spectrum of $b \rightarrow s\ell^+\ell^-$ decays was shown in Fig. 1.8. This is charac-
 938 terised by the presence of the photon pole at low q^2 and the narrow peaks of the
 939 J/ψ and $\psi(2S)$ resonances at intermediate values of q^2 . In the analysis, $\Lambda_b^0 \rightarrow J/\psi\Lambda$
 940 decays, in which the J/ψ decays into two muons and therefore has the same final
 941 state as the signal, are used as the normalisation channel. The rare and normal-
 942 isation channels are naturally distinguished by the q^2 intervals in which they are
 943 reconstructed. The Λ decay mode into a pion and a proton, $\Lambda \rightarrow p\pi$, is always used
 944 to reconstruct the decays. The intervals in which the rare channel is studied are:

- 945 • $0.1 < q^2 < 8 \text{ GeV}^2/c^4$, where the signal is unobserved and the selection is opti-
 946 mised to observe it. The upper bound of this interval is chosen to be sufficiently
 947 far from the J/ψ radiative tail at low masses and reduce its contamination into
 948 the rare sample;
- 949 • $11 < q^2 < 12.5 \text{ GeV}^2/c^4$, between two charmonium resonances, and
- 950 • $q^2 > 15 \text{ GeV}^2/c^4$, above $\psi(2S)$.

951 The first interval, below the J/ψ resonance, is referred to as “low- q^2 ” region, while
 952 the two intervals above the J/ψ resonance ($q^2 > 11 \text{ GeV}^2/c^4$) are referred to as
 953 “high- q^2 ” regions. These regions are then sub-divided into smaller intervals, as the
 954 available statistics allows, which results in $\sim 2 \text{ GeV}^2/c^4$ wide bins. The binning used
 955 is the following:

$$[0.1, 2.0, 4.0, 6.0, 8.0], J/\psi, [11.0, 12.5], \psi(2S), [15.0, 16.0, 18.0, 20.0]. \quad (3.1)$$

956 In addition the result is also provided in two integrated regions:

- 957 • $1.1\text{--}6.0 \text{ GeV}^2/c^4$: this interval is theoretically favoured to observe new physics
958 effects since it is far from the photon pole, which dominates at low q^2 values,
959 reducing the sensitivity to new physics contributions. The lower bound of
960 this interval is chosen to exclude the possible contribution from the ϕ
961 resonance, which appears at $\sim 1 \text{ GeV}^2/c^4$. The upper bound of the interval
962 is chosen to exclude completely a small contribution from the J/ψ resonance
963 that leaks below $8 \text{ GeV}^2/c^4$.
- 964 • $15.0\text{--}20.0 \text{ GeV}^2/c^4$: this interval is the one that is expected to contain most
965 of the rare decays and it is used as a natural cross check that the analysis is
966 stable when performed in smaller bins.

967 3.2 Candidate types

968 This analysis deals with Λ baryons, which have a lifetime of $(2.632 \pm 0.020) \times 10^{-10} \text{ s}$ [2].
969 These are considered long-lived particles in particle physics terms and can travel sev-
970 eral metres into the detector generating well distinguished secondary vertices. In
971 LHCb, Λ baryons can be reconstructed from tracks either with or without hits in
972 the VeLo (see Sec. 2.4) and therefore two candidates types are defined as follows:

- 973 • **Downstream candidates**: built from tracks without hits in the VeLo, “down-
974 stream tracks”, also denoted as “DD”.
- 975 • **Long candidates**: built from tracks which also have hits in the VeLo, “long
976 tracks”. These candidates, also denoted as “LL”, are characterised by a better
977 momentum resolution than the downstream ones thanks to the longer lever
978 arm available to their tracks.

979 Figure 3.1 shows the two types of candidates used in the analysis, together with
980 other possible track types in LHCb, which are not used in this analysis. As the long

and downstream candidate categories are characterised by different resolutions and kinematic properties, the analysis is performed separately on the two samples and the results are then combined.

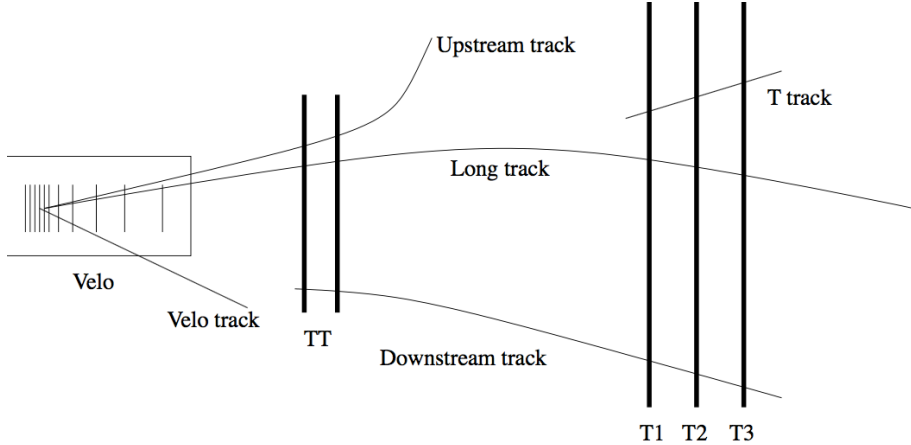


Figure 3.1: Representation of possible track types in LHCb. Candidates built from “long” and “downstream” tracks are used in this analysis [62].

3.3 Simulation

Samples of simulated events are needed in order to train a multivariate classifier, calculate the selection efficiency and study possible backgrounds; in particular for this analysis samples of $\sim 2 \cdot 10^6 \Lambda_b^0 \rightarrow J/\psi \Lambda$ and $\sim 5 \cdot 10^6 \Lambda_b^0 \rightarrow \Lambda\mu^+\mu^-$ simulated decays are used. Samples of simulated $B^0 \rightarrow J/\psi K_s^0$, $B^0 \rightarrow K_s^0\mu^+\mu^-$ and $B^+ \rightarrow \mu^+\mu^-K^{*+}$ decays are also used to study their contribution to the background. The events are generated using PYTHIA8; hadronic particles are decayed using EVTGEN and GEANT4 is used to simulate the interaction of final state particles with the detector. Simulated events are then reconstructed by the same reconstruction software that is used for real data. The L0 hardware trigger is emulated in the simulation, while for the software stage, HLT, the same code can be used as for data. Events are simulated using both 2011 and 2012 beam and detector conditions, in the same proportion as in recorded data. While the simulation gives a generally good description of data, some discrepancies remain. It is important that the simulation gives an accurate description of the data, in particular for the extraction of efficiencies. The next

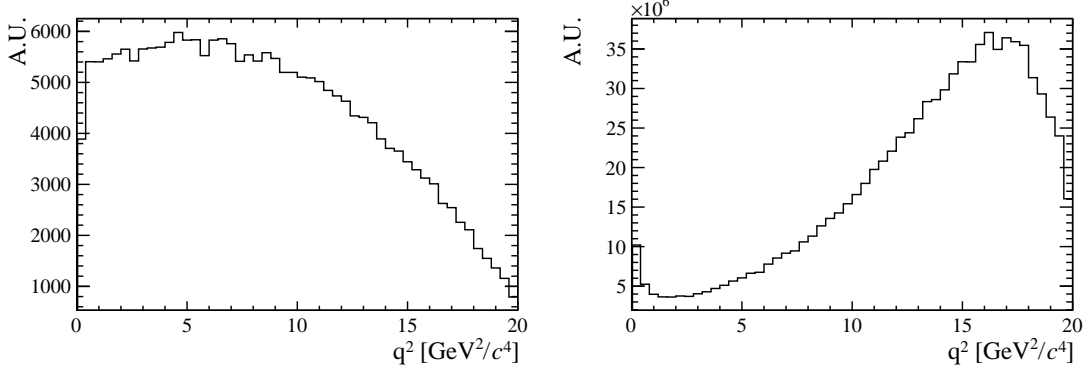


Figure 3.2: The q^2 spectrum of $\Lambda_b^0 \rightarrow \Lambda \mu^+ \mu^-$ simulated events according to the phase space of the decay (left) and re-weighted using the decay amplitudes (right).

999 sections therefore describe corrections applied to the simulation in order to provide
1000 a better description of data. In Appendix B data distributions are compared with
1001 simulated ones for variables relevant to this analysis.

1002 3.3.1 Decay Model

1003 Little is known about the decay structure of Λ_b^0 decays and therefore the simulation
1004 software generates events according to the phase space given by the available kine-
1005 matics. To obtain a more realistic q^2 dependence, the simulation is weighted using
1006 decay amplitudes based on the predictions in Ref. [101]. Equations in this paper are
1007 for the case of unpolarised Λ_b^0 production and for this analysis they are extended to
1008 include polarisation. Details about the models used are given in Appendix A.1. The
1009 value of the Λ_b^0 production polarisation, P_b , used in the calculations is $P_b = 0.06$ as
1010 measured by LHCb [102]. Figure 3.2 shows the phase space q^2 distribution and the
1011 one obtained by re-weighting the events. The latter can be qualitatively compared
1012 to the q^2 spectrum of a generic $b \rightarrow s\ell^+\ell^-$ decay shown in Fig. 1.8. For the normal-
1013 isation mode, the decay model used is described in Appendix A.3, with amplitude
1014 magnitudes and production polarisation taken from the measurements in Ref. [102].
1015 Phases are not yet measured and are therefore set to zero.

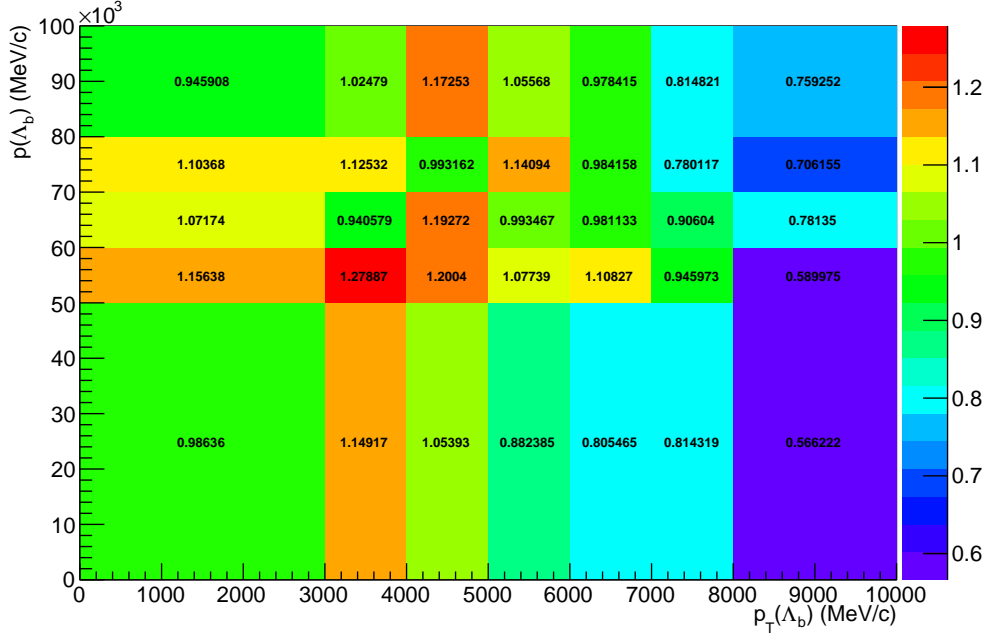
1016 3.3.2 Kinematic re-weighting

1017 Small data-simulation differences are found in the kinematic properties of the mother
1018 particle, Λ_b^0 , which also affect the final state particles. The simulation is re-weighted
1019 by comparing the momentum and transverse momentum of Λ_b^0 baryons in real and
1020 simulated $\Lambda_b^0 \rightarrow J/\psi \Lambda$ candidates that satisfy the pre-selection requirements (see
1021 Sec. 3.4). To do this a high purity data sample is obtained by selecting a nar-
1022 row invariant mass interval around the J/ψ and Λ_b^0 peaks; this contains about
1023 $4 \cdot 10^5$ candidates. The Λ_b^0 invariant mass distribution is then fitted to estimate
1024 the number of background decays under the peak. Finally, the background fraction,
1025 $f_b = B/(S + B)$, is used to statistically subtract the background from the kinemat-
1026 ical distributions as described by the equation:

$$S(p, p_T) = T(p, p_T) - f_b \cdot B(p, p_T), \quad (3.2)$$

1027 where $S(p, p_T)$ is the distribution of pure signal candidates, which we want to obtain,
1028 $T(p, p_T)$ is the total distribution of signal plus background, namely the distribution
1029 of all events in the signal interval, $5605 < m(p\pi\mu^+\mu^-) < 5635$ MeV/ c^2 , and $B(p, p_T)$
1030 is the pure background distribution obtained using candidates from the upper side-
1031 band, $m(p\pi\mu^+\mu^-) > 5800$ MeV/ c^2 .

1032 After the signal distributions have been obtained from data, they are compared
1033 with $\Lambda_b^0 \rightarrow J/\psi \Lambda$ simulated events and a weight, $w(p_{\Lambda_b^0}, p_{T\Lambda_b^0})$ is defined by taking
1034 the ratio of the two dimensional (p, p_T) distributions. The result is shown in Fig. 3.3,
1035 while Appendix B reports distributions of sideband subtracted data in the signal and
1036 sideband regions together with weighted and unweighted simulated events. In these
1037 plots the momentum and p_T distributions of Λ_b^0 baryons match by construction but
1038 the re-weighting also improves the agreement between the kinematical distributions
1039 of all final particles. Small differences remain due to the finite binning used for the
1040 weights calculation. Quality variables, such as the χ^2 of tracks and vertices, show
1041 little dependence on the kinematics and are relatively unaffected by the weighting
1042 procedure.



1054 3.4 Selection

1055 This section describes the requirements applied to reconstruct $\Lambda_b^0 \rightarrow \Lambda\mu^+\mu^-$ and
1056 $\Lambda_b^0 \rightarrow J/\psi\Lambda$ candidates. The selection procedure is divided into two steps: a
1057 pre-selection, where cuts are applied in order to be able to work with manage-
1058 able datasets and a multivariate analysis (MVA) which combines information from
1059 several variables. As a first step good quality tracks are selected by imposing re-
1060 quirements on their basic kinematic properties, such as the p_T of the final particles,
1061 and quality requirements, such as the track χ^2 . The selection then forms a dimuon
1062 candidate from two oppositely charged muons. In events containing a dimuon can-
1063 didate, two oppositely charged tracks are combined and retained as a Λ candidate
1064 if they form a good quality vertex which is well separated from all primary ver-
1065 tices. Finally, the dimuon and Λ candidates are combined to form Λ_b^0 baryons with
1066 requirements placed on the properties of this combination.

1067 3.4.1 Pre-selection

1068 The full list of pre-selection cuts is reported in Tab. 3.1. In the table χ_{IP}^2 is defined
1069 as the projected distance from a vertex divided by its uncertainty, for example the
1070 $\chi_{IP}^2(primary) > n$ requirement on Λ_b^0 means that the Λ_b^0 vertex must be at least
1071 \sqrt{n} standard deviations away from the primary vertex. Another quantity, found
1072 to be particularly powerful at removing combinatorial background, is a pointing
1073 variable called DIRA defined as the cosine of the angle between the direction of a
1074 particle's momentum and the flight direction from its mother vertex. Requiring a
1075 DIRA close to unity corresponds to the selection of particles with well-defined origin
1076 vertices. Figure 3.4 shows graphical representations of the χ_{IP}^2 and DIRA variables.
1077 The variable χ_{FD}^2 represents the flight distance of a particle from its origin vertex
1078 divided by the corresponding uncertainty. The χ_{trk}^2/ndf and χ_{vtx}^2/ndf quantities
1079 are the χ^2 from the fit to tracks and vertices, which are used to quantify their
1080 quality. The `GhostProb` quantity describes the probability of a track being fake. By

construction, cutting at a value of k , removes $(1 - k) \cdot 100\%$ of fake tracks. The `hasRich`, `hasCalo` and `isMuon` variables are binary indicators that the information from the RICH, calorimeter and muon detectors is available for the track. Loose PID requirements on the proton are also applied in the pre-selection. Details about PID quality estimators are given in Sec. 2.8. A large mass window around the Λ_b^0 peak is used to allow a fit to the sideband to be performed and to use sideband candidates to train a multivariate classifier. Rare candidates are selected by the q^2 region requirements described in Sec. 3.1, while resonant candidates are further constrained to have dimuon invariant masses in a $100 \text{ MeV}/c^2$ interval around the known J/ψ mass [2].

3.4.2 Neural Networks

The final selection is performed using a neural network classifier based on the NeuroBayes package. The input to the neural network consists of 14 variables carrying information about the kinematics of the decay, the quality of tracks and vertices and the PID of the muons. The list of the 10 most significant inputs is reported in Tab. 3.2, together with information about the importance of each input. Variables related to Λ and its daughters are considered as different inputs depending on the candidate type (long or downstream). This effectively corresponds to making a separate training for the two categories.

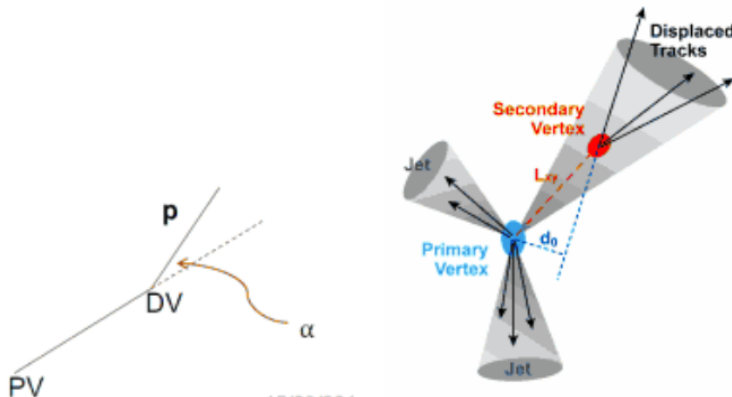


Figure 3.4: Graphical representation of the DIRA (left) and χ_{IP}^2 (right) variables.

Particle	Requirement
Λ_b^0	$4.6 < m(p\pi\mu\mu) < 7.0 \text{ GeV}/c^2$ $\text{DIRA} > 0.9999$ $\chi_{\text{IP}}^2 < 16.0$ $\chi_{\text{FD}}^2 > 121.0$ $\chi_{\text{vtx}}^2/ndf < 8.0$
Λ	$\chi_{\text{vtx}}^2/ndf < 30.0(25.0)$ $\text{Decay time} > 2 \text{ ps}$ $ m(p\pi) - m_A^{\text{PDG}} < 35(64) \text{ GeV}/c$
p/π	$p > 2 \text{ GeV}/c$ $p_T > 250 \text{ MeV}/c$ $\chi_{\text{IP}}^2 > 9(4)$
p (only long cand.)	hasRICH $\text{PID}p > -5$
μ	isMuon $\chi_{\text{trk}}^2/ndf < 5$ $\text{GhostProb} < 0.4$ $\text{PID}\mu > -3$ $\chi_{\text{IP}}^2 > 9.0$
Dimuon	$\chi_{\text{vtx}}^2/ndf < 12.0$ $ m(\mu\mu) - m_{J/\psi}^{\text{PDG}} < 100 \text{ MeV}/c^2 \quad (J/\psi \Lambda \text{ only})$

Table 3.1: Summary of the pre-selection requirements. Where two values are given, the main one applies to long candidates and the one in parenthesis to downstream candidates.

1100 The neural network is trained using representative samples of signal and background.
1101 A sample of simulated $\Lambda_b^0 \rightarrow \Lambda\mu^+\mu^-$ candidates is used as a proxy for the signal,
1102 while for the background a representative sample is given by candidates in the upper
1103 $m(p\pi\mu\mu)$ invariant mass sideband. Only the upper sideband, $m(p\pi\mu\mu) > 6 \text{ GeV}/c^2$,
1104 is used since it contains only combinatorial background, while the lower sideband
1105 may contain partially reconstructed and misreconstructed candidates. In the q^2
1106 spectrum of background samples the J/ψ and $\psi(2S)$ peaks are still present indicating
1107 that charmonium resonances are often combined with other random tracks. These
1108 candidates do not give a good description of purely combinatorial background and,
1109 in order to avoid biases, they are removed from the training sample by rejecting
1110 candidates in a $100 \text{ MeV}/c^2$ interval around the nominal J/ψ and $\psi(2S)$ masses [2].
1111 A total of $3 \cdot 10^4$ events is used for the training from each sample. This corresponds
1112 to approximately $\simeq 50\%$ of the available sideband data and $\simeq 20\%$ of the simulated

Table 3.2: Summary of the 10 most significant inputs to the neural network in order of importance. Column “adds” gives the significance added by a given input when it is added to the list of those ranked above. Column “only this” provides the power of a given input alone and “loss” shows how much information is lost when removing only a given input.

Input	adds	only this	loss
$\Lambda_{\text{DD}} p_T$	143.11	143.11	29.20
χ^2_{DTF}	77.81	134.00	51.10
$\min(\chi^2_{\text{IP}}, \mu)$	61.31	113.62	29.76
$\chi^2_{\text{IP}} \Lambda_b^0$	52.94	113.23	40.98
$\chi^2_{\text{IP}} \pi_{\text{LL}}$	20.29	60.72	12.82
$\min(\text{PID}, \mu)$	17.91	59.11	13.44
$\tau_{\Lambda_b^0}$	16.24	35.36	11.24
$\Lambda_b^0 \text{DIRA}$	12.28	73.96	9.98
$\Lambda_{\text{DD}} \text{flight distance}$	9.47	86.75	11.24
$\chi^2_{\text{IP}} \Lambda_{\text{DD}}$	10.58	59.84	8.88

sample. The full simulated sample is not used in the training as the same sample will also be used to study efficiencies. For reproducibility the events are sampled uniformly.

The single most important variable used for downstream candidates is the transverse momentum of Λ , which allows random combinations of tracks to be rejected as these have preferentially low p_T . In contrast, for long candidates the most powerful variable is the χ^2 from a kinematic fit that constrains the decay products of the Λ_b^0 , the Λ and the dimuon, to originate from their respective vertices. Other variables that contribute significantly are the χ^2_{IP} of Λ_b^0 , Λ and muons, the separation between the Λ_b^0 and Λ vertices and, finally, the muon PID.

Figure 3.5 shows distributions of neural network output for the signal and background samples and purity, $P = N_{\text{sig}}/N_{\text{bkg}}$, as a function of the neural network output. To check for potential overtraining, the distributions from test samples are also overlaid. These are found to follow the same shape but with different fluctuations giving no significant evidence of overtraining. In general it can be concluded that the neural network is able to separate signal from background and the training converged properly. It can happen that too much information is given

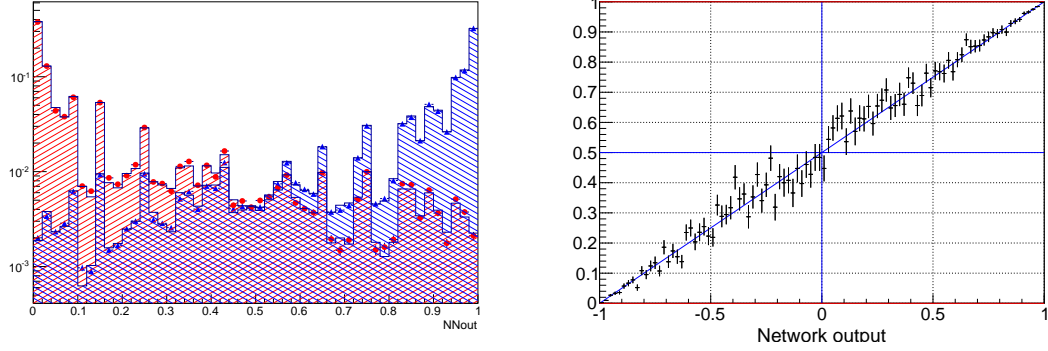


Figure 3.5: (left) Neural network output distribution for training (points) and test (stripes) samples, for signal (blue) and background (red) candidates. (right) Purity as a function of neural network output.

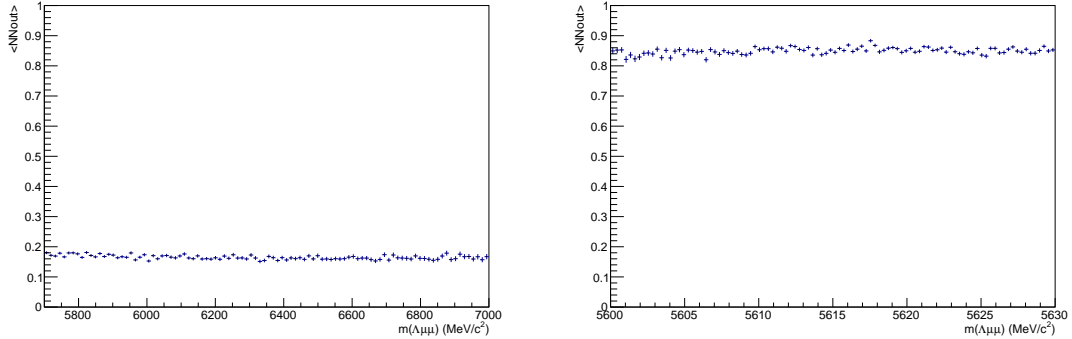


Figure 3.6: Average value of neural network output as a function of the 4-body invariant mass for data sideband (left) and simulated signal (right) candidates.

to the classifier, allowing the invariant mass of the candidates to be inferred from the input variables. This can generate fake peaks and it is therefore important to check for correlations between the 4-body invariant mass and the neural network output. Figure 3.6 reports the average neural network output as a function of the 4-body $m(p\pi\mu\mu)$ invariant mass for data and simulation. The distributions are flat indicating that no significant correlation is present.

3.4.3 MVA optimisation

In the high- q^2 region, where the signal is already observed, the requirement on the neural network output is chosen to maximise the significance, $N_S/\sqrt{N_S + N_B}$, where N_S and N_B are the numbers of expected signal and background candidates

respectively. N_S is derived from simulation but, as an arbitrary number of events can be generated, it needs to be normalised. To do this, the invariant mass distribution of real $\Lambda_b^0 \rightarrow J/\psi \Lambda$ candidates is fit after pre-selection (including all requirements except the MVA selection). This is possible as the peak of the resonant channel is already clearly visible before the MVA requirement. The resonant yield is then scaled by the ratio of between the $\Lambda_b^0 \rightarrow \Lambda \mu^+ \mu^-$ and $\Lambda_b^0 \rightarrow J/\psi \Lambda$ branching fractions as measured by LHCb on 2011 data,

$$\mathcal{B}(\Lambda_b^0 \rightarrow \Lambda \mu^+ \mu^-) / \mathcal{B}(\Lambda_b^0 \rightarrow J/\psi \Lambda) = 1.54 \times 10^{-3} \quad (3.3)$$

and by the $J/\psi \rightarrow \mu^+ \mu^-$ branching fraction, *i.e.*

$$N_S = N_{J/\psi} \cdot \frac{\mathcal{B}(\Lambda_b^0 \rightarrow \Lambda \mu^+ \mu^-)}{\mathcal{B}(\Lambda_b^0 \rightarrow J/\psi \Lambda) \cdot \mathcal{B}(J/\psi \rightarrow \mu^+ \mu^-)}. \quad (3.4)$$

The number of expected background candidates is derived by fitting the data side-band with an exponential and extrapolating into the signal region.

In the low- q^2 region, where the signal is unobserved, the so called ‘‘Punzi figure-of-merit’’, $N_S/(n_\sigma/2 + \sqrt{N_B})$, is maximised [103]. This figure-of-merit is considered to be optimal for discovery and the parameter n_σ corresponds to the number of expected standard deviations of significance, in this analysis $n_\sigma = 3$ is used. Moreover, the Punzi shape does not depend on the relative normalisation between signal and background, which is important since the signal is still unobserved at low- q^2 and the existing predictions vary significantly for this region. The dependence of the figure-of-merit for both q^2 regions is shown in Fig. 3.7, and curves of signal efficiency versus background rejection are shown in Fig. 3.8.

For the final selection the neural network output is required to be larger than 0.76 for candidates in the high- q^2 region and 0.97 for the low- q^2 ones. Using these requirements the neural network retains approximately 97 % (82 %) of long candidates and 96% (66 %) of downstream candidates for the high- (low-) q^2 selection, with respect to the pre-selected samples. After full selection $\sim 0.5\%$ of the events con-

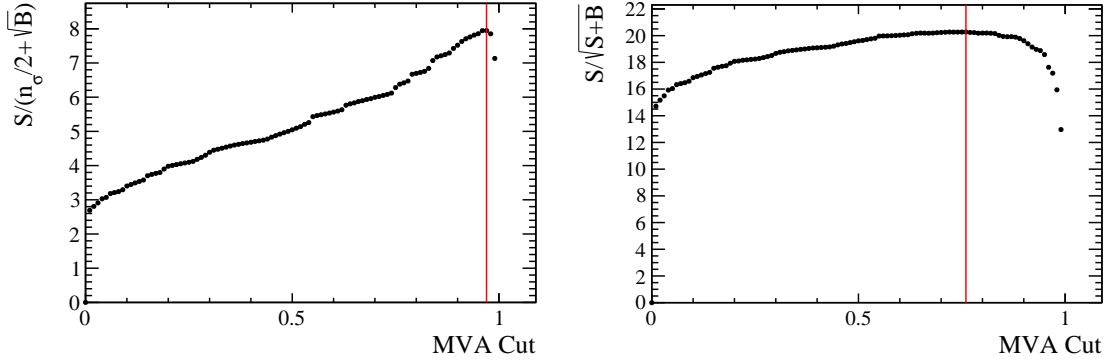


Figure 3.7: Dependence of the figure-of-merits on the neural network output requirement for the low- q^2 (left) and high- q^2 (right) regions. The vertical lines correspond to the chosen cuts.

tain multiple candidates which are randomly rejected keeping only one candidate per event. To normalise the branching ratio measurement $\Lambda_b^0 \rightarrow J/\psi \Lambda$ candidates are selected using both, low- and high- q^2 , requirements to normalise respectively low and high- q^2 intervals.

3.4.4 Trigger

Specific trigger lines are selected, corresponding to events triggered by the muons which formed the reconstructed candidate. This is denoted as Trigger On Signal (TOS). The trigger lines used in the analysis are listed in Tab. 3.3. The logical *or* of the lines on the same level is required and the logical *and* of those on different levels. The L0Muon trigger requires hits in the muon detector and triggers if a muon with $p_T > 1.5$ GeV/ c is identified. L0Dimuon imposes the same requirement on the sum of the transverse momenta of two tracks. The Hlt1TrackAllL0 performs a partial reconstruction of the events and applies basic requirements on the IP, χ^2 and p_T of tracks; it triggers if the L0 decision is confirmed. Hlt1TrackMuon applies looser requirements but in addition requires the `isMuon` variable (see Sec. 2.8) to be true to limit the yield. Finally, at the Hlt2 level, a complete reconstruction is done and a multivariate analysis is used to identify decay structures. One of the main variables used at this stage is the Distance Of Closest Approach (DOCA), which is

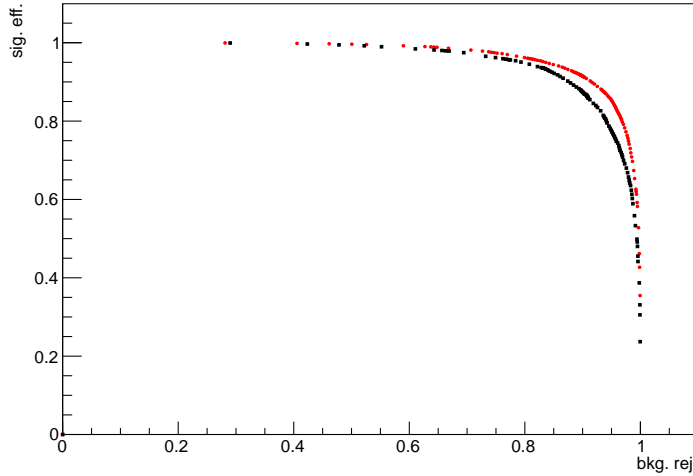


Figure 3.8: Receiver operating characteristic (ROC) curves for low- q^2 (black) and high- q^2 (red). They show the signal efficiency versus the background rejection. The optimal points on these curves are the closest ones to (1,1).

required to be less than 0.2 mm to form a 2-body object.

Table 3.3: Summary of the trigger lines used to select events at various levels. Trigger is always required to be due to the tracks of the candidate itself.

Trigger Level	Lines
L0	LOMuon LODiMuon
Hlt1	Hlt1TrackAllL0 Hlt1TrackMuon
Hlt2	Hlt2Topo [2-4] BodyBBDT Hlt2TopoMu [2-4] BodyBBDT Hlt2SingleMuon Hlt2DiMuonDetached

1182

1183 3.4.5 Background from specific decays

1184 Candidates from other decays can be reconstructed as the decays of interest if par-
 1185 ticles are not reconstructed or mis-identified. A survey of possible backgrounds
 1186 concluded that the only physics background to take into account comes from mis-
 1187 reconstructed decays of B^0 to K_s^0 with two muons in the final state, whether via
 1188 J/ψ or not, where the K_s^0 is reconstructed as a Λ with a $p \rightarrow \pi$ identity swap.

1189 The lack of background from other decays is mainly due to the particular topology
 1190 of the Λ decay, which is long-lived and decays at a displaced vertex. To study
 1191 the effect of misreconstructed $B^0 \rightarrow J/\psi K_s^0$ and $B^0 \rightarrow K_s^0\mu^+\mu^-$ decays simulated
 1192 samples are used. On data the $B^0 \rightarrow J/\psi K_s^0$ contribution is clearly visible in the
 1193 resonant channel mass distribution. This background is not suppressed with specific
 1194 cuts in this analysis as its mass shape is sufficiently distinct from the Λ_b^0 signal and
 1195 its contribution can be reliably modelled in the mass fits (see Sec. 3.5.1). For the
 1196 rare case a rough estimate of the K_s^0 background size is obtained using the yield in
 1197 the resonant channel rescaled by the measured ratio between the rare and resonant
 1198 branching fractions. Details are given in Sec. 3.5.1 and numbers of events predicted
 1199 are reported in Tab. 3.4. This contribution, although close to negligible is again
 1200 considered in the fit. A possible pollution due to $B^+ \rightarrow \mu^+\mu^-K^{*+}$ decays, where
 1201 the K^{*+} further decays into $K_s^0\pi$ is also investigated using a dedicated simulated
 1202 sample and found to be negligible. Finally, $\Lambda_b^0 \rightarrow J/\psi \Lambda$ events radiating photons
 1203 from the final state, can escape the J/ψ veto and be reconstructed in the rare chan-
 1204 nel sample. Analysing simulated events it was found that the only contribution is
 1205 in the closest q^2 interval to the J/ψ tail, $6 < q^2 < 8$ GeV $^2/c^4$. In this interval
 1206 1.3% of the $\Lambda_b^0 \rightarrow J/\psi \Lambda$ candidates are reconstructed but only 0.06% fall into the
 1207 4-body invariant mass window used for the fits. This corresponds to ~ 6 events,
 1208 4 of which in the downstream category. Given the low yield and that these events
 1209 do not peak under the signal but show a decaying distribution at the edge of the
 1210 fit mass window, this background is considered as absorbed in the combinatorial
 1211 background. Figure 3.9 shows the 4-body invariant mass distribution of simulated
 1212 $\Lambda_b^0 \rightarrow J/\psi \Lambda$ events falling into the rare q^2 region and the distribution of simulated
 1213 $B^+ \rightarrow \mu^+\mu^-K^{*+}$ events mis-reconstructed as $\Lambda_b^0 \rightarrow J/\psi \Lambda$ decays.

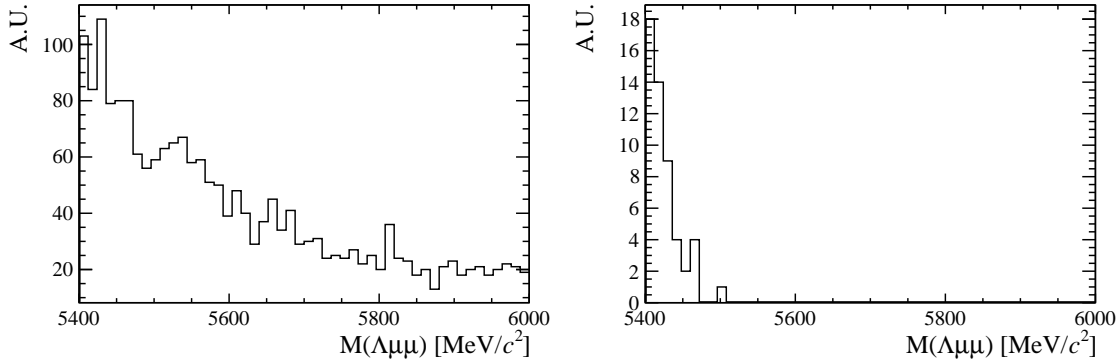


Figure 3.9: Invariant mass distributions of simulated $B^+ \rightarrow \mu^+ \mu^- K^{*+}$ (left) and $\Lambda_b^0 \rightarrow J/\psi \Lambda$ (right) candidates passing the full selection. Only $\Lambda_b^0 \rightarrow J/\psi \Lambda$ candidates reconstructed in $q^2 < 8 \text{ GeV}^2/c^4$ are selected. Distributions are shown in the invariant mass range relevant for the analysis (see Sec. 3.5.1).

1214 3.5 Yield extraction

1215 Extended unbinned maximum likelihood fits are used to extract the yields of the
1216 rare and resonant channels. The likelihood has the form:

$$\mathcal{L} = e^{-(N_S + N_C + N_B)} \times \prod_{i=1}^N [N_S P_S(m_i) + N_C P_C(m_i) + N_B P_B(m_i)] \quad (3.5)$$

1217 where N_S , N_C and N_B are respectively the numbers of signal, combinatorial and K_s^0
1218 background candidates and the $P_i(m_i)$ are the corresponding probability density
1219 functions (PDF). The fit variable is the 4-body $m(p\pi\mu\mu)$ invariant mass obtained
1220 from a kinematical fit of the full decay chain in which each particle is constrained
1221 to point to its assigned origin vertex and the invariant mass of the $p\pi$ system is
1222 constrained to be equal to the world average for the Λ baryon mass. In the resonant
1223 case a further constrain is used on the dimuon mass to be equal to the known J/ψ
1224 mass. This method allows to improve the mass resolution giving better defined
1225 peaks and therefore a more stable fit. For brevity, in the following these variables
1226 are simply referred to as ‘‘invariant mass’’.

₁₂₂₇ 3.5.1 Fit description

₁₂₂₈ The fit is performed through the following steps:

- ₁₂₂₉ • simulated distributions are fit to extract initial parameters;
- ₁₂₃₀ • the resonant data sample is fitted;
- ₁₂₃₁ • the rare sample is fitted fixing some parameters to those obtained in the pre-
- ₁₂₃₂ vious cases.

₁₂₃₃ In the first step simulated $\Lambda_b^0 \rightarrow J/\psi \Lambda$ distributions are fitted using the signal PDF
₁₂₃₄ alone. This is done separately for downstream and long candidates. Figure 3.10
₁₂₃₅ shows distributions of candidates selected in the resonant sample with the fit function
₁₂₃₆ overlaid. The signal is described as the sum of two Crystal Ball functions (CB)
₁₂₃₇ with common mean (m_0) and tail slope (n). This is also known as Double Crystal
₁₂₃₈ Ball (DCB) function. A single Crystal Ball [104] is a probability density function
₁₂₃₉ commonly used to model processes involving energy loss. In particular it is used to
₁₂₄₀ describe resonances' peaks with radiative tails. This function consists of a Gaussian
₁₂₄₁ core and a power-law tail below a certain threshold and has form

$$C(x; \alpha, n, \bar{x}, \sigma) = N \cdot \begin{cases} \exp\left(-\frac{(x-\bar{x})^2}{2\sigma}\right) & \text{if } \frac{(x-\bar{x})}{\sigma} > \alpha, \\ A \left(B - \frac{(x-\bar{x})}{\sigma}\right)^{-n} & \text{if } \frac{(x-\bar{x})}{\sigma} < \alpha, \end{cases} \quad (3.6)$$

₁₂₄₂ where for normalisation and continuity

$$\begin{aligned} A &= \left(\frac{c}{|\alpha|}\right)^n \cdot \exp\left(-\frac{\alpha^2}{2}\right), \\ B &= \frac{n}{|\alpha|} - |\alpha|. \end{aligned} \quad (3.7)$$

₁₂₄₃ The full PDF for the resonant channel is therefore:

$$P_S(m; m_0, \alpha_1, \alpha_2, f, n) = f \cdot CB(m; m_0, \sigma_1, \alpha_1, n) + (1-f)CB(m; m_0, \sigma_2, \alpha_2, n), \quad (3.8)$$

₁₂₄₄ where f is the relative fraction of candidates falling into the first CB function.

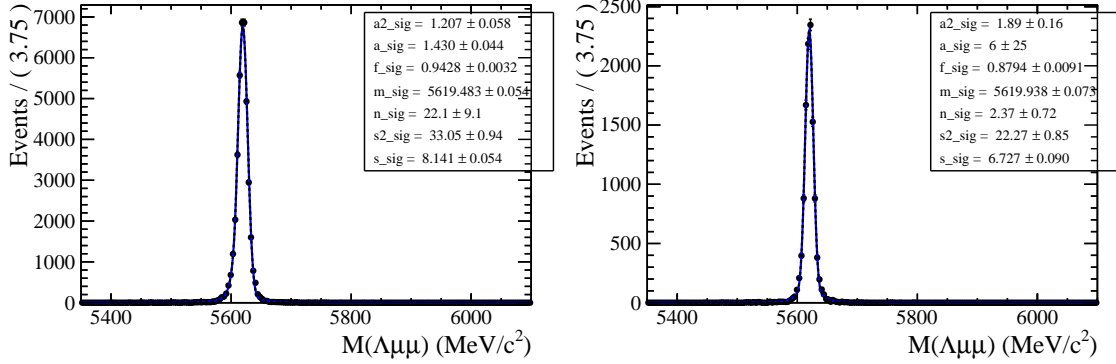


Figure 3.10: Invariant mass distribution of $\Lambda_b^0 \rightarrow J/\psi \Lambda$ downstream (left) and long (right) candidates. The points show simulated data and the blue line is the signal fit function.

1245 In a second step the fit to the resonant channel data sample is performed. For this fit
 1246 the tail slope parameter, “ n ”, which is highly correlated with α_1 and α_2 , is fixed to
 1247 the value found in the fit to simulated data. In this fit two background components
 1248 are modelled: the combinatorial background, parameterized with an exponential
 1249 and the background from $B^0 \rightarrow J/\psi K_s^0$ decays. The shape used to describe the
 1250 K_s^0 background is obtained from a $B^0 \rightarrow J/\psi K_s^0$ simulated sample to which the full
 1251 selection is applied. The invariant distribution of these candidates is fit with a DCB
 1252 function, which is then used to model the K_s^0 background in the $\Lambda_b^0 \rightarrow J/\psi \Lambda$ fit. The
 1253 fit to the simulated $B^0 \rightarrow J/\psi K_s^0$ events is reported in Fig. 3.11. When the K_s^0 shape
 1254 is introduced in the fit to the data all its parameters are fixed. This is particularly
 1255 important when fitting long candidates, where the K_s^0 peak is less evident, which
 1256 does not allow to constrain many parameters. On the other hand, in order to take
 1257 into account possible data-simulation differences, an horizontal shift is added and
 1258 left floating (by adding a constant to the central value of the DCB, $m_0 \rightarrow m_0 + m'$).
 1259 In summary, the free parameters in the fit to the resonant $\Lambda_b^0 \rightarrow J/\psi \Lambda$ sample are
 1260 the yields of the signal and the combinatorial and K_s^0 backgrounds, the slope of the
 1261 exponential and the horizontal shift of the K_s^0 shape. Note that all the parameters
 1262 of the PDFs used to fit the long and downstream samples are independent.
 1263 Finally, the rare $\Lambda_b^0 \rightarrow \Lambda \mu^+ \mu^-$ data sample is fit. In this case the fit to the long and
 1264 downstream samples is performed simultaneously to obtain a more stable conver-

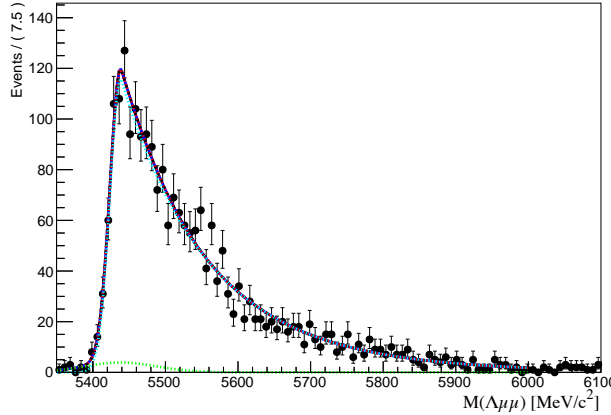


Figure 3.11: Invariant mass distribution of simulated $B^0 \rightarrow J/\psi K_s^0$ events after full selection fitted with a Double Crystal Ball function.

gence. For this fit the signal is modelled with the same shape used in the resonant case as there is no physical reason why they should be different. This method is also useful to limit systematic uncertainties as the result will be given as a ratio between rare and resonant quantities. However, the low statistics available in the rare sample does not allow to constrain many parameters. Therefore, all parameters of the signal shape are fixed to the ones derived from the fit to the $J/\psi\Lambda$ channel. However, to account for possible differences, arising from a different resolution in different q^2 regions, a scale factor is multiplied to the widths of the two gaussian cores of the signal DCB: $\sigma_1 \rightarrow c(q^2) \cdot \sigma_1$ and $\sigma_2 \rightarrow c(q^2) \cdot \sigma_2$, where the two scale factors are the same. These factors are fixed to values obtained by fitting rare $\Lambda_b^0 \rightarrow \Lambda\mu^+\mu^-$ simulated events in each q^2 bin and comparing the widths with the ones found on the fit to the resonant simulated sample, namely

$$c = \sigma_{\mu^+\mu^-}^{MC} / \sigma_{J/\psi}^{MC}. \quad (3.9)$$

These values are found to be ~ 1.9 for downstream candidates and ~ 2.3 for long candidates, corresponding to the fact that in the resonant case a further constrain on the dimuon mass is used, which improves the resolution by a factor of ~ 2 . The dependence of the scaling factor on q^2 is found to be small. For the fits on the long and downstream samples the parameters are always separately fixed to the

1282 corresponding $J/\psi \Lambda$ fits; in this analysis shape parameters are never shared between
1283 the two candidate categories.

1284 The modelled background components are, also in the rare case, the combinatorial
1285 background, described with an exponential function and the K_s^0 background. The
1286 slope of the background is visibly different depending on the q^2 interval. This is
1287 partly due to the fact that at high q^2 the combinatorial changes slope because of
1288 a kinematical limit at low 4-body masses imposed by the q^2 requirements. The
1289 exponential slopes are therefore left as independent parameters in each q^2 interval.
1290 The background component from $B^0 \rightarrow K_s^0 \mu^+ \mu^-$ decays is modelled using the same
1291 shapes used for the resonant channel. However, in this case the horizontal shift is
1292 fixed to what found for the resonant channel. The expected amount of misrecon-
1293 structed $B^0 \rightarrow K_s^0 \mu^+ \mu^-$ candidates is small and does not allow to determine reliably
1294 its yield. Therefore, this is fixed to the yield of $B^0 \rightarrow J/\psi K_s^0$ decays rescaled by the
1295 expected ratio of branching fractions between the resonant and rare channels. The
1296 q^2 distribution of $B^0 \rightarrow K_s^0 \mu^+ \mu^-$ simulated events is used to predict the yield as a
1297 function of q^2 . Table 3.4 reports the number of predicted $B^0 \rightarrow K_s^0 \mu^+ \mu^-$ candidates
1298 in each q^2 interval obtained with the following formula:

$$N_{K_s^0 \mu^+ \mu^-}(q^2) = N_{J/\psi K_s^0} \frac{B(B^0 \rightarrow K_s^0 \mu^+ \mu^-)}{B(B^0 \rightarrow K_s^0 J/\psi)} \cdot \frac{1}{\varepsilon_{rel}} \cdot B(J/\psi \rightarrow \mu^+ \mu^-) \frac{N(q^2)_{MC}}{N_{MC}^{tot}} \quad (3.10)$$

1299 where $N(q^2)_{MC}$ is the number of simulated rare candidates falling in a q^2 interval af-
1300 ter full selection and N_{MC}^{tot} is the total number of simulated events and $\varepsilon_{rel} = \varepsilon_{\mu\mu}/\varepsilon_{J/\psi}$
1301 is the relative selection efficiency between the two channels.

1302 As the fit to the rare sample is performed simultaneously on long and downstream
1303 candidates, their two yields are not free to vary separately but are parameterised as
1304 a function of the common branching fraction using the following formula:

$$N(\Lambda \mu^+ \mu^-)_k = \left[\frac{d\mathcal{B}(\Lambda \mu^+ \mu^-)/dq^2}{\mathcal{B}(J/\psi \Lambda)} \right] \cdot N(J/\psi \Lambda)_k \cdot \varepsilon_k^{\text{rel}} \cdot \frac{\Delta q^2}{\mathcal{B}(J/\psi \rightarrow \mu^+ \mu^-)}, \quad (3.11)$$

1305 where $k = (\text{LL}, \text{DD})$, Δq^2 is the width of the q^2 interval and the only free param-

Table 3.4: Predicted numbers of $B^0 \rightarrow K_s^0\mu^+\mu^-$ events in each considered q^2 interval.

q^2 interval [GeV $^2/c^4$]	Downstream	Long
0.1–2.0	0.9	0.1
2.0–4.0	0.9	0.1
4.0–6.0	0.8	0.1
6.0–8.0	1.1	0.1
11.0–12.5	1.9	0.2
15.0–16.0	1.1	0.1
16.0–18.0	2.0	0.2
18.0–20.0	1.1	0.1
1.1–6.0	2.1	0.1
15.0–20.0	4.2	0.5

ter is the relative branching fraction ratio of the rare over J/ψ channels. For the branching fraction of the $J/\psi \rightarrow \mu^+\mu^-$ decay the value reported in the PDG book, $(5.93 \pm 0.06) \cdot 10^{-2}$ [2] is used and ε^{rel} corresponds to the relative efficiency between the rare and resonant channels obtained in Sec. 3.6. In this formula the efficiencies and the normalisation yield appear as constants, namely $N(\Lambda\mu^+\mu^-)_k = C_k \cdot \mathcal{B}^{rel}$.

3.5.2 Fit results

Figures 3.12 and 3.13 show fitted invariant mass distributions for the normalisation channel, selected with the high- q^2 and low- q^2 requirements respectively. Table 3.5 reports the measured yields of $\Lambda_b^0 \rightarrow J/\psi\Lambda$ candidates found using the low- and high- q^2 selections. Values for the signal shape parameters are shown on Fig. 3.12. Fits to the rare $\Lambda_b^0 \rightarrow \Lambda\mu^+\mu^-$ samples are shown in Fig. 3.14 for the integrated $15 < q^2 < 20$ and $1.1 < q^2 < 6.0$ GeV $^2/c^4$ q^2 intervals, while fitted invariant mass distribution in all other considered q^2 intervals are in Figs. 3.15 and 3.16 for downstream and long candidates respectively. The yields of rare candidates obtained from the fit are listed in Tab. 3.6 together with their significances. Most candidates are found in the downstream sample, which comprises $\sim 80\%$ of the total yield. Note that, since the fit is simultaneous to the two candidate categories, their yields are not parameters free to vary independently but are correlated via the branching ratio. The statistical significance of the observed signal yields is evaluated as the change

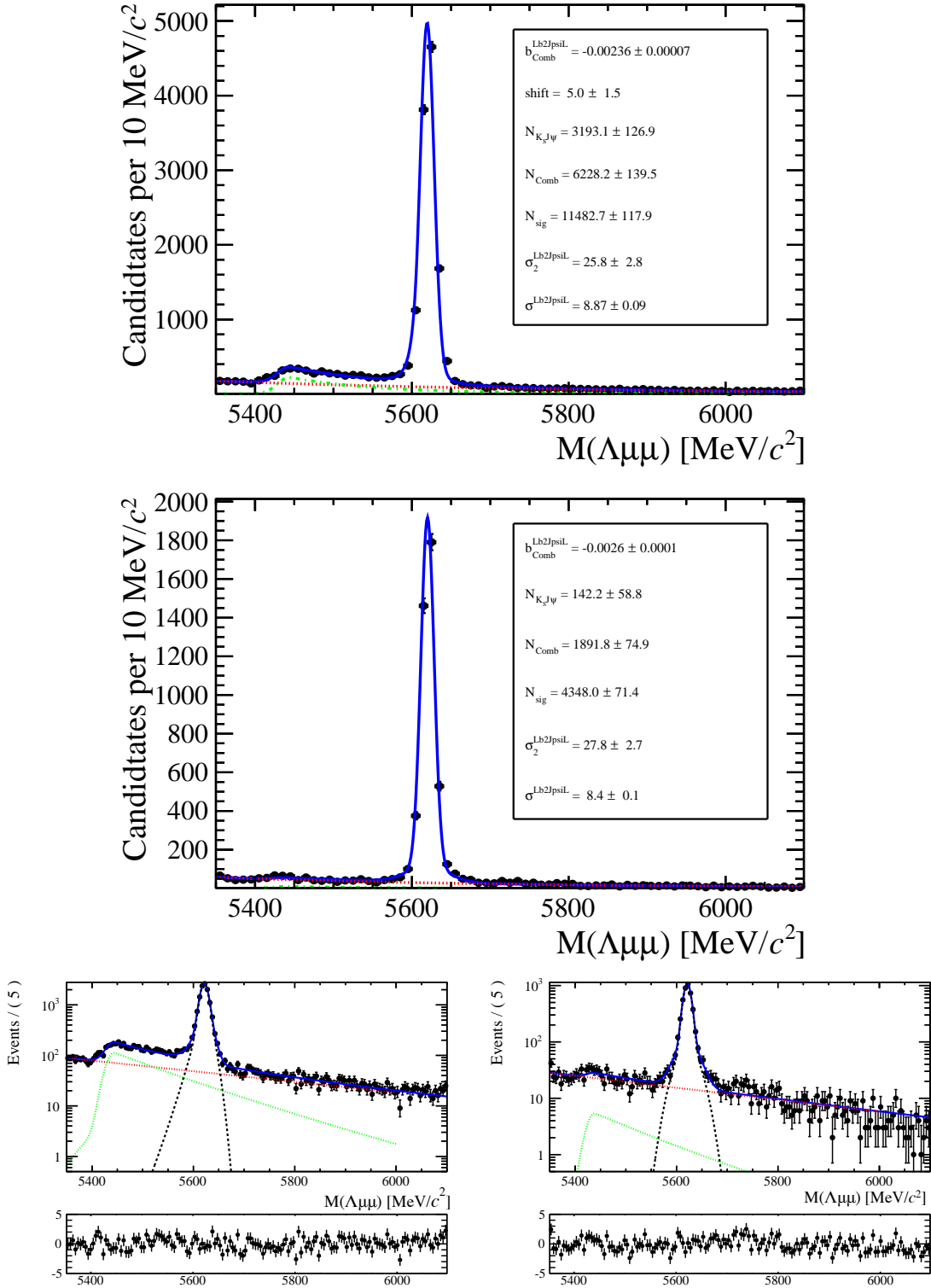


Figure 3.12: Invariant mass distributions of $\Lambda_b^0 \rightarrow J/\psi \Lambda$ downstream (top) and long (middle) candidates selected with high q^2 requirements. Bottom plots are the same as the upper ones but shown in logarithmic scale. Black points show data. The blue solid line represents the total fit function, the black dashed line the signal, the red dashed line the combinatorial background and the green dashed line the $B^0 \rightarrow K_s^0 \mu^+ \mu^-$ background.

Table 3.5: Number of $\Lambda_b^0 \rightarrow J/\psi \Lambda$ candidates in the downstream and long categories found using the for low- and high- q^2 requirements; uncertainties are statistical only.

Selection	Long	Downstream
high- q^2	4313 ± 70	$11\,497 \pm 123$
low- q^2	3363 ± 59	7225 ± 89

Table 3.6: Signal yields, N_S , obtained from the invariant mass fit to $\Lambda_b^0 \rightarrow \Lambda\mu^+\mu^-$ candidates in each q^2 interval together with their statistical significance. The $8 - 11$ and $12.5 - 15$ GeV^2/c^4 q^2 intervals are excluded from the study as they are dominated by resonant decays via charmonium resonances.

q^2 interval [GeV^2/c^4]	DD	LL	Tot. yield	Significance
0.1 – 2.0	6.9 ± 2.2	9.1 ± 3.0	16.0 ± 5.3	4.4
2.0 – 4.0	1.8 ± 1.7	3.0 ± 2.8	4.8 ± 4.7	1.2
4.0 – 6.0	0.4 ± 0.9	0.6 ± 1.4	0.9 ± 2.3	0.5
6.0 – 8.0	4.3 ± 2.0	7.2 ± 3.3	11.4 ± 5.3	2.7
11.0 – 12.5	14.6 ± 2.9	42.8 ± 8.5	60 ± 12	6.5
15.0 – 16.0	13.5 ± 2.2	43.5 ± 7.2	57 ± 9	8.7
16.0 – 18.0	28.6 ± 3.3	88.8 ± 10.1	118 ± 13	13
18.0 – 20.0	22.4 ± 2.6	78.0 ± 8.9	100 ± 11	14
1.1 – 6.0	3.6 ± 2.4	5.7 ± 3.8	9.4 ± 6.3	1.7
15.0 – 20.0	64.6 ± 4.7	209.6 ± 15.3	276 ± 20	21

¹³²⁵ in the logarithm of the likelihood function, $\sqrt{2\Delta \ln \mathcal{L}}$, when the signal component is

¹³²⁶ excluded from the fit, relative to the nominal fit in which it is present.

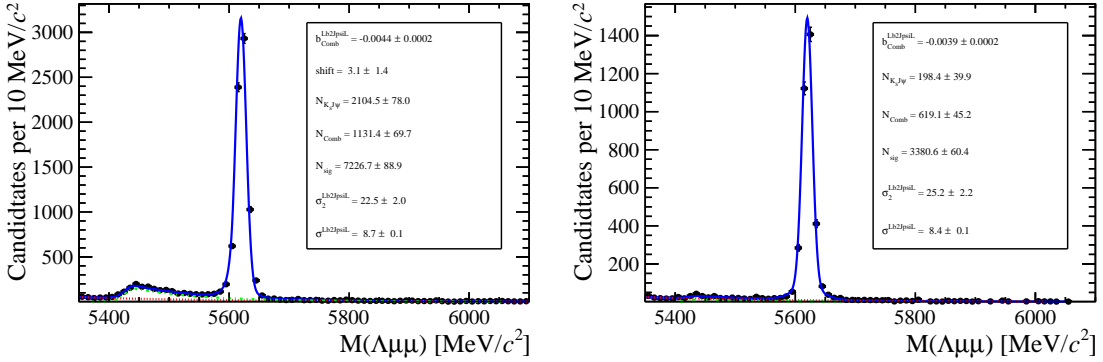


Figure 3.13: Invariant mass distribution of $\Lambda_b^0 \rightarrow J/\psi \Lambda$ for downstream (left) and long (right) candidates selected with low q^2 requirements.

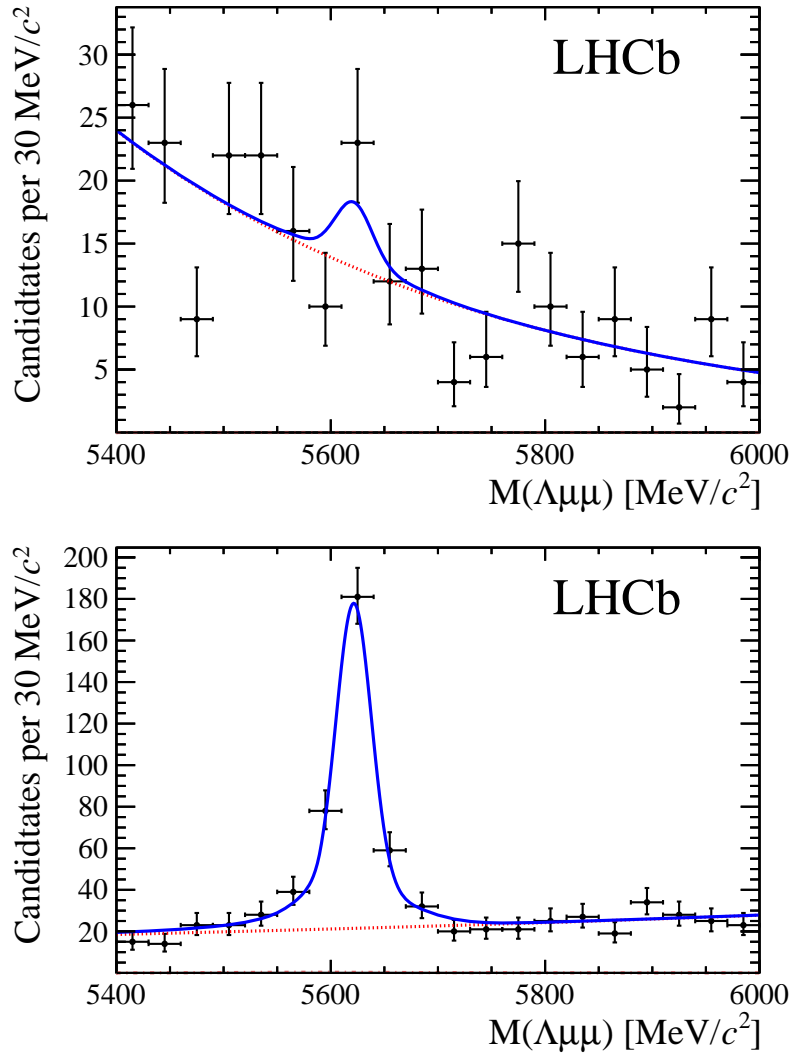


Figure 3.14: Invariant mass distributions of $\Lambda_b^0 \rightarrow \Lambda \mu^+ \mu^-$ candidates in the integrated $0.1 - 6.0 \text{ GeV}^2/c^4$ (top) and $15 - 20 \text{ GeV}^2/c^4$ (bottom) q^2 intervals. Points show data combining long and downstream candidates together. The blue solid line represents the total fit function and the dashed red line the combinatorial background.

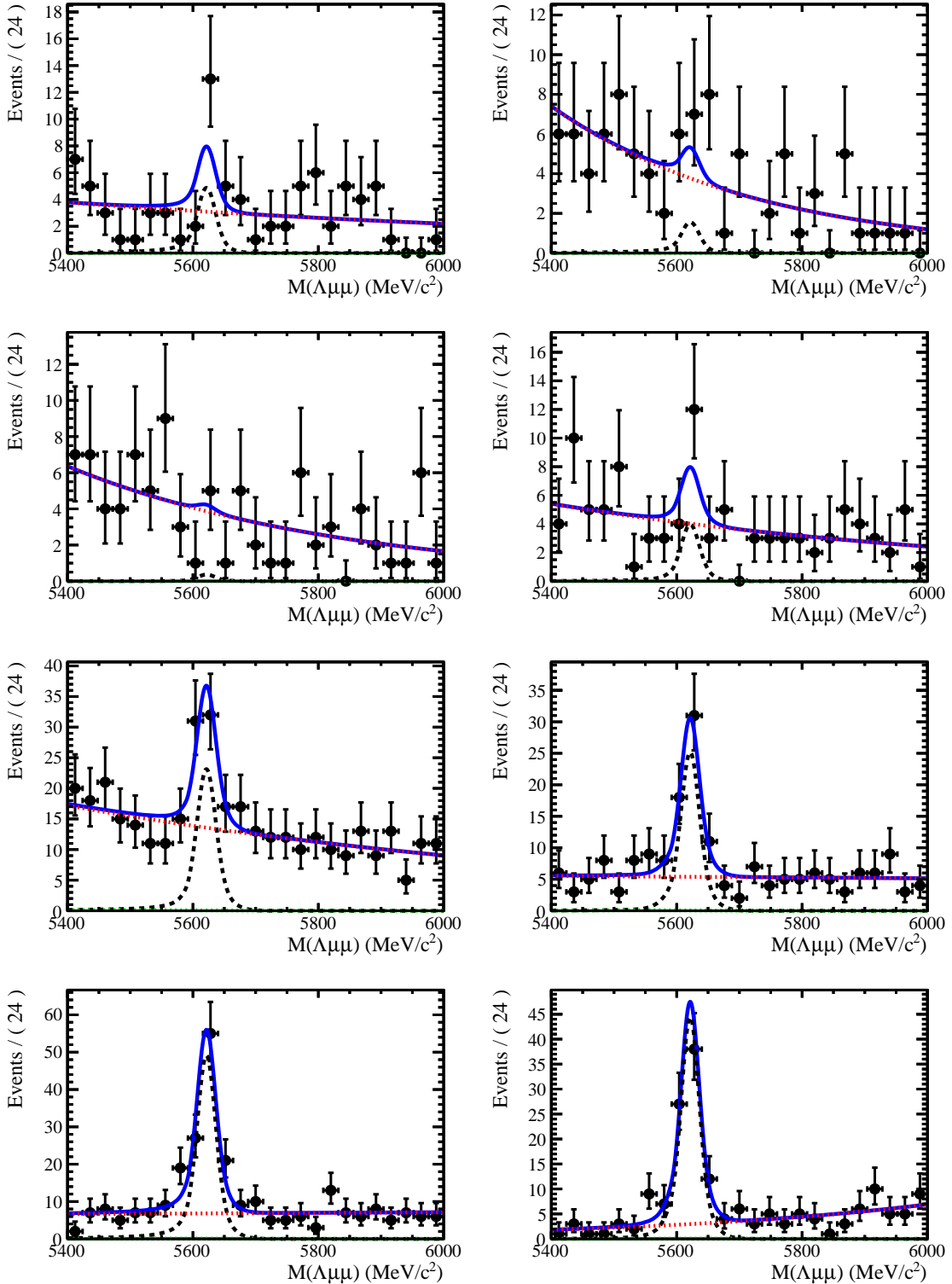


Figure 3.15: Invariant mass distributions of rare $\Lambda_b^0 \rightarrow \Lambda\mu^+\mu^-$ downstream candidates in the considered q^2 intervals.

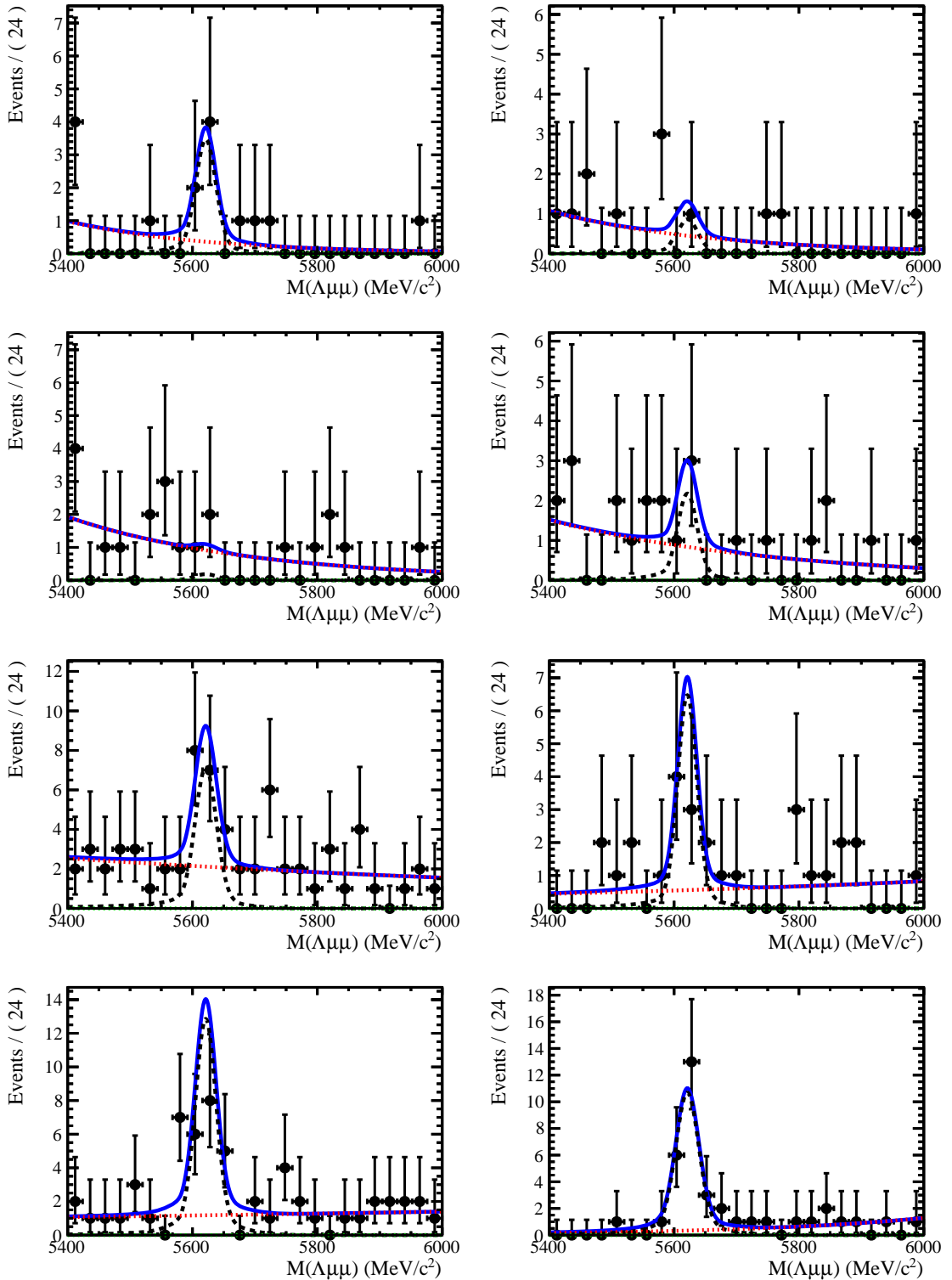


Figure 3.16: Invariant mass distributions of rare $\Lambda_b^0 \rightarrow \Lambda\mu^+\mu^-$ long candidates in the considered q^2 intervals.

₁₃₂₇ **3.6 Efficiency**

₁₃₂₈ The selection efficiency is calculated for each decay according to the formula

$$\varepsilon^{tot} = \varepsilon(Geom)\varepsilon(Det|Geom)\varepsilon(Reco|Det)\varepsilon(MVA|Reco)\varepsilon(Trig|MVA). \quad (3.12)$$

₁₃₂₉ In this expression the first term gives the efficiency to have final state particles
₁₃₃₀ in the LHCb acceptance. The second term handles the possibility of Λ escaping
₁₃₃₁ the detector or interacting with it and therefore never decaying into $p\pi$; this term
₁₃₃₂ is referred to as “detection” efficiency. The third term carries information about
₁₃₃₃ the reconstruction and pre-selection efficiencies, which are kept together given that
₁₃₃₄ boundaries between them are completely artificial. The fourth part deals with the
₁₃₃₅ efficiency of the neural network candidates that passed the pre-selection. Finally,
₁₃₃₆ the last term handles the trigger efficiency for candidates which are accepted by the
₁₃₃₇ full selection. Most of the efficiency components are evaluated using the simulated
₁₃₃₈ samples described in Sec. 3.3. Only the efficiency of the PID requirement for the
₁₃₃₉ proton (see Tab. 3.1) is separately derived with a data–driven method because the
₁₃₄₀ simulation does not provide a good description of PID variables. Representative
₁₃₄₁ absolute efficiencies’ values are given in the next sections. However, for the analysis
₁₃₄₂ itself only the relative efficiency, $\varepsilon(\Lambda_b^0 \rightarrow \Lambda\mu^+\mu^-)/\varepsilon(\Lambda_b^0 \rightarrow J/\psi\Lambda)$, is used.

₁₃₄₃ **3.6.1 Geometric acceptance**

₁₃₄₄ In order to save disk space and time the simulation only includes events in which
₁₃₄₅ the final muons are in the detector acceptance and therefore can be reconstructed.
₁₃₄₆ This corresponds to a requirement for each of the muons to be in an interval
₁₃₄₇ $10 < \theta < 400$ mrad, where θ is the angle between the muon momentum and the
₁₃₄₈ beam line. The efficiency of this requirement is obtained by using a separate simu-
₁₃₄₉ lated sample, where events are generated in the full space. The geometric efficiency
₁₃₅₀ varies between 18% at high- q^2 and 20% at low- q^2 ; Fig. 3.17 shows the dependence
₁₃₅₁ of this efficiency as a function of q^2 .

1352 3.6.2 Reconstruction and neural network efficiencies

1353 The efficiency to reconstruct the decays together with the pre-selection requirements
 1354 is evaluated from simulated data. The reconstruction efficiency is subdivided in
 1355 “Detection” and “Reconstruction and pre-selection” efficiencies. In fact, since Λ
 1356 is a long lived particle, there is a non-negligible probability that it interacts in
 1357 the detector or escapes from it and therefore never decays in proton and pion. The
 1358 reconstruction efficiency includes the probability for the tracks to produce observable
 1359 signatures and to pass the pre-selection requirements. This component does not
 1360 include the efficiency of the PID cut that appears in Tab. 3.1, which is kept separate
 1361 because PID variables are not well described by the simulation. The detection
 1362 efficiency varies between 88% at low- q^2 and 92% at high- q^2 while the reconstruction
 1363 efficiency is almost flat in q^2 at 6.6% for downstream candidates and 2.0% for long
 1364 candidates. The MVA selection efficiency is again evaluated from simulated samples
 1365 and it is observed to vary from 55% to 88% for downstream candidates and from
 1366 74% to 96% for long candidates. Fig. 3.17 shows the dependence of these efficiencies
 1367 as a function of q^2 . The sudden jump in MVA efficiency at ~ 9 GeV/ c^2 is due to
 1368 the fact that a different figure-of-merit is used to optimise the MVA requirement in
 1369 the low- and high- q^2 regions, which results in different efficiencies.

1370 3.6.3 Trigger efficiency

1371 The trigger efficiency is again evaluated using a simulated sample. It increases with
 1372 q^2 and varies from $\sim 57\%$ to $\sim 86\%$ for both downstream and long candidates.
 1373 Fig. 3.17 shows the dependence of this efficiency as a function of q^2 . Using the
 1374 high statistics resonant channel it is possible to crosscheck using data the trigger
 1375 efficiency obtained using the simulation. In LHCb triggered events can fall into two
 1376 categories: events triggered by a track which is part of a signal candidate, Trigger
 1377 On Signal (TOS), or by other tracks in the event, Trigger Independent of Signal
 1378 (TIS). As the TIS and TOS categories are not exclusive the TIS sample provides a

1379 control sample which can be used to obtain the efficiency for TOS trigger. This can
1380 be calculated with the formula:

$$\varepsilon_{\text{TOS}} = \frac{\text{TIS and TOS}}{\text{TIS}}. \quad (3.13)$$

1381 As data contains background the numbers of signal candidates in the “TIS” and
1382 “TIS and TOS” categories are not just determined by counting but from fits to the
1383 4-body invariant mass, $m(p\pi\mu\mu)$, distributions after applying these requirements.
1384 This procedure takes the name of TISTOS method. Using the data–driven method
1385 an efficiency of $(70 \pm 5)\%$ is obtained, while this is calculated to be $(73.33 \pm 0.02)\%$
1386 using the simulation. Results are therefore compatible within 1σ .

1387 3.6.4 PID efficiency

1388 For long tracks a PID requirement on protons ($\text{PID}_p > -5$) is applied. The simulation
1389 is known not to describe PID variables well and therefore a data-driven method is
1390 used to obtain this efficiency component. This is done using the `PIDCalib` package
1391 (see Sec. 2.8.1), which uses as calibration samples decays where particles can be
1392 identified due to their kinematic properties. In the case of protons a sample of
1393 Λ particles is used, where the proton can be identified because it always has the
1394 highest momentum. The package allows to divide the phase space in bins of variables
1395 relevant for PID performances; in this analysis momentum and pseudorapidity are
1396 used. Using the calibration sample the efficiency is derived in each two-dimensional
1397 bin. Finally, to take into account that the decay channel under study could have
1398 different kinematical distributions than the calibration sample these efficiency tables
1399 are used to re-weight the simulation. The PID efficiency varies from 97.3% at low- q^2
1400 to 98.2% at high- q^2 .

Table 3.7: Absolute efficiency values for $\Lambda_b^0 \rightarrow J/\psi \Lambda$; uncertainties are statistical only.

Efficiency	Downstream	Long
$\varepsilon(Geom)$	0.1818 ± 0.0003	
$\varepsilon(Det)$	0.9017 ± 0.0003	
$\varepsilon(Reco)$	0.0724 ± 0.0004	0.0203 ± 0.0002
$\varepsilon(PID)$	–	97.89 ± 0.005
$\varepsilon(MVA)$	0.882 ± 0.002	0.942 ± 0.002
$\varepsilon(Trig)$	0.697 ± 0.003	0.734 ± 0.005
Full Selection	0.0445 ± 0.0003	0.0140 ± 0.0002
Total	0.00729 ± 0.00005	0.00230 ± 0.00003

1401 3.6.5 Relative efficiencies

1402 In the previous sections absolute efficiencies values were given for the rare channel,
 1403 which are summarised in Fig. 3.17. This section reports the corresponding relative
 1404 efficiencies with respect to the $\Lambda_b^0 \rightarrow J/\psi \Lambda$ channel, which will be used to correct the
 1405 yields and obtain the differential branching fraction. Table 3.7 reports the absolute
 1406 efficiency values for the J/ψ channel used to derive the relative efficiencies. Rela-
 1407 tive geometric, detection and PID efficiencies are listed in Tab. 3.8, while Tabs. 3.9
 1408 and 3.10 report relative reconstruction, trigger and MVA efficiencies separately for
 1409 downstream and long candidates. Since the latter three components are obtained
 1410 from the same simulated sample their statistical uncertainties are correlated. There-
 1411 fore, the total of the three is also reported as a single efficiency and labeled ‘‘Full
 1412 Selection’’. Finally, Tab. 3.13 reports the total of all relative efficiencies, which will
 1413 be then used to correct the raw yields and calculate the differential branching frac-
 1414 tion. Uncertainties reflect the statistics of both rare and resonant samples, while
 1415 systematic uncertainties are discussed in following sections.

Table 3.8: Relative geometric, detection and PID relative efficiencies between $\Lambda_b^0 \rightarrow \Lambda\mu^+\mu^-$ and $\Lambda_b^0 \rightarrow J/\psi\Lambda$ decays; uncertainties reflect the statistics of both samples.

q^2 [GeV $^2/c^4$]	Geometric	Detection	PID
0.1 – 2.0	1.2976 ± 0.0050	0.9751 ± 0.0006	0.99418 ± 0.00013
2.0 – 4.0	1.1541 ± 0.0043	0.9814 ± 0.0005	0.99523 ± 0.00013
4.0 – 6.0	1.1043 ± 0.0044	0.9872 ± 0.0006	0.99699 ± 0.00012
6.0 – 8.0	1.0778 ± 0.0045	0.9939 ± 0.0006	0.99805 ± 0.00011
11.0 – 12.5	1.0431 ± 0.0058	1.0074 ± 0.0007	1.00151 ± 0.00010
15.0 – 16.0	1.0426 ± 0.0084	1.0188 ± 0.0010	1.00431 ± 0.00008
16.0 – 18.0	1.0296 ± 0.0068	1.0255 ± 0.0008	1.00215 ± 0.00008
18.0 – 20.0	1.0288 ± 0.0087	1.0333 ± 0.0010	1.00226 ± 0.00005
1.1 – 6.0	1.1396 ± 0.0031	0.9835 ± 0.0004	0.99589 ± 0.00009
15.0 – 20.0	1.0320 ± 0.0048	1.0269 ± 0.0006	1.00281 ± 0.00006

Table 3.9: Relative efficiencies between $\Lambda_b^0 \rightarrow \Lambda\mu^+\mu^-$ and $\Lambda_b^0 \rightarrow J/\psi\Lambda$ decays for downstream candidates; uncertainties reflect the statistics of both samples.

q^2 [GeV $^2/c^4$]	Reconstruction	MVA	Trigger	Full Selection
0.1 – 2.0	0.721 ± 0.009	0.706 ± 0.010	0.805 ± 0.011	0.410 ± 0.009
2.0 – 4.0	0.920 ± 0.010	0.661 ± 0.008	0.870 ± 0.010	0.529 ± 0.010
4.0 – 6.0	0.997 ± 0.010	0.662 ± 0.008	0.895 ± 0.010	0.590 ± 0.011
6.0 – 8.0	1.050 ± 0.011	0.665 ± 0.008	0.960 ± 0.010	0.671 ± 0.012
11.0 – 12.5	1.112 ± 0.014	1.007 ± 0.006	1.069 ± 0.009	1.197 ± 0.019
15.0 – 16.0	1.019 ± 0.018	1.000 ± 0.009	1.175 ± 0.012	1.197 ± 0.026
16.0 – 18.0	0.968 ± 0.014	0.961 ± 0.008	1.200 ± 0.010	1.115 ± 0.020
18.0 – 20.0	0.832 ± 0.016	0.943 ± 0.010	1.231 ± 0.012	0.966 ± 0.023
1.1 – 6.0	0.950 ± 0.007	0.663 ± 0.005	0.876 ± 0.007	0.551 ± 0.007
15.0 – 20.0	0.929 ± 0.010	0.963 ± 0.005	1.204 ± 0.007	1.077 ± 0.014

Table 3.10: Relative efficiencies between $\Lambda_b^0 \rightarrow \Lambda\mu^+\mu^-$ and $\Lambda_b^0 \rightarrow J/\psi\Lambda$ decays for long candidates; uncertainties reflect the statistics of both samples.

q^2 [GeV $^2/c^4$]	Recostruction	MVA	Trigger	Full Selection
0.1 – 2.0	0.96 ± 0.02	0.863 ± 0.012	0.79 ± 0.02	0.65 ± 0.02
2.0 – 4.0	0.97 ± 0.02	0.803 ± 0.012	0.89 ± 0.02	0.69 ± 0.02
4.0 – 6.0	1.04 ± 0.02	0.824 ± 0.012	0.92 ± 0.02	0.79 ± 0.02
6.0 – 8.0	1.05 ± 0.02	0.825 ± 0.012	0.96 ± 0.02	0.84 ± 0.02
11.0 – 12.5	1.10 ± 0.03	1.002 ± 0.008	1.01 ± 0.02	1.10 ± 0.03
15.0 – 16.0	0.89 ± 0.03	0.987 ± 0.013	1.13 ± 0.02	0.98 ± 0.04
16.0 – 18.0	0.84 ± 0.03	0.985 ± 0.010	1.17 ± 0.02	0.97 ± 0.03
18.0 – 20.0	0.67 ± 0.03	0.944 ± 0.017	1.18 ± 0.02	0.75 ± 0.04
1.1 – 6.0	1.00 ± 0.02	0.820 ± 0.008	0.89 ± 0.01	0.73 ± 0.02
15.0 – 20.0	0.78 ± 0.02	0.973 ± 0.008	1.16 ± 0.01	0.89 ± 0.02

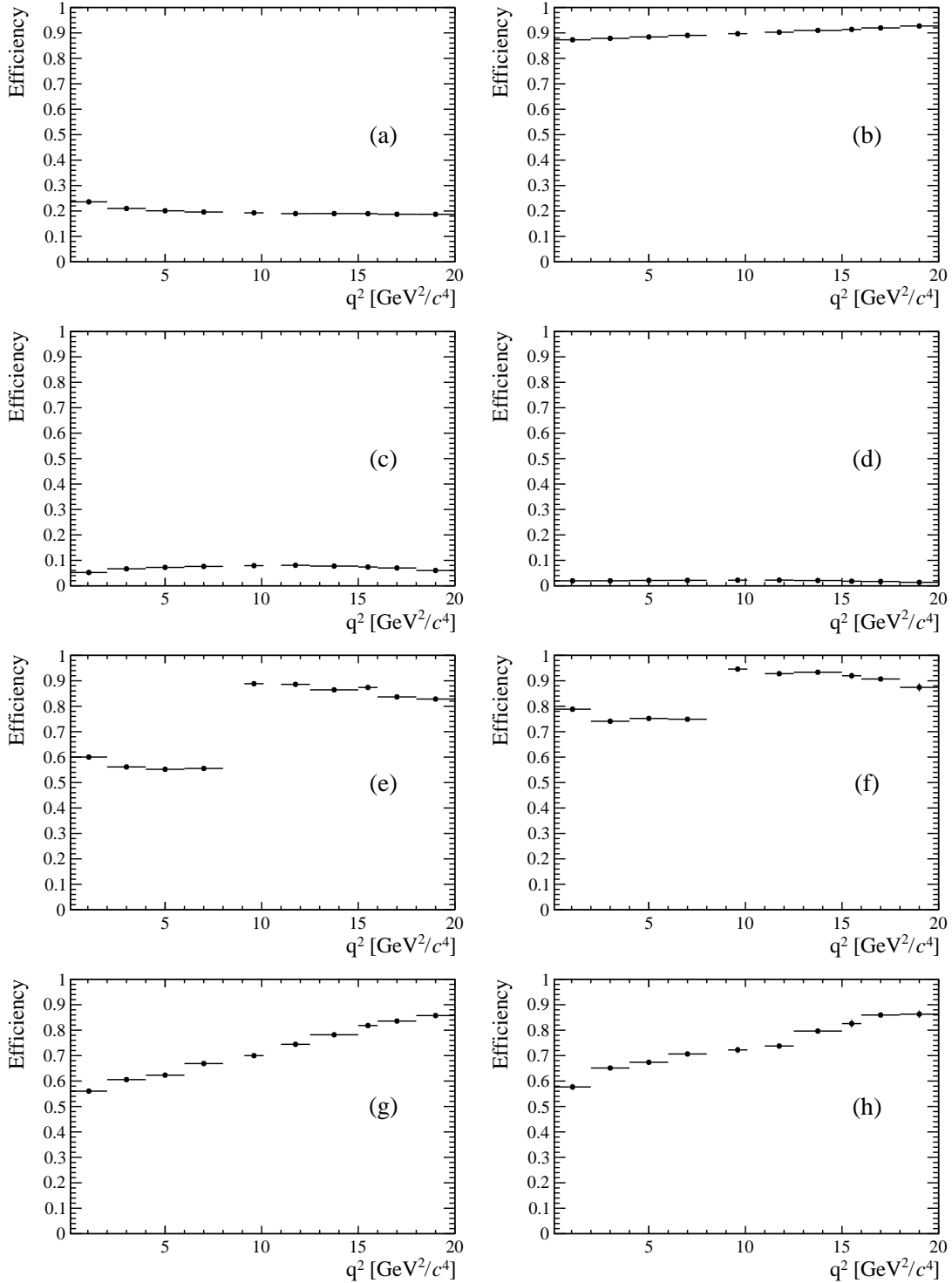


Figure 3.17: Absolute efficiencies as a function of q^2 : geometric efficiency (a), detection efficiency (b), reconstruction efficiency for DD (c) and LL (d) candidates, MVA efficiency for DD (e) and LL (f) and trigger efficiency for DD (g) and LL (h).

¹⁴¹⁶ **3.7 Systematic uncertainties**

¹⁴¹⁷ This section describes the main considered sources of systematic uncertainty.

¹⁴¹⁸ **3.7.1 Systematic uncertainty on the yields**

¹⁴¹⁹ The choice of specific PDFs to model the invariant mass distributions could result in
¹⁴²⁰ a bias. To asses the effect of the signal PDF choice as a first step a number of models
¹⁴²¹ are tried on the $\Lambda_b^0 \rightarrow J/\psi \Lambda$ data sample to understand which ones are plausible.
¹⁴²² Table 3.11 reports the χ^2 and corresponding p-values obtained using different models
¹⁴²³ including: the default model (a DCB function), a simple Gaussian function, a single
¹⁴²⁴ Crystal Ball function and the sum of two Gaussians (Double Gauss, DG). The only
¹⁴²⁵ two models that give a reasonable p-value are the default DCB and the sum of two
¹⁴²⁶ Gaussian functions. In a second step simulated experiments are generated and fit
¹⁴²⁷ with the two chosen models. Events are generated according to a density function
¹⁴²⁸ given by the default model with parameters taken from the fit to data, separately
¹⁴²⁹ for each q^2 interval. In this way, for each q^2 interval, a specific shape is reproduced
¹⁴³⁰ including data-like background level and slope. Furthermore, a number of events
¹⁴³¹ comparable to the one found in data is generated. For each experiment a normalised
¹⁴³² bias is calculated as

$$b = \left(\frac{N_{\ell\ell}^{DCB}}{N_{J/\psi}^{DCB}} - \frac{N_{\ell\ell}^{DG}}{N_{J/\psi}^{DG}} \right) / \frac{N_{\ell\ell}^{DCB}}{N_{J/\psi}^{DCB}} \quad (3.14)$$

¹⁴³³ where $N_{\ell\ell}^{model}$ and $N_{J/\psi}^{model}$ are the numbers of rare and resonant candidates observed
¹⁴³⁴ using a specific model. The average bias over 1000 pseudo-experiments is taken as
¹⁴³⁵ systematic uncertainty. Note that in each case the rare and normalisation channels
¹⁴³⁶ are fit with the same signal model and, while for the default case the rare parameters
¹⁴³⁷ are fixed to what found for the resonant channel, they are left free to vary in the
¹⁴³⁸ second model in order to asses at the same time the systematic due to the parameters
¹⁴³⁹ constraints.

Table 3.11: χ^2 , NDF, p-values and number of signal events obtained fitting $\Lambda_b^0 \rightarrow J/\psi \Lambda$ data using different models.

Model	χ^2/ndf	NDF	p-value	N_{evts}
DCB (default)	1.0	187	0.51	9965.4
Gauss	1.8	193	~ 0	9615.7
Double Gauss	1.1	191	0.45	9882.4
CB	1.5	191	~ 0	9802.4

1441 For the background PDF systematic the rare channel is re-fit leaving the yield of
1442 the K_s^0 component free to vary, which is instead fixed to the predicted value in the
1443 default fit. The same procedure as for the signal PDF is applied.

1444 Results are reported in Tab. 3.12. The most affected q^2 interval is the one in the
1445 middle of the charmonium resonances, where a combination of lower statistics and
1446 higher background leaves more freedom to the signal shape. Finally, a background
1447 component for $B^+ \rightarrow K^{*+}(K_s^0\pi^+)\mu^+\mu^-$ decays is added to the fit, modelled using
1448 the distribution of simulated events after full selection. No significant bias is found
1449 for this component.

q^2 [GeV $^2/c^4$]	Sig. PDF bias (%)	Bkg. PDF bias (%)	Tot. sys. (%)
0.1 – 2.0	3.2	1.1	3.4
2.0 – 4.0	2.9	2.4	3.8
4.0 – 6.0	4.6	4.8	6.6
6.0 – 8.0	1.2	1.7	2.0
11.0 – 12.5	2.6	1.8	3.2
15.0 – 16.0	1.3	2.5	2.8
16.0 – 18.0	0.6	1.3	1.4
18.0 – 20.0	1.7	1.8	2.5
1.1 – 6.0	0.1	4.2	4.2
15.0 – 20.0	1.0	0.2	1.1

Table 3.12: Values of systematic uncertainties due to the choice of signal and background shapes in bins of q^2 .

¹⁴⁵¹ 3.7.2 Systematic uncertainties on the efficiency determination

¹⁴⁵² Systematic uncertainties on the efficiency determination are due to the limited
¹⁴⁵³ knowledge of the decay properties such as the Λ_b^0 lifetime and production polarisa-
¹⁴⁵⁴ tion. The systematic uncertainties are directly evaluated on the relative efficiencies
¹⁴⁵⁵ as these are the ones that are actually used in the analysis. It should be noted that
¹⁴⁵⁶ not all sources contribute to each part of the efficiency. For brevity, this section only
¹⁴⁵⁷ reports estimates of the systematic uncertainties obtained, while the full information
¹⁴⁵⁸ is contained in Appendix C.

¹⁴⁵⁹ 3.7.2.1 Effect of new physics on the decay model

¹⁴⁶⁰ New physics could affect the decay model used to simulate events by adding contri-
¹⁴⁶¹ butions to the C_7 and C_9 Wilson Coefficients. This would result in a modification of
¹⁴⁶² the simulated q^2 spectra and therefore of the efficiency obtained from simulation. To
¹⁴⁶³ asses this systematic the Wilson Coefficients are modified by adding a new physics
¹⁴⁶⁴ component ($C_i \rightarrow C_i + C_i^{\text{NP}}$). Figure 3.18 shows q^2 spectra obtained weighting
¹⁴⁶⁵ the simulation for a model embedding the default and 3 modified sets of Wilson
¹⁴⁶⁶ Coefficients. The used values, reported on the plot legend, are inspired to main-
¹⁴⁶⁷ tain compatibility with the recent LHCb result about the P'_5 observable [48]. The
¹⁴⁶⁸ biggest effect is observed in the very low q^2 , below 2 GeV^2/c^4 , where the efficiency
¹⁴⁶⁹ can change up to 7%, while it changes 3-4 % between 3 and 4 GeV^2/c^4 and 2-3 %
¹⁴⁷⁰ in the rest of the spectrum. As this analysis is performed under the hypothesis that
¹⁴⁷¹ the decays are described by a the SM, these values are given in order to provide the
¹⁴⁷² full information but are not added as systematic uncertainties.

¹⁴⁷³ 3.7.2.2 Simulation statistics

¹⁴⁷⁴ The limited statistics of the simulated samples used to determine efficiencies is
¹⁴⁷⁵ considered as a source of systematic uncertainty. While it is not the dominant

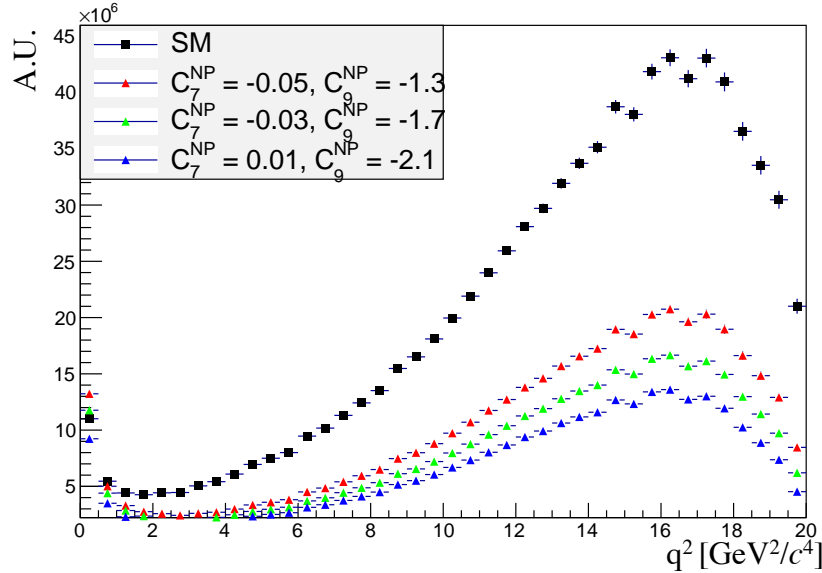


Figure 3.18: The q^2 spectrum of $\Lambda_b^0 \rightarrow \Lambda\mu^+\mu^-$ simulated events weighted with models embedding different sets of Wilson Coefficients. The black distribution corresponds to the weights used to calculate nominal efficiencies.

¹⁴⁷⁶ source, its size does not allow to completely neglect it. When reporting relative
¹⁴⁷⁷ efficiency values the statistical uncertainty due to the rare and resonant channels is
¹⁴⁷⁸ always considered.

¹⁴⁷⁹ 3.7.2.3 Production polarisation and decay structure

¹⁴⁸⁰ One of the main unknown, which affects the determination of the efficiencies, is the
¹⁴⁸¹ angular structure of the decays and, connected to it, also the production polarisation,
¹⁴⁸² which is a parameter of the model. To assess the systematic uncertainty due to the
¹⁴⁸³ knowledge of the production polarisation for $\Lambda_b^0 \rightarrow \Lambda\mu^+\mu^-$ decays the polarisation
¹⁴⁸⁴ parameter in the model is varied within one standard deviation from the central
¹⁴⁸⁵ value of the most recent LHCb measurement, $P_b = 0.06 \pm 0.09$ [102]. The full
¹⁴⁸⁶ observed difference is taken as systematic uncertainty. To assess the systematic
¹⁴⁸⁷ uncertainty due to the decay structure an alternative set of form factors is used
¹⁴⁸⁸ based on lattice QCD calculation [105]. The two models are compared and the full
¹⁴⁸⁹ difference is taken as systematic uncertainty. In total this results in an uncertainty of

¹⁴⁹⁰ $\sim 1.3\%$ for long candidates and $\sim 0.6\%$ for downstream candidates, mostly coming
¹⁴⁹¹ from the knowledge of the production polarisation.

¹⁴⁹² 3.7.2.4 Λ_b^0 lifetime

¹⁴⁹³ The Λ_b^0 lifetime is known with limited precision. For the efficiencies' evaluation the
¹⁴⁹⁴ world average value, 1.482 ps^{-1} [106], is used which is varied within one standard
¹⁴⁹⁵ deviation from the measured value to asses the systematic uncertainty. Only the
¹⁴⁹⁶ case where both signal and normalisation channel are varied in same direction are
¹⁴⁹⁷ considered. The largest difference from the default lifetime case is taken as sys-
¹⁴⁹⁸ tematic uncertainty, which is found to range from $\sim 0.4\%$ at low- q^2 to $\sim 0.1\%$ at
¹⁴⁹⁹ high- q^2 .

¹⁵⁰⁰ 3.7.2.5 Downstream candidates reconstruction efficiency

¹⁵⁰¹ Other analysis in LHCb using particles reconstructed with downstream tracks showed
¹⁵⁰² that the efficiency for these candidates is not well simulated. For example, Fig. 3.19
¹⁵⁰³ shows the ratio between the reconstruction efficiency for downstream candidates in
¹⁵⁰⁴ data and simulation found analysing K_s^0 events [107]. This effect is not yet fully
¹⁵⁰⁵ understood and is currently under study. It seems to be mainly due to a poor simu-
¹⁵⁰⁶ lation of the vertexing efficiency for downstream tracks. As the analysis is performed
¹⁵⁰⁷ separately for downstream and long candidates and efficiencies are calculated sepa-
¹⁵⁰⁸ rately, the effect of this mis-modelling, present in both the rare and resonant chan-
¹⁵⁰⁹ nels, mostly cancels their ratio. Nevertheless, a systematic uncertainty is assessed by
¹⁵¹⁰ re-weighting simulated downstream candidates by the efficiency ratio between data
¹⁵¹¹ and simulation found for K_S as a function of momentum (see Fig. 3.19). The effi-
¹⁵¹² ciencies obtained using the weighted and unweighted simulation are compared and
¹⁵¹³ the full difference is taken as systematic uncertainty. As the discrepancy shows little
¹⁵¹⁴ dependence on momentum, dependencies due to the different momentum distribu-
¹⁵¹⁵ tions of Λ and K_s^0 are assumed to be negligible. This results in a $\sim 0.4\%$ systematic

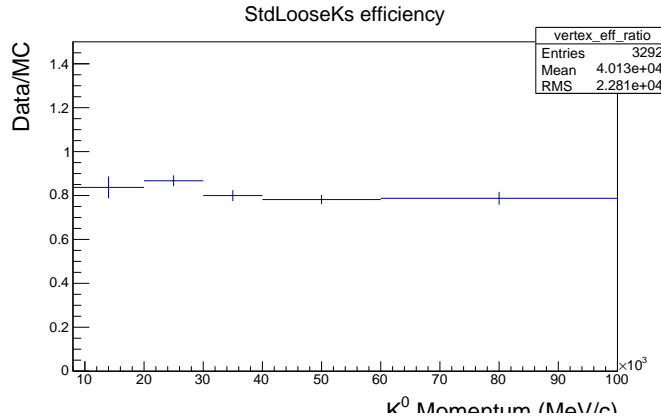


Figure 3.19: Ratio of reconstruction efficiency in data and simulation found using K_S events [107].

1516 uncertainty at low- q^2 and 1.2% at high- q^2 , only for downstream candidates.

1517 3.7.2.6 Data-simulation discrepancies

1518 The simulation used to calculate the efficiencies is weighted as described in Sec. 3.3.2
 1519 to improve the simulation' description of data. The influence of this procedure on the
 1520 efficiency determination is checked by comparing values obtained with and without
 1521 re-weighting. The effect is negligible with respect to other systematics considered.

1522 3.8 Differential branching fraction extraction

1523 In this section the differential branching fraction of the $\Lambda_b^0 \rightarrow \Lambda\mu^+\mu^-$ decay is
 1524 calculated relative to the $\Lambda_b^0 \rightarrow J/\psi\Lambda$ channel as a function of q^2 . The values are
 1525 directly obtained from the fit to the rare sample by parameterising the downstream
 1526 and long yields with the following formula:

$$N(\Lambda\mu^+\mu^-)_k = \left[\frac{d\mathcal{B}(\Lambda\mu^+\mu^-)/dq^2}{\mathcal{B}(J/\psi\Lambda)} \right] \cdot N(J/\psi\Lambda)_k \cdot \varepsilon_k^{\text{rel}} \cdot \frac{\Delta q^2}{\mathcal{B}(J/\psi \rightarrow \mu^+\mu^-)}, \quad (3.15)$$

1527 where $k = (\text{LL}, \text{DD})$, Δq^2 is the width of the q^2 interval, $\mathcal{B}(J/\psi \rightarrow \mu^+\mu^-) = (5.93 \pm$
 1528 $0.06) \cdot 10^{-2}$ [2] and the only free parameter is the relative branching fraction ratio.

Table 3.13: Absolute values of the total relative efficiency and the absolute value of the uncorrelated uncertainty (σ_{uncorr}^k), together with relative values of the correlated uncertainty (σ_{corr}).

q^2 [GeV $^2/c^4$]	Eff. (DD)	σ_{uncorr}^{DD}	Eff. (LL)	σ_{uncorr}^{LL}	σ_{corr}
0.1 – 2.0	0.694	0.058	1.136	0.066	1.0%
2.0 – 4.0	0.693	0.027	0.907	0.047	2.7%
4.0 – 6.0	0.699	0.018	0.964	0.044	2.7%
6.0 – 8.0	0.733	0.020	0.953	0.048	2.7%
11.0 – 12.5	1.254	0.032	1.140	0.057	3.4%
15.0 – 16.0	1.260	0.035	1.035	0.060	3.0%
16.0 – 18.0	1.163	0.029	0.997	0.048	1.7%
18.0 – 20.0	1.023	0.027	0.782	0.040	2.7%
1.1 – 6.0	0.696	0.032	0.950	0.058	1.0%
15.0 – 20.0	1.132	0.014	0.927	0.031	1.4%

1529 Table 3.13 summarises the total relative efficiencies, ε^{rel} , for downstream and long
 1530 candidates together with their correlated and uncorrelated uncertainties, where the
 1531 correlation is intended between the downstream and long samples. On the table
 1532 the uncorrelated uncertainty corresponds to the total systematic uncertainty on the
 1533 efficiency determination. The correlated uncertainty is given in percent form since
 1534 it can be applied to either downstream, long candidates or their combination. This
 1535 includes the PDF systematic described in Sec. 3.7.1 and the systematic due to the
 1536 uncertainty on the $J/\psi \rightarrow \mu^+\mu^-$ branching fraction.

1537 Figure 3.20 shows the differential branching fraction obtained by fitting the down-
 1538 stream and long samples independently, while the combined result, obtained fitting
 1539 both samples simultaneously, is shown in Fig. 3.21. Measured values are also listed
 1540 in Tab. 3.14, where the statistical uncertainty on the rare channel and the total
 1541 systematic uncertainty are shown separately. The statistical uncertainty is calcu-
 1542 lated using the MINOS application of the MINUIT package [108], which provides an
 1543 asymmetric interval. The normalisation and systematic uncertainties are evaluated
 1544 by pushing the efficiencies and normalisation yields up and down by one standard
 1545 deviation and re-performing the fit. The different efficiencies used translate into a
 1546 different branching fraction and the full difference with respect to the default fit is
 1547 taken as systematic uncertainty in each direction.

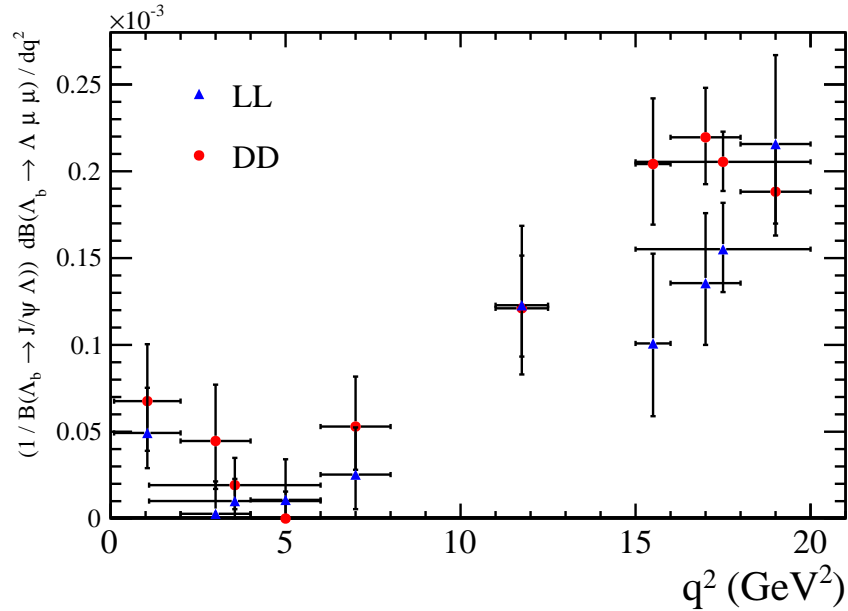


Figure 3.20: Measured values of the differential branching fraction of the $\Lambda_b^0 \rightarrow \Lambda \mu^+ \mu^-$ decay relative to the $\Lambda_b^0 \rightarrow J/\psi \Lambda$ decay as a function of q^2 obtained fitting the downstream and long samples independently. Error bars represent the total statistical and systematic uncertainty.

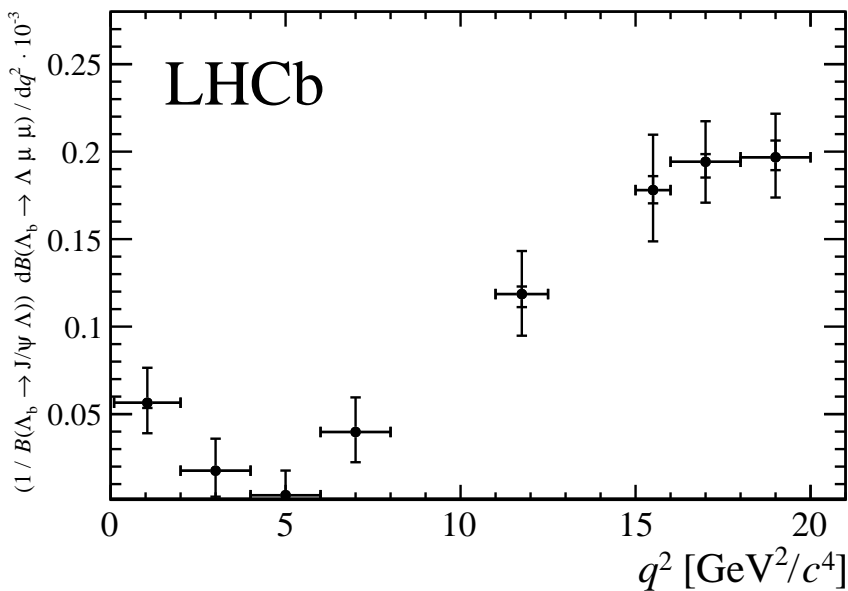


Figure 3.21: Differential branching fraction of the $\Lambda_b^0 \rightarrow \Lambda \mu^+ \mu^-$ decay normalised to the $\Lambda_b^0 \rightarrow J/\psi \Lambda$ mode. The inner error bar represents the systematic uncertainty and the outer error bar includes the statistical uncertainty.

Table 3.14: Measured differential branching fraction of the $\Lambda_b^0 \rightarrow \Lambda\mu^+\mu^-$ decay relative to $\Lambda_b^0 \rightarrow J/\psi\Lambda$ decays; uncertainties are statistical and systematic respectively.

q^2 interval [GeV $^2/c^4$]	$\frac{d\mathcal{B}(\Lambda_b^0 \rightarrow \Lambda\mu^+\mu^-)/dq^2}{\mathcal{B}(\Lambda_b^0 \rightarrow J/\psi\Lambda)} \cdot 10^{-3}$ [(GeV $^2/c^4$) $^{-1}$]		
0.1 – 2.0	0.56	+0.20 –0.17	+0.03 –0.03
2.0 – 4.0	0.18	+0.18 –0.15	+0.01 –0.01
4.0 – 6.0	0.04	+0.14 –0.04	+0.01 –0.01
6.0 – 8.0	0.40	+0.20 –0.17	+0.01 –0.02
11.0 – 12.5	1.19	+0.24 –0.23	+0.04 –0.07
15.0 – 16.0	1.78	+0.31 –0.28	+0.08 –0.08
16.0 – 18.0	1.94	+0.23 –0.22	+0.04 –0.09
18.0 – 20.0	1.97	+0.23 –0.22	+0.10 –0.07
1.1–6.0	0.14	+0.10 –0.09	+0.01 –0.01
15.0–20.0	1.90	+0.14 –0.14	+0.04 –0.06

Finally, values for the absolute branching fraction of the $\Lambda_b^0 \rightarrow \Lambda\mu^+\mu^-$ decay are obtained by multiplying the relative values listed in Tab. 3.14 by the branching fraction of the normalisation channel, $\mathcal{B}(\Lambda_b^0 \rightarrow J/\psi\Lambda) = (6.3 \pm 1.3) \times 10^{-4}$ [2]. Values are shown in Fig. 3.22 and summarised in Tab. 3.15, where the uncertainty due to the knowledge of the normalisation channel, which is correlated across q^2 , is shown separately. The SM predictions on the plot are obtained from Ref. [105].

Evidence for the signal is found for the first time in the interval $0.1 < q^2 < 2.0$ GeV $^2/c^4$, where an enhanced yield is expected due to the proximity of the photon pole and in the region between the two charmonium resonances. The uncertainty on the relative branching fraction is dominated by the size of the available data sample, while, the uncertainty on the absolute values is dominated by the precision with which the branching fraction of the normalisation channel is known. The measurement is consistent with the theoretical predictions in the high- q^2 region but lies below the predictions in the low- q^2 region. Improved predictions published after the publication of the LHCb result are reported in Appendix D, where a better agreement is found.

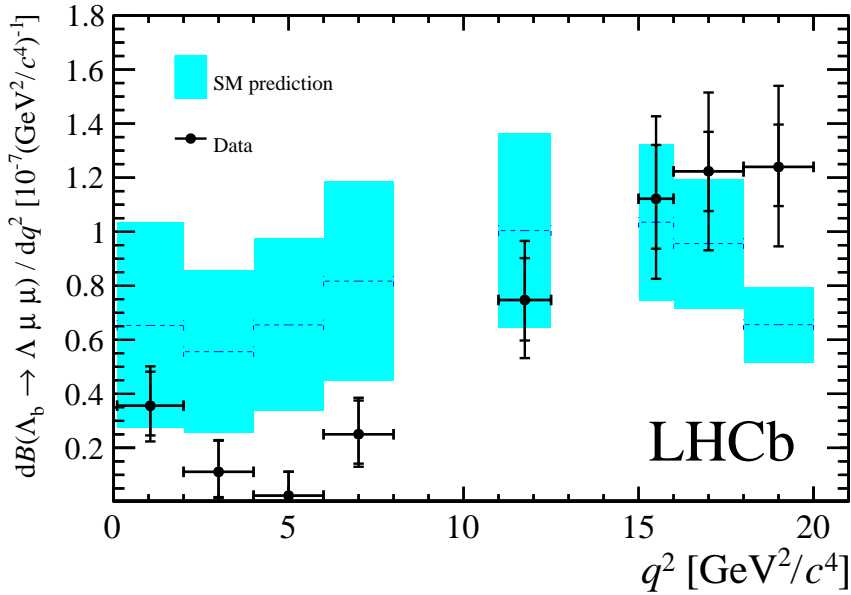


Figure 3.22: Measured $\Lambda_b^0 \rightarrow \Lambda \mu^+ \mu^-$ branching fraction as a function of q^2 with SM predictions [105] superimposed. The inner error bars represent the total uncertainty on the relative branching fraction (statistical and systematic), while the outer error bar also includes the uncertainties due to the knowledge of the branching fraction of the normalisation mode.

Table 3.15: Measured differential branching fraction of the $\Lambda_b^0 \rightarrow \Lambda \mu^+ \mu^-$ decay, where the uncertainties are statistical, systematic and due to the knowledge of the normalisation mode, $\Lambda_b^0 \rightarrow J/\psi \Lambda$, respectively.

q^2 interval [GeV^2/c^4]	$d\mathcal{B}(\Lambda_b^0 \rightarrow \Lambda \mu^+ \mu^-)/dq^2 \cdot 10^{-7} [(\text{GeV}^2/c^4)^{-1}]$	$+0.12$	$+0.02$	± 0.07
0.1 – 2.0	0.36	-0.11	-0.02	
2.0 – 4.0	0.11	$+0.12$	$+0.01$	± 0.02
4.0 – 6.0	0.02	$+0.09$	$+0.01$	± 0.01
6.0 – 8.0	0.25	-0.11	-0.01	± 0.05
11.0 – 12.5	0.75	$+0.15$	$+0.03$	± 0.15
15.0 – 16.0	1.12	-0.18	-0.05	± 0.23
16.0 – 18.0	1.22	-0.14	-0.06	± 0.25
18.0 – 20.0	1.24	$+0.14$	$+0.06$	± 0.26
1.1 – 6.0	0.09	$+0.06$	$+0.01$	± 0.02
15.0 – 20.0	1.20	-0.09	-0.04	± 0.25

CHAPTER 4

Angular analysis of $\Lambda_b^0 \rightarrow \Lambda\mu^+\mu^-$ decays

Neglecting the production polarisation of Λ_b^0 , the $\Lambda_b^0 \rightarrow \Lambda\mu^+\mu^-$ decay angular distribution can be described as a function of three angles and q^2 . The first two angles are the ones which are relevant for the analysis in this chapter and are defined in Fig. 4.1, where θ_ℓ is the angle between the positive (negative) muon direction in the dimuon rest frame and the dimuon system direction in the Λ_b^0 ($\bar{\Lambda}_b^0$) rest frame, and, similarly, θ_h is defined as the angle between the proton and the Λ baryon directions, in the Λ and Λ_b^0 rest frames. The third angle is the angle between the dimuon and Λ decay planes, which is integrated over in this analysis. This chapter describes a measurement of two forward-backward asymmetries in the leptonic (A_{FB}^ℓ) and in the hadronic (A_{FB}^h) systems. These forward-backward asymmetries are defined as

$$A_{FB}^i(q^2) = \frac{\int_0^1 \frac{d^2\Gamma}{dq^2 d\cos\theta_i} d\cos\theta_i - \int_{-1}^0 \frac{d^2\Gamma}{dq^2 d\cos\theta_i} d\cos\theta_i}{d\Gamma/dq^2}, \quad (4.1)$$

1568 where $d^2\Gamma/dq^2 d\cos\theta_i$ is the two-dimensional differential rate and $d\Gamma/dq^2$ is rate
 1569 integrated over the angles.

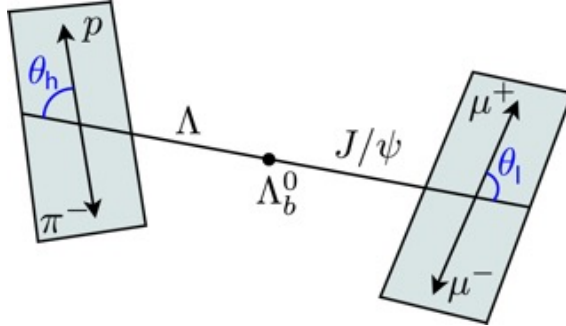


Figure 4.1: Graphical representation of the angles for the $\Lambda_b^0 \rightarrow \Lambda\mu^+\mu^-$ decay.

1570 The A_{FB}^ℓ observable was measured by LHCb also for $B^0 \rightarrow K^{*0}\mu^+\mu^-$ decays which
 1571 are going through the same quark level transition as $\Lambda_b^0 \rightarrow \Lambda\mu^+\mu^-$ decays. Instead
 1572 the hadronic asymmetry, A_{FB}^h , is interesting only in the Λ_b^0 case as it is zero by
 1573 definition in the B^0 case, due to the strong decay of the K^{*0} .

1574 4.1 One-dimensional angular distributions

1575 This section describes the derivation of the functional form of the differential distri-
 1576 butions as a function of $\cos\theta_\ell$ and $\cos\theta_h$, which are used to measure the observables.
 1577 The content of this section is based on the calculations in Ref. [101].

1578 For unpolarised Λ_b^0 production, integrating over the three angles the differential
 1579 branching fraction is given in Eq. 11 of Ref. [101] as

$$\frac{d\Gamma(\Lambda_b \rightarrow \Lambda \ell^+ \ell^-)}{dq^2} = \frac{v^2}{2} \cdot \left(U^{V+A} + L^{V+A} \right) + \frac{2m_\ell^2}{q^2} \cdot \frac{3}{2} \cdot \left(U^V + L^V + S^A \right), \quad (4.2)$$

1580 and the lepton helicity angle differential distribution, given in Eq. 15, has the form

$$\begin{aligned} \frac{d\Gamma(\Lambda_b \rightarrow \Lambda \ell^+ \ell^-)}{dq^2 d\cos\theta_\ell} &= v^2 \cdot \left[\frac{3}{8} (1 + \cos^2\theta_\ell) \cdot \frac{1}{2} U^{V+A} + \frac{3}{4} \sin^2\theta_\ell \cdot \frac{1}{2} L^{V+A} \right] \\ &- v \cdot \frac{3}{4} \cos\theta_\ell \cdot P^{VA} + \frac{2m_\ell^2}{q^2} \cdot \frac{3}{4} \cdot \left[U^V + L^V + S^A \right]. \end{aligned} \quad (4.3)$$

In these formulas m_ℓ is the mass of the lepton and $v = \sqrt{1 - 4m_\ell^2/q^2}$; U denotes the unpolarised-transverse contributions, L the longitudinal contributions and S the scalar contribution. The apices V and A represent respectively vector and axial-vector currents, with $X^{V+A} = X^V + X^A$. The authors of Ref. [101] define then the lepton-side forward-backward asymmetry as

$$A_{FB}^\ell = -\frac{3}{2} \frac{v \cdot P^{VA}}{v^2 \cdot (U^{V+A} + L^{V+A}) + \frac{2m_\ell^2}{q^2} \cdot 3 \cdot (U^V + L^V + S^A)}. \quad (4.4)$$

For this analysis the massless leptons limit, $m_\ell \rightarrow 0$, is used, which is a good approximation except at very low q^2 . Combining the previous equations ad taking the massless limit the differential rates simplify to

$$\frac{d\Gamma}{dq^2} = \frac{v^2}{2} \cdot (U^{V+A} + L^{V+A}) \quad (4.5)$$

and

$$\frac{d\Gamma}{dq^2 d \cos \theta_\ell} = \frac{v^2}{2} \left[\frac{3}{8} (1 + \cos^2 \theta_\ell) U^{V+A} + A_{FB}^\ell \cos \theta_\ell (U^{V+A} + L^{V+A}) + \frac{3}{4} \sin^2 \theta_\ell (L^{V+A}) \right]. \quad (4.6)$$

Equations 4.5 and 4.6 can be then combined to achieve the form

$$\begin{aligned} \frac{d\Gamma}{dq^2 d \cos \theta_\ell} &= \frac{d\Gamma}{dq^2} \left[\frac{3}{8} (1 + \cos^2 \theta_\ell) \frac{U^{V+A}}{U^{V+A} + L^{V+A}} + A_{FB}^\ell \cos \theta_\ell + \right. \\ &\quad \left. \frac{3}{4} \sin^2 \theta_\ell \frac{L^{V+A}}{U^{V+A} + L^{V+A}} \right]. \end{aligned} \quad (4.7)$$

The amplitude combination in the last term can be viewed as the ratio between the longitudinal and the sum of longitudinal and unpolarised contributions and therefore one can define the longitudinal fraction

$$f_L = \frac{L^{V+A}}{U^{V+A} + L^{V+A}}, \quad (4.8)$$

which leads to the functional form used in the analysis

$$\frac{d\Gamma}{dq^2 d \cos \theta_\ell} = \frac{d\Gamma}{dq^2} \left[\frac{3}{8} (1 + \cos^2 \theta_\ell) (1 - f_L) + A_{FB}^\ell \cos \theta_\ell + \frac{3}{4} \sin^2 \theta_\ell f_L \right]. \quad (4.9)$$

¹⁵⁹² Using the same steps the proton helicity distribution is given in Ref. [101] as

$$\frac{d\Gamma(\Lambda_b \rightarrow \Lambda(\rightarrow p\pi^-)\ell^+\ell^-)}{dq^2 d \cos \theta_h} = \text{Br}(\Lambda \rightarrow p\pi^-) \frac{d\Gamma(\Lambda_b \rightarrow \Lambda \ell^+\ell^-)}{dq^2} \left(\frac{1}{2} + A_{FB}^h \cos \theta_h \right), \quad (4.10)$$

¹⁵⁹³ and A_{FB}^h is defined as

$$A_{FB}^h = \frac{1}{2} \alpha_\Lambda P_z^\Lambda(q^2), \quad (4.11)$$

¹⁵⁹⁴ where $P_z^\Lambda(q^2)$ is the polarisation of the daughter baryon, Λ , and $\alpha_\Lambda = 0.642 \pm 0.013$ [2]

¹⁵⁹⁵ is the Λ decay asymmetry parameter.

¹⁵⁹⁶ The above expressions assume that Λ_b^0 is produced unpolarised, which is in agree-
¹⁵⁹⁷ ment with the recent LHCb measurement [109]. Possible effects due to a non zero
¹⁵⁹⁸ production polarisation are investigated as systematic uncertainties (see Sec. 4.5.5).

¹⁵⁹⁹ 4.2 Multi-dimensional angular distributions

To incorporate effects of production polarisation this was introduced in the equations. In the modified version an angle θ is defined as the angle between the Λ direction in the Λ_b^0 rest frame with respect to $\hat{n} = \hat{p}_{inc} \times \hat{p}_{\Lambda_b^0}$, where \hat{p}_{inc} represents the direction of the incoming proton; this angle is sensitive to the production polarisation. Integrating over all the angles but θ_ℓ results in the same distribution as in the unpolarised case (Eq. 4.3). Therefore, in the case of uniform efficiency, the lepton side forward-backward asymmetry, A_{FB}^ℓ , is unaffected by the production polarisation. To be able to estimate the effect of the production polarisation in the case of non-uniform efficiency, the differential distribution in θ and θ_ℓ is derived,

which in the massless leptons limit becomes (up to a constant multiplicative factor)

$$\frac{d\Gamma(\Lambda_b \rightarrow \Lambda \ell^+ \ell^-)}{dq^2 d\cos\theta d\cos\theta_\ell} = \frac{d\Gamma}{dq^2} \left\{ \frac{3}{8} (1 + \cos^2\theta_\ell) (1 - f_L) + A_{FB}^\ell \cos\theta_\ell + \frac{3}{4} \sin^2\theta_\ell f_L + P_b \cos\theta \left[-\frac{3}{4} \sin\theta_\ell^2 O_{Lp} + \frac{3}{8} (1 + \cos\theta_\ell^2) O_P \right. \right. \\ \left. \left. - \frac{3}{8} \cos\theta_\ell O_{UVA} \right] \right\}, \quad (4.12)$$

where three more observables are defined

$$O_{Lp} = \frac{L_P^V + L_P^A}{U^{V+A} + L^{V+A}}, \\ O_P = \frac{P^V + P^A}{U^{V+A} + L^{V+A}}, \\ O_{UVA} = \frac{U^{VA}}{U^{V+A} + L^{V+A}}.$$

- ₁₆₀₀ In the massless leptons approximation two of these quantities are related to the
₁₆₀₁ hadron side forward-backward asymmetry as

$$\frac{1}{2} \alpha_\Lambda (O_P + O_{Lp}) = A_{FB}^h. \quad (4.13)$$

Following the same steps as for the lepton case, after integrating over all the angles but θ_h one finds that the hadron side, A_{FB}^h , is also unaffected by the production polarisation in case of uniform efficiency and the differential distribution in θ and θ_h has the form

$$\frac{d\Gamma(\Lambda_b \rightarrow \Lambda \ell^+ \ell^-)}{dq^2 d(\cos\theta) d(\cos\theta_h)} = \frac{d\Gamma}{dq^2} [1 + 2A_{FB}^h \cos\theta_h + P_b (O_P - O_{Lp}) \cos\theta \\ + \alpha_\Lambda P_b (1 - 2f_L) \cos\theta \cos\theta_h]. \quad (4.14)$$

- ₁₆₀₂ In order to use these distributions, expectations for the three additional observables,
₁₆₀₃ which do not enter one-dimensional distributions, are needed. Expectations are
₁₆₀₄ calculated using form factors and numerical inputs from Ref. [101] and are listed in
₁₆₀₅ Appendix A.1.

For completeness, the differential distribution in $\cos \theta_\ell$ and $\cos \theta_h$ has the form

$$\begin{aligned} \frac{d\Gamma(\Lambda_b \rightarrow \Lambda \ell^+ \ell^-)}{dq^2 d\cos \theta_h d\cos \theta_\ell} = & \frac{3}{8} + \frac{6}{16} \cos^2 \theta_\ell (1 - f_L) - \frac{3}{16} \cos^2 \theta_\ell f_L + A_{FB}^l \cos \theta_\ell + \\ & \left(\frac{3}{2} A_{FB}^h - \frac{3}{8} \alpha_A O_P \right) \cos \theta_h - \frac{3}{2} A_{FB}^h \cos^2 \theta_\ell \cos \theta_h - \frac{3}{16} f_L + \\ & \frac{9}{16} f_L \sin^2 \theta_\ell + \frac{9}{8} \alpha_A \cos^2 \theta_\ell \cos \theta_h O_P - \\ & \frac{3}{2} \alpha_A \cos \theta_\ell \cos \theta_h O_{UVA}. \end{aligned} \quad (4.15)$$

1606 4.3 Angular resolution

1607 This section describes a study of the angular resolution performed in order to achieve
 1608 a better understanding of detector and reconstruction effects. This will be then
 1609 used to study systematic uncertainties (see Sec. 4.5.5). The study is performed by
 1610 analysing simulated events and comparing generated and reconstructed quantities.
 1611 Figure 4.2 shows the difference between true and measured angular observables,
 1612 $\cos \theta_\ell$ and $\cos \theta_h$, as a function of the observables themselves. These distributions
 1613 are centred at zero indicating no bias in the measurement. The spread of these
 1614 distributions around the central value can be interpreted as an estimate of the angular
 1615 resolution. Taking vertical slices of the plots in Fig. 4.2 one obtains approximately
 1616 gaussian distributions centred at zero. These are fit with a single gaussian and
 1617 its width is interpreted as the angular resolution. Table 4.1 reports the average
 1618 resolutions for the two angular observables separately for long and downstream
 1619 candidates. Candidates built from long tracks are characterised by a better angular
 1620 resolution due to a better momentum and vertex resolution.

Table 4.1: Average angular resolutions integrated over the full interval and the full available q^2 .

Observable	Downstream	Long
$\cos \theta_\ell$	0.015	0.010
$\cos \theta_h$	0.066	0.014

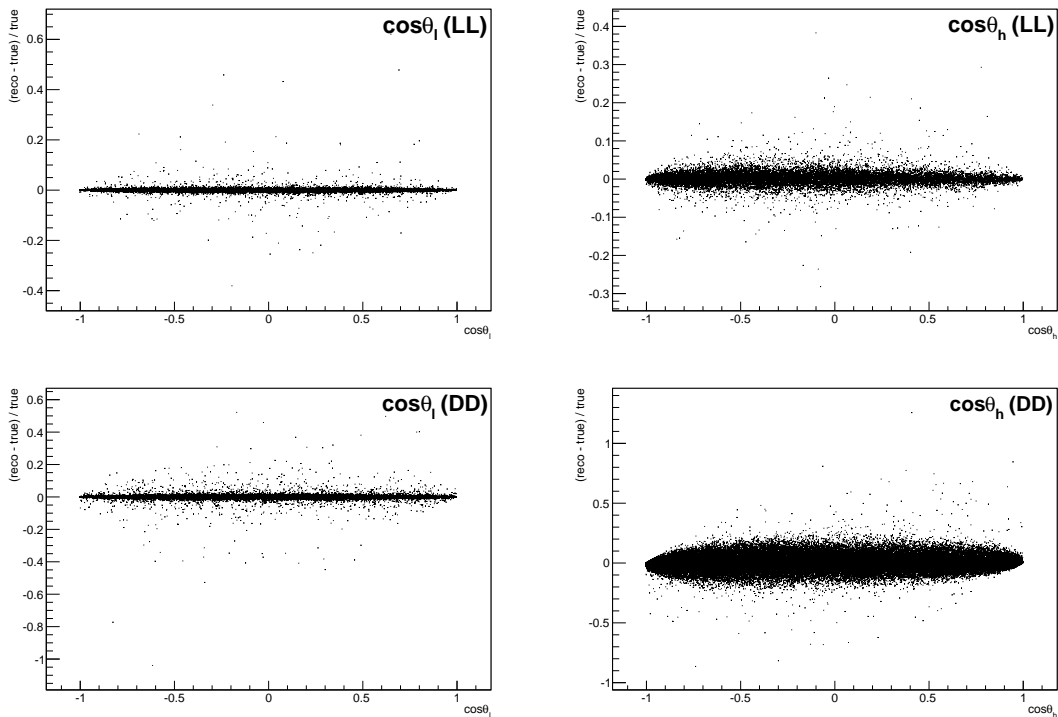


Figure 4.2: Difference between generated and reconstructed angular observables, $\cos\theta_\ell$ (left) and $\cos\theta_h$ (right) as a function of the observables themselves for long (top) and downstream (bottom) candidates. The spread of these distributions can be interpreted as the angular observables' resolution.

₁₆₂₁ **4.4 Fit strategy**

₁₆₂₂ There are physical boundaries to the values of the parameters of interests: A_{FB}^h is
₁₆₂₃ limited in the $[-0.5, 0.5]$ interval and for the f_L and A_{FB}^ℓ parameters the physical
₁₆₂₄ region, given by $|A_{\text{FB}}^\ell| < 3/4 \cdot (f_L - 1)$, is the triangle shown in Fig. 4.3. If the
₁₆₂₅ measured value is close to the border of the physical region the fit does not always
₁₆₂₆ converge. Therefore a “brute force” fitting technique is applied. For this purpose fit
₁₆₂₇ parameters are divided into two categories: parameters of interest (PoIs), A_{FB}^ℓ , A_{FB}^h
₁₆₂₈ and f_L and all other parameters, which are referred to as “nuisances”. The value
₁₆₂₉ of the Log-Likelihood ($\log \mathcal{L}$) of the fit model with respect to data is evaluated in
₁₆₃₀ a grid of points in the PoIs’ allowed area to find the function’s minimum. A first
₁₆₃₁ coarse scan finds a candidate minimum and then the procedure is reiterated two
₁₆₃₂ more times in finer intervals around it. For each point all the nuisances are fitted
₁₆₃₃ using a maximum likelihood fit. Using this method the best fit point is therefore
₁₆₃₄ constrained inside the physical region. If the minimum of the log-likelihood is found
₁₆₃₅ to be outside it, the closest point on the boundary is chosen as the best fit.

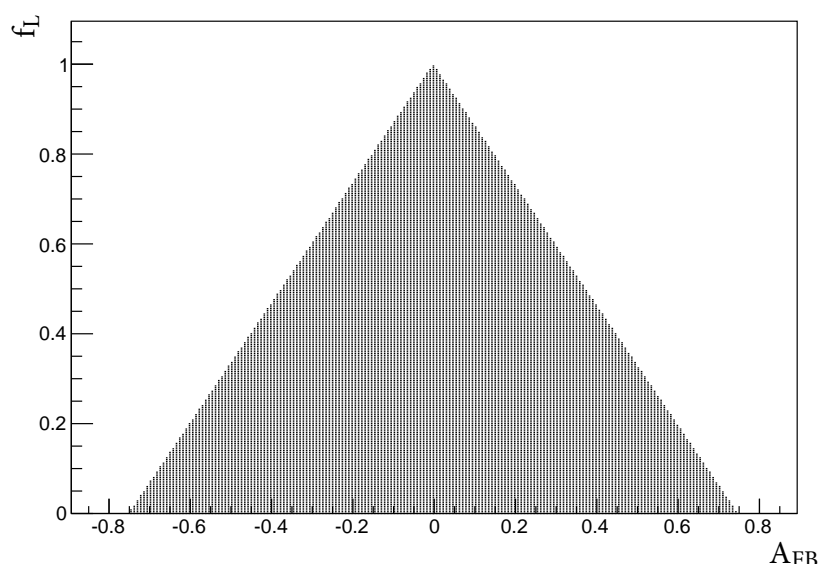


Figure 4.3: The physical $(A_{\text{FB}}^\ell, f_L)$ parameter space. The dark region corresponds to points where the PDF is positive in the whole $[-1, 1] \cos \theta_\ell$ interval.

1636 4.4.1 Feldman-cousins plug-in method

1637 Physical boundaries of the parameter space could result in a wrong estimation of
1638 the uncertainties, especially if the measured value is close to the boundary. To deal
1639 with this effect the likelihood-ordering method [110] is used to estimate uncertainties
1640 and nuisance parameters are accounted for using the plug-in method [111]. This is
1641 a unified method to calculate confidence intervals and upper/lower limits, based on
1642 simulated experiments and has the advantage of having a well defined frequentist
1643 coverage.

1644 The method is constituted by the following steps:

- 1645 1. fit real data distributions with all parameters free;
- 1646 2. fit real data fixing the PoIs to a value of choice while keeping nuisance param-
1647 eters free;
- 1648 3. generate simulated samples following the distribution given by the fit model,
1649 where all nuisance parameters are taken from the fit in point 2 and PoIs are
1650 fixed to the same value used in point 2;
- 1651 4. repeat the two fits made on data (points 1 and 2) on each simulated sample:
1652 fit with all parameters free and with fixed PoIs;
- 1653 5. calculate the minimum values of the Log-Likelihoods for all cases;
- 1654 6. calculate the percentage of simulated experiments in which the free-to-fixed
1655 likelihood ratio is bigger than in data: $\log \mathcal{L}_{fixed} / \log \mathcal{L}_{free} > (\log \mathcal{L}_{fixed} / \log \mathcal{L}_{free})_{data}$;
- 1656 7. repeat the procedure for many values of the PoIs scanning around the best fit
1657 point.

1658 The confidence interval at $k\%$ is given by the points where the free-to-fixed likelihood
1659 ratio is bigger in data than simulation for $(1 - k)\%$ of times. As an example, Fig. 4.4

1660 shows the p-values obtained with the plug-in method for A_{FB}^h and f_L . A two-
 1661 dimensional region can also be scanned giving a grid of p-values, which translates
 into two-dimensional confidence regions.

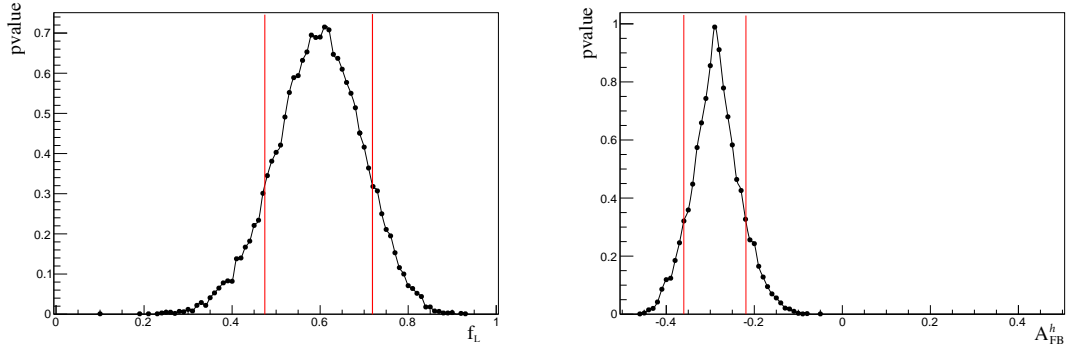


Figure 4.4: Dependence of the p-value on the values of the angular observables f_L (left) and A_{FB}^h (right) in simulated experiments. The red lines mark the points at p-value 32% corresponding to a 68% CL.

1662

1663 4.4.2 Modelling the angular distributions

1664 The observables are obtained from fits to one-dimensional angular distributions.

1665 The PDFs used to model the data are defined as

$$P^k(\cos \theta_{\ell/h}) = [(1 - f_b) \cdot P_S(\cos \theta_{\ell/h}) + f_b \cdot P_B^k(\cos \theta_{\ell/h})] \times \varepsilon^k(\cos \theta_{\ell/h}), \quad (4.16)$$

1666 where $k = (\text{LL}, \text{DD})$. The first term represents the signal which is modelled by the
 1667 theoretical shapes, P_S , given by Eqs. 4.9 and 4.10, respectively for the lepton and
 1668 hadron cases, while the second term represents the background, which is parame-
 1669 terised with a linear function: $P_B^k(\cos \theta_{\ell/h}) = (c \cdot \cos \theta_{\ell/h} + q)$. Both terms are multi-
 1670 plied by an acceptance function ε described in Sec. 4.4.3. Imposing the PDF normal-
 1671 isation the background model is left with one free parameter which is fixed by fitting
 1672 candidates in the Λ_b^0 invariant mass sideband, $m(p\pi\mu\mu) > 5700 \text{ MeV}/c^2$, which con-
 1673 tains only background. Finally, f_b is the background fraction: $f_b = B/(S + B)$. To
 1674 limit systematic effects due to the background parameterisation the fit is performed
 1675 in a restricted invariant mass region around the Λ_b^0 mass peak dominated by the

1676 signal: $5580 < m(p\pi\mu\mu) < 5660$ MeV/ c^2 (“signal region”). The background frac-
1677 tion, f_b , is obtained by looking at the 4-body $m(p\pi\mu\mu)$ invariant mass distribution
1678 in a wider interval and fitting it to extract the fraction of background in the signal
1679 region. In the fit to the angular distributions this is then gaussian constrained to the
1680 obtained value. Figure 4.5 shows the angular distributions of sideband candidates
1681 for the high- q^2 integrated interval with overlaid the background function. Note that
1682 a different acceptance shape is used for the downstream and long samples and for
1683 each q^2 interval. In summary the only free fit parameter in each of the final fits to
data is the forward-backward asymmetry (and f_L in the leptonic case).

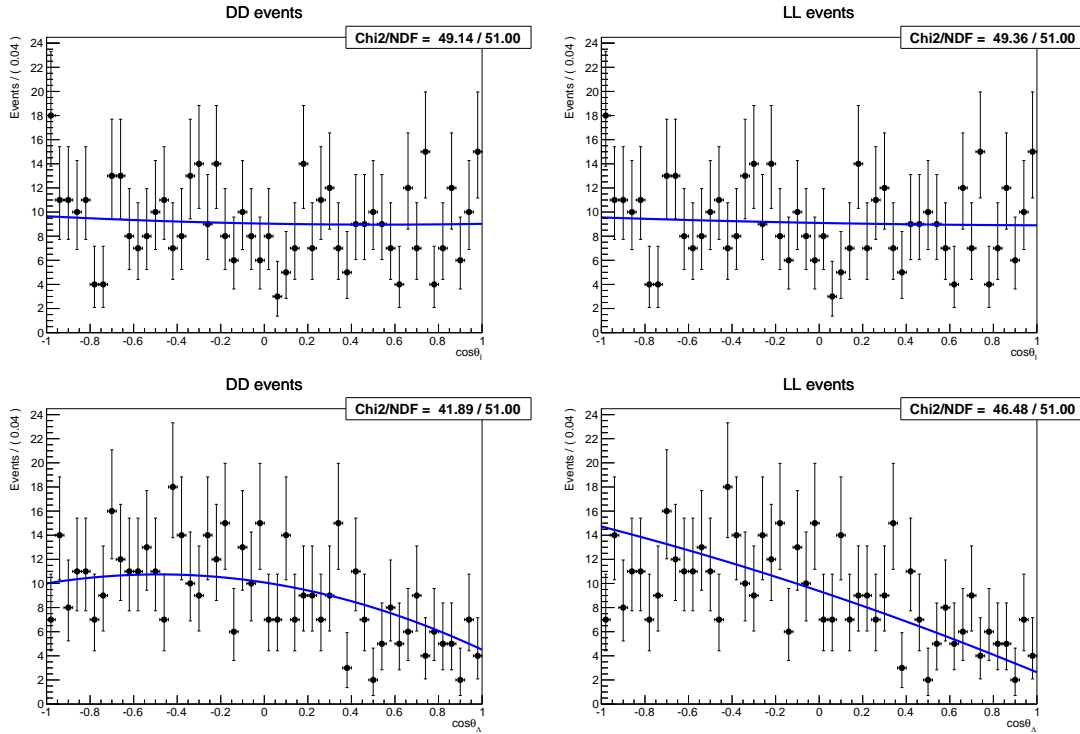


Figure 4.5: Background distribution as a function of $\cos \theta_\ell$ (top) and $\cos \theta_h$ (bottom) for downstream (left) and long (right) candidates in the 15-20 GeV $^2/c^4$ q^2 interval.

1684

1685 4.4.3 Angular acceptance

1686 Selection requirements on the minimum momentum of the muons can distort the
1687 $\cos \theta_\ell$ distribution by removing candidates with extreme values of the angle. Simi-
1688 larly, the impact parameter requirements affect $\cos \theta_h$ because very forward hadrons

tend to have smaller impact parameter values. While in principle one could take this into account by an additional weight, to minimise the distortion of the uncertainties estimate, the efficiency function is incorporated in the fit model. The angular efficiency is parametrised using a second-order polynomial, whose parameters are determined separately for long and downstream candidates by fitting simulated events. An independent set of parameters is obtained also for each q^2 interval. These parameters are then fixed for the fits to data. Using polynomial functions allows to calculate the PDF normalisation analytically. Figure 4.6 shows the acceptance as a function of $\cos \theta_h$ and $\cos \theta_\ell$ for the $15 - 20 \text{ GeV}^2/c^4$ integrated q^2 interval obtained using a $\Lambda_b^0 \rightarrow \Lambda \mu^+ \mu^-$ simulated sample. For the lepton side, even though the efficiency is symmetric by construction, all parameters are left free to float, namely it is not constrained to be symmetric.

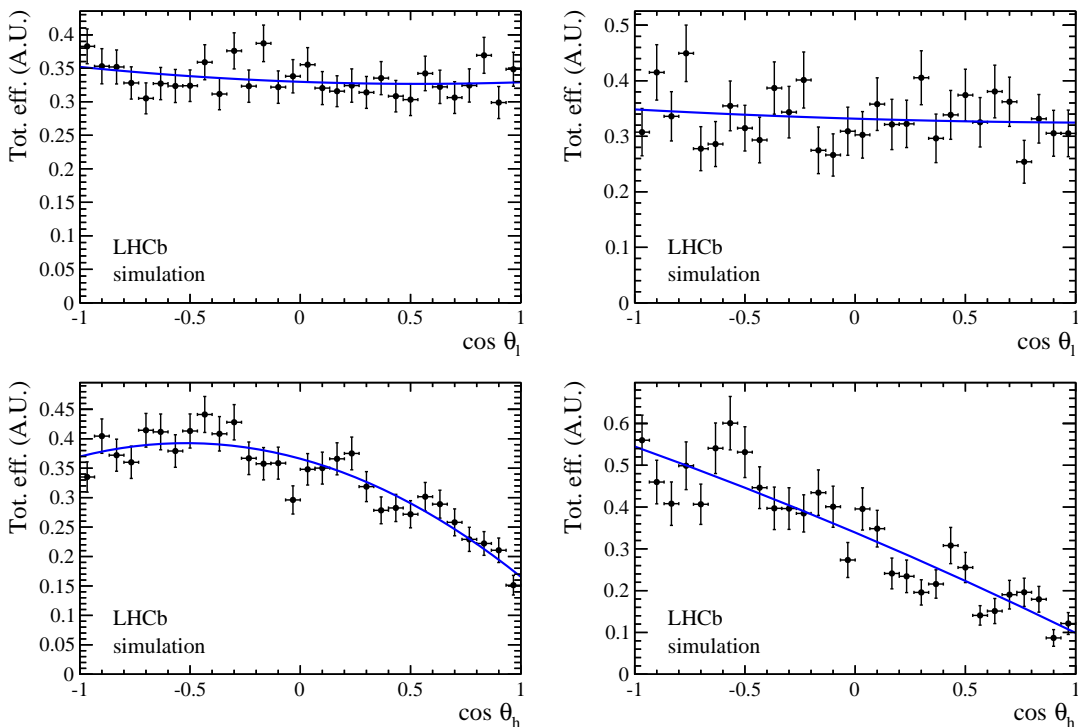


Figure 4.6: Efficiency as a function of $\cos \theta_\ell$ (top) and $\cos \theta_h$ (bottom) for downstream (left) and long (right) candidates in the $15 - 20 \text{ GeV}^2/c^4$ q^2 interval.

1701 4.4.4 Studies on a three-dimensional fit

1702 One other way of extracting the angular observables would be to fit at the same time
1703 both angles and also the invariant mass distribution in order to have a better handle
1704 on the level of background. In this case one can use more of the information available.
1705 On the other hand it is necessary to use a larger mass window including more
1706 background and this method involves more parameters to fit. In fact, in the 3D case
1707 in addition to the A_{FB}^ℓ , f_L and A_{FB}^h parameters, there are two background fractions
1708 and the two exponential slopes for the invariant mass background. Furthermore,
1709 to take correctly into account correlations three more observables enter the fit (see
1710 Eq. 4.12). As an high number of free parameters is difficult to constrain with the very
1711 limited statistics available, pseudo-experiments are used to check which method gives
1712 the best sensitivity. Events are generated in a 3D $(\cos\theta_\ell, \cos\theta_h, m_{p\pi\mu\mu})$ space. The
1713 generated values of the observables are $A_{\text{FB}}^\ell = 0$, $f_L = 0.7$ and $A_{\text{FB}}^h = -0.37$, which
1714 are data-like values inspired to a preliminary measurement in the highest statistics
1715 interval. Also the overall statistics and the fraction of background candidates in the
1716 mass window are generated to be data-like using information from the preliminary
1717 fit to data. Each pseudo-experiment is fitted with both the 1D and 3D methods.
1718 Figure 4.7 reports distributions of parameters of interest obtained from the fit in the
1719 1D and 3D cases. The RMS of these distributions can be taken as a measure of the
1720 sensitivity of each method. Table 4.2 lists the RMSs obtained from both methods;
1721 for all parameters of interest the 1D fit method gives a smaller RMS, hence a better
sensitivity.

Table 4.2: RMS values for pseudo-experiments on the extraction of the three parameters of interests with the 1D or 3D fitting methods.

q^2 [GeV $^2/c^4$]	Fit type	A_{FB}^h	A_{FB}^ℓ	f_L
15.0 – 20.0	1D	0.070	0.055	0.099
	3D	0.092	0.095	0.153
11.0 – 12.5	1D	0.142	0.128	0.198
	3D	0.249	0.254	0.303

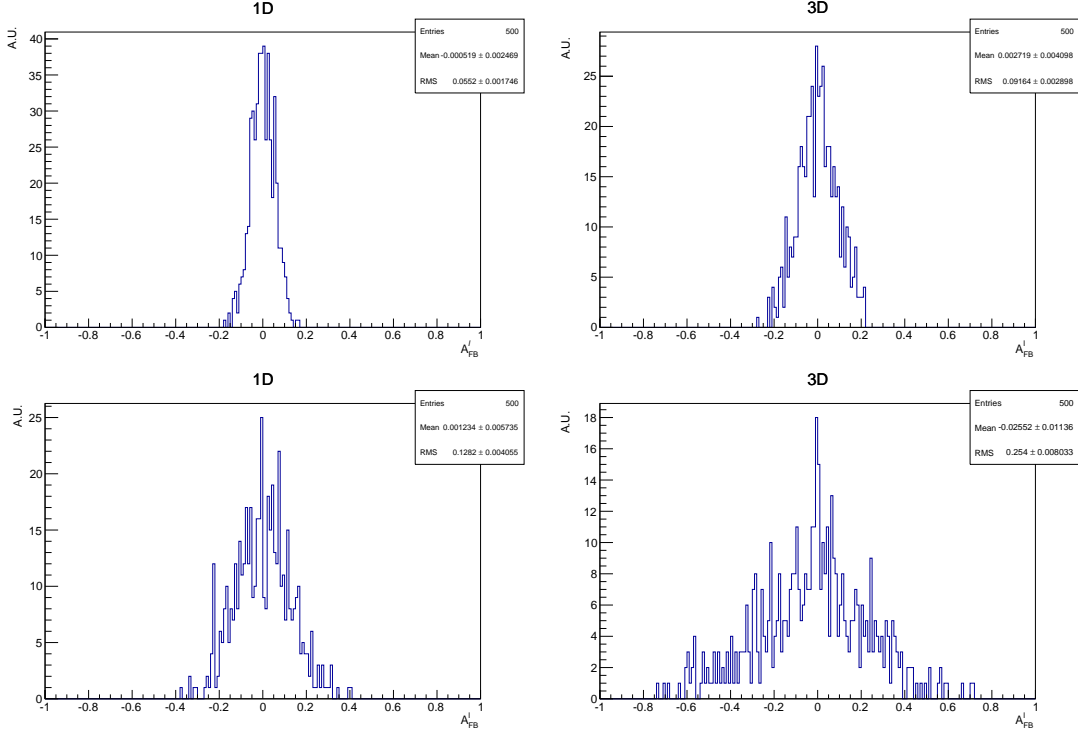


Figure 4.7: Values of the A_{FB}^ℓ parameter observed in pseudo-experiments with input $A_{FB}^\ell = 0$ using the 1D fit method (left) and the 3D one (right). Events are generated with parameters and statistics corresponding to what is observed in the highest statistics interval (top), $15 - 20$ GeV^2/c^4 , and in the lowest statistics one, $11 - 12.5$ GeV^2/c^4 .

1723 4.5 Systematics uncertainties on angular observables

1724 The following section describes the five main sources of systematic uncertainties
 1725 that are considered for the angular observables measurement and, finally, results
 1726 are reported in Sec. 4.7. Results are derived only for q^2 intervals where the signal
 1727 significance, shown in Tab. 3.6, is above 3 standard deviations. This includes all
 1728 q^2 intervals above the J/ψ resonance and the lowest q^2 interval, where an increased
 1729 yield is due to the presence of the photon pole.

1730 4.5.1 Angular correlations

1731 The angular acceptance is non-flat as a function of $\cos \theta_\ell$ and $\cos \theta_h$. Therefore, while
 1732 integrating the full angular distribution, terms that cancel with perfect efficiency

may remain and generate a bias in the final result. In order to deal with this effect simulated events are generated in a two-dimensional $(\cos\theta_\ell, \cos\theta_h)$ space according to the theoretical distribution described by Eq. 4.15 multiplied by a two-dimensional efficiency function obtained from simulation. Then, one-dimensional projections are taken and fit using the default one-dimensional efficiency functions. The distributions of observed deviations from the generated value, $\Delta x = x_{true} - x_{measured}$, are approximately gaussian and their mean is non-zero by more than 3σ . Therefore, the mean biases are taken as systematic uncertainties, which correspond to the absolute uncertainties $\Delta A_{FB}^\ell = 0.032$, $\Delta f_L = 0.028$, $\Delta A_{FB}^h = 0.013$ independent of q^2 .

4.5.2 Resolution

The angular resolution could bias the observables measurement generating an asymmetric migration of events. This is especially important in the $\cos\theta_h$ case, due to its worse resolution and considerably asymmetric distribution. Simulated experiments are used to assess this systematic. Events are generated according to the measured distributions including efficiencies. The generated events are then smeared by the angular resolution (gaussian smearing). To be conservative the case with biggest angular resolution, downstream candidates, is always used. Finally, the smeared and not-smeared distributions are fit with the same PDF. The average deviation from the default values are reported in Tab. 4.3 as a function of q^2 and assigned as systematic uncertainties.

Table 4.3: Values of simulated $\cos\theta_\ell$ and $\cos\theta_h$ resolutions and systematic uncertainties on angular observables due to the finite resolution in bins of q^2 .

q^2 [GeV $^2/c^4$]	σ_ℓ	σ_h	ΔA_{FB}^ℓ	Δf_L	ΔA_{FB}^h
0.1 – 2.0	0.0051	0.061	0.0011	-0.0022	-0.007
11.0 – 12.5	0.0055	0.067	0.0016	-0.0051	-0.013
15.0 – 16.0	0.0059	0.070	0.0006	-0.0054	-0.010
16.0 – 18.0	0.0064	0.070	0.0014	-0.0077	-0.010
18.0 – 20.0	0.0081	0.074	0.0014	-0.0062	-0.010
15.0 – 20.0	0.0066	0.072	0.0013	-0.0076	-0.011

¹⁷⁵³ 4.5.3 Efficiency description

¹⁷⁵⁴ An imprecise determination of the reconstruction and selection efficiency can intro-
¹⁷⁵⁵ duce an extra oddity and therefore bias the measurement. To asses this effect the
¹⁷⁵⁶ kinematic re-weighting described in Sec. 3.3.2 is removed from the simulation and
¹⁷⁵⁷ the efficiency is determined again. Simulated events are then fit using the same the-
¹⁷⁵⁸ oretical PDF and multiplied by the efficiency functions obtained with and without
¹⁷⁵⁹ kinematical weights. As in the previous cases the average bias is taken as systematic
¹⁷⁶⁰ uncertainty; results are shown in Tab. 4.4. Furthermore, the effect of the limited
simulated statistics is taken into account and added to the systematic uncertainty.

Table 4.4: Values systematic uncertainties due to limited knowledge of the efficiency function on the three angular observables in bins of q^2

q^2 [GeV $^2/c^4$]	A_{FB}^ℓ	f_L	A_{FB}^h
0.1 – 2.0	0.0020	0.0440	0.0093
11.0 – 12.5	0.0069	0.0027	0.0069
15.0 – 16.0	0.0018	0.0046	0.0109
16.0 – 18.0	0.0012	0.0043	0.0159
18.0 – 20.0	0.0030	0.0017	0.0148
15.0 – 20.0	0.0002	0.0046	0.0138

Table 4.5: Values of systematic uncertainties due to the statistics of the simulated samples on the three angular observables in bins of q^2 .

q^2 [GeV $^2/c^4$]	A_{FB}^ℓ	f_L	A_{FB}^h
0.1 – 2.0	0.00151	0.00170	0.00213
11.0 – 12.5	0.00121	0.00154	0.00196
15.0 – 16.0	0.00004	0.00017	0.00103
16.0 – 18.0	0.00065	0.00246	0.00417
18.0 – 20.0	0.00023	0.00372	0.00162
15.0 – 20.0	0.00039	0.00091	0.00137

¹⁷⁶¹

¹⁷⁶² 4.5.4 Background parameterisation

¹⁷⁶³ There is a certain degree of arbitrariness in the choice of a parameterisation for the
¹⁷⁶⁴ background, especially for q^2 intervals with low statistics. To asses possible biases

1765 due to the choice of a specific PDF, simulated experiments are generated using the
1766 shapes obtained from fits to data and the same statistics as observed in data for
1767 each q^2 interval. Each pseudo-experiment is fit with two models: the default one, a
1768 “line times efficiency” function and the efficiency function alone, corresponding to
1769 the assumption that background distributions are originally flat and only modified
1770 by the interaction with the detector. The average bias with respect to the default
1771 model is taken as systematic uncertainty; results are reported in Tab. 4.6.

Table 4.6: Values of systematic uncertainties due to the choice of background parameterisation in bins of q^2 .

q^2 [GeV $^2/c^4$]	A_{FB}^ℓ	f_L	A_{FB}^h
0.1 – 2.0	0.003	0.049	0.053
11.0 – 12.5	0.045	0.034	0.035
15.0 – 16.0	0.010	0.038	0.026
16.0 – 18.0	0.026	0.036	0.022
18.0 – 20.0	0.011	0.031	0.025
15.0 – 20.0	0.007	0.014	0.017

1772

1773 4.5.5 Polarisation

1774 To study the effect of a non-zero Λ_b^0 production polarisation simulated events are
1775 generated using the distributions given by Eqs. 4.12 and 4.14 as a function of the
1776 angle under study ($\cos\theta_\ell$ or $\cos\theta_h$) and $\cos\theta$, defined in Sec. 4.2, which is sensitive
1777 to polarisation. Similarly to the procedure used for the branching ratio measure-
1778 ment, events are generated varying the value of the polarisation within one standard
1779 deviation from the LHCb measurement [102]. As in the theoretical functions $\cos\theta$ is
1780 always odd, it would always drop out when integrating over θ in the case of perfect
1781 efficiency, yielding no bias by construction. Therefore, the generated distributions
1782 are also multiplied by the two-dimensional efficiency function. No significant bias is
1783 found.

¹⁷⁸⁴ **4.6 J/ψ cross-check**

¹⁷⁸⁵ To validate the fitting procedure this is applied to the high statistics $\Lambda_b^0 \rightarrow J/\psi \Lambda$
¹⁷⁸⁶ sample. For this purpose events are selected with an additional requirement on the
¹⁷⁸⁷ proton PID, $\text{PID}_p > 10$. This is needed to reduce the $B^0 \rightarrow K_s^0 J/\psi$ background,
¹⁷⁸⁸ which is particularly important for the hadronic side fit, since the K_s^0 events are
¹⁷⁸⁹ not distributed in a flat way in the $\cos \theta_h$ variable and would therefore bias the fit.
¹⁷⁹⁰ Figure 4.8 shows the invariant mass distributions after this requirement is applied,
¹⁷⁹¹ which can be compared with the ones in Fig. 3.12. After the PID cut there are
¹⁷⁹² 0.2% of K_s^0 events left in the downstream sample and a fraction compatible with
¹⁷⁹³ zero in the long sample. The signal model used for the angular fit to $\Lambda_b^0 \rightarrow$
¹⁷⁹⁴ $J/\psi \Lambda$ candidates is the same defined for the rare case and described in Sec. 4.4.2.
¹⁷⁹⁵ For the background instead the higher statistics allows to leave more freedom to
¹⁷⁹⁶ the fit. Therefore a second-order Chebyshev polynomial is used, where the two
¹⁷⁹⁷ parameters are free to vary. As for the rare case the background fractions are
¹⁷⁹⁸ gaussian-constrained to what found from the invariant mass fit. Figures 4.9 and 4.10
¹⁷⁹⁹ show fitted angular distributions for the J/ψ channel. The measured values of the
¹⁸⁰⁰ observables are $A_{\text{FB}}^\ell = -0.002^{+0.011}_{-0.011}$, $A_{\text{FB}}^h = -0.402^{+0.010}_{-0.009}$ and $f_L = 0.485^{+0.019}_{-0.020}$, where
¹⁸⁰¹ the uncertainties are 68% Feldman-Cousins confidence intervals. The lepton side
¹⁸⁰² asymmetry is measured to be zero as expected for a tree level $b \rightarrow c\bar{c}s$ process.

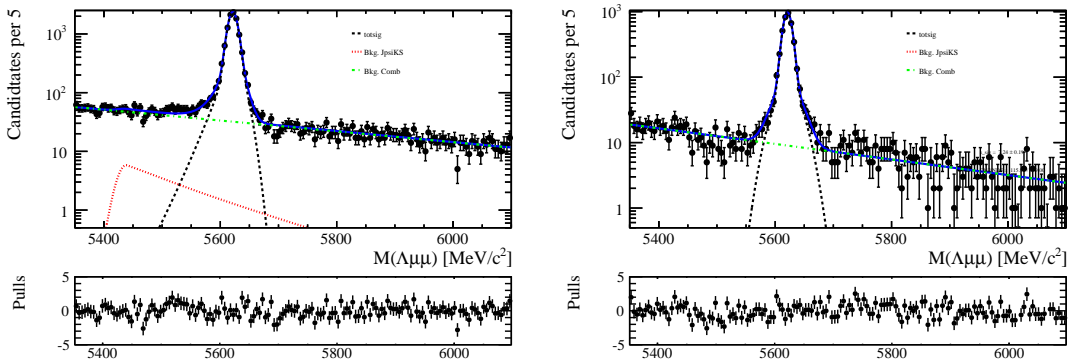


Figure 4.8: Invariant mass distribution of $\Lambda_b^0 \rightarrow J/\psi \Lambda$ downstream (left) and long (right) candidates with an extra proton PID cut to remove K_s^0 background.

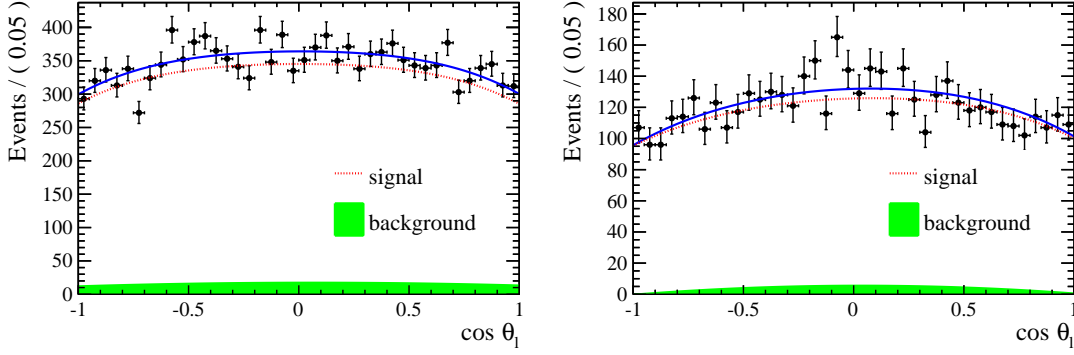


Figure 4.9: Fitted $\cos \theta_\ell$ angular distribution for $\Lambda_b^0 \rightarrow J/\psi \Lambda$ candidates reconstructed using downstream (left) and long (right) tracks.

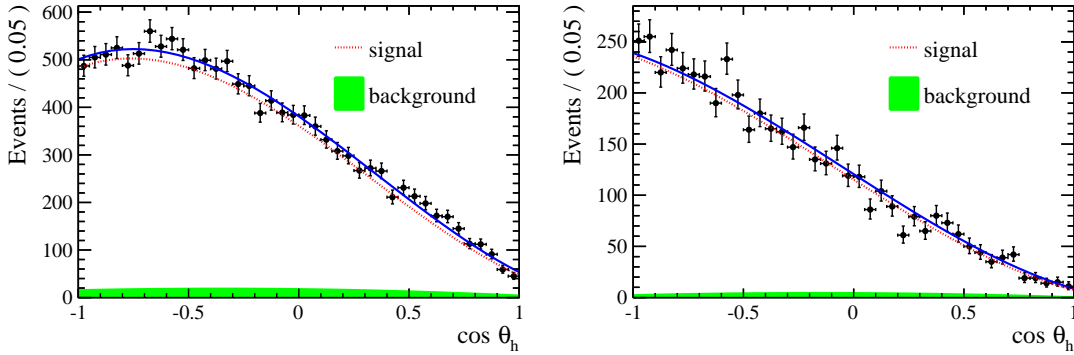


Figure 4.10: Fitted $\cos \theta_h$ angular distribution for $\Lambda_b^0 \rightarrow J/\psi \Lambda$ candidates reconstructed using downstream (left) and long (right) tracks.

1803 4.7 Results

1804 Figures 4.11 and 4.12 show fits to the angular distributions for the $15 - 20$ $\text{GeV}^2/c^4 q^2$
 1805 interval and Tab. 4.7 reports measured values of A_{FB}^ℓ , A_{FB}^h and f_L in all intervals.
 1806 The asymmetries are also shown in Fig. 4.13 together with SM predictions obtained
 1807 from Ref. [105]. The statistical uncertainties on these tables are obtained using the
 1808 likelihood-ratio ordering method described in Sec. 4.4.1, where only one of the two
 1809 observables is treated as the PoI at a time. The statistical uncertainties on A_{FB}^ℓ and
 1810 f_L are also reported in Fig. 4.14 as two-dimensional 68 % confidence level regions,
 1811 where the likelihood-ratio ordering method is applied by varying both observables
 1812 at the same time and therefore taking correlations into account. Total systematic
 1813 uncertainties correspond to the square root sum of the single considered sources.

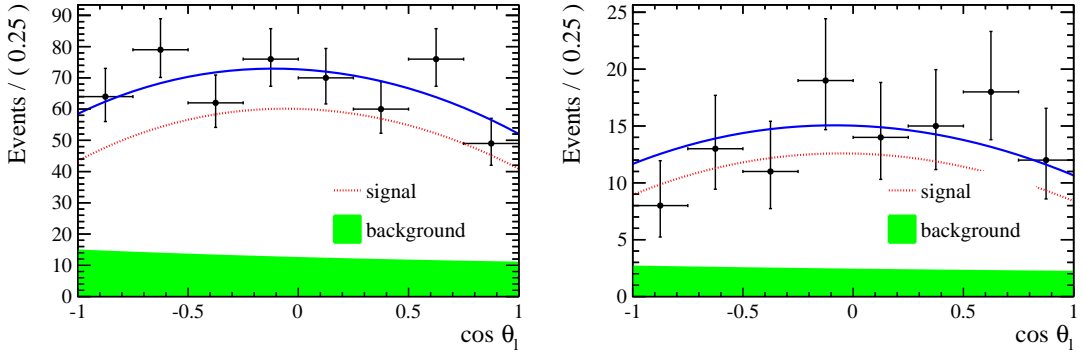


Figure 4.11: Fitted $\cos \theta_\ell$ angular distributions for downstream (left) and long (right) candidates in the $15 - 20 \text{ GeV}^2/c^4 q^2$ interval.

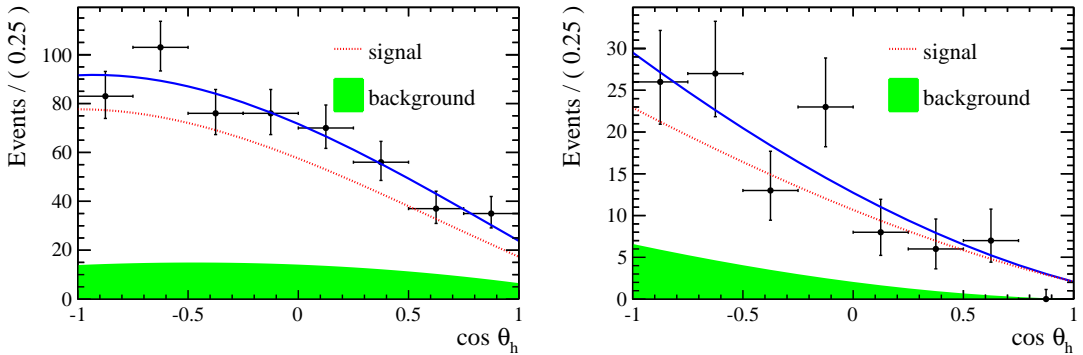


Figure 4.12: Fitted $\cos \theta_h$ angular distributions for downstream (left) and long (right) candidates in the $15 - 20 \text{ GeV}^2/c^4 q^2$ interval.

Table 4.7: Measured values of leptonic and hadronic angular observables; uncertainties are statistical and systematic.

$q^2 [\text{GeV}^2/c^4]$	A_{FB}^ℓ	f_L	A_{FB}^h
0.1 – 2.0	$0.37^{+0.37}_{-0.48} \pm 0.03$	$0.56^{+0.23}_{-0.56} \pm 0.08$	$-0.12^{+0.31}_{-0.28} \pm 0.15$
11.0 – 12.5	$0.01^{+0.19}_{-0.18} \pm 0.06$	$0.40^{+0.37}_{-0.36} \pm 0.06$	$-0.50^{+0.10}_{-0.00} \pm 0.04$
15.0 – 16.0	$-0.10^{+0.18}_{-0.16} \pm 0.03$	$0.49^{+0.30}_{-0.30} \pm 0.05$	$-0.19^{+0.14}_{-0.16} \pm 0.03$
16.0 – 18.0	$-0.07^{+0.13}_{-0.12} \pm 0.04$	$0.68^{+0.15}_{-0.21} \pm 0.05$	$-0.44^{+0.10}_{-0.05} \pm 0.03$
18.0 – 20.0	$0.01^{+0.15}_{-0.14} \pm 0.04$	$0.62^{+0.24}_{-0.27} \pm 0.04$	$-0.13^{+0.09}_{-0.12} \pm 0.03$
15.0 – 20.0	$-0.05^{+0.09}_{-0.09} \pm 0.03$	$0.61^{+0.11}_{-0.14} \pm 0.03$	$-0.29^{+0.07}_{-0.07} \pm 0.03$

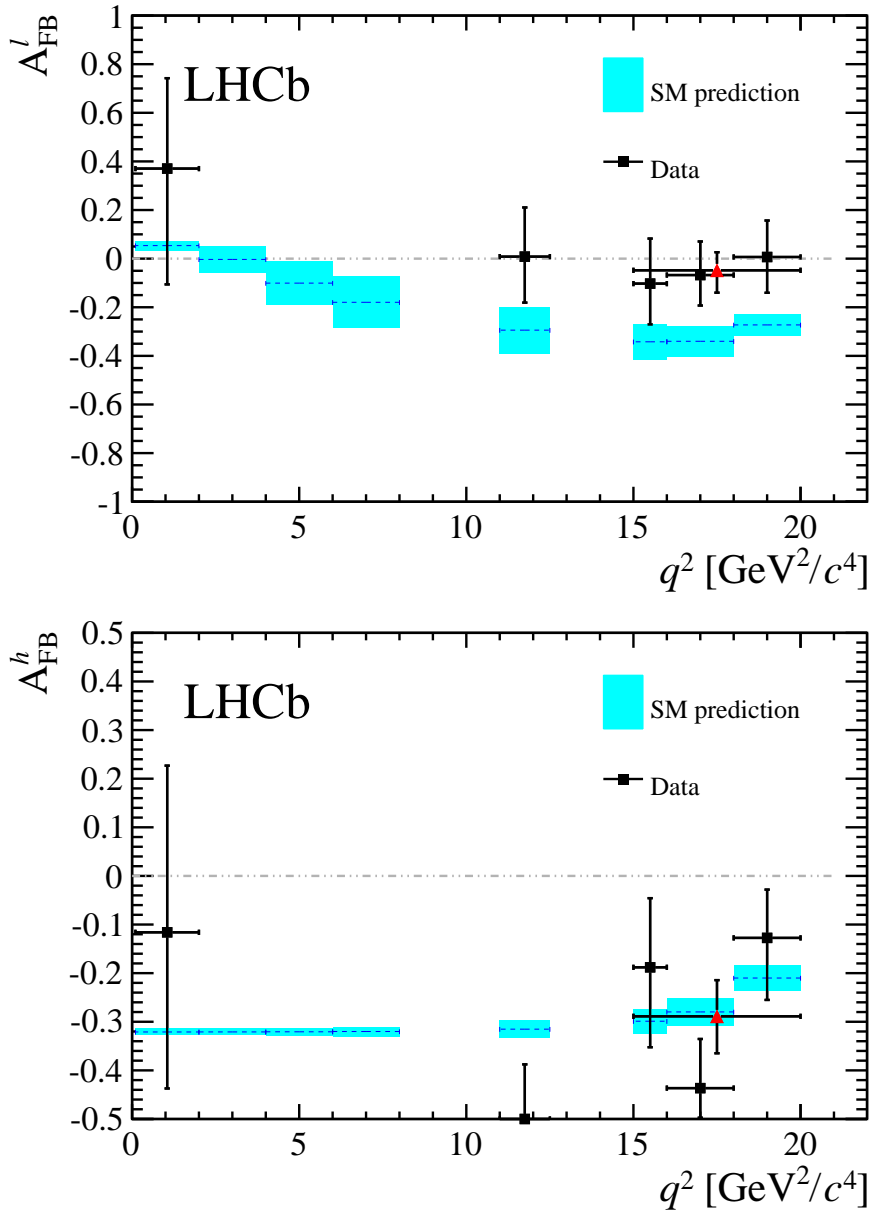


Figure 4.13: Measured values of the leptonic (top) and the hadronic (bottom) forward-backward asymmetries. Data points are only shown for q^2 intervals where the signal yield is found to be statistically significant, see text for details. The (red) triangle represents the values for the $15 < q^2 < 20$ GeV^2/c^4 integrated interval. Standard Model predictions are obtained from Ref. [112].

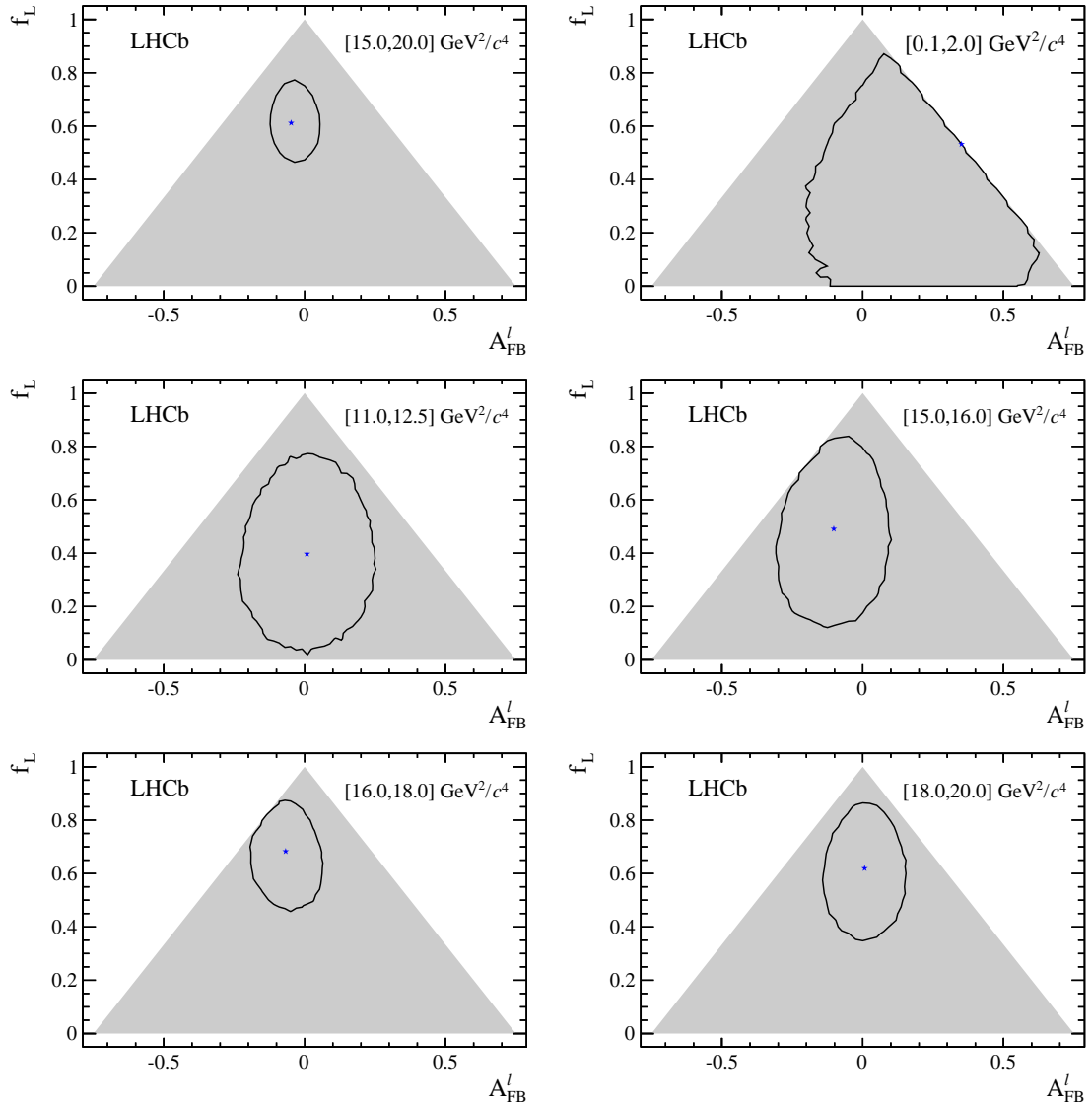


Figure 4.14: Two-dimensional 68 % CL regions (black) as a function of A_{FB}^L and f_L . The shaded areas highlight the region in which the PDF is positive over the whole $\cos \theta_\ell$ range. The best fit points are indicated by the (blue) stars.

1814

CHAPTER 5

1815

1816

Testing lepton flavour universality with $R_{K^{*0}}$

1817

1818 Lepton Favour Universality (LFU) is the equality of the weak coupling constants
1819 for all leptons. FCNC processes, which are forbidden in the SM at tree level and
1820 happen only at loop level, are an ideal laboratory to study LFU as new physics
1821 contributing in the loops could break the flavour symmetry.

1822 In this work $b \rightarrow s\mu^+\mu^- (e^+e^-)$ decays are studied to test LFU between electrons
1823 and muons. In particular, the B^0 meson semileptonic decays $B^0 \rightarrow K^{*0}\ell^+\ell^-$ are
1824 considered. Figure 5.1 shows the possible Feynman diagrams producing such decays
1825 while Fig. 5.2 illustrates how these Feynman diagrams may include new particles.
1826 A series of recent LHCb measurements [31] points to a tension with SM predictions,
1827 which make these processes very interesting to better understand the nature of the
1828 discrepancy.

1829 In order to exploit the sensitivity of loop diagrams, in 2004 Hiller and Kruger pro-

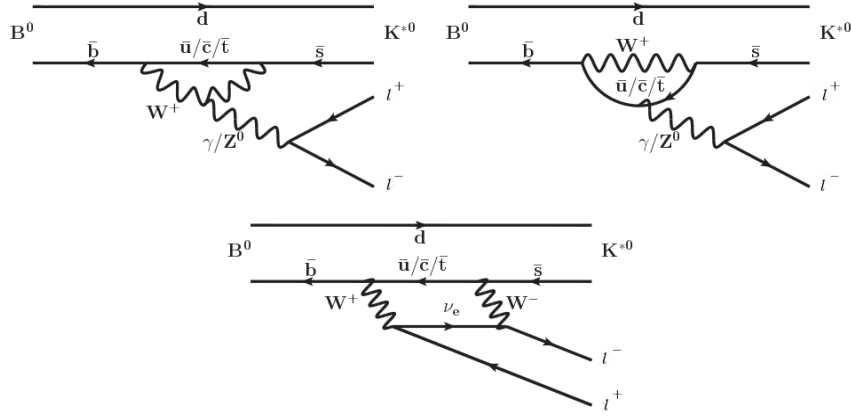


Figure 5.1: Loop diagrams producing $B^0 \rightarrow K^{*0} \ell^+ \ell^-$ decays.

1830 posed the measurement of the R_H ratio [113], defined as

$$R_H = \frac{\int_{4m_\mu^2}^{m_b} \frac{d\mathcal{B}(B^0 \rightarrow H \mu^+ \mu^-)}{dq^2} dq^2}{\int_{4m_\mu^2}^{m_b} \frac{d\mathcal{B}(B^0 \rightarrow H e^+ e^-)}{dq^2} dq^2}, \quad (5.1)$$

1831 where H can be an inclusive state containing an s quark (X_s) or an s -quark resonance
1832 like K or K^{*0} . In this quantity the differential branching fraction is integrated over
1833 the squared dilepton invariant mass, q^2 , from $q_{min}^2 = 4m_\mu^2$, which is the threshold
1834 for the $\mu\mu$ process, up to $q_{max}^2 = m_b^2$.

1835 The advantage of using ratios of branching fractions as observables is that, in the
1836 theoretical prediction, hadronic uncertainties cancel out. Furthermore, experimen-
1837 tally, some of the systematic uncertainties on the ratios are reduced giving a better
1838 measurement. For example, what is measured is the number of $\mu\mu$ and ee decays
1839 happening in a certain period of time. Then, the luminosity, \mathcal{L} , is used to obtain
1840 a cross section, σ , using $R = \mathcal{L}\sigma$, where R is the rate at which the decays occur.
1841 The luminosity measurement is usually a source of systematic uncertainty, but it
1842 appears on both sides of the ratio and therefore cancels out.

Since the SM does not distinguish between lepton flavours, the predicted value of the ratio is $R_H = 1$, under the assumption of massless leptons. Taking into account effects of order m_μ^2/m_b^2 Hiller and Kruger calculate that in the SM and in the full q^2

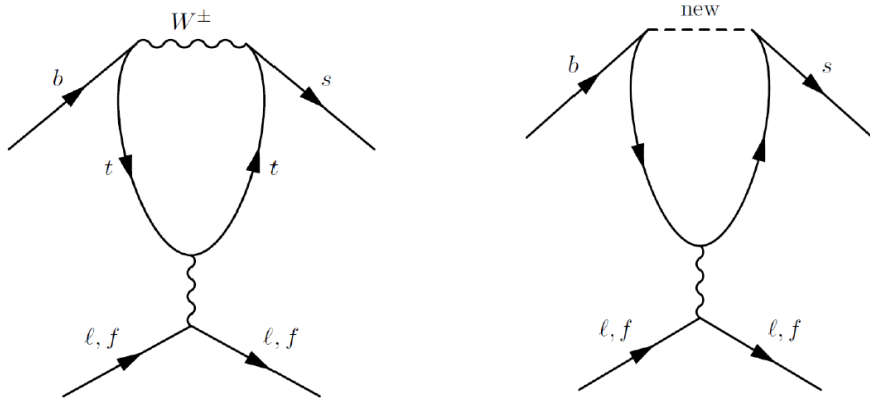


Figure 5.2: Example of penguin diagrams, on the left involving SM particles and on the right involving new possible particles.

range [113]:

$$R_{X_s} = 0.987 \pm 0.006, \quad (5.2)$$

$$R_K = 1.0000 \pm 0.0001, \quad (5.3)$$

$$R_{K^{*0}} = 0.991 \pm 0.002; \quad (5.4)$$

$$(5.5)$$

¹⁸⁴³ under the assumptions that:

- ¹⁸⁴⁴ • right-handed currents are negligible;
- ¹⁸⁴⁵ • (pseudo-)scalar couplings are proportional to the lepton mass;
- ¹⁸⁴⁶ • there are no CP-violating phases beyond the SM.

¹⁸⁴⁷ The measurement of the R_H ratios is of particular interest after the recent measure-
¹⁸⁴⁸ ment of the branching fraction of the $B_s^0 \rightarrow \mu^+ \mu^-$ decay [42], where no evidence of
¹⁸⁴⁹ new physics was found. In fact the quantities $(R_H - 1)$ and $\mathcal{B}(B_s^0 \rightarrow \mu^+ \mu^-)$ remain
¹⁸⁵⁰ proportional with

$$\frac{R_H - 1}{\mathcal{B}(B_s^0 \rightarrow \mu^+ \mu^-)} \sim 2 \cdot 10^{-5}. \quad (5.6)$$

¹⁸⁵¹ A joint measurement of these two quantities can give much information and constrain
¹⁸⁵² MFV models. If $R_H = 1$ and $\mathcal{B}(B_s^0 \rightarrow \mu^+ \mu^-)$ is close to the SM prediction as it is

1853 measured to be this will allow to put strong constraints on extensions of the SM. If
1854 instead $R_H > 1$ and the equation above is not verified, this would mean that one of
1855 the assumptions listed above are not verified, which can happen in some extensions of
1856 the SM as Super-Symmetric models with broken R-parity. A series of recent LHCb
1857 measurements [31] shows tensions with SM predictions, which makes it interesting
1858 to further investigate these processes.

1859 5.1 Combining ratios

1860 The full power of the R_H ratios in understanding new physics scenarios comes from
1861 their combinations. In Ref. [114] Hiller and Schmaltz propose the measurement
1862 of the double ratios, $X_H = R_H/R_K$, which not only can test LFU but also allow
1863 to disentangle the kind of new physics that lies behind. These ratios are in fact
1864 sensitive to FCNCs of right-handed currents. Furthermore, in Ref. [114] the study
1865 is extended to B_s^0 decays such as $B_s^0 \rightarrow \phi\ell^+\ell^-$ and $B_s^0 \rightarrow \eta\ell^+\ell^-$.

1866 Parity and Lorentz invariance require that the Wilson Coefficients with left-handed
1867 chirality (C) and their right-handed counterparts (C') appear in the decay amplitude
1868 of exclusive decays in determined combinations, e.g.

$$\begin{aligned} C + C' : & K, K_{\perp}^{*0}, \dots \\ C - C' : & K_0(1430), K_{\parallel}^{*0}, \dots \end{aligned} \tag{5.7}$$

1869 where the labels for the K^{*0} meson represent its longitudinal (0), parallel (\parallel) and
1870 perpendicular (\perp) transversity components. The C contributions are universal to
1871 all decays and therefore X_H double ratios are sensitive to right-handed currents. In
1872 fact the R_H ratios can be expressed in terms of their deviation from unity as

$$\begin{aligned} R_K &\simeq 1 + \Delta_+, \\ R_{K_0(1430)} &\simeq 1 + \Delta_-, \\ R_{K^{*0}} &\simeq 1 + p(\Delta_- - \Delta_+) + \Delta_+, \end{aligned} \tag{5.8}$$

where the Δ_{\pm} quantities are combinations of Wilson coefficients described in Eq. 10 of Ref. [114] and the parameter p is the polarisation of K^{*0} that in Ref. [114] is determined to be close to 1 simplifying the formula to $R_{K^{*0}} \simeq 1 + \Delta_-$. In particular one can observe the following correlations:

- $R_K < 1$, as it is measured to be, and $X_{K^{*0}} > 1$ points to dominant BSM contributions into C_{LR} (see definition in Sec. 1.5.2);
- a SM like $R_K \sim 1$ together with $X_{K^{*0}} \neq 1$ requires BSM with $C_{LL} + C_{RL} \simeq 0$;
- $R_K \neq 1$ and $X_{K^{*0}} \simeq 1$ corresponds to new physics in C_{LL} .

5.2 Experimental status

The R_K and $R_{K^{*0}}$ ratios have been measured at the B-factories [115, 116], and R_K has been recently measured also at LHCb [117], which represents the most precise measurement to date; measured values are summarised in Tab. 5.1. The LHCb measurement manifests a 2.6σ deviation from the SM prediction. This is particularly interesting as this discrepancy can be explained with a new physics contribution in C_9 which also explains other existing tensions [53, 48, 54]. It is also worth mentioning the measurement of the $\mathcal{B}(\bar{B}^0 \rightarrow D^{*+}\tau^-\bar{\nu}_\tau)/\mathcal{B}(\bar{B}^0 \rightarrow D^{*+}\mu^-\bar{\nu}_\mu)$ ratio which probes LFU and was measured to be 2.1σ larger than the value expected from the assumption of lepton universality in the SM [118]. By profiting of the large dataset collected during Run-I, the LHCb experiment is expected to reduce the uncertainty on $R_{K^{*0}}$ by at least a factor of 2 with respect to the B-factories.

Table 5.1: Experimental status of the $R_{K^{(*)}}$ measurements.

Ratio	Belle	BaBar	LHCb
R_K	$1.06 \pm 0.48 \pm 0.05$	$1.38^{+0.39+0.06}_{-0.41-0.07}$	$0.745^{+0.090}_{-0.074} \pm 0.036$
$R_{K^{*0}}$	$0.93 \pm 0.46 \pm 0.12$	$0.98^{+0.30+0.08}_{-0.31-0.08}$	—

1893 5.3 Analysis strategy

1894 The aim of the analysis in this chapter is to measure the $R_{K^{*0}}$ ratio using pp collision
 1895 data collected by the LHCb detector in 2011 and 2012, corresponding to 3 fb^{-1} of
 1896 integrated luminosity. The $B^0 \rightarrow K^{*0}\mu^+\mu^-$ and $B^0 \rightarrow K^{*0}e^+e^-$, “rare channels”,
 1897 are reconstructed via the K^{*0} decay into a kaon and a pion with opposite charges.

1898 The analysis has to separate signal candidates from background candidates which
 1899 have similar observed properties. The selection presented in Sec. 5.6 aims to max-
 1900 imise the yield while minimising the background contamination. Two types of back-
 1901 grounds are identified: “peaking background” and “combinatorial background”. The
 1902 first comes from the mis-reconstruction of other decays or from partially recon-
 1903 structed events. This type of background, because its specific kinematic properties,
 1904 usually peaks in some variable, such as the invariant mass of all final particles.
 1905 Therefore these candidates can be removed using specific cuts. The combinatorial
 1906 background instead comes from the random combination of particles and can be
 1907 lowered selecting candidates with good-quality tracks and vertices.

1908 To further reduce the systematic uncertainties the measurement is performed as the
 1909 double ratio

$$R_{K^{*0}} = \frac{N_{B^0 \rightarrow K^{*0}\mu^+\mu^-}}{N_{B^0 \rightarrow K^{*0}J/\psi \rightarrow \mu^+\mu^-}} \cdot \frac{N_{B^0 \rightarrow K^{*0}J/\psi \rightarrow e^+e^-}}{N_{B^0 \rightarrow K^{*0}e^+e^-}} \cdot \frac{\varepsilon_{B^0 \rightarrow K^{*0}J/\psi \rightarrow \mu^+\mu^-}}{\varepsilon_{B^0 \rightarrow K^{*0}\mu^+\mu^-}} \cdot \frac{\varepsilon_{B^0 \rightarrow K^{*0}e^+e^-}}{\varepsilon_{B^0 \rightarrow K^{*0}J/\psi \rightarrow e^+e^-}}, \quad (5.9)$$

1910 where decays reaching the same final states as the rare channels via a J/ψ resonance,
 1911 $B^0 \rightarrow K^{*0}(J/\psi \rightarrow \ell^+\ell^-)$, also referred to as “charmonium” or “resonant” channels,
 1912 are used as control samples. These decays are distinguished from the rare channel
 1913 using the invariant mass of the dilepton pair. As new physics is expected not to
 1914 affect tree level $b \rightarrow c\bar{c}s$ processes the ratio between the J/ψ channels is 1 and there-
 1915 fore $R'_{K^{*0}} = R_{K^{*0}} \times R_{J/\psi} = R_{K^{*0}}$. On the other hand using the relative efficiencies
 1916 between the rare and resonant channels allows to cancel out many systematic effects
 1917 resulting in a better control of systematic uncertainties.

¹⁹¹⁸ For brevity, the rare channels will also be denoted as “ $\ell\ell$ ”, or specifically “ ee ” and
¹⁹¹⁹ “ $\mu\mu$ ”, and the resonant channels as “ $J/\psi(\ell\ell)$ ”, or “ $J/\psi(ee)$ ” and “ $J/\psi(\mu\mu)$ ”.

¹⁹²⁰ 5.4 Dilepton invariant mass intervals

¹⁹²¹ Three q^2 intervals are considered in this work:

¹⁹²² • the “low- q^2 ” region between 0.0004 and 1.1 GeV^2/c^4 , where the $b \rightarrow s\ell^+\ell^-$
¹⁹²³ process is dominated by the photon pole;

¹⁹²⁴ • the “central- q^2 ” region, [1.1,6.0] GeV^2/c^4 ;

¹⁹²⁵ • the “high- q^2 ” region, above 15 GeV^2/c^4 .

¹⁹²⁶ The central- q^2 region is the most interesting place to look for new physics. In fact,
¹⁹²⁷ at low q^2 values, below 1 GeV^2/c^4 the photon pole dominates leaving little space for
¹⁹²⁸ new physics to be found. The choice of the lower limit of the low- q^2 interval is driven
¹⁹²⁹ by the need to reject the background due to the $B^0 \rightarrow K^{*0}\gamma$ decay where the photon
¹⁹³⁰ converts into electrons in the material. The lower bound of the central interval is
¹⁹³¹ set at 1.1 GeV^2/c^4 , in order to exclude the contribution from $\phi \rightarrow \ell^+\ell^-$ decays, that
¹⁹³² can dilute new physics effects, while the upper bound is chosen to be sufficiently
¹⁹³³ far away from the J/ψ radiative tail, where predictions cannot be cleanly obtained.

¹⁹³⁴ The 6 – 15 GeV^2/c^4 region is characterised by the presence of the narrow peaks of
¹⁹³⁵ the J/ψ and $\psi(2S)$ resonances. The lower bound of the high- q^2 region, where the
¹⁹³⁶ signal in the electron channel is still unobserved, is chosen to be sufficiently far from
¹⁹³⁷ the $\psi(2S)$ resonance. Rare and normalisation channels are selected depending on
¹⁹³⁸ the q^2 interval they fall into (for details see Sec. 5.6).

¹⁹³⁹ 5.4.1 Control channels

¹⁹⁴⁰ Beyond the normalisation channels, $B^0 \rightarrow K^{*0}(J/\psi \rightarrow e^+e^-/\mu^+\mu^-)$, extra-control
¹⁹⁴¹ channels are used to perform cross-checks and better constrain some of the back-
¹⁹⁴² ground components in the electron fit; in particular, $B^0 \rightarrow K^{*0}(\gamma \rightarrow e^+e^-)$, also
¹⁹⁴³ denoted as “ $\gamma(ee)$ ”, and $B^0 \rightarrow K^{*0}(\psi(2S) \rightarrow e^+e^-)$, also denoted as “ $\psi(2S)(ee)$ ”.
¹⁹⁴⁴ All the normalisation and control channels are distinguished depending on the q^2
¹⁹⁴⁵ interval they fall into (for details see Sec. 5.6).

¹⁹⁴⁶ 5.5 Data samples and simulation

¹⁹⁴⁷ Simulated samples are used to study the properties of backgrounds, determine effi-
¹⁹⁴⁸ ciencies and to train a multivariate classifier. The hard interactions are generated
¹⁹⁴⁹ with PYTHIA8 hadronic particles are decayed using EVTGEN and, finally, propa-
¹⁹⁵⁰ gated into the detector using GEANT4 and reconstructed with the same software
¹⁹⁵¹ used for data. Samples are generated with both 2011 and 2012, magnet up and
¹⁹⁵² down conditions and are combined in the right proportions, according to the lumi-
¹⁹⁵³ nosities registered on data. The next section describes the corrections applied to
¹⁹⁵⁴ the simulation to obtain a better description of data.

¹⁹⁵⁵ 5.5.1 Data-simulation corrections

¹⁹⁵⁶ Since the multivariate classifier training (see Sec. 5.6.6) and the calculation of most
¹⁹⁵⁷ of the efficiency components (see Sec. 5.9) are obtained from the study of simulated
¹⁹⁵⁸ events it is important to verify that the simulation provides a reliable reproduction
¹⁹⁵⁹ the data. In particular it is important to match data and Monte Carlo in the
¹⁹⁶⁰ kinematics of the final particles and the occupancy of the detector. The kinematics
¹⁹⁶¹ of the decays is characterised by the transverse momentum spectrum of the B^0 .
¹⁹⁶² Discrepancies in this distribution cause also the spectra of the final particles to differ

from data and affect the efficiency determination as its value often depends on the momentum of the final particles. The occupancy of the detector is relevant as it is correlated to the invariant mass shape of the signal because of the addition of energy clusters in the electromagnetic calorimeter, which affects the electron's momenta especially when bremsstrahlung photons are emitted before the magnet. The hit multiplicity in the SPD detector is a proxy for the detector occupancy. Since it is important that these quantities are well modelled, the simulation is reweighted so that their distributions in data and simulation match. The weight is calculated using resonant $B^0 \rightarrow K^{*0}(J/\psi \rightarrow \ell^+\ell^-)$ candidates, for which the signal peak is already visible in data after pre-selection (see Sec. 5.6). However, the data still includes a high level of background and distributions cannot be directly compared. The sPlot technique [69] is used to statistically subtract the background from data and obtain pure signal distributions using the invariant mass as the control variable. Figure 5.3 shows fits to the 4-body invariant mass of candidates after pre-selection. Data and simulation are then compared and the ratio between the two distributions is used to reweight the simulation. The discrepancy in the SPD hits multiplicity is solved as a first step and then the B^0 transverse momentum distributions are compared between data and simulation reweighted for the SPD multiplicity only. Distributions of B^0 transverse momentum and SPD multiplicity are reported in Fig. 5.4 and ratios of these distributions, which are used to reweight the simulation, are reported in Fig. 5.5. The weights for the SPD multiplicity are calculated separately for 2011 and 2012 events, because distributions are significantly different in the two years. The binnings are chosen to have approximately the same number of events in each bin to limit fluctuations. Further corrections are made by reweighting the simulation for PID efficiency using the `PIDCalib` package as described in Sec. 5.9.3 and, finally, ee samples are also reweighted for L0 trigger efficiency as described in Sec. 5.9.4. Weights are always applied throughout unless specified.

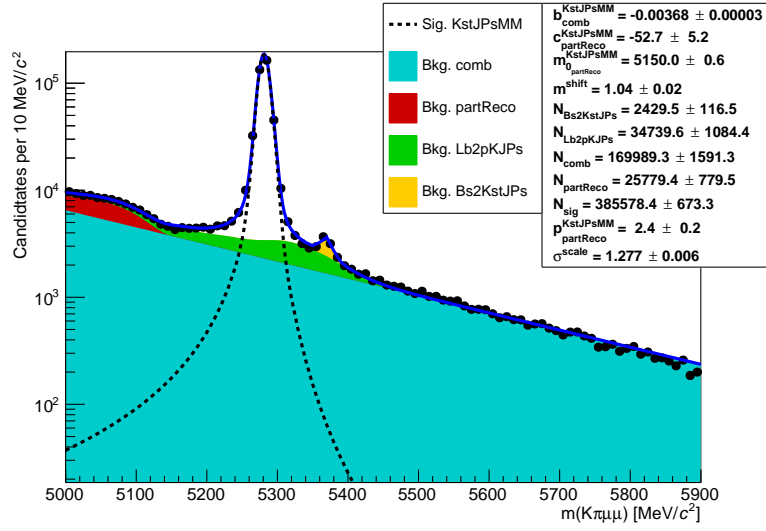


Figure 5.3: Fitted 4-body invariant mass distributions of muonic resonant candidates used to obtain ${}_s\mathcal{W}$ eights.

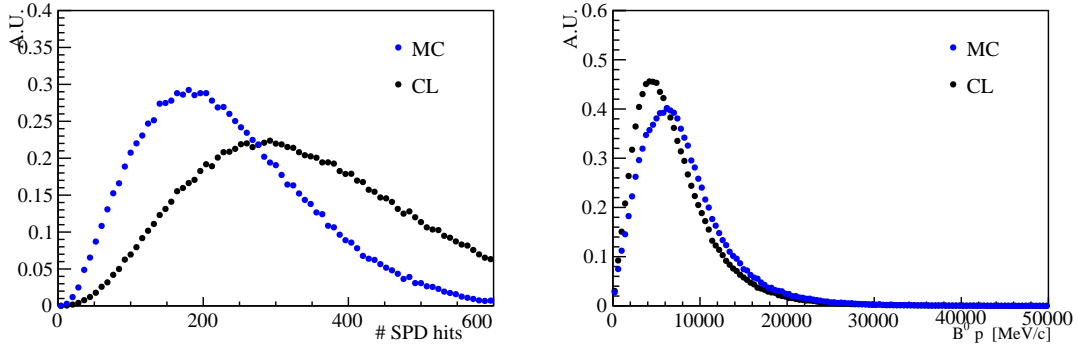


Figure 5.4: Distributions of number of SPD hits (left) and B^0 transverse momentum (right) in data and MC.

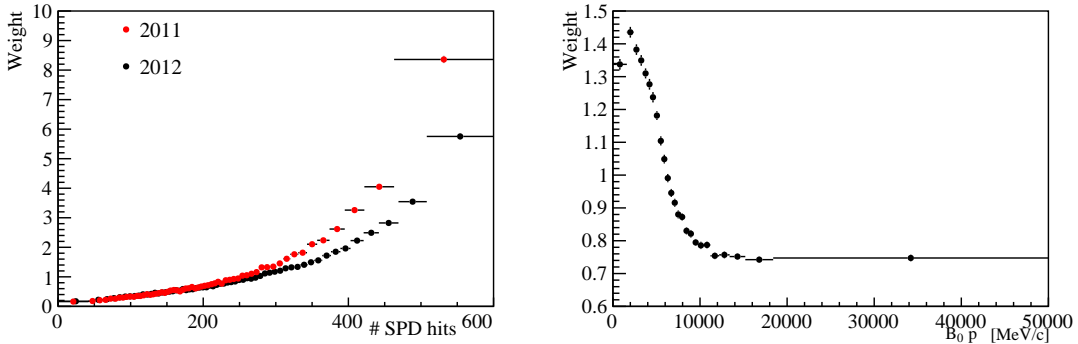


Figure 5.5: Ratios of simulated over real data distributions used to correct the simulation as a function of the number of SPD hits (left) and the B^0 transverse momentum (right).

1990 **5.6 Selection**

1991 The selection process, described in this section, is divided into several steps:

- 1992 • first of all candidates have to fall into the detector acceptance, produce hits and
1993 be selected on the basis of quality features, such as χ^2 of tracks and vertices
1994 and basic kinematic cuts. This stage is called “stripping”. Furthermore, it
1995 is required that the events are triggered by specific trigger lines and cuts are
1996 applied to remove backgrounds from specific decays. All these first three steps
1997 are referred to as “pre-selection”;
- 1998 • secondly, particle identification requirements are applied to remove part of
1999 misreconstructed background and clear the way for the last step;
- 2000 • in the final step a neural network is used to remove combinatorial background.
2001 Furthermore, for the electron channels, which are more challenging, the kine-
2002 matic structure of the decays is also used to improve the samples’ purity.

2003 In order to identify the $J/\psi(\mu\mu)$ candidates a dimuon invariant mass interval of
2004 $100 \text{ MeV}/c^2$ around the nominal J/ψ peak [2] is selected. On the other hand it is
2005 not possible to use a narrow interval around $J/\psi(ee)$ mass peak as the invariant
2006 mass distribution is characterised by a long radiative tail at low masses due to
2007 bremsstrahlung radiation. Furthermore, a requirement on $m(ee)$ would distort the
2008 4-body $m(K\pi ee)$ mass distribution which is not advisable as is important to be able
2009 to fit a wide mass range in order to constrain the backgrounds. For these reasons the
2010 interval to select $J/\psi(ee)$ candidates is chosen to go as low as possible in q^2 without
2011 overlapping with the rare channel interval. Candidates are therefore identified as
2012 $J/\psi(ee)$ if they fall in the q^2 interval $6 < q^2 < 11 \text{ GeV}^2/c^4$. Similarly, candidates are
2013 identified as $\psi(2S)(ee)$ if they fall into $11 < q^2 < 15 \text{ GeV}^2/c^4$ and $\gamma(ee)$ if they fall
2014 into $q^2 < 0.004 \text{ GeV}^2/c^4$. Table 5.2 summarises the requirements used to distinguish
2015 samples corresponding to different decay channels. Figure 5.6 shows two-dimensional
2016 distributions of q^2 versus the 4-body invariant mass for candidates passing the full

Table 5.2: Summary of the channel categories.

Type	Sample	q^2
$\mu\mu$	$B^0 \rightarrow K^{*0} \mu^+ \mu^-$ (low)	$0.0004 < q^2 < 1.1 \text{ GeV}^2/c^4$
	$B^0 \rightarrow K^{*0} \mu^+ \mu^-$ (central)	$1.1 < q^2 < 6 \text{ GeV}^2/c^4$
	$B^0 \rightarrow K^{*0} \mu^+ \mu^-$ (high)	$q^2 > 15 \text{ GeV}^2/c^4$
	$B^0 \rightarrow K^{*0}(J/\psi \rightarrow \mu^+ \mu^-) (m(K\pi\mu\mu))$	$ m_{\mu\mu} - m_{J/\psi}^{PDG} < 100 \text{ MeV}/c^2$
ee	$B^0 \rightarrow K^{*0} e^+ e^-$ (low)	$0.0004 < q^2 < 1.1 \text{ GeV}^2/c^4$
	$B^0 \rightarrow K^{*0} e^+ e^-$ (central)	$1.1 < q^2 < 6 \text{ GeV}^2/c^4$
	$B^0 \rightarrow K^{*0} e^+ e^-$ (high)	$q^2 > 15 \text{ GeV}^2/c^4$
	$B^0 \rightarrow K^{*0}(J/\psi \rightarrow e^+ e^-) (m(K\pi ee))$	$6 < q^2 < 11 \text{ GeV}^2/c^4$
Control samples		
	$B^0 \rightarrow K^{*0}(\gamma \rightarrow e^+ e^-) (m(K\pi ee))$	$q^2 < 0.0004 \text{ GeV}^2/c^4$
	$B^0 \rightarrow K^{*0}(J/\psi \rightarrow e^+ e^-) (m(K\pi ee))$	$6 < q^2 < 11 \text{ GeV}^2/c^4$
	$B^0 \rightarrow K^{*0}(\psi(2S) \rightarrow e^+ e^-) (m(K\pi ee))$	$11 < q^2 < 15 \text{ GeV}^2/c^4$

selection. Horizontal bands can be clearly seen at q^2 values corresponding to the J/ψ and $\psi(2S)$ resonances. On the plot for muons it is also evident a vertical band which corresponds to the rare decay.

5.6.1 Trigger and Stripping

Events are triggered for the $\mu\mu$ and the ee channels by the trigger lines reported in Tab. 5.3, where the logical *and* of L0, HLT1 and HLT2 lines is required and the logical *or* of the lines on the same level. The candidates are required to be triggered-on-signal (TOS) for most of the stages, namely it is required for the particle which triggered to be one of the particles used to build the signal candidates. Only for `LOGlobal`, used in the electron case, a trigger-independent-of-signal (TIS) is required. The `L0Muon` trigger requires hits in the muon detector, while `L0Electron` and `L0Hadron` use information from the calorimeters; `HLT1TrackAllL0` adds information from the trackers and triggers if the L0 decision is confirmed; finally, `HLT2Topo[2,3]BodyBBDT` uses a full reconstruction of the event and a neural network trained on candidates with a specific topology in order to detect specific decay structures.

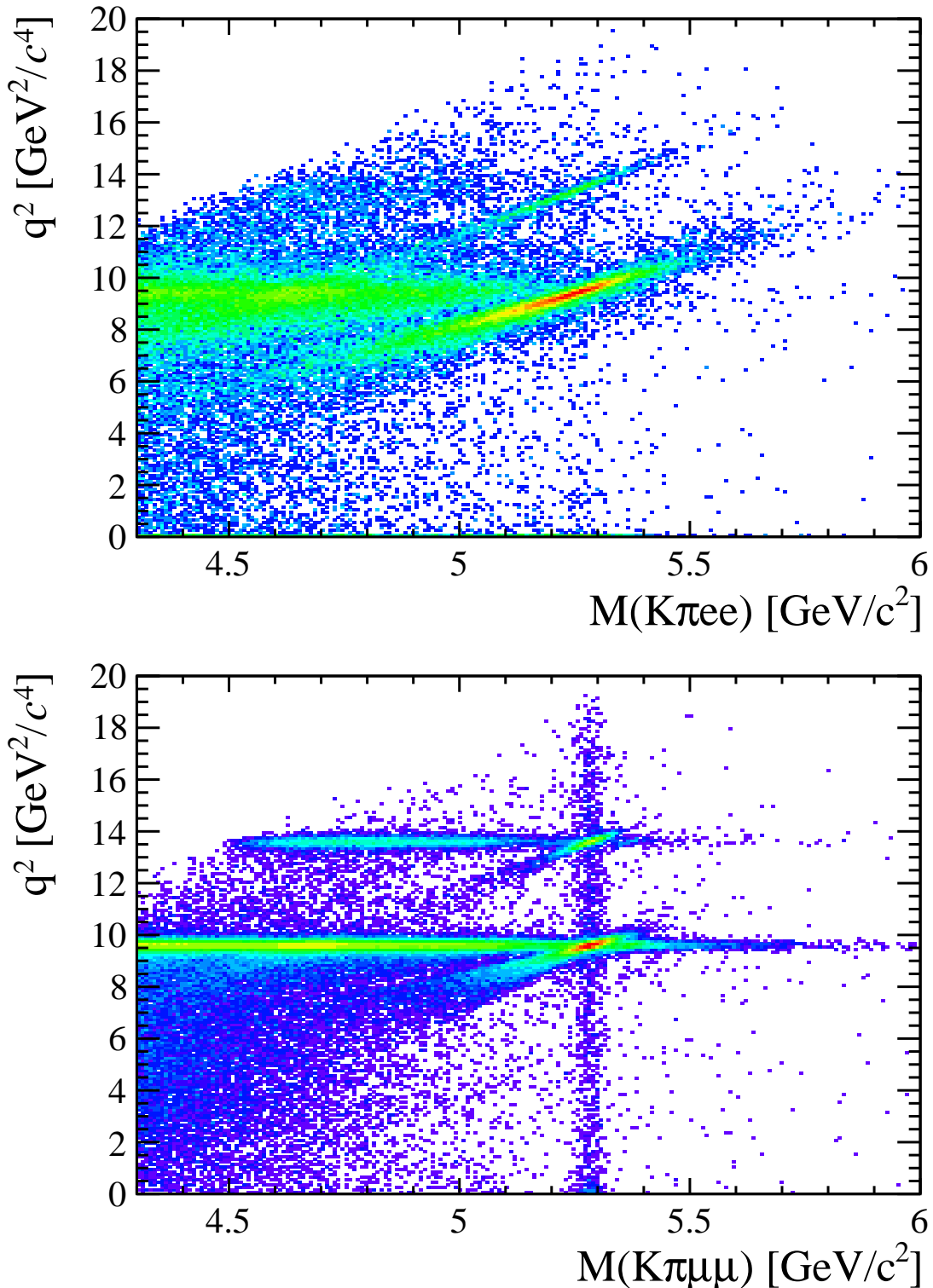


Figure 5.6: Two-dimensional distributions of q^2 versus 4-body $m(K\pi\ell\ell)$ invariant mass for the electron (top) and muon (bottom) channels in 2012 data.

Table 5.3: Summary of the trigger lines used to select the $\mu\mu$ and the ee channels. Where not explicitly indicated, the lines are required to be TOS.

$\mu\mu$ candidates	ee candidates
L0Muon	L0Electron L0Hadron L0Global (TIS)
Hlt1TrackAllL0 Hlt1TrackMuon	Hlt1TrackAllL0
Hlt2Topo[2,4]BodyBBDT Hlt2TopoMu[2,4]BodyBBDT Hlt2DiMuonDetachedDecision	Hlt2Topo[2,4]BodyBBDT Hlt2TopoE[2,4]BodyBBDT

2033 For the electron channels the L0 lines have different properties, therefore the analysis
 2034 is performed separately for three categories of events, depending on the L0 trigger
 2035 that fired them. These categories are defined to be exclusive in the following way:

- 2036 • **L0E**: events triggered by at least one of the electrons in the signal candidate
 2037 (`L0Electron_TOS`);
- 2038 • **L0H**: events triggered by at least one of the hadrons in the signal candidate
 2039 and not by `L0Electron` (`L0Hadron_TOS && !L0Electron_TOS`);
- 2040 • **L0I**: events triggered by particles not in the signal candidate and not by the
 2041 previous cases (`L0Global_TIS && !(L0Electron_TOS || L0Hadron_TOS)`).

2042 The majority of the selected events falls in the L0E category, while the L0H category
 2043 is more efficient at low q^2 were the K^{*0} has more momentum. Because L0I is defined
 2044 to be independent of the signal candidate, the corresponding signal efficiency is the
 2045 same in the rare and resonant cases and cancels out in their ratio.

2046 Candidates are then required to pass the kinematic and quality cuts summarised
 2047 in Tab. 5.4. The meaning of the variables in the table was already explained in
 2048 Sec. 3.4. Loose PID cuts are applied in preselection to limit the size of the samples,
 2049 while tighter cuts are applied in a second stage. A large mass window is kept
 2050 around the B^0 peak in order to be able to use the sideband to train the multivariate

Table 5.4: Summary of stripping requirements.

Particle	Requirements
π	$\chi^2_{\text{IP}}(\text{primary}) > 9$
K	$\text{PID}_K > -5$ $\chi^2_{\text{IP}}(\text{primary}) > 9$ hasRICH
K^{*0}	$p_T > 500 \text{ MeV}/c$ $ m_{K\pi} - m_{K^{*0}}^{\text{PDG}} < 300 \text{ MeV}/c^2$ $\chi^2_{\text{IP}}(\text{primary}) > 9$ Origin vertex $\chi^2/\text{ndf} < 25$
μ	$p_T > 300 \text{ MeV}/c$ $\chi^2_{\text{IP}}(\text{primary}) > 9$ isMuon
e	$p_T > 300 \text{ MeV}/c$ $\chi^2_{\text{IP}}(\text{primary}) > 9$ hasCalo $\text{PID}_e > 0$
$\ell\ell$	$m_{\ell\ell} < 5500 \text{ MeV}/c^2$ End vertex $\chi^2/\text{ndf} < 9$ Origin vertex χ^2 separation > 16
B^0	$\text{DIRA} > 0.9995$ End vertex $\chi^2/\text{ndf} < 9$ $\chi^2_{\text{IP}}(\text{primary}) < 25$ Primary vertex χ^2 separation > 100

classifier and to constrain the backgrounds. Track and vertex quality cuts are also applied using the $\chi^2_{track}/\text{ndf}$, `GhostProb`, and χ^2_{vtx}/ndf variables. The `GhostProb` quantity describes the probability of a track being fake. By construction cutting at 0.4 removes $(1 - 0.4) \cdot 100 = 60\%$ of fake tracks. For details about the definition of the variables used see Ref. [119].

5.6.2 PID

After preselection there still are high levels of misreconstructed background. In particular, as the ID of kaons and pions are not constrained, the samples still contain both ID combinations for most candidates, therefore tighter PID cuts are applied. In the LHCb analysis framework the particle identification probability can be quantified using the “`ProbNN`” variables [120]. These variables are the output of a neural network which takes as input information from the calorimeters, the RICH detectors the muon system and the tracking system. Unlike the DLL variables (see Sec. 2.8) the `ProbNN` are bound from 0 to 1 and can be therefore directly be interpreted as probabilities. For example `ProbNNk` is the probability for a reconstructed particle to be a kaon. Figure 5.7 shows distributions of the correct ID variables in the

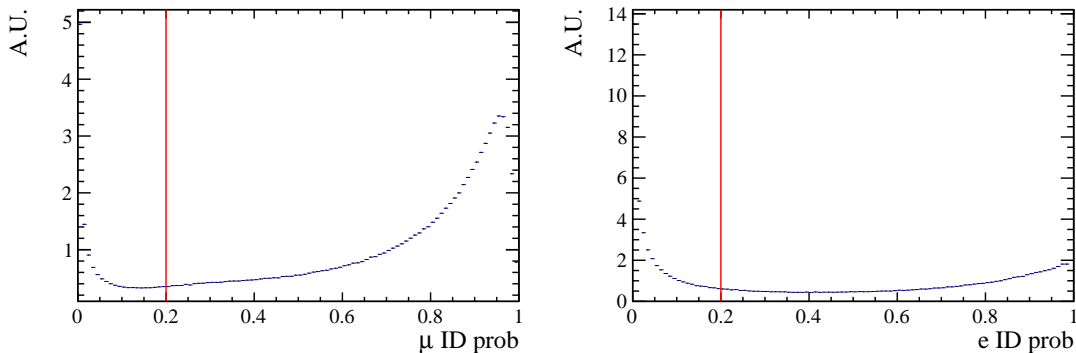


Figure 5.7: Correct ID probability distributions for muons (left) and electron (right) in 2012 data.

2066
2067 2012 data sample while Fig. 5.8 shows in a two-dimensional plane the probability
2068 of correct identification and mis-identification of kaons and pions. These plots are
2069 characterised by clear peak at maximal ID probability and minimal mis-ID probabil-

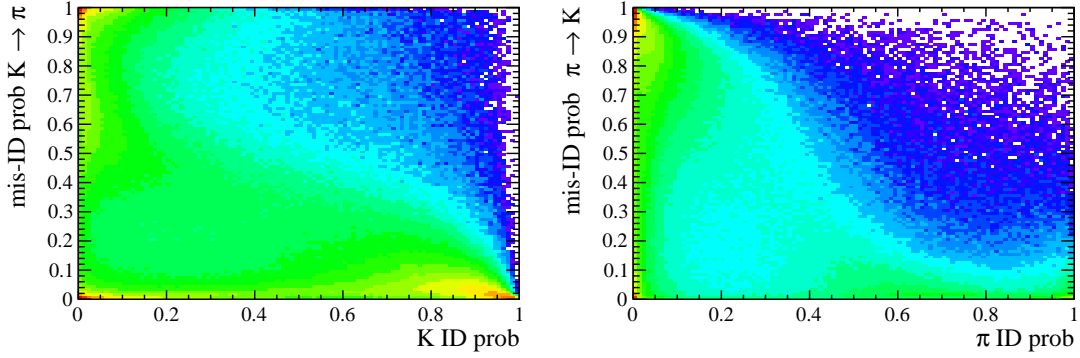


Figure 5.8: On the horizontal axis of these plots is shown the correct ID probabilities for kaons (left) and pions (right), while the vertical axis show the mis-ID probability.

2070 ity, corresponding to particles to which a well defined identification can be assigned.
 2071 In order to maximise the power of the PID requirements probabilities of correct ID
 2072 and mis-ID are combined using the following cuts:

$$\begin{aligned} \pi &\rightarrow \text{ProbNNpi} \times (1 - \text{ProbNNk}) \times (1 - \text{ProbNNp}) > 0.1 \\ K &\rightarrow \text{ProbNNk} \times (1 - \text{ProbNNp}) > 0.05 \\ \mu &\rightarrow \min(\text{ProbNNmu}, \text{ProbNNmu}) > 0.2 \\ e &\rightarrow \min(\text{ProbNNe}, \text{ProbNNe}) > 0.2 \end{aligned}$$

2073
 2074 In the first formula, for example, `ProbNNpi` is the probability of correctly identifying
 2075 the pion as a pion, while `ProbNNk` is the probability of mistaking it for a kaon. There-
 2076 fore by maximising the quantity “`ProbNNpi` × (1 - `ProbNNk`)”, one can maximise
 2077 the correct ID probability and minimise at the same time the mis-ID probability.

2078 5.6.3 Peaking backgrounds

2079 Backgrounds due to specific decays usually peak in some variable because of their
 2080 distinctive kinematic properties and therefore they can be removed without sig-
 2081 nificant signal efficiency loss. The following sections describe the main sources of
 2082 peaking background. The same cuts are applied to the muon and electron channels,
 2083 unless specified.

2084 5.6.3.1 Charmonium vetoes

2085 Charmonium resonances such as J/ψ and $\psi(2S)$ peak in q^2 . The choice of q^2 bin-
 2086 ning described in Sec. 5.4 constitutes a natural veto for these decays. Simulated
 2087 events were used to check if resonant candidates leak inside the q^2 intervals cho-
 2088 sen for the rare channel analysis. For the muonic channels the leakage is negli-
 2089 gible as the peaks are sharper due to a better resolution and muons emit fewer
 2090 bremsstrahlung photons, resulting in shorter radiative tails. The electronic chan-
 2091 nels are instead characterised by a worse resolution and at the same time electrons
 2092 can radiate several bremsstrahlung photons, yielding long tails at low q^2 . Analysing
 2093 Monte Carlo events it was found that 1.3–2% (depending on the trigger category)
 2094 of $B^0 \rightarrow K^*(J/\psi \rightarrow e^+e^-)$ candidates leak into the $1.1 < q^2 < 6$ GeV^2/c^4 interval
 2095 and 1.8% of $\psi(2S)$ events leak above 15 GeV^2/c^4 . The contribution from these
 2096 candidates is modelled in the fit.

2107 5.6.3.2 ϕ veto

2108 It can happen that a kaon from the decay $B_s \rightarrow \phi\ell^+\ell^-$, where the ϕ decays in two
 2109 kaons, is mis-identified as a pion and therefore causes the ϕ to be reconstructed as a
 2110 K^{*0} . This results in a candidate with a value of $m(K\pi)$ that is less than the nominal
 2111 K^{*0} mass but still high enough to pass the selection requirements. Figure 5.9 shows
 2112 the plot of $m(K\pi)$ versus $m(K\pi\ell\ell)$, where the kaon mass hypothesis is assigned to
 2113 the pion. A peak can clearly be seen around the ϕ mass ($1020 \text{ MeV}/c^2$). To remove
 2114 this background only candidates with $m_{K(\pi \rightarrow K)} > 1040 \text{ MeV}/c^2$ are selected. This
 2115 results in a 98% background rejection while keeping a 99% signal efficiency. The ϕ
 2116 could also constitute a background when it decays into two leptons but the branching
 2117 ratio of this decay is small compared to the one into kaons and this contribution is
 2118 taken into account by the choice of the q^2 intervals (see Sec. 5.4).

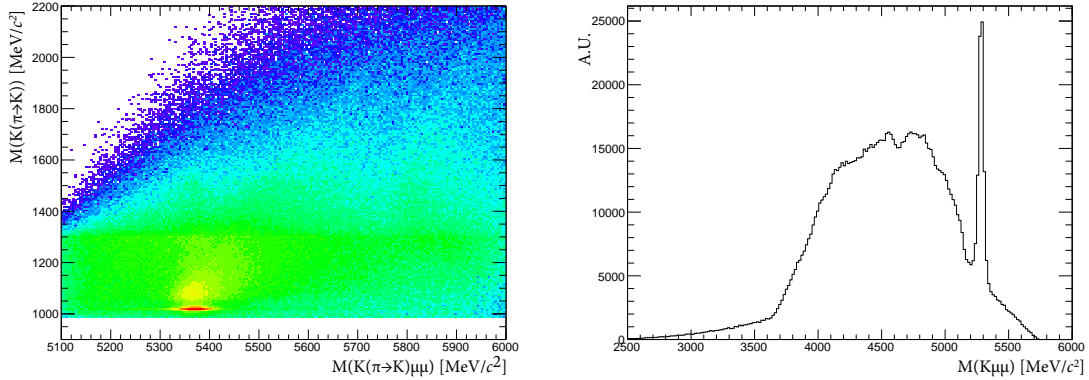


Figure 5.9: (left) Distribution of 2011 data events as a function of the variables ($m_{K(\pi \rightarrow K)}$) and ($m_{K(\pi \rightarrow K)\mu\mu}$), where $\pi \rightarrow K$ means that the kaon mass is given to the pions too. (right) The invariant mass distribution of the three-body system ($K\mu\mu$), where the peak due to the $B^+ \rightarrow K^+\mu^+\mu^-$ decay is visible.

2110 5.6.3.3 $B^+ \rightarrow K^+\ell^+\ell^-$ plus a random pion

2111 $B^+ \rightarrow K^+\ell^+\ell^-$ decays can contaminate the upper B^0 mass sideband if they are com-
2112 bined with a soft pion from somewhere else in the event and therefore reconstructed
2113 as a B^0 decay. Similarly a kaon can be mis-identified as a pion and combined with
2114 an other kaon in the event. Figure 5.9 shows the invariant mass distribution of the
2115 three-body $K\mu^+\mu^-$ system, $m(K\mu\mu)$. This is characterised by a narrow peak at
2116 the B^+ mass. Since these candidates have $m(K\pi\ell\ell) > 5380$ MeV/ c^2 there is no
2117 contribution under the B^0 peak, but they can cause problems when using sidebands
2118 events to train the neural network. An effective veto for this decay was found to
2119 be $\max(m_{K\ell\ell}, m_{(K \rightarrow \pi)\ell\ell}) < 5100$ MeV/ c^2 , which results in 95% background rejection
2120 while keeping 99% signal efficiency.

2121 5.6.3.4 Λ_b decays

2122 $\Lambda_b^0 \rightarrow J/\psi \Lambda$ decays are unlikely to be reconstructed as $B^0 \rightarrow K^{*0}\ell^+\ell^-$ because the
2123 Λ is long-lived and decays further in the detector with a separate vertex. How-
2124 ever, simulated events were used to check how many candidates fall into the B^0
2125 samples, which results to be negligible. The $\Lambda_b^0 \rightarrow J/\psi pK$ decay, when the pro-

2126 ton is mis-identified, can instead contribute more easily since the $m(pK)$ is above
2127 the Λ threshold and therefore they must come from Λ^* resonances, which are not
2128 long-lived. This background is already reduced by the PID requirements but a
2129 non-negligible contribution is still expected, which is modelled in the fit.

2130 5.6.3.5 $B^0 \rightarrow (D^- \rightarrow K e^- \bar{\nu}) e^+ \nu$

2131 The $B^0 \rightarrow D^- e^+ \nu$ decay, where the D^- in turn decays semileptonically to $K^{*0} e^- \nu$
2132 has the same final particles as the $B^0 \rightarrow K^{*0} e^+ e^-$ decay plus two neutrinos which
2133 are not reconstructed. This decay has a branching ratio four orders of magnitude
2134 larger than $B^0 \rightarrow K^{*0} e^+ e^-$ in the low- q^2 region and it may pass the selection
2135 requirements when the two neutrinos carry a low momentum. To lower the level
2136 of this background the angle θ_ℓ is used, which is defined as the angle between the
2137 direction of the e^+ (e^-) in the di-electron rest frame and the direction of the di-
2138 electron in the B^0 (\bar{B}^0) rest frame. Low momentum neutrinos demand the D^- and
2139 the e^+ to be almost back-to-back in the B^0 rest frame giving the e^+ a relatively
2140 large energy compared to the e^- . As a consequence, the direction of the e^+ is close
2141 to the direction of the di-electron pair, thus the θ_ℓ angle is close to 0. This explains
2142 why the distribution of background selected in data with an invariant mass cut of
2143 $m(K^{*0} ee) < 4800$ MeV/ c^2 is asymmetric towards higher $\cos(\theta_\ell)$ values as it can be
2144 seen in Fig. 5.10(*left*). The cut is chosen to be $|\cos(\theta_\ell)| < 0.8$, and is not applied in
2145 the high- q^2 bin as the variable loses its discriminating power.

2146 In the muon channels the background from $B^0 \rightarrow (D^- \rightarrow K \mu^- \bar{\nu}) \mu^+ \nu$ decays is
2147 suppressed by the choice of the fitting range.

2148 5.6.3.6 $B^0 \rightarrow K^{*0}(\gamma \rightarrow e^+ e^-)$

2149 For the low- q^2 region, a potentially dangerous peaking background is due to the
2150 $B^0 \rightarrow K^{*0}(\gamma \rightarrow e^+ e^-)$ decay followed by a conversion of the photon in the detector.
2151 The branching fraction of $B^0 \rightarrow K^{*0}(\gamma \rightarrow e^+ e^-)$ has been measured to be $\mathcal{B} = (4.33 \pm$

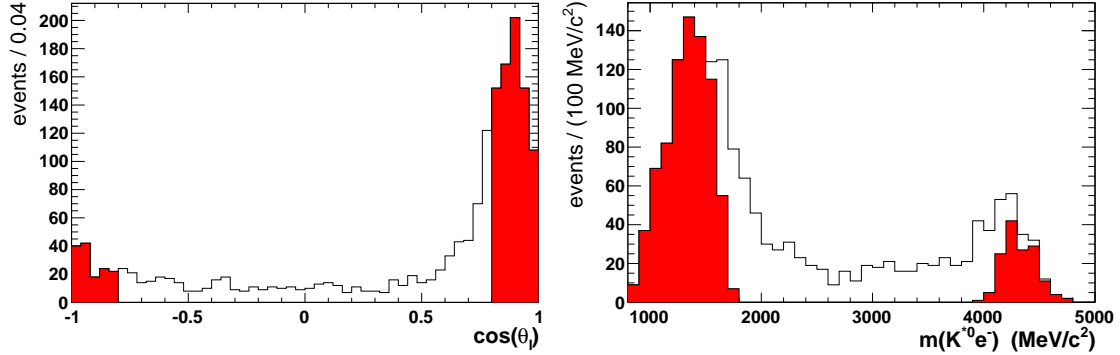


Figure 5.10: Distribution of (left) $\cos(\theta_\ell)$ and of (right) the $m(K^{*0}e^-)$ invariant mass, where the $B^0 \rightarrow (D^- \rightarrow Ke^-\bar{\nu})e^+\nu$ background is selected by requiring $m(K^{*0}e^+e^-) < 4800 \text{ MeV}/c^2$. The red distribution corresponds to events with $|\cos(\theta_\ell)| > 0.8$.

2152 $0.15) \times 10^{-5}$ and when the photon converts to an electron and a positron has similar
 2153 characteristics to $B^0 \rightarrow K^{*0}e^+e^-$. In LHCb around 40% of the photons convert
 2154 before the calorimeter. Although only a small fraction of these, $\sim 10\%$, converts in
 2155 the VELO and are reconstructed as long tracks, the resulting B^0 mass should peak
 2156 under that of the signal, making it a dangerous background. To veto this signal-
 2157 like background an effective veto is in the reconstructed invariant mass window for
 2158 the e^+e^- pair that was chosen above $20 \text{ MeV}/c^2$. Furthermore, the e^+e^- pair from
 2159 $B^0 \rightarrow K^{*0}(\gamma \rightarrow e^+e^-)$ has a vertex at the point of conversion of the photon, but it
 2160 may still be reconstructed as originating from the B^0 decay when the e^+e^- -vertex is
 2161 determined with a large error. Therefore a requirement is applied on the uncertainty
 2162 of the reconstructed z -coordinate of the e^+e^- pair: $\sigma_z(e^+e^-) < 30\text{mm}$. iSimulation
 2163 is used to predict the contamination from $B^0 \rightarrow K^{*0}(\gamma \rightarrow e^+e^-)$ events in the signal
 2164 region which is found to be $(3.2 \pm 1.6)\%$.

2165 5.6.3.7 Other peaking backgrounds

2166 Contamination from $B^0 \rightarrow K^{*0}\eta$ and $B^0 \rightarrow K^{*0}\pi^0$ where η and the pion decay
 2167 into two photons was considered and found to be small. Furthermore, a potentially
 2168 dangerous background could come from events where the identity of the kaon and
 2169 the pion are swapped as these candidates peak under the signal. Their contribution

is found to be small, 0.5%, however the effect of their modelling into the fit is taken into account in the systematic uncertainties. Finally, charmonium decays where the identity of the kaon, or the pion, and one of the muons are swapped is a potentially dangerous background. These decays are rejected by requiring that the hadron- μ invariant mass $m((h \rightarrow \mu)\mu)$, where the muon mass hypothesis is assigned to the hadron, is not compatible with a J/ψ ($\psi(2S)$) resonance: $|m((h \rightarrow \mu)\mu) - m_{J/\psi,(\psi(2S))}| > 60 \text{ MeV}/c^2$.

5.6.4 Partially-reconstructed background

Partially-reconstructed candidates are defined as decays where one or more particles in the final state are not reconstructed, resulting in $m(K\pi\ell\ell)$ values smaller than m_{B^0} , but with tails that can still contaminate the signal peak. Sources of mis-reconstructed background are decays involving higher hadronic states such as $B^0 \rightarrow (Y \rightarrow K\pi X)(J/\psi \rightarrow e^+e^-)$, where X represents one or more not reconstructed particles. The Y state can be a K^* resonance as well as D mesons that decay semileptonically (e.g. $B^0 \rightarrow D^-\ell^+\bar{\nu}_\ell$ followed by $D^- \rightarrow K^{*0}\ell^-\nu_\ell$). In case of the $J/\psi(ee)$ channel, an additional source of mis-reconstructed background are decays of higher $c\bar{c}$ resonances, $B^0 \rightarrow (K^{*0} \rightarrow K\pi)(Y \rightarrow (J/\psi \rightarrow e^+e^-)X)$. To reject this backgrounds in the $\mu^+\mu^-$ channels the 4-body invariant mass $m(K\pi\mu\mu)$ is recalculated using `DecayTreeFitter` with a vertex constraint. For the resonant case this also includes a J/ψ mass constraint to the dilepton pair; in this case the 4-body mass is denoted as $m(K\pi\mu\mu)_{J/\psi}$. Partially-reconstructed candidates are pushed towards low constrained-mass values, resulting in no contamination above 5150 MeV/c^2 . This requirement is implicitly applied for the muon channels by the definition of the invariant mass fit-windows. The same requirement is also applied to select the $J/\psi(ee)$ and $\psi(2S)(ee)$ samples. However, the vertex constrain alone is not sufficient to cleanup the electron rare channels. Furthermore, to correctly model the long radiative tail of the mass shapes, a fit region that extends down to 4500 MeV/c^2 is needed. As a consequence the partially-reconstructed background is

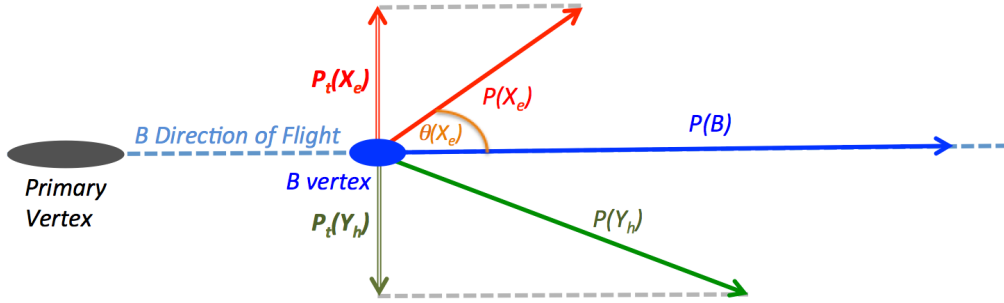


Figure 5.11: Schema of the kinematic of a $B \rightarrow Y_h X_e$ decay, highlighting the quantities relevant for the definition of the bremsstrahlung correction factor, α .

2198 still relevant for the electron rare channels and extends below the signal peak. For
 2199 this reason this background is modelled in the fit for the rare channels (for details
 2200 see Sec. 5.8.2.2).

2201 5.6.5 Bremsstrahlung corrected mass

2202 An additional handle against backgrounds that contaminate the ee channels is pro-
 2203 vided the analysis of the kinematics of the decay. In fact for the B^0 daughters the
 2204 momentum component orthogonal to the flight direction of the B^0 meson should
 2205 cancel out. The flight direction is defined using the primary and the decay vertices
 2206 and sketch is shown in Fig. 5.11.

The ratio between the p_T of the K^{*0} and the di-electron pair can be used to check this hypothesis

$$\alpha = \frac{p_T(K^*)}{p_T(e^+e^-)}.$$

When α deviates from one, some energy is missing in the final state. For signal events, the missing energy is most likely carried away by bremsstrahlung photons emitted by the electrons. Therefore we can use α to correct the electron momentum as

$$p_{\text{corr}}(e^+e^-) = \alpha \times p(e^+e^-).$$

2207 Since bremsstrahlung photons are emitted in the same direction of the electron,

the same α correction can be applied to the longitudinal component of the electron momentum. In contrast, the missing particles in partially-reconstructed background candidates are not necessarily emitted in the direction of the electrons, and therefore the α correction does not work properly. A similar argument applies to the combinatorial background.

The corrected momenta can be used to re-calculate the invariant mass of the B^0 candidate, which in the following will be called Bremsstrahlung Corrected Mass (m_{BCM}). The resolution of m_{BCM} depends on the quality of the vertex reconstruction and on the B^0 lifetime, and degrades as a function of q^2 . Figure 5.12 shows the dependence of the $B^0 \chi_{\text{FD}}^2$ (flight distance χ^2) as a function of m_{BCM} in the considered q^2 regions.

As the correction does not work properly for backgrounds this leads the candidates to spread out making m_{BCM} a discriminating variable between signal and background shapes. A two-dimensional cut is adopted

$$m_{\text{BCM}} > a_{\text{BCM}} + b_{\text{BCM}} \cdot \log(\chi_{\text{FD}}^2)$$

where the a_{BCM} and b_{BCM} coefficients are optimised as described in Sec. 5.6.7.

No cut is applied at high- q^2 nor on the muon channels for which the bremsstrahlung radiation is negligible.

5.6.6 Multivariate analysis

The final selection is performed using a Neural Network classifier (NN) based on the NEUROBAYES package [79, 80]. The multivariate analysis is intended to remove some combinatorial background and obtain a clearer signal peak. In order to avoid biases, a k -fold approach is adopted to train and optimise the classifier, using $k = 10$. This method consists in dividing the samples in k equally sized subsamples; k classifiers are then trained and optimised each on $(k - 1)$ samples and applied to

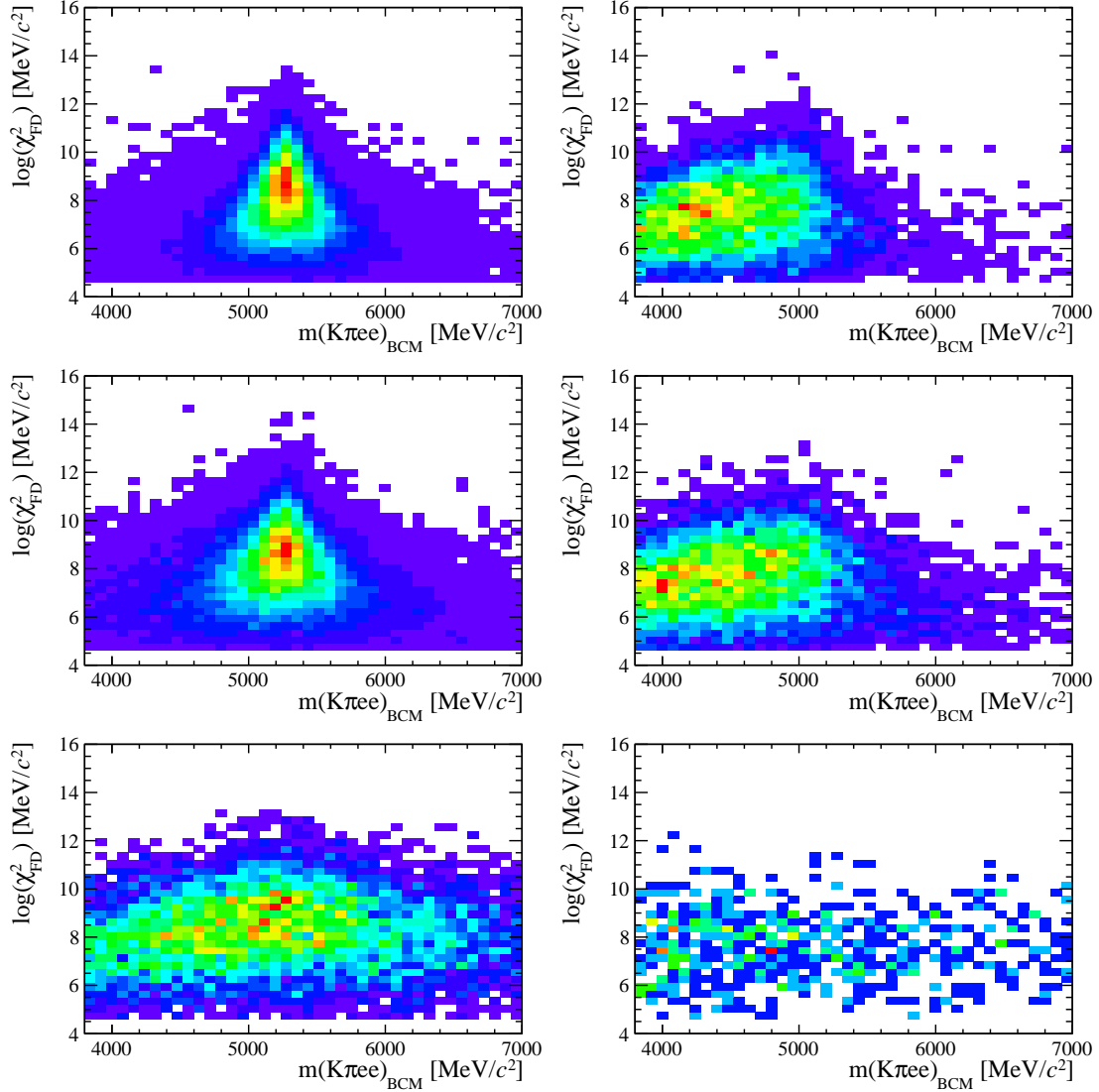


Figure 5.12: Two-dimensional distribution of χ^2_{FD} vs. m_{BCM} for (left) $B^0 \rightarrow K^{*0} e^+ e^-$ signal and (right) partially-reconstructed background. From top to bottom the low-, central- and high- q^2 intervals.

the k th one. This approach ensures that a classifier is never applied to the events used for its training. Each classifier is trained on half of the events included in the $(k - 1)$ samples and optimised using the other half, which ensures that events used for training are not used for optimisation.

2233 Samples:

2234 Representative samples of the signal and background are needed to train the clas-
2235 sifier. For the signal, fully reconstructed $B^0 \rightarrow K^{*0} \mu^+ \mu^-$ and $B^0 \rightarrow K^{*0} e^+ e^-$ sim-

Table 5.5: List of variables used as inputs for the neural-network training.

Particle	Variables
B^0	p_T , χ_{IP}^2 , χ_{FD}^2 , χ_{vtx}^2/ndf , DIRA, χ_{DTF}^2/ndf
K^{*0}	p_T , χ_{IP}^2 , χ_{FD}^2 , χ_{vtx}^2/ndf , DIRA
h	$min, max(p_{T,K}, p_{T,\pi})$, $min, max(\chi_{IP,K}^2, \chi_{IP,\pi}^2)$
$\ell\ell$	p_T , χ_{IP}^2 , χ_{FD}^2 , χ_{vtx}^2/ndf , DIRA
ℓ	$min, max(p_{T,\ell^+}, p_{T,\ell^-})$, $min, max(\chi_{IP,\ell^+}^2, \chi_{IP,\ell^-}^2)$

ulated events can be used. Instead a sample representative of the background can be obtained using real data candidates in the upper B^0 sideband: $m(K\pi\mu\mu) > 5400 \text{ MeV}/c^2$ and $m(K\pi ee) > 5600 \text{ MeV}/c^2$. The lower sideband is not used in the training as it contains a significant fraction of mis-reconstructed background. All pre-selection cuts are applied to the background samples used for the training. As L0 and PID variables are not well described in simulation these cuts are not applied to the simulation but their effect is taken into account by the event weight. An approximately equal number of signal and background events is used for the training which corresponds to about 1000 events for the electron case and 10,000 for the muon one.

Training:

The the neural-network input consists of 24 variables containing information about the kinematic of the decays and the quality of tracks and vertices. All the variables used are listed in Tab. 5.5. In these figures the variable with ID = 1 is the neural-network output and the other IDs are reported in Tab. 5.5. The single most discriminating variable used is the χ^2 of a kinematic fit that constrains the decay product of the B^0 , the K^{*0} and the dimuon, to originate from their respective vertices. Other variables that contribute significantly are the χ_{IP}^2 of J/ψ and K^{*0} , the transverse momentum of the B^0 and the pointing direction (DIRA) of the reconstructed B^0 to the primary vertex.

Figure 5.13 shows neural network output distributions for signal and background. On this plot the distributions from the test samples are also overlaid in order to check for overtraining. The distributions follow the same shape but with different

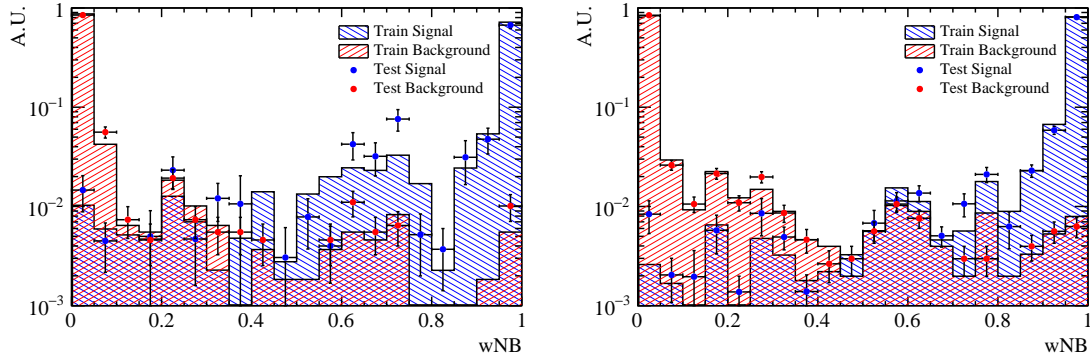


Figure 5.13: NN output distributions for training (solid) and test (stripes) samples, for simulated signal and data sideband events. For the electron (left) and muon (right) training.

fluctuations indicating no significant overtraining. In general it can be concluded that the neural network is able to separate signal from background and that the training converged properly.

It can happen that too much information is given to the classifier, which becomes able to calculate the invariant mass of the candidates from its inputs. This could generate fake peaks and it is therefore important to check for correlations between the B^0 mass and the neural-network output. Figure 5.15 reports plots of the average neural-network output as a function of the B^0 mass on sideband data and simulated signal events. The distributions are flat showing that no significant correlation is present.

5.6.7 Optimisation

In order to optimise the requirements on the m_{BCM} and the neural network output the expected signal significance, $N_S/\sqrt{N_S + N_B}$, is maximised, where N_S (N_B) is number of rare signal (background) candidates. When the BCM requirement is applied, the optimisation is performed in a three-dimensional space (t_{MVA} , a_{BCM} , b_{BCM}) where t_{MVA} is the neural-network output threshold below which a candidate is considered background, and a_{BCM} and b_{BCM} are the parameters of the BCM cut described in Sec. 5.6.5. Otherwise, only the MVA cut is optimised (for all muons

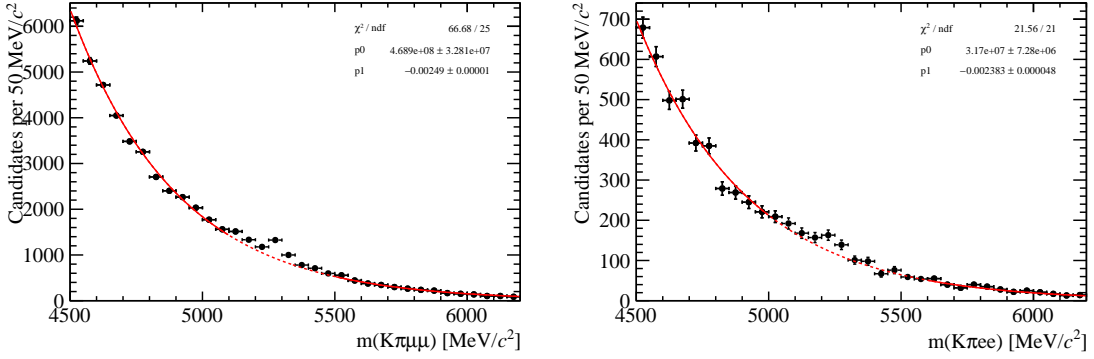


Figure 5.14: Fit to the data sidebands performed to estimate the amount of residual background in the signal mass window for (left) muons and (right) electrons. The region corresponding to the dashed line is excluded from the fit.

²²⁷⁷ samples and the high- q^2 electron sample).

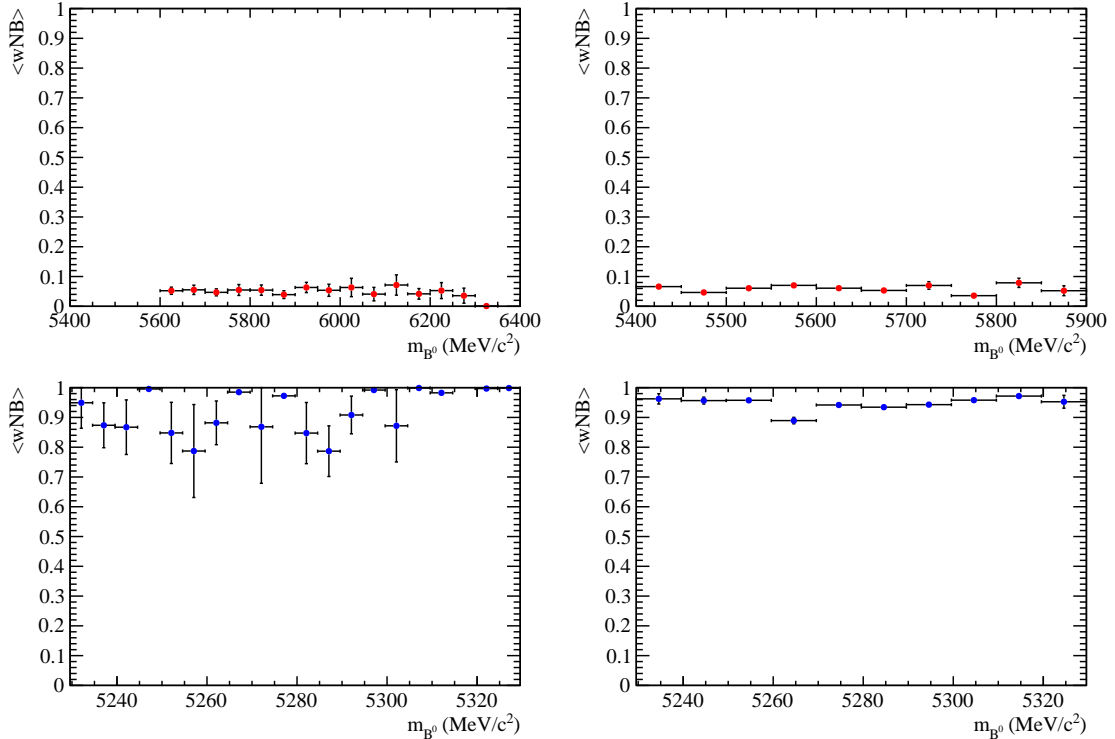


Figure 5.15: Average value of neural-network output as a function of B^0 mass for data sideband (top) and simulated signal (bottom) events for the electron (left) and muon (right) training.

The number of signal events accepted by a given requirement is determined using a data-driven method. Firstly, $B^0 \rightarrow K^{*0}(J/\psi \rightarrow \ell^+\ell^-)$ candidates selected with all the requirements except for the MVA, and BCM when applicable, cut are fitted to

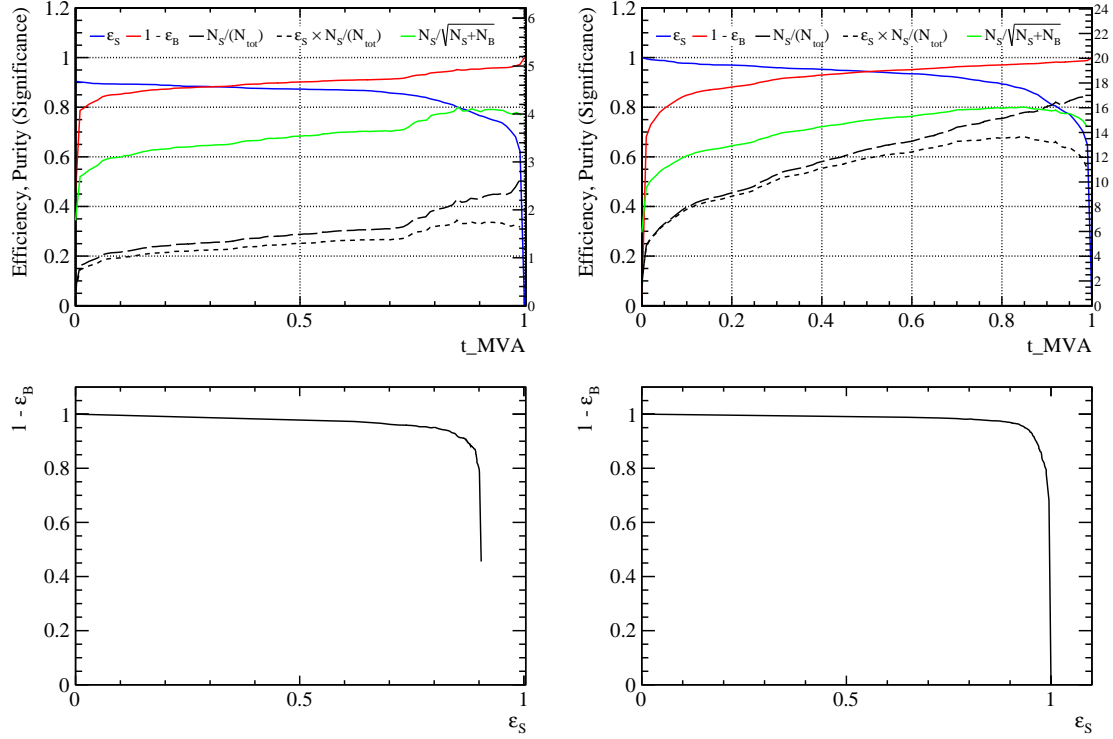


Figure 5.16: (top) Dependence of figure-of-merit on the requirement on neural network output. (bottom) Signal efficiency versus background rejection. Plots correspond to the electron (left) and muons (right) samples.

determine the total yield. This number is then scaled by the ratio of the signal to $B^0 \rightarrow K^{*0}(J/\psi \rightarrow \ell^+\ell^-)$ branching fractions and the efficiency ratio as a function of the cut

$$N_S = N_{J/\psi(\ell\ell)} \cdot \frac{\mathcal{B}(\text{S})}{\mathcal{B}(B^0 \rightarrow K^{*0}(J/\psi \rightarrow \ell^+\ell^-))} \cdot \frac{\epsilon_S}{\epsilon_{J/\psi(\ell\ell)}}.$$

2278 The number of background events is also derived from data by fitting the back-
2279 ground in the lower- and upper-mass sidebands with an exponential function, and
2280 extrapolating the residual yield in the signal region (Fig. 5.14). Because the back-
2281 ground shape changes as a function of the requirement that is being optimised, the
2282 sidebands are refitted for each considered cut value.

2283 The cut optimisation is performed in a signal mass window of ± 100 MeV/ c^2 around
2284 the nominal B^0 mass for muons, and between 5000 and 5400 MeV/ c^2 for electrons.
2285 The average result of the k-fold optimisations is taken as the nominal requirement.
2286 The variation of the signal and background efficiency, signal purity and figure-of-

2287 merit as a function of the neural-network output requirement for the central- q^2 is
2288 shown in Fig. 5.16 together with curves of the background rejection as a function of
2289 the signal efficiency. After full selection about $\sim 3\%$ of events still contain multiple
2290 candidates which are removed at random keeping only a single candidate per event.

2291 **5.7 Selection summary**

2292 Table 5.6 summarises the requirements applied for each cut after stripping.

Table 5.6: Summary of the selection requirements. The last column indicates to which q^2 intervals the requirement is applied.

Type		Requirement	q^2
Quality	All tracks	$\chi^2/\text{ndf} < 3$	all
		$\text{GhostProb} < 0.4$	all
ID	K^{*0}	$ m(K\pi) - m_{K^{*0}}^{\text{PDG}} < 100 \text{ MeV}/c^2$	all
PID	K	$\text{ProbNNk} \cdot (1 - \text{ProbNNp}) > 0.05$	all
	π	$\text{ProbNNpi} \cdot (1 - \text{ProbNNk}) \cdot (1 - \text{ProbNNp}) > 0.1$	all
	μ	$\text{ProbNNmu} > 0.2$	all mm
	e	$\text{ProbNNe} > 0.2$	all e^+e^-
BKG	Swap	$ m((h \rightarrow \mu)\mu) - m_{J/\psi,(\psi(2S))}^{\text{PDG}} > 60 \text{ MeV}/c^2$	all
	$B^+ \rightarrow K^+\ell^+\ell^-$	$\max(m(K\ell\ell), m((\pi \rightarrow K)\ell\ell)) < 5.1 \text{ GeV}/c^2$	all
	$B_s^0 \rightarrow \phi\ell^+\ell^-$	$m(K(\pi \rightarrow K)) > 1040 \text{ MeV}/c^2$	all
	$B^0 \rightarrow D^-e^+\nu$	$ \cos \theta_\ell < 0.8$	except ee high-
	$B^0 \rightarrow K^{*0}\gamma$	$\sigma_z(e^+e^-) < 30 \text{ mm}$	except $\gamma(ee)$
	Comb	$\text{NNout} > 0.68$	$\mu\mu$ low-
		$\text{NNout} > 0.64$	ee low-
		$\text{NNout} > 0.85$	$\mu\mu$ central-
		$\text{NNout} > 0.97$	ee central-
		$\text{NNout} > 0.40$	$\mu\mu$ high-
		$\text{NNout} > 0.93$	ee high-
		$\text{NNout} > 0.06$	$J/\psi(\mu\mu)$
		$\text{NNout} > 0.20$	$J/\psi(ee)$
		$\text{NNout} > 0.16$	$\gamma(ee)$
		$\text{NNout} > 0.68$	$\psi(2S)(ee)$
	Part-reco	$m(K\pi\ell\ell)_{J/\psi} > 5150 \text{ MeV}/c^2$	$J/\psi(ee)$
Comb, part-reco		$m_{\text{BCM}} > 4680 + 31 \cdot \log(\chi_{\text{FD}}^2)$	ee low-
		$m_{\text{BCM}} > 4437 + 64 \cdot \log(\chi_{\text{FD}}^2)$	ee central-
		$m_{\text{BCM}} > 3380 + 140 \cdot \log(\chi_{\text{FD}}^2)$	$\gamma(ee)$

2293 5.8 Mass fits

2294 The signal yields are extracted using a simultaneous unbinned maximum likelihood fit to the 4-body invariant mass, $m(K\pi\ell\ell)$, of the rare and normalisation
 2295 samples. The simultaneous fit allows to share parameters e.g. those describing
 2296 data-simulation differences. The yields of the rare channels are parameterised as a
 2297 function of the corresponding J/ψ yields as
 2298

$$N_{\ell\ell}(r_{\ell\ell}, N_{J/\psi}) = N_{J/\psi} \cdot \varepsilon^{\text{rel}} \cdot r_{\ell\ell}, \quad (5.10)$$

2299 where ε^{rel} is the relative efficiency between the rare and resonant channels (given
 2300 in Tab. 5.10). Consequently, $r_{\ell\ell}$ corresponds to the efficiency corrected ratio of the
 2301 raw rare and resonant yields:

$$R_{\ell\ell} = \frac{N_{\ell\ell}/\varepsilon^{\ell\ell}}{N_{J/\psi}/\varepsilon^{J/\psi(\ell\ell)}}. \quad (5.11)$$

2302 The two ratios, R_{ee} and $R_{\mu\mu}$, are then used to determine the $R_{K^{*0}}$ quantity, as
 2303 described in Sec. 5.11. The following subsections contain a description of the line
 2304 shapes used to model the signal and background components in each sample.

2305 5.8.1 Muon channels

2306 For the rare and resonant $\mu\mu$ channels the fitted variable is the $m(K\pi\mu\mu)$ invariant
 2307 mass coming from a kinematic fit where all vertices are required to point to
 2308 their mother particle. In the resonant case it is beneficial to also constrain the the
 2309 dimuon mass to the known J/ψ mass; in this case the invariant mass is referred to
 2310 as $m(K\pi\mu\mu)_{J/\psi}$. The effect of the kinematical constraint is to improve the mass
 2311 resolution by roughly a factor of 2, which results in a more stable fit. Furthermore,
 2312 mis-reconstructed background candidates are pushed away from the B^0 peak, which
 2313 allows to use a wider mass window to better constrain the combinatorial background
 2314 slope. The mass spectrum is fitted in the range 5150–5800 MeV/ c^2 with the lower

2315 limit chosen to totally exclude partially reconstructed background. As it is not
2316 needed to model partially reconstructed backgrounds in the fit this also eliminates
2317 the systematic uncertainties associated with the knowledge of their shape.

2318 5.8.1.1 $B^0 \rightarrow K^{*0}(J/\psi \rightarrow \mu^+\mu^-)$ PDF

The signal PDF adopted to describe the reconstructed $m(K\pi\mu\mu)$ invariant mass of $B^0 \rightarrow K^{*0}(J/\psi \rightarrow \mu^+\mu^-)$ candidates is the sum of a Double Crystal Ball [104] (DCB) function with opposite-side tails and a Gaussian function with a common mean, μ :

$$\mathcal{P}_{\text{sig}}(m|\vec{\lambda}) = f_{\text{CB1}} \cdot \mathcal{P}_{\text{CB}}(m|\mu, \sigma_1, \alpha_1, n_1) + f_{\text{CB2}} \cdot \mathcal{P}_{\text{CB}}(m|\mu, \sigma_2, \alpha_2, n_2) + (1 - f_{\text{CB1}} - f_{\text{CB2}}) \cdot \mathcal{P}_{\text{Gauss}}(m|\mu, \sigma_3),$$

2319 where f_{CB_i} is the relative fraction of candidates falling in the i^{th} Crystal Ball func-
2320 tion, σ_i is the width, α_i and n_i are the parameters controlling the power law tail of
2321 each CB, and σ_3 is the width of the Gaussian function.

2322 As a first step, the parameters of the signal PDF are extracted by fitting the
2323 $m(K\pi\mu\mu)$ distribution on $B^0 \rightarrow K^{*0}(J/\psi \rightarrow \mu^+\mu^-)$ simulation and fixed for the
2324 fit to the data. Figure E.1 shows the fitted simulated distribution for the normal-
2325 isation channel, while fits or the rare channel in the three q^2 bins are reported in
2326 Appendix E. In order to account for possible discrepancies in the invariant mass
2327 distribution between data and simulation, the mass is allowed to shift, $\mu \rightarrow \mu + m'$,
2328 and the widths are allowed to scale, $\sigma_i \rightarrow c \cdot \sigma_i$, where the scale factor c is common
2329 between the three σ s.

In summary, the signal PDF for the $J/\psi(\mu\mu)$ channel fit on data is defined as

$$\mathcal{P}_{J/\psi(\mu\mu)}(m|m', c) = f_{\text{CB1}} \cdot \mathcal{P}_{\text{CB}}(m|m', c) + f_{\text{CB2}} \cdot \mathcal{P}_{\text{CB}}(m|m', c) + (1 - f_{\text{CB1}} - f_{\text{CB2}}) \cdot \mathcal{P}_{\text{Gauss}}(m|m', c).$$

2330 where the only free parameters are the mass shift, m' and the width scale factor, c .

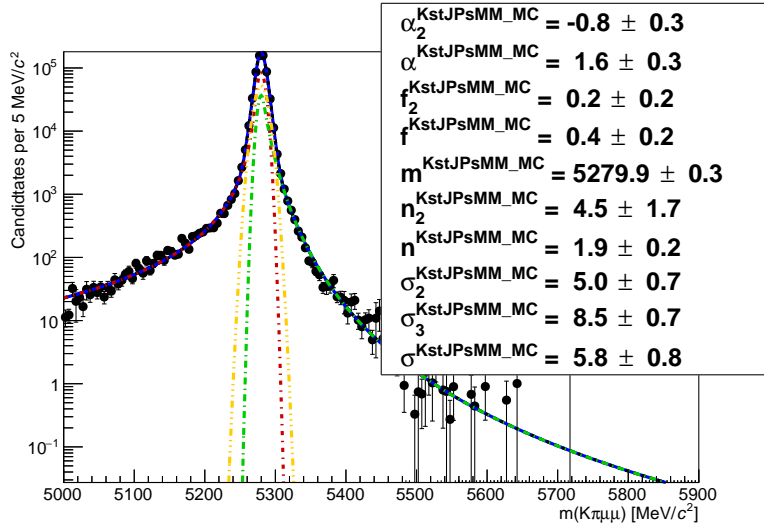


Figure 5.17: Fitted $m(K\pi\mu\mu)$ mass spectrum for $K^{*0}J/\psi$ simulated events.

2331 The following backgrounds are considered:

- 2332 • *Combinatorial*: modelled with an exponential function;
- 2333 • $\Lambda_b^0 \rightarrow pK(J/\psi \rightarrow \mu^+\mu^-)$: described using simulated events to which the
2334 full selection selection and weights for the pK Dalitz plot are applied; this
2335 distribution has a broad shape under the signal peak and is smoothed using
2336 the RooKeysPdf class of the ROOFIT [121] package;
- 2337 • $B_s^0 \rightarrow K^{*0}(J/\psi \rightarrow \mu^+\mu^-)$: described using the same PDF adopted for the
2338 signal, but a different central value, μ , which is set at the B_s^0 nominal mass.
2339 The same shift m' is used as for the signal.

2340 5.8.1.2 $B^0 \rightarrow K^{*0}\mu^+\mu^-$ PDF

The signal PDF adopted to describe the reconstructed 4-body invariant mass of the $B^0 \rightarrow K^{*0}\mu^+\mu^-$ candidates is a DCB function with opposite-side tails with a common mean, μ . The parameters of the PDF are fixed to values obtained by fitting simulated candidates, separately in each q^2 interval. As for the charmonium channel, the mass is allowed to shift and the widths are allowed to scale with a

common factor:

$$\mathcal{P}_{\text{mm},q^2}(m|m'_{q^2}, c_{q^2}) = f_{\text{core},q^2} \cdot \mathcal{P}_{\text{CB}}(m|m'_{q^2}, c_{q^2}) + (1 - f_{\text{core},q^2}) \cdot \mathcal{P}_{\text{CB}}(m|m'_{q^2}, c_{q^2}).$$

where f_{core,q^2} is the relative fraction of candidates falling in the first Crystal Ball function, m'_{q^2} is the mass shift and c_{q^2} is the width scale. The subscript “ q^2 ” indicates that independent parameters are used for each q^2 interval. The background is described by an exponential function in all the three q^2 bins.

5.8.1.3 Summary

In summary, the free parameters of the simultaneous fit to the $J/\psi(\mu\mu)$ and mm candidates are the signal and background yields, the combinatorial background slopes, the mass shifts and the width scales. Figure 5.19 shows the results of the fit to the rare and resonant $\mu\mu$ candidates. Values of the fitted parameters are reported on the plots.

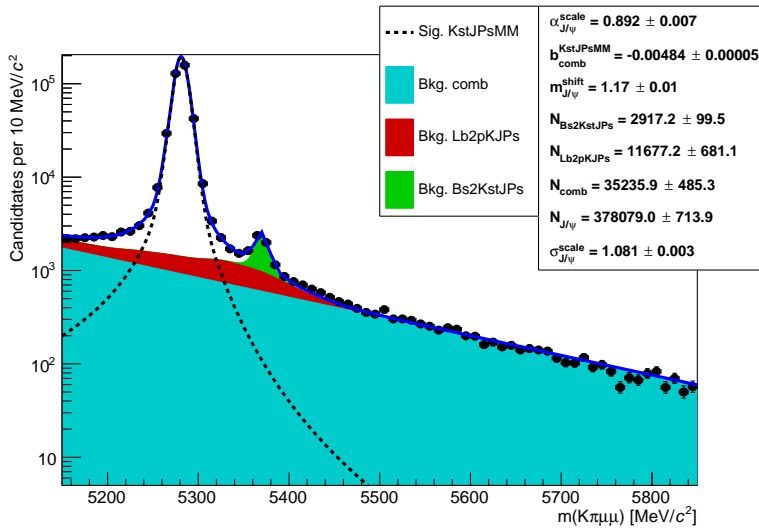


Figure 5.18: Fitted $m(K\pi\mu\mu)_{J/\psi}$ invariant mass distribution for $J/\psi(\mu\mu)$ candidates in logarithmic scale. Dashed black lines represent the signal PDFs and filled shapes the background components.

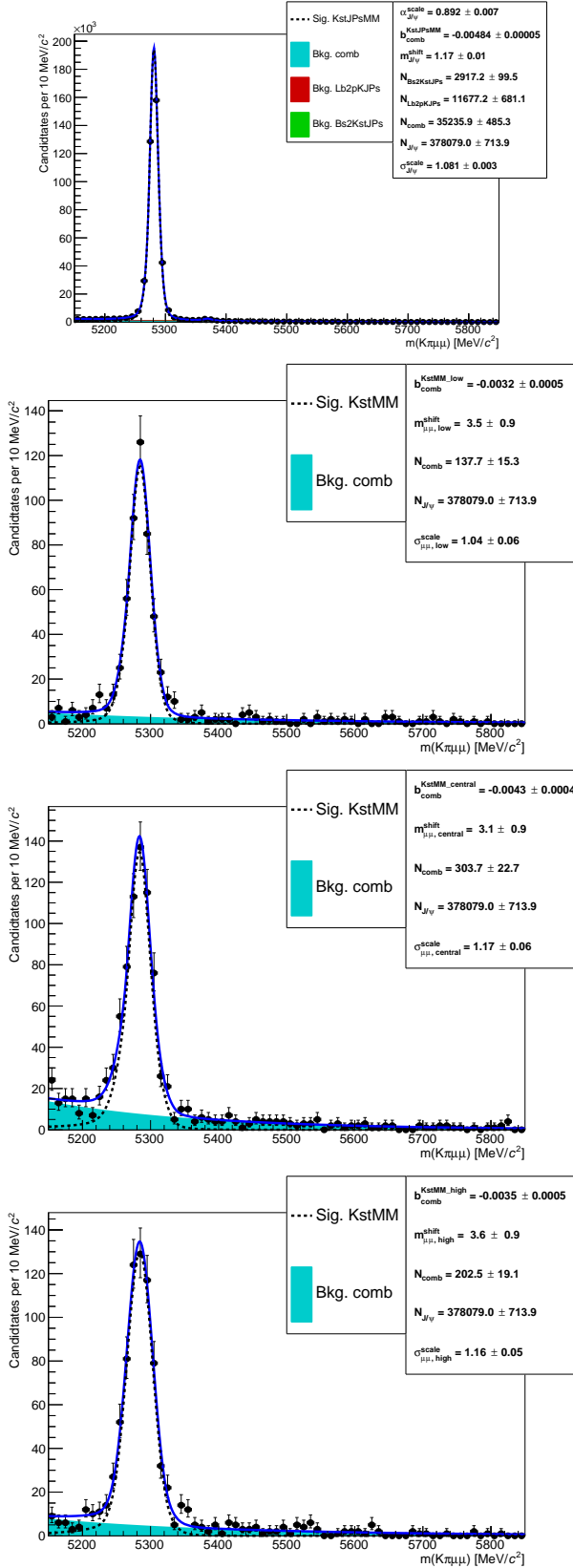


Figure 5.19: From top to bottom fitted $m(K\pi\mu\mu)_{J/\psi}$ invariant mass distributions for $J/\psi(\mu\mu)$ candidates and fitted $m(K\pi\mu\mu)$ distributions for rare candidates in the low-, central- and high- q^2 intervals. Dashed black lines represent the signal PDFs and filled shapes the background components.

²³⁵¹ 5.8.2 Electron channels

²³⁵² Also in the electron case the fitted variable is the 4-body invariant mass coming
²³⁵³ from a kinematic fit. In general, this does not include constraints to intermediate
²³⁵⁴ resonances, unless specified. When constraints to intermediate resonances are ap-
²³⁵⁵ plied the invariant mass is referred to as $m(K\pi ee)_R$, where $R = J/\psi$ or $\psi(2S)$.
²³⁵⁶ The reconstructed invariant mass of the B^0 depends on which L0 line triggered
²³⁵⁷ the event. For this reason, a simultaneous fit to the 4-body invariant mass of the
²³⁵⁸ $B^0 \rightarrow K^{*0}(J/\psi \rightarrow e^+e^-)$ and $B^0 \rightarrow K^{*0}e^+e^-$ channels in the three trigger categories
²³⁵⁹ is performed. In each trigger category, the $J/\psi(ee)$ and ee yields are extracted from
²³⁶⁰ the following signal channel categories:

- ²³⁶¹ • $B^0 \rightarrow K^{*0}(J/\psi \rightarrow e^+e^-)$, with a J/ψ mass constraint, $m(K\pi ee)_{J/\psi}$;
- ²³⁶² • $B^0 \rightarrow K^{*0}e^+e^-$ in the three q^2 intervals.

²³⁶³ Extra control channels are fit simultaneously:

- ²³⁶⁴ • $B^0 \rightarrow K^{*0}(\gamma \rightarrow e^+e^-)$ to constrain the yield of partially-reconstructed back-
²³⁶⁵ ground in the low- q^2 and the leakage of $B^0 \rightarrow K^{*0}\gamma$ into the low- q^2 ;
- ²³⁶⁶ • $B^0 \rightarrow K^{*0}(J/\psi \rightarrow e^+e^-)$, without the J/ψ mass constraint, to constrain
²³⁶⁷ the leakage into the central- q^2 and the parameters that model residual data-
²³⁶⁸ simulation discrepancies;
- ²³⁶⁹ • $B^0 \rightarrow K^{*0}(\psi(2S) \rightarrow e^+e^-)$, with a $\psi(2S)$ mass constraint, $m(K\pi ee)_{\psi}$, to
²³⁷⁰ constrain the leakage to lower and higher q^2 values.

²³⁷¹ When fitting the variable without a J/ψ mass constraint it is important to fit a
²³⁷² wider mass range to better constrain the parameters modelling the radiative tail
²³⁷³ and the backgrounds; a mass window [4500,6200] MeV/ c^2 is used. The lower limit
²³⁷⁴ is given by the point in which the q^2 cut (at 6 GeV $^2/c^4$ to separate the rare and
²³⁷⁵ resonant channels) starts to affect the 4-body invariant mass distribution.

2376 The invariant mass distributions are different depending on the trigger category
2377 and also on the number of bremsstrahlung photons recovered. Therefore, our sam-
2378 ples are divided in three trigger categories, as described in Sec. 5.6.1, and three
2379 bremsstrahlung categories defined as:

- 2380 • 0γ : candidates with no photon emitted
- 2381 • 1γ : candidates with one photon by either of the electrons
- 2382 • 2γ : candidates with one photon emitted by each electron

2383 All samples are fitted simultaneously, which allows a better use of the available
2384 statistics as the simultaneous fit gathers information from the three categories at
2385 the same time. Furthermore, using this method the results for the three categories
2386 are naturally combined in a single r_{ee} ratio. The PDFs used to fit the invariant mass
2387 distributions are described in the next subsections.

2388 5.8.2.1 Signal PDFs for the electron channels

2389 As for the muon channels, simulated candidates are fitted first to constrain the shape
2390 parameters for the subsequent fit to data. The signal PDFs are built using the
2391 following method:

- 2392 • Simulated $B^0 \rightarrow K^{*0} J/\psi (ee)$ and $B^0 \rightarrow K^{*0} ee$ events are divided in each
2393 trigger and bremsstrahlung category and an independent fit is performed to
2394 each sample. A different fit is also performed for the central, J/ψ and high q^2
2395 intervals. In the case of the high- q^2 interval it is particularly important to keep
2396 signal tail parameters independent from J/ψ channel ones because, as can be
2397 seen in Fig. 5.20, the invariant mass distributions are significantly different for
2398 the two intervals.
- 2399 • For each trigger category a PDF is built as the sum of the three PDFs of the

Table 5.7: Percentages of events with 0, 1 and 2 emitted photons in the three trigger categories, obtained from simulated events.

Trigger	0 γ (%)	1 γ (%)	2 γ (%)
$B^0 \rightarrow K^{*0}e^+e^-$ low- q^2			
L0E	34.2	56.0	9.8
L0H	27.8	58.1	14.2
L0I	31.7	56.9	11.4
$B^0 \rightarrow K^{*0}e^+e^-$ central- q^2			
L0E	29.2	50.0	20.8
L0H	23.6	50.5	26.0
L0I	28.5	49.9	21.6
$B^0 \rightarrow K^{*0}e^+e^-$ high- q^2			
L0E	20.6	51.2	28.2
L0I	10.0	53.8	36.2
$B^0 \rightarrow K^{*0}(\gamma \rightarrow e^+e^-)$			
L0E	40.4	59.6	–
L0H	32.2	67.8	–
L0I	39.3	60.7	–
$B^0 \rightarrow K^{*0}(J/\psi \rightarrow e^+e^-)$			
L0E	29.0	50.1	20.8
L0H	18.9	51.3	29.8
L0I	26.9	51.7	21.4
$B^0 \rightarrow K^{*0}(\psi(2S) \rightarrow e^+e^-)$			
L0E	27.2	51.3	21.5
L0H	17.4	51.5	31.2
L0I	22.0	55.0	23.0

2400 bremsstrahlung categories:

$$\mathcal{P}^{L0}(m) = f_{0\gamma}^{L0}\mathcal{P}_{0\gamma}^{L0}(m) + f_{1\gamma}^{L0}\mathcal{P}_{1\gamma}^{L0}(m) + (1 - f_{0\gamma}^{L0} - f_{1\gamma}^{L0})\mathcal{P}_{2\gamma}^{L0}(m), \quad (5.12)$$

2401 where the $\mathcal{P}(m)_{n\gamma}^{L0}$ functions are the chosen PDFs for the trigger and bremsstrahlung
 2402 categories and the $f_{n\gamma}^{L0}$ parameters are the relative fractions of events falling
 2403 in each category.

- 2404 • Most parameters are fixed (details later) and the combined PDF, $P(m)$, is
 2405 used to fit real data divided only in trigger categories.

2406 The distribution of the $m(K\pi ee)$ mass in the 0γ category is characterised by a
 2407 sharp tail on the righthand side and is described with a Crystal Ball function (CB),

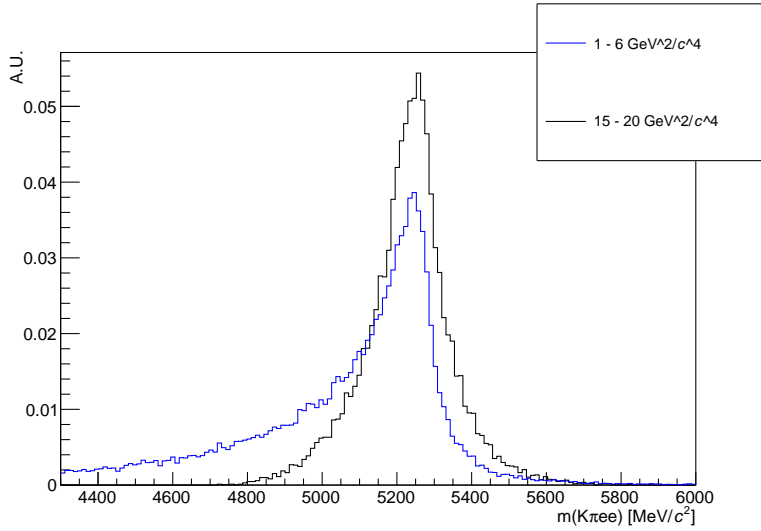


Figure 5.20: Simulated invariant mass of the $K\pi ee$ system in the $1.1 < q^2 < 6$ and $q^2 > 15 \text{ GeV}^2/c^4$ intervals.

while the 1γ and 2γ categories are modelled using the sum of a Crystal Ball and a Gaussian function (CBG) with independent parameters. In all the bremsstrahlung categories the distribution of the 4-body invariant mass with a mass with the J/ψ mass constraint is modelled using the sum of a DCB and a Gaussian functions as done in the muon fit. To account for possible data-simulation discrepancies, the mass (widths) of each trigger PDF is allowed to shift (scale), similarly to the muon channels. However, due to the larger background contamination these parameters are shared between the rare and the $B^0 \rightarrow K^{*0}(J/\psi \rightarrow e^+e^-)$ control sample (no J/ψ mass constraint). The tail parameters are similar between the $J/\psi(ee)$ and the central- q^2 but this is not the case at high- q^2 , as can be seen in Fig. 5.20, due to the migration of candidates in the tail to lower reconstructed q^2 . For this reason the initial parameters for each candidate type are obtained fitting a simulated sample of the same candidate type.

The $f_{n\gamma}^{L0}$ fractions have been shown to be in good agreement between resonant data and simulation and therefore they are fixed to the simulated values, separately for the normalisation channel and each q^2 interval. Table 5.7 lists the percentages of candidates with 0, 1 and 2 recovered photons for each trigger category.

²⁴²⁵ In summary the signal PDF for the fit on data is defined as:

$$\begin{aligned}\mathcal{P}_{sig}(m; c, m')^{\text{trg}} &= f_{0\gamma}^{\text{L0}} \mathcal{P}_{0\gamma}^{\text{L0}}(m; c, m') \\ &+ f_{1\gamma}^{\text{L0}} \mathcal{P}_{1\gamma}^{\text{L0}}(m; c, m') + (1 - f_{0\gamma}^{\text{L0}} - f_{1\gamma}^{\text{L0}}) \mathcal{P}_{2\gamma}^{\text{L0}}(m; c, m')\end{aligned}\quad (5.13)$$

²⁴²⁶ where the free parameters are: c , the scaling factor for the widths, and m' , the mass
²⁴²⁷ shift.

²⁴²⁸ 5.8.2.2 Background PDFs for the electron channels

²⁴²⁹ This section reports the background components considered for each fitted sample.

²⁴³⁰ $B^0 \rightarrow K^{*0} e^+ e^-$ low- q^2

²⁴³¹ • *Combinatorial*: described using an exponential function; the yield and slope
²⁴³² parameters are free to vary in the fit;

²⁴³³ • *Partially-reconstructed* (hadronic): the shape is obtained from a $K_1^+(1270)$
simulated samples smoothed with a `RooKeysPdf`. Simulated distributions are
shown in Fig. 5.21. The fraction of partially-reconstructed candidates with
respect to signal ones is expected to be very similar to that in $B^0 \rightarrow K^{*0}(\gamma \rightarrow$
 $e^+ e^-)$ and therefore the normalisation is fixed as:

$$N_{e^+ e^-, \text{low}}^{\text{part-reco}} = N_{e^+ e^-} \cdot \frac{N_{\gamma(ee)}^{\text{part-reco}}}{N_{\gamma(ee)}},$$

²⁴³⁴ where $N_{\gamma(ee)}^{\text{part-reco(hadronic)}} / N_{\gamma(ee)}$ is the fraction of the hadronic partially-reconstructed
background relative to the signal yield in the $B^0 \rightarrow K^{*0}(\gamma \rightarrow e^+ e^-)$ channel;

²⁴³⁵ • $B^0 \rightarrow K^{*0} \gamma$ leakage: the leakage from the $B^0 \rightarrow K^{*0}(\gamma \rightarrow e^+ e^-)$ decay
in the low- q^2 region is modelled using a simulated candidates that pass the
low- q^2 requirements: the distribution is smoothed using a `RooKeysPdf`; the

normalisation is fixed to the $B^0 \rightarrow K^{*0}(\gamma \rightarrow e^+e^-)$ yield, $N_{\gamma(ee)}$ as:

$$N_{e^+e^-, \text{low}}^{\text{leak}} = N_{\gamma(ee)} \cdot f_{\gamma(ee)}^{\text{leak, MC}},$$

where $f_{\gamma(ee)}^{\text{leak, MC}}$ is the fraction of $\gamma(ee)$ simulated candidates which leaks in the low- q^2 region.

$B^0 \rightarrow K^{*0}e^+e^-$ central- q^2

- *Combinatorial*: described using an exponential function; the yield and slope parameters are free to vary in the fit.
- *Partially-reconstructed* (hadronic): modelled using simulation as described for the low- q^2 but in this case the normalisation is left free to vary.
- $B^0 \rightarrow K^{*0}J/\psi$ leakage: the leakage from the J/ψ radiative tail into the central- q^2 interval is modelled by selecting simulated $B^0 \rightarrow K^{*0}(J/\psi \rightarrow e^+e^-)$ candidates which pass the central- q^2 requirements and smoothing the distributions with kernel estimation method. The normalisation is fixed to the $B_s^0 \rightarrow K^{*0}(J/\psi \rightarrow e^+e^-)$ yield, $N_{J/\psi ee}$, as:

$$N_{e^+e^-, \text{central}}^{\text{leak}} = N_{J/\psi ee} \cdot f_{J/\psi ee}^{\text{leak, MC}},$$

where $f_{J/\psi ee}^{\text{leak, MC}}$ is the fraction of $B^0 \rightarrow K^{*0}(J/\psi \rightarrow e^+e^-)$ simulated events reconstructed in the central- q^2 interval.

$B^0 \rightarrow K^{*0}e^+e^-$ high- q^2

- *Combinatorial*: modelled using a shape obtained by reversing the NN output cut on data, which has the effect of selecting background candidates instead of signal ones. Figure 5.22 shows the invariant mass distributions for different anti-cuts on the electron and muon samples at high- q^2 . The shapes are very similar between the two samples and as a function of the cut value. In order

2450 to have a larger statistics, the shape is taken from the muon sample with a
 2451 tight NN output anti-cut at 0.1 and smoothed with a `RooKeysPdf`;

- 2452 • *Partially-reconstructed* (hadronic): modelled using simulation as described for
 2453 the previous intervals; the normalisation is left free to vary.
- $B^0 \rightarrow K^{*0}\psi(2S)$ leakage: the leakage from the $\psi(2S)$ radiative tail is modelled
 using simulated $B^0 \rightarrow K^{*0}(\psi(2S) \rightarrow e^+e^-)$ events in the high- q^2 region. The
 normalisation is fixed to the $B^0 \rightarrow K^{*0}(\psi(2S) \rightarrow e^+e^-)$ yield, $N_{\psi(2S)(ee)}$ as:

$$N_{e^+e^-, \text{high}}^{\text{leak}} = N_{\psi(2S)(ee)} \cdot f_{\psi(2S)(ee)}^{\text{leak, MC}},$$

2454 where $f_{\psi(2S)(ee)}^{\text{leak, MC}}$ is the fraction of $B^0 \rightarrow K^{*0}(\psi(2S) \rightarrow e^+e^-)$ simulated candi-
 2455 dates leaking in the high- q^2 interval.

2456 $B^0 \rightarrow K^{*0}\gamma$

- 2457 • *Combinatorial*: described using an exponential function; the yield and slope
 2458 parameters are free to vary in the fit;
- *Partially-reconstructed* (hadronic): modelled using simulation as described for
 the previous intervals; the normalisation is left free to vary and used to con-
 strain the fraction of partially-reconstructed candidates in the low- q^2 interval.
- $B^0 \rightarrow K^{*0}e^+e^-$ leakage: as the $K^{*0}\gamma$ was added to the low- q^2 also the low- q^2
 leakage is added to $K^*\gamma$. The yield is constrained to the N_{ee}^{low} yield.

2464 $B^0 \rightarrow K^{*0}J/\psi$ and $B^0 \rightarrow K^{*0}\psi(2S)$

2465 The following backgrounds are considered for the fits to the invariant mass of $B^0 \rightarrow$
 2466 $K^{*0}(J/\psi \rightarrow e^+e^-)$ candidates:

- 2467 • *Combinatorial*: described using an exponential function. The yield and slope
 2468 parameters are free to vary in the fit;

- 2469 • $\Lambda_b^0 \rightarrow pK(J/\psi \rightarrow e^+e^-)$: described using simulated events to which the full
 2470 selection is applied. This distribution has a broad shape under the signal peak
 2471 and is smoothed using a `RooKeysPdf`. The normalisation is constrained to
 2472 the $\Lambda_b^0 \rightarrow pK(J/\psi \rightarrow \mu^+\mu^-)$ yield returned by the $\mu\mu$ fit after correcting for
 2473 efficiency differences between final states with muons and electrons.
- 2474 • $B_s^0 \rightarrow K^{*0}(J/\psi \rightarrow e^+e^-)$: described using the same PDF adopted for the signal,
 2475 but a different central value, m_0 , which is set at the B_s^0 nominal mass. The
 2476 normalisation is constrained to the $B^0 \rightarrow K^{*0}(J/\psi \rightarrow \mu^+\mu^-)$ yield returned
 2477 by the $\mu\mu$ fit after correcting for efficiency differences between final states with
 2478 muons and electrons;

2479 The J/ψ mass constraint has the effect of pushing the partially-reconstructed back-
 2480 ground away from the peak outside the fit window. The J/ψ control sample is se-
 2481 lected using the requirement that the 4-body mass constrained using `DecaTreeFitter`
 2482 is above 5150 MeV/ c , which explicitly removes the partially-reconstructed back-
 2483 ground; this cut does not produce significant distortion to the unconstrained in-
 2484 variant mass distribution in the considered window. For these reasons this back-
 2485 ground does not need to be modelled in either of these cases. For the fit to
 2486 $B^0 \rightarrow K^{*0}(\psi(2S) \rightarrow e^+e^-)$, which includes a $\psi(2S)$ mass constraint, only the com-
 2487 binatorial background is considered and described using an exponential function.

2488

2489 5.8.2.3 Summary of the fit to the electron samples

2490 In summary, the free parameters in the fit to data are:

- 2491 • the $B^0 \rightarrow K^{*0}(J/\psi \rightarrow e^+e^-)$, $B^0 \rightarrow K^{*0}(\psi(2S) \rightarrow e^+e^-)$ and $B^0 \rightarrow K^{*0}(\gamma \rightarrow$
 2492 $e^+e^-)$ yields in each trigger category;
- 2493 • the r_{ee} ratio common to all trigger categories; one for the low, one for the
 2494 central- and one for the high- q^2 region;

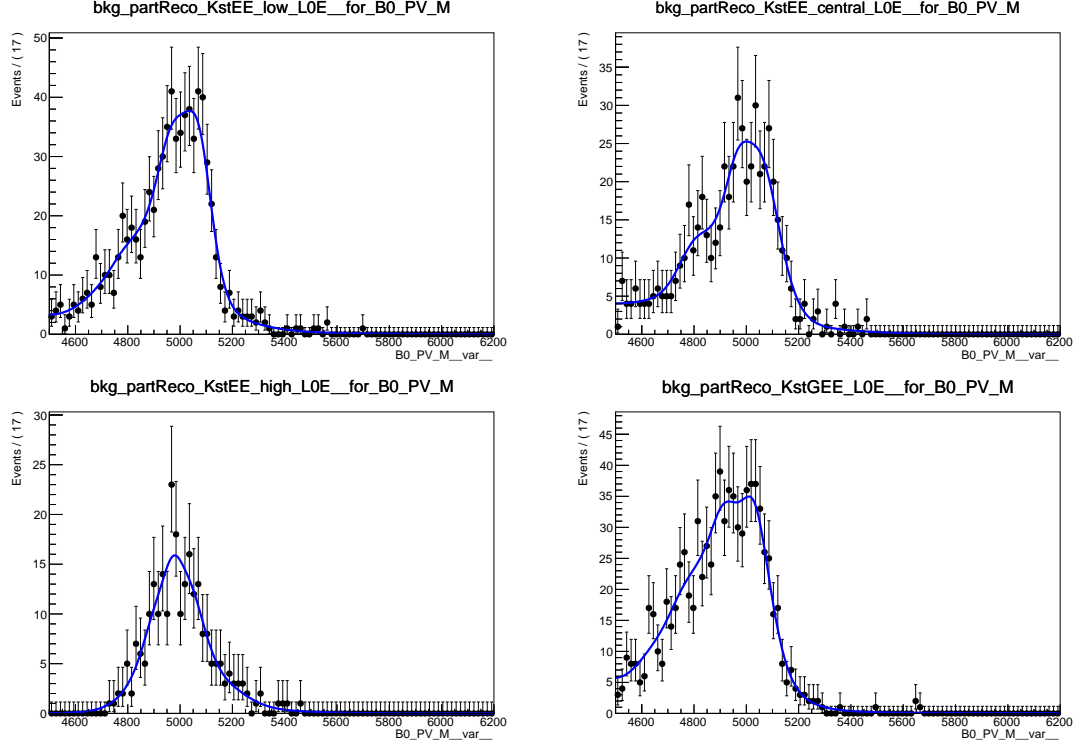


Figure 5.21: Distributions of the $m(K\pi ee)$ invariant mass of decays involving higher K^{*0} resonances for the (top left) low- (top right) central-, (bottom left) high- q^2 intervals and (bottom right) $B^0 \rightarrow K^{*0}(\gamma \rightarrow e^+e^-)$.

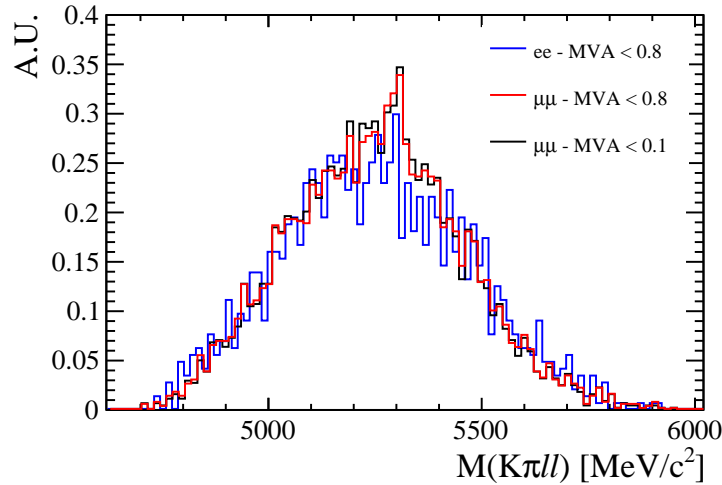


Figure 5.22: Distributions of the $m(K\pi\ell\ell)$ invariant mass for $B^0 \rightarrow K^{*0}\ell^+\ell^-$ candidates selected with a reversed cuts on the NN output.

- 2495 • one mass shift, m' , and one width scale factor, c , for the signal PDF common
 2496 between $B^0 \rightarrow K^{*0}(J/\psi \rightarrow e^+e^-)$ and $B^0 \rightarrow K^{*0}e^+e^-$, but different for the

2497 three trigger categories and for $B^0 \rightarrow K^{*0}(\psi(2S) \rightarrow e^+e^-)$ and $B^0 \rightarrow K^{*0}(\gamma \rightarrow$
2498 $e^+e^-)$;

- 2499 • the yield and slope, when applicable (e.g. no slope at high- q^2), of the combinatorial background in each trigger category and for each channel;
- 2500
- 2501 • the yield of the backgrounds when not fixed as described in the previous section.
- 2502

2503 Fits to simulated $B^0 \rightarrow K^{*0}(J/\psi \rightarrow e^+e^-)$ candidates are shown in Appendix E,
2504 while fits to real candidates are shown in Fig. 5.23 for the normalisation channel, in
2505 Fig. 5.24 for the rare channel and in Fig. 5.25 for the control channels. For simplicity
2506 the latter two figures show the sub of the three trigger categories, while the separate
2507 plots are reported in Appendix F, where fitted parameters are also reported on the
2508 plots. In the high- q^2 interval, above $15 \text{ GeV}^2/c^4$, the efficiency for the L0Hadron
2509 trigger becomes very low as the K^* has very low momentum. In this region only
2510 9 candidates are found spread in the interval $4500 < m(K\pi ee) < 6000 \text{ MeV}/c^2$.
2511 Therefore only L0E and L0I triggered events are fitted in this region.

2512 5.8.3 Event yields

2513 Table 5.8 reports raw yields obtained from the fits described in the previous subsec-
2514 tions. The values for the rare channels are not directly floating in the fits but, as
2515 described in Sec. 5.8, they are parameterised as a function of the number of resonant
2516 events found and the ratios R_{ee} and $R_{\mu\mu}$ between the resonant and rare branching
2517 fractions.

Table 5.8: Raw yields of events found fitting invariant mass distributions of the rare and resonant events.

Sample	1.1–6 GeV^2/c^4	15–20 GeV^2/c^4	J/ψ
$\mu\mu$	626 ± 30	605 ± 27	333113 ± 604
ee L0E	132 ± 17	137 ± 27	48601 ± 326
ee L0H	31.7 ± 4.2	—	4324 ± 94
ee L0I	49.6 ± 6.5	—	12791 ± 172

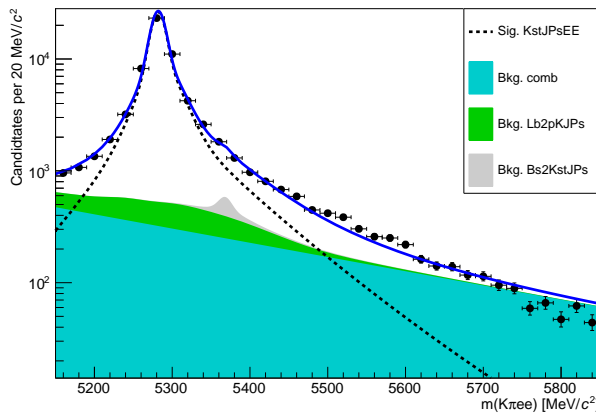


Figure 5.23: Fit to the mass constrained $m(K\pi ee)$ invariant mass of $B^0 \rightarrow K^{*0}(J/\psi \rightarrow e^+e^-)$ candidates. The dashed black line (shaded shapes) represents the signal (background) PDF.

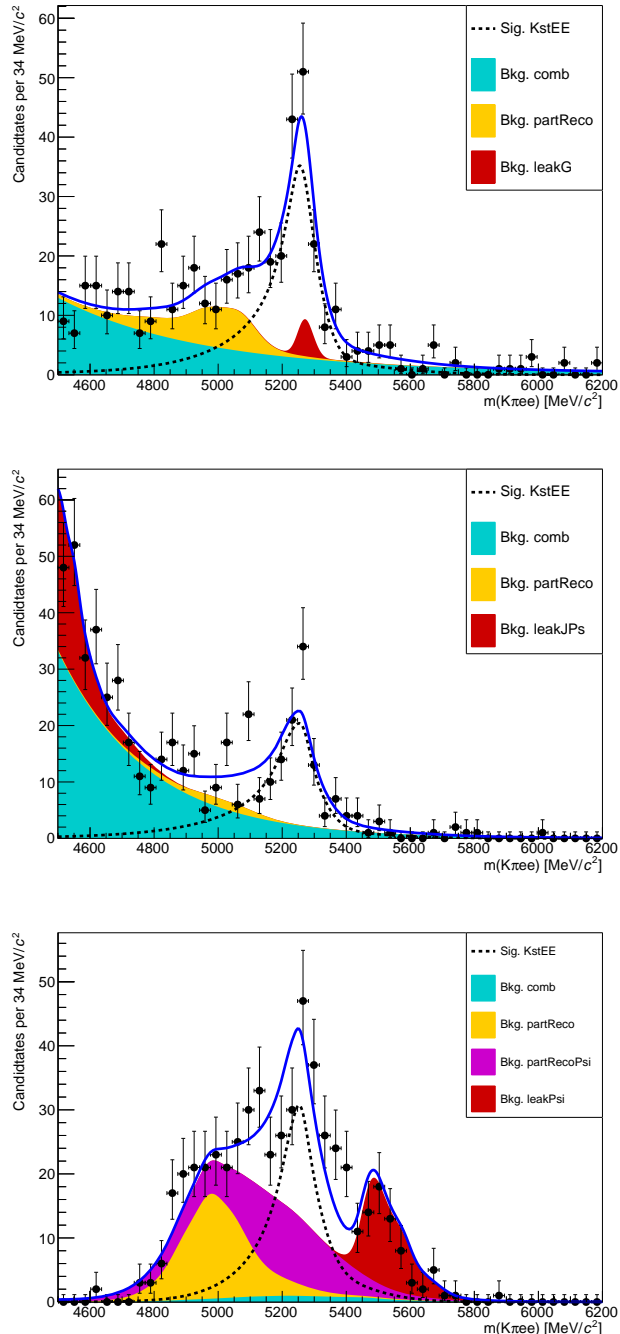


Figure 5.24: Fit to the $m(K\pi ee)$ invariant mass of $B^0 \rightarrow K^{*0} e^+ e^-$ candidates. From top to bottom for the low-, central- and high- q^2 intervals. The dashed black line (shaded shapes) represents the signal (background) PDF.

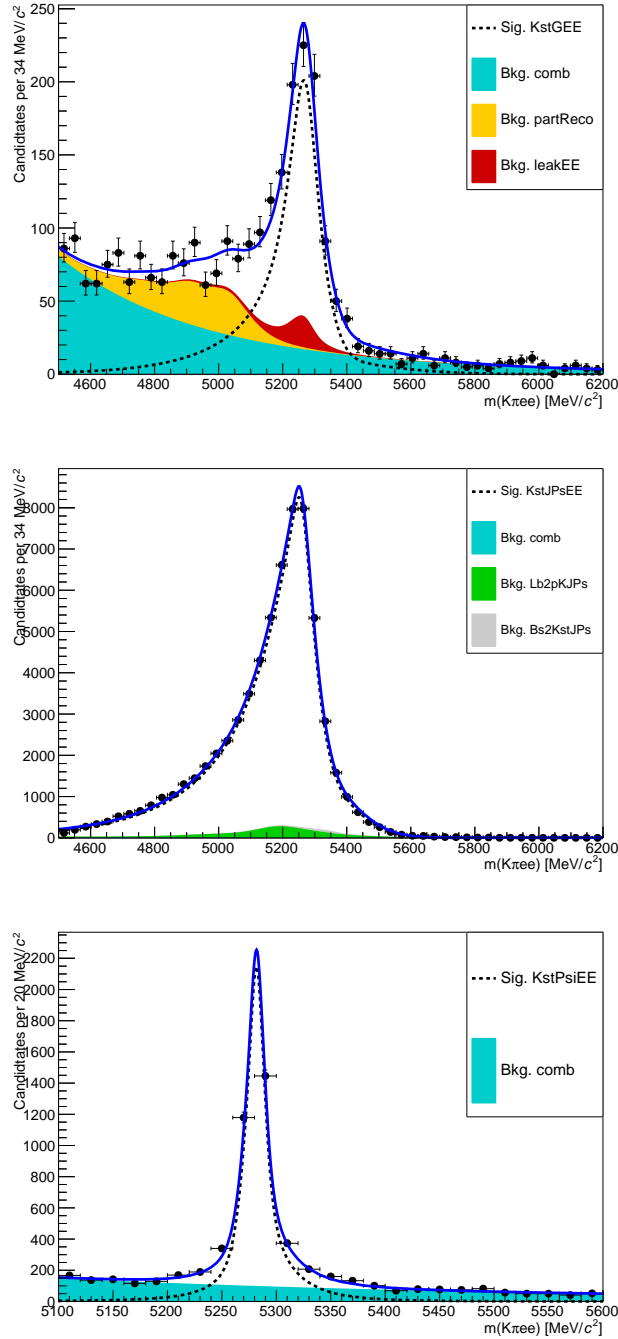


Figure 5.25: Fit to the $m(K\pi ee)$ invariant mass of control channel candidates. From top to bottom: invariant mass distribution without mass constraint of $B^0 \rightarrow K^{*0}(\gamma \rightarrow e^+e^-)$ and $B^0 \rightarrow K^{*0}(J/\psi \rightarrow e^+e^-)$ candidates and mass constrained mass of $B^0 \rightarrow K^{*0}(\psi(2S) \rightarrow e^+e^-)$ candidates. The dashed black line (shaded shapes) represents the signal (background) PDF.

2518 **5.9 Efficiency**

The efficiency for each of the decay channels is calculated according to the formula

$$\varepsilon^{tot} = \varepsilon^{\text{geom}} \cdot \varepsilon^{\text{reco|geom}} \cdot \varepsilon^{\text{PID|reco}} \cdot \varepsilon^{\text{trig|PID}} \cdot \varepsilon^{\text{MVA|trig}} \cdot \varepsilon^{\text{BCM|MVA}}$$

2519, where the first term is the efficiency to have final state particles in the LHCb
2520 detector acceptance; the second term ($\varepsilon^{\text{reco|geom}}$) carries information on reconstruc-
2521 tion and stripping efficiency; the third ($\varepsilon^{\text{PID|reco}}$) corresponds to the efficiency of
2522 the PID requirements; the fourth ($\varepsilon^{\text{trig|PID}}$) handles the trigger efficiency for those
2523 events which are selected by the pre-selection process; and, finally, the latter term
2524 deals with the efficiency of the neural network classifier. Reconstruction, trigger,
2525 MVA and BCM efficiencies are evaluated using simulated data samples with the
2526 trigger efficiency for $B^0 \rightarrow K^* J/\psi$ being cross-checked using the data-driven TIS-
2527 TOS method as described in Sec. 3.6.3. The PID efficiency is calculated with a
2528 data-driven method as described in Sec. 5.9.3.

2529 Absolute efficiencies for the muon and electron normalisation channel are reported in
2530 Tab. 5.9 and relative efficiencies between the rare and resonant channel, $\varepsilon(\ell\ell)/\varepsilon(J/\psi(\ell\ell))$,
2531 are listed in Tab. 5.10; these are the efficiencies which are used in the fit.

Table 5.9: Absolute efficiencies for the resonant ee and $\mu\mu$ channels.

ε	$\mu\mu$	ee		
		L0E	L0H	L0I
$\varepsilon^{\text{geom}}$	0.1598 ± 0.0005		0.1589 ± 0.0005	
$\varepsilon^{\text{reco geom}}$	0.0947 ± 0.0001		0.0603 ± 0.0001	
$\varepsilon^{\text{PID reco}}$	0.8148 ± 0.0000		0.8222 ± 0.0000	
$\varepsilon^{\text{trig PID}}$	0.7511 ± 0.0005	0.1939 ± 0.0005	0.0163 ± 0.0002	0.0707 ± 0.0003
$\varepsilon^{\text{MVA trig}}$	0.8944 ± 0.0004	0.8597 ± 0.0007	0.8983 ± 0.0006	0.8276 ± 0.0017
$\varepsilon^{\text{Total}}$	0.0083 ± 0.0000	0.0013 ± 0.0000	0.0001 ± 0.0000	0.0005 ± 0.0000

Table 5.10: Relative efficiencies, $\varepsilon^{rel} = \varepsilon^{\ell\ell}/\varepsilon^{J/\psi}$, for the ee and $\mu\mu$ channels in the central and high q^2 intervals.

ε	$\mu\mu$	ee		
		L0E	L0H	L0I
low-q^2				
ε^{geom}	1.0200 ± 0.0091		1.0429 ± 0.0084	
$\varepsilon^{reco geom}$	0.1309 ± 0.0010		0.1961 ± 0.0007	
$\varepsilon^{PID reco}$	0.9861 ± 0.0003		0.9718 ± 0.0001	
$\varepsilon^{trig PID}$	0.8103 ± 0.0048	0.6478 ± 0.0058	2.5556 ± 0.0455	1.2748 ± 0.0139
$\varepsilon^{MVA trig}$	0.9528 ± 0.0024	0.9568 ± 0.0014	0.9570 ± 0.0013	0.9463 ± 0.0030
$\varepsilon^{BCM MVA}$	–	0.9394 ± 0.0014	0.9492 ± 0.0013	0.9590 ± 0.0023
ε^{tot}	0.7810 ± 0.0168	0.5809 ± 0.0097	2.2685 ± 0.0514	1.1073 ± 0.0200
central-q^2				
ε^{geom}	1.0200 ± 0.0091		1.0429 ± 0.0084	
$\varepsilon^{reco geom}$	0.1891 ± 0.0012		0.1580 ± 0.0006	
$\varepsilon^{PID reco}$	0.9784 ± 0.0002		0.9672 ± 0.0001	
$\varepsilon^{trig PID}$	0.8925 ± 0.0038	0.7909 ± 0.0069	2.1344 ± 0.0439	1.1208 ± 0.0141
$\varepsilon^{MVA trig}$	0.9068 ± 0.0024	0.8397 ± 0.0024	0.8512 ± 0.0022	0.7946 ± 0.0054
$\varepsilon^{BCM MVA}$	–	0.8960 ± 0.0020	0.8978 ± 0.0020	0.9283 ± 0.0037
ε^{tot}	0.7171 ± 0.0124	0.8145 ± 0.0157	2.2235 ± 0.0595	1.0542 ± 0.0236
high-q^2				
ε^{geom}	1.0200 ± 0.0091		1.0429 ± 0.0084	
$\varepsilon^{reco geom}$	0.1172 ± 0.0009		0.0530 ± 0.0003	
$\varepsilon^{PID reco}$	1.0286 ± 0.0001		1.0113 ± 0.0002	
$\varepsilon^{trig PID}$	1.1122 ± 0.0038	1.5639 ± 0.0148	–	0.8090 ± 0.0195
$\varepsilon^{MVA trig}$	0.8986 ± 0.0027	0.8228 ± 0.0036	–	0.7201 ± 0.0115
ε^{tot}	0.7843 ± 0.0155	0.6063 ± 0.0131	–	0.2745 ± 0.0095

2532 5.9.1 Geometric efficiency

2533 In order to save disk space, simulated samples only contain decays with final daugh-
 2534 ters in the LHCb detector acceptance, which can therefore be reconstructed. This
 2535 corresponds to the requirement for each of the final particles to have polar angle θ
 2536 between 10 and 400 mrad. The efficiency of this cuts is obtained using a generator
 2537 level simulated sample.

2538 5.9.2 Reconstruction efficiency and bin migration

2539 The reconstruction efficiency is here defined as the efficiency to reconstruct each
 2540 decay channel given that its daughters are into the geometrical acceptance of the
 2541 detector. This includes both the probability that the final particles generate ob-
 2542 servable signatures and the efficiency of all the pre-selection requirements described
 2543 in Sec. 5.6, including those done to remove peaking backgrounds. The efficiency of
 2544 the PID cuts is kept separate as it is known to be not well simulated and there are
 2545 reliable data-driven methods which can be used to extract it (see Sec. 5.9.3).

2546 5.9.2.1 Bin migration

2547 It can happen that events generated in a q^2 interval are reconstructed in a different
 2548 one, this is referred to as “bin migration” and can be due to two different effects.
 2549 First of all, as the resolution of real detectors is not perfect, events close to the edges
 2550 of the considered intervals can fall on the wrong side of the edge. This effect is only
 2551 important in case of non-flat true distributions, as the amount of bin migration in the
 2552 two directions is different. The second possible source of bin migration are systematic
 2553 effects due, for example, to the presence of bremsstrahlung photons that cannot be
 2554 recovered. It is particularly important to take into account the bin migration in the
 2555 electron channels case because more photons are radiated from the final state and
 2556 the mass resolution is worse. Figure 5.26 shows the response matrix for simulated

2557 $B^0 \rightarrow K^{*0} e^+ e^-$ events, which represents the correlation between reconstructed and
2558 generated q^2 . In the ideal case of perfect resolution this plot would look like a
2559 diagonal line and in case no bias is present its slope would be 1. Table 5.11 lists the
2560 net amounts of bin migration, M_{net} , in the considered q^2 intervals defined as:

$$M_{net} = N(\text{in} \rightarrow \text{in}) + N(\text{out} \rightarrow \text{in}) - N(\text{in} \rightarrow \text{out}) \quad (5.14)$$

2561 where $N(\text{in} \rightarrow \text{in})$ is the number of candidates that are generated and reconstructed
2562 inside the considered interval, $N(\text{out} \rightarrow \text{in})$ the number of candidates that are gen-
2563 erated outside the interval but reconstructed inside and $N(\text{in} \rightarrow \text{out})$ the number of
2564 candidates generated inside that fall outside. The reconstruction efficiency is calcu-
2565 lated comparing generated to reconstructed samples and therefore already includes
2566 bin migration effects. Nevertheless, it is useful to single out this component to better
 asses the corresponding systematic uncertainty.

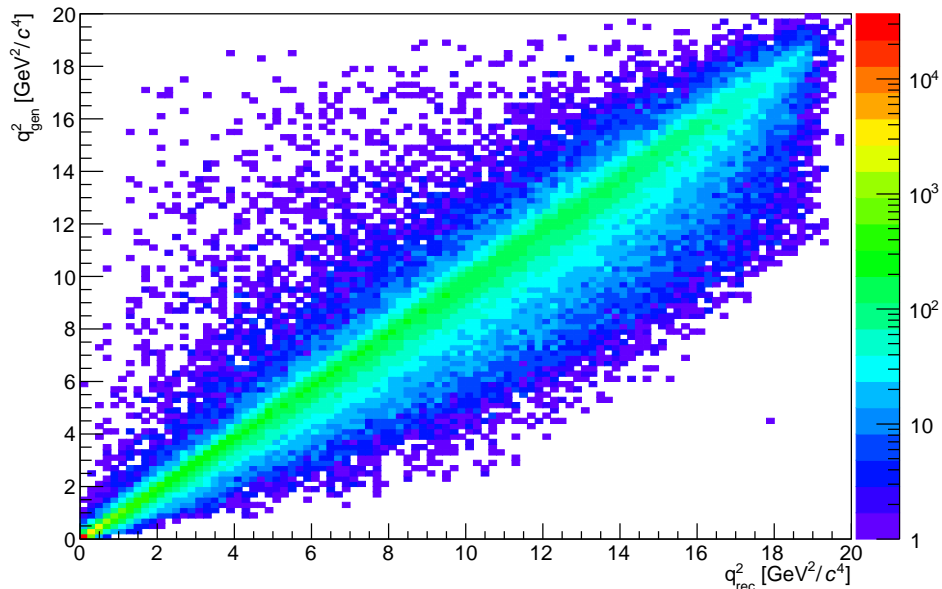


Figure 5.26: Generated versus reconstructed q^2 in simulated $B^0 \rightarrow K^{*0} e^+ e^-$ events.

2568 5.9.3 PID efficiency

2569 The simulation is known not to reliably describe particle ID variables and therefore
 2570 a data-driven method is used to obtain this efficiency component. This is done using
 2571 the **PIDCalib** package described in Sec. 2.8.1. Furthermore, the same method is used
 2572 to weight the simulation in order to calculate the MVA and trigger efficiencies. The
 2573 package **PIDCalib** allows to divide the phase-space in intervals of quantities relevant
 2574 for the determination of the PID efficiency and obtain a data-driven efficiency for
 2575 each interval. For this analysis the phase-space is divided in equi-populated bins
 2576 of momentum and pseudorapidity of the particle under study. Figure 5.27 shows
 2577 performance tables for pions, kaons, muons and electrons. Once the efficiency tables
 2578 are obtained for each particle, the total efficiency is calculated for each candidate
 2579 as the product of the four final particles efficiencies. $\varepsilon^{ev} = \varepsilon_K \cdot \varepsilon_\pi \cdot \varepsilon_{\ell_1} \cdot \varepsilon_{\ell_2}$. Finally,
 2580 as the decay channel under study generally has different kinematical distributions
 2581 than the calibration sample, the total efficiency is found by averaging over simulated
 2582 events.

$$\varepsilon_{PID} = \frac{1}{N} \sum_i^N \varepsilon_K(p_K^i, \eta_K^i) \cdot \varepsilon_\pi(p_\pi^i, \eta_\pi^i) \cdot \varepsilon_\ell(p_{\ell_1}^i, \eta_{\ell_1}^i) \cdot \varepsilon_K(p_{\ell_2}^i, \eta_{\ell_2}^i) \quad (5.15)$$

2583

2584 5.9.4 Trigger efficiency

2585 While the trigger efficiency for the muon channels is calculated using simulated
 2586 events, for the electron channels a combination of simulation and data-driven meth-
 2587 ods is used. The efficiency of the software stage, HLT, is always obtained from

Table 5.11: Net bin migration amounts (M_{net}) in the considered q^2 intervals. Positive values indicate “net in”, negative values “net out”.

Sample	low- q^2	central- q^2	J/ψ	high- q^2
$\mu\mu$	0.0002 ± 0.0001	-0.0021 ± 0.0003	0.0032 ± 0.0004	-0.0012 ± 0.0000
ee	0.0268 ± 0.0005	0.0663 ± 0.0009	-0.4277 ± 0.0048	-0.0445 ± 0.0003

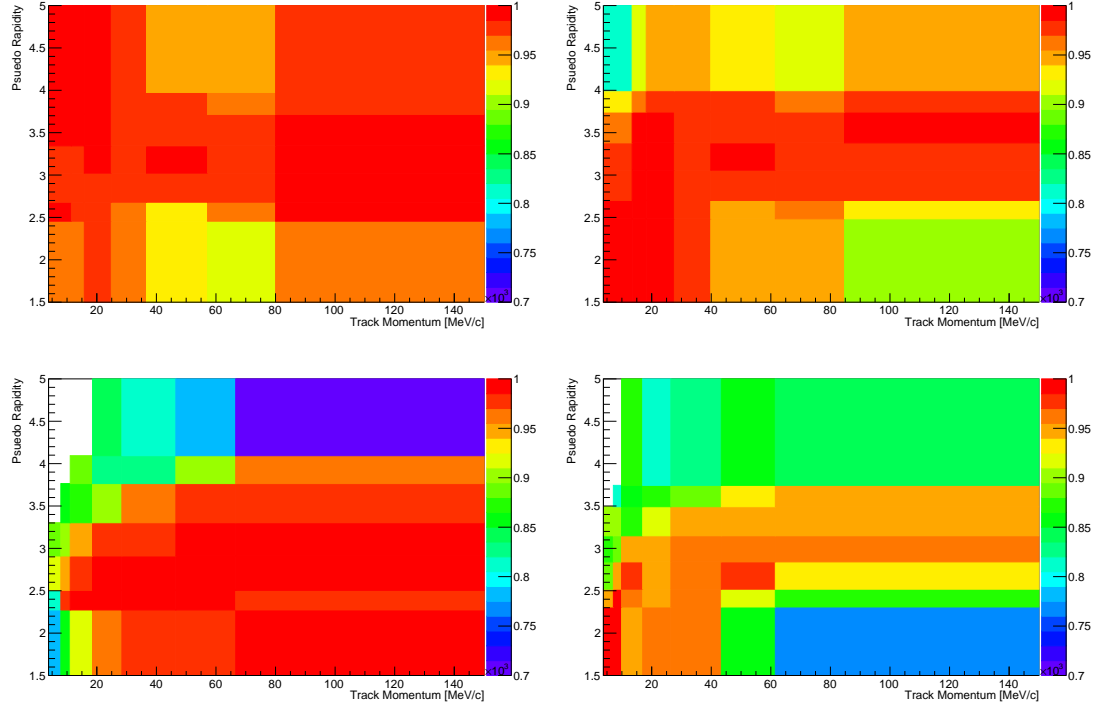


Figure 5.27: Performance tables obtained with data-driven methods for pions (top left), kaons (top right), muons (bottom left) and electrons (bottom right).

simulation, while the efficiency of the hardware stage, L0, is obtained using a data-driven method as described in the next subsection. For both muon and electron channels it is possible to use the resonant sample to cross-check the efficiency obtained using the simulation, as explained in Sec. 5.9.4.2.

5.9.4.1 Electron triggers

For the electron channels data is fitted separately in three trigger categories: L0E, L0H and L0I. Therefore the efficiency is calculated separately for each category. While the HLT (1 and 2) efficiency is always derived using simulated events, the L0Electron and L0Hadron efficiencies cannot be reliably modelled in simulation. In fact data-simulation discrepancies are caused by the ageing of the calorimeters, which is not simulated in the Monte Carlo. The ageing modifies the response of the calorimeters with time, which affects the L0 trigger efficiency. Therefore this must be calibrated using data driven-methods.

Tables of efficiencies are obtained applying the TISTOS method to a calibration sample. For each trigger category these tables contain the efficiency as a function of p_T of the considered particle and are given for different calorimeter regions as these have different properties (e.g. cell size) due to the different position with respect to the beam line. The considered regions are the inner and outer HCAL, and the inner, middle and outer ECAL. Figure 5.28 shows data-driven efficiencies for the L0Electron trigger in the three ECAL regions.

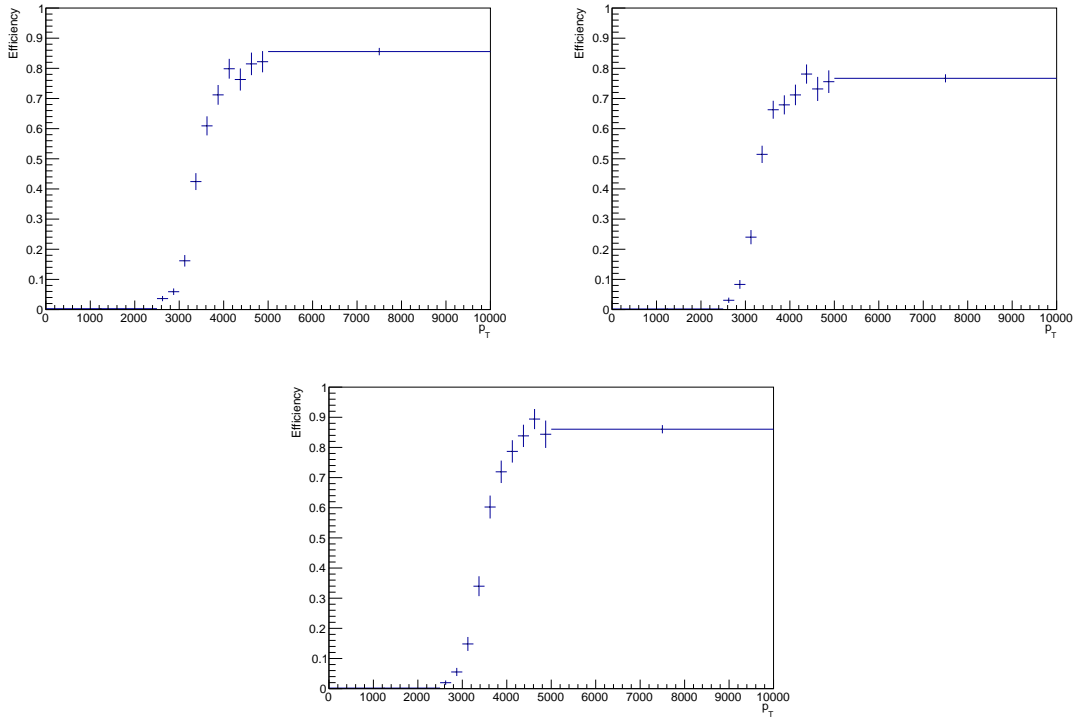


Figure 5.28: Data-driven L0Electron trigger efficiencies as a function of the transverse momentum of the electrons for the three ECAL regions.

2607

The probabilities of an event being triggered by L0Electron or L0Hadron are calculated for each candidate as:

$$P_{L0E} = \varepsilon(e^+) + \varepsilon(e^-) - \varepsilon(e^+)\varepsilon(e^-) \text{ and } P_{L0H} = \varepsilon(\pi) + \varepsilon(K) - \varepsilon(\pi)\varepsilon(K).$$

2608 The probability of TIS trigger is defined to be independent of the signal and therefore
2609 must be the same in the rare and resonant channels and cancel in their ratio.

2610 Then event by event efficiencies for the three trigger categories are defined to be
2611 exclusive in the following way:

- 2612 • L0E: $\varepsilon^{L0E} = P_{L0E}$, namely the probability that at least one electron triggered;
- 2613 • L0H: $\varepsilon^{L0H} = P_{L0H} \cdot (1 - P_{L0E})$, namely the probability that at least one hadron
2614 triggered but none of the electrons;
- 2615 • L0I: $\varepsilon^{L0I} = (1 - P_{L0H}) \cdot (1 - P_{L0E})$, namely the probability that neither the
2616 hadrons or the electrons in the candidate triggered. Note that in this case ε^{L0I}
2617 does not correspond to the efficiency of TIS trigger but to the probability that
2618 the event does not fall into the L0E or L0H categories.

2619 Finally, as in the PID case, the total efficiency is found averaging over all events of
2620 a simulated sample:

$$\varepsilon^{\text{trg}} = \frac{1}{N} \sum_i^N \varepsilon^{\text{trg}}(p_T^i) \quad (5.16)$$

2621 where “trg” is a label indicating the trigger category under consideration.

2622 5.9.4.2 TISTOS cross-check

2623 The efficiency obtained using the simulation is cross-checked applying the TISTOS
2624 method, already described in Sec. 3.6.3, to resonant data. For this purpose a sample
2625 of $B^0 \rightarrow K^{*0}(J/\psi \rightarrow e^+e^-)$ candidates triggered independent-of-signal (TIS) is used
2626 as control sample. As data also contains non negligible amounts of background
2627 a narrow interval around the peak, dominated by the signal, is selected and the
2628 *sPlot* method is used to remove residual background in the data sample. Results
2629 are shown in Tab. 5.12, where the efficiency obtained using the TISTOS method is
2630 compared between data and simulation. These are found to be in agreement for the
2631 muon channel, while they show deviations in the electron channels. In particular
2632 a significant discrepancy is found, for the L0I category, for which the procedure
2633 explained in Sec. 5.9.4.1 does not ensure a correct calibration. The table also reports

Table 5.12: Trigger efficiencies obtained using the TISTOS method on simulated and real $B^0 \rightarrow K^{*0} J/\psi (\rightarrow \ell^+ \ell^-)$ decays.

Sample	MC	Data	Correction factor
$J/\psi \rightarrow \mu\mu$	0.797 ± 0.002	0.803 ± 0.004	1.0073
$J/\psi \rightarrow ee$ LOE	0.268 ± 0.002	0.255 ± 0.004	0.9536
$J/\psi \rightarrow ee$ L0H	0.028 ± 0.001	0.026 ± 0.002	0.9269
$J/\psi \rightarrow ee$ L0I	0.017 ± 0.001	0.011 ± 0.001	0.6760

²⁶³⁴ a correction factor obtained according to the formula

$$f = 1 + \frac{\varepsilon_{data}^{\text{TISTOS}} - \varepsilon_{MC}^{\text{TISTOS}}}{\varepsilon_{MC}^{\text{TISTOS}}}, \quad (5.17)$$

²⁶³⁵ which can be used to correct the absolute resonant yields. On the other hand, even
²⁶³⁶ though discrepancies are present, they should cancel out in the ratio between the
²⁶³⁷ rare and J/ψ channels; only the residual discrepancy on this ratio is relevant for
²⁶³⁸ the measurement of $R_{K^{*0}}$. In order to check if discrepancies cancel out we need to
²⁶³⁹ obtain a data-driven efficiency also for the rare channels. To do this the TISTOS
²⁶⁴⁰ efficiency obtained on $B^0 \rightarrow K^{*0}(J/\psi \rightarrow \ell^+ \ell^-)$ candidates must be reweighted for
²⁶⁴¹ the difference in the kinematics between the rare and resonant channels. This is
²⁶⁴² done by determining the TISTOS efficiency as function of the maximum p_T of the
²⁶⁴³ particles that fired L0 (the leptons for `L0Electron` and `L0Muon`, the kaon and the
²⁶⁴⁴ pion for `L0Hadron`, and all final state particles for `L0Global`). Results are shown
²⁶⁴⁵ in Fig. 5.29 and used to re-weight the distribution of rare simulated candidates.
²⁶⁴⁶ The ratios $\varepsilon_{\ell\ell}^{\text{tistos}} / \varepsilon_{J/\psi}^{\text{tistos}}$ obtained using the data-driven method and simulation are
²⁶⁴⁷ compared and found to be fully compatible. This means that, even though the
²⁶⁴⁸ TISTOS correction has an effect on the absolute efficiency of each channel, this
²⁶⁴⁹ becomes negligible on their ratio. Therefore, no correction due to this effect is
²⁶⁵⁰ applied for the calculation of the $R_{K^{*0}}$ ratio.

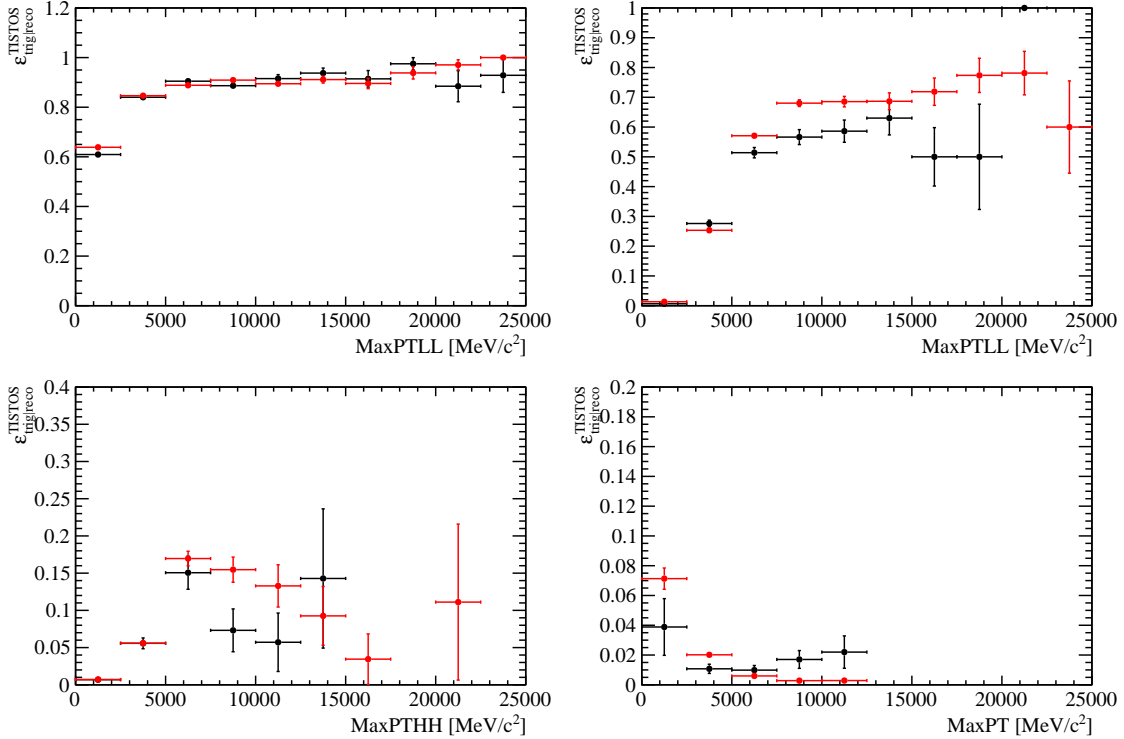


Figure 5.29: Trigger efficiency obtained applying the TISTOS method on $B^0 \rightarrow J/\psi K^*$ candidates as a function of the maximum p_T of the two muons (top left) or the two electrons for the L0E category (top right), the maximum p_T of p and π for L0H (bottom left) and the maximum p_T of all the final particles for L0I (bottom right).

2651 5.9.5 Neural networks and BCM efficiencies

2652 The neural network and BCM efficiencies are evaluated from fully weighted
 2653 simulated samples, and separately for each trigger category for the electron channels.
 2654 In order to check for biases one can compare the efficiency obtained using $B^0 \rightarrow$
 2655 $K^{*0}(J/\psi \rightarrow \ell^+\ell^-)$ events and rare $B^0 \rightarrow K^{*0}\ell^+\ell^-$ events in the same q^2 region
 2656 selected for the resonant case. The ratio between the two should be close to unity
 2657 with small deviations due the fact that the q^2 interval width is finite and the events
 2658 are distributed differently inside the interval. This ratio is found to be 0.997 ± 0.004
 2659 for the $\mu\mu$ channels and on average 0.981 ± 0.005 for the ee channels. Values for the
 2660 electron channels show a small deviation from one due to the very large q^2 interval
 2661 used to select the resonant channel ($6\text{--}11$ GeV²/c⁴).

Table 5.13: Summary of the relative percent systematic uncertainties on $R_{K^{*0}}$.

Source	low- q^2 (%)	central- q^2 (%)	high- q^2 (%)
Signal shape	1.65	1.10	2.92
Bremsstrahlung categories	0.04	0.06	0.37
Swap	0.30	0.12	0.13
$\Lambda_b^0 \rightarrow pK\ell^+\ell^-$	0.25	0.28	0.77
Partially-reconstructed	0.11	4.13	0.10
Combinatorial	0.00	0.02	8.02
J/ψ leakage	0.06	0.01	0.10
$\psi(2S)$ leakage	0.03	0.01	2.00
RooKeysPdf ($\rho = 1.1$)	0.11	0.28	0.14
RooKeysPdf ($\rho = 1.3$)	0.10	0.24	0.49
Efficiency	0.65	0.74	0.83
TISTOS	2.47	2.30	2.80
Bin migration	0.69	1.43	1.19

2662 5.10 Systematic uncertainties

2663 This section describes the main sources of systematic uncertainties considered. Other
 2664 sources, which would matter in measurements of absolute quantities, cancel in the
 2665 ratio between the rare and resonant channels. A list of the systematic uncertainties
 2666 that are considered and their effect on the $R_{K^{*0}}$ ratio is summarised in Tab. 5.13.
 2667 The total uncertainty is evaluated by summing in quadrature the single components.

2668 5.10.1 Choice of signal and background PDFs

2669 There is a certain arbitrariness in the choice of PDFs to model signal and background
 2670 contributions in the invariant mass fits, which could translate in a bias on the final
 2671 result. The systematic uncertainty due to the parameterisation of line shapes is
 2672 studied in the following ways.

2674 For the signal PDF:

- 2675 • *Shape*: in the electron channels the PDF is changed from a Crystal Ball and
2676 Gaussian to a Double Crystal Ball. Modifying the PDF has a negligible effect
2677 in the muon modes, while it affects the electron ones. Furthermore the data-
2678 simulation discrepancy parameters (m' and c) are constrained using the $B^0 \rightarrow$
2679 $K^{*0}(\gamma \rightarrow e^+e^-)$ sample instead of $B^0 \rightarrow K^{*0}(J/\psi \rightarrow e^+e^-)$.
- 2680 • *Bremsstrahlung categories*: gaussian constraints are applied to the relative
2681 fractions of the bremsstrahlung categories, instead of fixing them to the values
2682 observed on simulation. This yields a $\sim \%$ systematic on $R_{K^{*0}}$ in the central-
2683 and high- q^2 region.

2684 For the background PDFs:

- 2685 • *Swaps*: a component that describes candidates where the particle identities are
2686 swapped is added both to the muon and electron resonant fits, and constrained
2687 to the number of candidates expected from simulation. This amounts to a $\sim \%$
2688 variation on $R_{K^{*0}}$ in the central- and high- q^2 region.
- 2689 • $\Lambda_b^0 \rightarrow pK J/\psi (\rightarrow e^+e^-)$: the normalisation is left free to vary. This results in
2690 a $\sim \%$ variation on $R_{K^{*0}}$ in the central- and high- q^2 region.
- 2691 • *Partially-reconstructed*: the yield of the mis-reconstructed background to $B^0 \rightarrow$
2692 $K^{*0}e^+e^-$ is left free to vary in the fit. This only applies to the central- q^2 in-
2693 terval as this contribution is already free to vary in the high- q^2 range. This
2694 yields a $\sim \%$ systematic on $R_{K^{*0}}$.
- 2695 • *Combinatorial*: the PDF at high- q^2 is changed from an exponential (anti-MVA
2696 cut) to an anti-MVA cut (exponential) for the $\mu\mu$ (ee) mode. This amounts
2697 to a $\sim \%$ variation on $R_{K^{*0}}$ in the central- and high- q^2 region.
- 2698 • $\Lambda_b^0 \rightarrow pK\ell^+\ell^-$: this background is added to the fit to the rare channel and
2699 returns zero yield for both the muon and the electron samples. Therefore this
2700 yields no systematic uncertainty.

- 2701 • *Leakage*: gaussian constraints are applied to the amounts of $B^0 \rightarrow K^{*0}(J/\psi \rightarrow$
 2702 $e^+e^-)$ leakage in the central- q^2 region and to the $B^0 \rightarrow K^{*0}(\psi(2S) \rightarrow e^+e^-)$
 2703 leakage in the high- q^2 region, which are fixed in the default fit. This results in
 2704 a $\sim \%$ variation on $R_{K^{*0}}$ in the central- and high- q^2 region.

2705 Furthermore in all case where a simulated sample is used and smoothed to obtain a
 2706 PDF the kernel of the density estimation is varied by ± 0.1 from the value used in
 2707 the nominal fit.

2708 5.10.2 Efficiency determinations

2709 The statistical uncertainty on the efficiency determinations is taken as the corre-
 2710 sponding systematic uncertainty. The correlation among the electron trigger cate-
 2711 gories is taken into account (e.g. L0E and L0H are anti-correlated). A further source
 2712 of systematic uncertainty associated to the trigger efficiency is estimated using the
 2713 data-simulation differences observed in Sec. 5.9.4.2. Ratios of efficiencies for the
 2714 rare to resonant decays are found to be compatible between the electron and muon
 2715 modes, indicating that the effect on $R_{K^{*0}}$ is negligible, but the statistical precision
 2716 on the determinations is taken as an extra systematic uncertainty.

2717 5.10.3 Bin migration

2718 The determination of the reconstruction efficiency is affected by the knowledge of
 2719 the amount of bin migration as explained in Sec. 5.9.2. This amount depends on
 2720 the shape of the q^2 distribution, which in turn depends on the simulated $B^0 \rightarrow$
 2721 $K^{*0}e^+e^-$ decay model. In order to asses this systematic, simulated samples are
 2722 generated using different models corresponding to different form factors [122, 123].
 2723 The q^2 distributions obtained using each model are compared with the ones obtained
 2724 using the default one [124]. Figure 5.30 shows normalised ratios between these
 2725 q^2 distributions and the default one, which are used to re-weight the simulation.

2726 The amount of bin migration is recalculated using the simulation reweighted to
 2727 reproduce each model; Table 5.14 lists the percent variations obtained. The largest
 2728 difference between two values is taken as systematic uncertainty. This results in a
 2729 $\sim 5\%$ uncertainty for the central- q^2 interval and $\sim 11\%$ for the high- q^2 one, which
 represent in both channel the biggest systematic uncertainty.

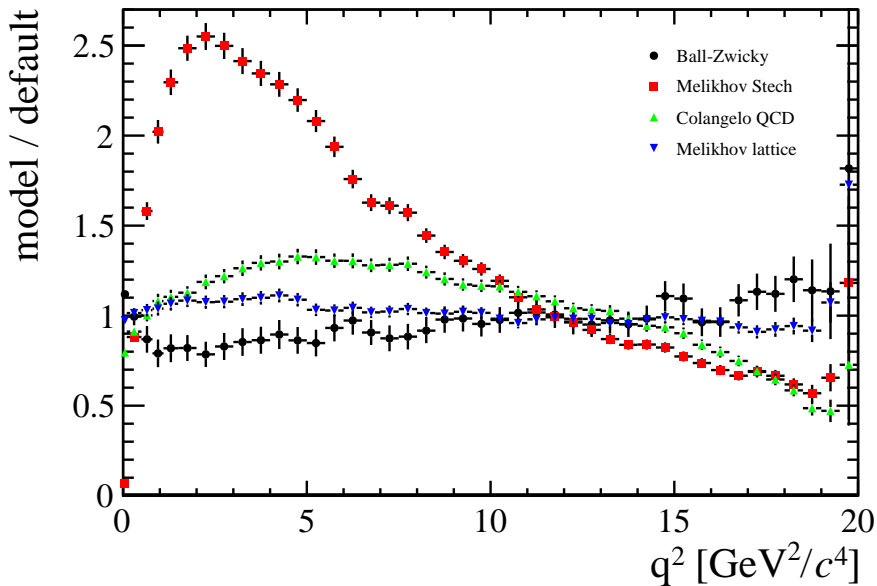


Figure 5.30: Ratios between the q^2 distributions obtained using different form factors models with respect to the default model.

Table 5.14: Percent variation on the bin migration amount obtained using different form factors models.

Model	low- q^2	central- q^2	central- q^2
Ball-Zwicky (6)	-0.3	1.0	0.2
Colangelo 2pt QCD (3)	0.4	0.4	0.8
Melikhov lattice (4)	0.1	-0.4	-0.4

2730

2731 5.11 Result extraction

2732 This section presents the procedure to obtain the $R_{K^{*0}}$ ratio together with methods
 2733 to check robustness of the analysis.

²⁷³⁴ **5.11.1 $R_{J/\psi}$ sanity check**

²⁷³⁵ In order to cross-check the analysis procedure, the ratio between the measured
²⁷³⁶ branching ratio of the electron and muon resonant channels is calculated:

$$r_{J/\psi} = \frac{\mathcal{B}(B^0 \rightarrow K^{*0} J/\psi (\rightarrow \mu^+ \mu^-))}{\mathcal{B}(B^0 \rightarrow K^{*0} J/\psi (\rightarrow e^+ e^-))} = \frac{\varepsilon_{J/\psi(\mu\mu)} \cdot N_{B^0 \rightarrow K^{*0} J/\psi (\rightarrow e^+ e^-)}}{\varepsilon_{J/\psi(ee)} \cdot N_{B^0 \rightarrow K^{*0} J/\psi (\rightarrow \mu^+ \mu^-)}}. \quad (5.18)$$

²⁷³⁷ Unlike absolute branching fractions calculations, the determination of $R_{J/\psi}$ repre-
²⁷³⁸ sents a better sanity test as it is not affected by uncertainties due to the knowledge
²⁷³⁹ of the amount of collected luminosity, \mathcal{L} , or the fragmentation fraction, f_d , the
²⁷⁴⁰ probability for a b quark to produce a B^0 meson. These quantities come with large
²⁷⁴¹ uncertainties but they cancel in the $r_{J/\psi}$ ratio.

²⁷⁴² **5.11.2 $R_{K^{*0}}$**

²⁷⁴³ The ratio $R_{K^{*0}}$ is extracted by dividing the r_{ee} and $r_{\mu\mu}$ parameters described in
²⁷⁴⁴ Sec. 5.8. These ratios are direct parameters of the fit but they can also be built from
²⁷⁴⁵ the yields in Tab. 5.8 and the efficiencies in Tab. 5.10. In summary the definition of
²⁷⁴⁶ the $R_{K^{*0}}$ ratio is the following:

$$R_{K^{*0}} = \frac{r_{ee}}{r_{\mu\mu}} = \frac{N_{ee}}{N_{J/\psi(ee)}} \cdot \frac{N_{J/\psi(\mu\mu)}}{N_{\mu\mu}} \cdot \frac{\varepsilon_{J/\psi(ee)}}{\varepsilon_{ee}} \cdot \frac{\varepsilon_{\mu\mu}}{\varepsilon_{J/\psi(\mu\mu)}}. \quad (5.19)$$

²⁷⁴⁷ As the electron ratio R_{ee} is a shared parameter in the simultaneous fit to the three
²⁷⁴⁸ electron categories its value is already a combination of the three samples.

2749

CHAPTER 6

2750

2751

Conclusions

2752

2753 In this work rare decays were analysed in order to look for hints of new physics using
2754 data collected by the LHCb detector at centre-of-mass energies of 7 and 8 TeV and
2755 corresponding to a total integrated luminosity of 3.0 fb^{-1} .

2756 First, a measurement of the differential branching fraction of the rare $\Lambda_b^0 \rightarrow \Lambda\mu^+\mu^-$
2757 decay was performed together with the first measurement of angular observables
2758 for this decay. Evidence for the signal was found for the first time in the q^2 region
2759 between the two charmonium resonances and below the square of the J/ψ mass,
2760 in particular in the $0.1 < q^2 < 2.0 \text{ GeV}^2/c^4$ interval, where an increased yield is
2761 expected due to the vicinity of the photon pole. Due to a larger data sample and
2762 a better control of systematic effects, the uncertainty on the measurement in the
2763 $15 < q^2 < 20 \text{ GeV}^2/c^4$ interval are reduced by approximately a factor of three with
2764 respect to the previous LHCb measurements. The branching fraction measurements
2765 are compatible with SM predictions in the high- q^2 region, above the square of the
2766 J/ψ mass, but lie below the predictions in the low- q^2 region. In the angular analysis

of $\Lambda_b^0 \rightarrow \Lambda\mu^+\mu^-$ decays two forward-backward asymmetries, in the $p\pi$ and dimuon systems, were measured. The measurements of the A_{FB}^h observable are in good agreement with the SM predictions, while for the A_{FB}^ℓ observable they are consistently above the predictions. Following the publication of these studies improved predictions were produced, which are reported in Appendix D. Theoretical values are now compatible with the branching fraction measurements at low- q^2 and overestimate the experimental values at high- q^2 . The situation regarding the angular observables is unchanged but the significance of the existing discrepancies is enhanced due to the improved uncertainties on the predicted values.

Secondly, an analysis is set up to test flavour universality between electrons and muons exploiting rare decays. A set of requirements is defined to select the rare and normalisation, $B^0 \rightarrow K^{*0}\ell^+\ell^-$ and $B^0 \rightarrow K^{*0}(J/\psi \rightarrow \ell^+\ell^-)$ modes in both electron and muons channels, which includes the definition of a multivariate classifier. Efficiencies are obtained for this selection for all channels. A study of the possible backgrounds to these channels is performed, which results in a set of requirements to lower their yield in the selected samples and a set of PDFs to model the remaining contributions in the invariant mass fits. Preliminary fits to the 4-body invariant mass distributions of all channels are performed. Finally, a preliminary study of the systematic uncertainties is presented and a set a procedure to obtain the result and check its robustness are defined. The results are currently blinded.

2787

2788

REFERENCES

2789

- 2790 [1] **LHCb** Collaboration, R. Aaij et al., *Differential branching fraction and*
2791 *angular analysis of $\Lambda_b^0 \rightarrow \Lambda\mu^+\mu^-$ decays*, *JHEP* **1506** (2015) 115,
2792 [[arXiv:1503.07138](https://arxiv.org/abs/1503.07138)].
- 2793 [2] **Particle Data Group** Collaboration, K. Olive et al., *Review of Particle*
2794 *Physics*, *Chin.Phys.* **C38** (2014) 090001.
- 2795 [3] **ATLAS** Collaboration, G. Aad et al., *Observation of a new particle in the*
2796 *search for the Standard Model Higgs boson with the ATLAS detector at the*
2797 *LHC*, *Phys. Lett.* **B716** (2012) 1–29, [[arXiv:1207.7214](https://arxiv.org/abs/1207.7214)].
- 2798 [4] **CMS** Collaboration, S. Chatrchyan et al., *Observation of a new boson at a*
2799 *mass of 125 GeV with the CMS experiment at the LHC*, *Phys. Lett.* **B716**
2800 (2012) 30–61, [[arXiv:1207.7235](https://arxiv.org/abs/1207.7235)].
- 2801 [5] L. Susskind, *Dynamics of Spontaneous Symmetry Breaking in the*
2802 *Weinberg-Salam Theory*, *Phys.Rev.* **D20** (1979) 2619–2625.
- 2803 [6] S. Glashow, *Partial Symmetries of Weak Interactions*, *Nucl.Phys.* **22** (1961)
2804 579–588.
- 2805 [7] “Wikipedia.” https://en.wikipedia.org/wiki/Standard_Model.
2806 Accessed: 2016-02-26.
- 2807 [8] D. J. Gross and F. Wilczek, *Ultraviolet Behavior of Nonabelian Gauge*
2808 *Theories*, *Phys. Rev. Lett.* **30** (1973) 1343–1346.
- 2809 [9] **LHCb** Collaboration, R. Aaij et al., *Observation of the resonant character*
2810 *of the $Z(4430)^-$ state*, *Phys. Rev. Lett.* **112** (2014), no. 22 222002,
2811 [[arXiv:1404.1903](https://arxiv.org/abs/1404.1903)].

- 2812 [10] **LHCb** Collaboration, R. Aaij et al., *Observation of $J/\psi p$ resonances*
 2813 *consistent with pentaquark states in $\Lambda_b^0 \rightarrow J/\psi K^- p$ decays*,
 2814 [arXiv:1507.03414](https://arxiv.org/abs/1507.03414).
- 2815 [11] C. Wu, E. Ambler, R. Hayward, D. Hoppes, and R. Hudson, *Experimental*
 2816 *Test of Parity Conservation in Beta Decay*, *Phys. Rev.* **105** (1957) 1413–1414.
- 2817 [12] F. Strocchi, *Spontaneous Symmetry Breaking in Local Gauge Quantum Field*
 2818 *Theory: The Higgs Mechanism*, *Commun. Math. Phys.* **56** (1977) 57.
- 2819 [13] N. Cabibbo, *Unitary Symmetry and Leptonic Decays*, *Phys. Rev. Lett.* **10**
 2820 (1963) 531–533. [,648(1963)].
- 2821 [14] M. Kobayashi and T. Maskawa, *CP Violation in the Renormalizable Theory*
 2822 *of Weak Interaction*, *Prog. Theor. Phys.* **49** (1973) 652–657.
- 2823 [15] J. Charles, O. Deschamps, S. Descotes-Genon, H. Lacker, A. Menzel, et al.,
 2824 *Current status of the Standard Model CKM fit and constraints on $\Delta F = 2$*
 2825 *New Physics*, *Phys. Rev.* **D91** (2015), no. 7 073007, [[arXiv:1501.05013](https://arxiv.org/abs/1501.05013)].
- 2826 [16] F. Zwicky, *Spectral displacement of extra galactic nebulae*, *Helv. Phys. Acta* **6**
 2827 (1933) 110–127.
- 2828 [17] M. Gavela and Hernandez, *Standard model CP violation and baryon*
 2829 *asymmetry*, *Mod. Phys. Lett.* **A9** (1994) 795–810, [[hep-ph/9312215](https://arxiv.org/abs/hep-ph/9312215)].
- 2830 [18] S. Carlip, *Quantum gravity: A Progress report*, *Rept. Prog. Phys.* **64** (2001)
 2831 885, [[gr-qc/0108040](https://arxiv.org/abs/gr-qc/0108040)].
- 2832 [19] M. Maltoni, *Status of three-neutrino oscillations*, *PoS EPS-HEP2011*
 2833 (2011) 090.
- 2834 [20] B. T. Cleveland, T. Daily, R. Davis, Jr., J. R. Distel, K. Lande, C. K. Lee,
 2835 P. S. Wildenhain, and J. Ullman, *Measurement of the solar electron neutrino*
 2836 *flux with the Homestake chlorine detector*, *Astrophys. J.* **496** (1998) 505–526.
- 2837 [21] **Super-Kamiokande** Collaboration, Y. Fukuda et al., *Evidence for*
 2838 *oscillation of atmospheric neutrinos*, *Phys. Rev. Lett.* **81** (1998) 1562–1567,
 2839 [[hep-ex/9807003](https://arxiv.org/abs/hep-ex/9807003)].
- 2840 [22] **KamLAND** Collaboration, K. Eguchi et al., *First results from KamLAND:*
 2841 *Evidence for reactor anti-neutrino disappearance*, *Phys. Rev. Lett.* **90** (2003)
 2842 021802, [[hep-ex/0212021](https://arxiv.org/abs/hep-ex/0212021)].
- 2843 [23] J. L. Feng, *Naturalness and the Status of Supersymmetry*,
 2844 *Ann. Rev. Nucl. Part. Sci.* **63** (2013) 351–382, [[arXiv:1302.6587](https://arxiv.org/abs/1302.6587)].
- 2845 [24] B. Pontecorvo, *Neutrino Experiments and the Problem of Conservation of*
 2846 *Leptonic Charge*, *Sov. Phys. JETP* **26** (1968) 984–988. [*Zh. Eksp. Teor.*
 2847 *Fiz.* **53**, 1717 (1967)].

- [25] Z. Maki, M. Nakagawa, and S. Sakata, *Remarks on the unified model of elementary particles*, *Prog. Theor. Phys.* **28** (1962) 870–880.
- [26] P. Fayet and S. Ferrara, *Supersymmetry*, *Phys.Rept.* **32** (1977) 249–334.
- [27] L. Randall and R. Sundrum, *A Large mass hierarchy from a small extra dimension*, *Phys.Rev.Lett.* **83** (1999) 3370–3373, [[hep-ph/9905221](#)].
- [28] J. R. Ellis, G. Gelmini, C. Jarlskog, G. G. Ross, and J. W. F. Valle, *Phenomenology of Supersymmetry with Broken R-Parity*, *Phys. Lett.* **B150** (1985) 142.
- [29] G. Isidori and D. M. Straub, *Minimal Flavour Violation and Beyond*, *Eur.Phys.J.* **C72** (2012) 2103, [[arXiv:1202.0464](#)].
- [30] A. J. Buras, *Minimal flavor violation*, *Acta Phys.Polon.* **B34** (2003) 5615–5668, [[hep-ph/0310208](#)].
- [31] T. Blake, T. Gershon, and G. Hiller, *Rare b hadron decays at the LHC*, *Ann.Rev.Nucl.Part.Sci.* **65** (2015) 8007, [[arXiv:1501.03309](#)].
- [32] A. J. Buras, D. Buttazzo, J. GIRRbach-Noe, and R. Knegjens, *Can we reach the Zeptouniverse with rare K and B_{s,d} decays?*, *JHEP* **1411** (2014) 121, [[arXiv:1408.0728](#)].
- [33] G. Hiller and M. Schmaltz, *R_K and future b → sℓℓ physics beyond the standard model opportunities*, *Phys.Rev.* **D90** (2014) 054014, [[arXiv:1408.1627](#)].
- [34] K. G. Chetyrkin, M. Misiak, and M. Munz, *Weak radiative B meson decay beyond leading logarithms*, *Phys.Lett.* **B400** (1997) 206–219, [[hep-ph/9612313](#)].
- [35] G. Buchalla, A. J. Buras, and M. E. Lautenbacher, *Weak decays beyond leading logarithms*, *Rev.Mod.Phys.* **68** (1996) 1125–1144, [[hep-ph/9512380](#)].
- [36] A. J. Buras, *Weak Hamiltonian, CP violation and rare decays*, [hep-ph/9806471](#).
- [37] M. Della Morte, J. Heitger, H. Simma, and R. Sommer, *Non-perturbative Heavy Quark Effective Theory: An application to semi-leptonic B-decays*, *Nucl.Part.Phys.Proc.* **261-262** (2015) 368–377, [[arXiv:1501.03328](#)].
- [38] C. W. Bauer, S. Fleming, D. Pirjol, and I. W. Stewart, *An Effective field theory for collinear and soft gluons: Heavy to light decays*, *Phys.Rev.* **D63** (2001) 114020, [[hep-ph/0011336](#)].
- [39] A. Khodjamirian, T. Mannel, A. Pivovarov, and Y.-M. Wang, *Charm-loop effect in B → K^(*)ℓ⁺ℓ⁻ and B → K^{*}γ*, *JHEP* **1009** (2010) 089, [[arXiv:1006.4945](#)].

- [40] **LHCb** Collaboration, R. Aaij et al., *Observation of a resonance in $B^+ \rightarrow K^+ \mu^+ \mu^-$ decays at low recoil*, *Phys. Rev. Lett.* **111** (2013) 112003, [[arXiv:1307.7595](#)].
- [41] C. Bobeth, M. Gorbahn, T. Hermann, M. Misiak, E. Stamou, et al., *$B_{s,d} \rightarrow l^+ l^-$ in the Standard Model with Reduced Theoretical Uncertainty*, *Phys. Rev. Lett.* **112** (2014) 101801, [[arXiv:1311.0903](#)].
- [42] **CMS, LHCb** Collaboration, V. Khachatryan et al., *Observation of the rare $B_s^0 \rightarrow \mu^+ \mu^-$ decay from the combined analysis of CMS and LHCb data*, *Nature* **522** (2015) 68–72, [[arXiv:1411.4413](#)].
- [43] **LHCb** Collaboration, R. Aaij et al., *Differential branching fractions and isospin asymmetry of $B \rightarrow K^{(*)} \mu^+ \mu^-$ decays*, *JHEP* **06** (2014) 133, [[arXiv:1403.8044](#)].
- [44] **LHCb** Collaboration, R. Aaij et al., *Differential branching fraction and angular analysis of the decay $B_s^0 \rightarrow \phi \mu^+ \mu^-$* , *JHEP* **07** (2013) 084, [[arXiv:1305.2168](#)].
- [45] **LHCb** Collaboration, R. Aaij et al., *Differential branching fraction and angular analysis of the decay $B^0 \rightarrow K^{*0} \mu^+ \mu^-$* , *JHEP* **08** (2013) 131, [[arXiv:1304.6325](#)].
- [46] **LHCb** Collaboration, R. Aaij et al., *Measurement of form-factor-independent observables in the decay $B^0 \rightarrow K^{*0} \mu^+ \mu^-$* , *Phys. Rev. Lett.* **111** (2013) 191801, [[arXiv:1308.1707](#)].
- [47] **LHCb** Collaboration, R. Aaij et al., *Angular analysis of the $B^0 \rightarrow K^{*0} \mu^+ \mu^-$ decay using 3 fb^{-1} of integrated luminosity*, *JHEP* **02** (2016) 104, [[arXiv:1512.04442](#)].
- [48] S. Descotes-Genon, J. Matias, and J. Virto, *Understanding the $B \rightarrow K^* \mu^+ \mu^-$ Anomaly*, *Phys. Rev.* **D88** (2013) 074002, [[arXiv:1307.5683](#)].
- [49] **LHCb** Collaboration, R. Aaij et al., *Angular analysis of charged and neutral $B \rightarrow K \mu^+ \mu^-$ decays*, *JHEP* **05** (2014) 082, [[arXiv:1403.8045](#)].
- [50] **LHCb** Collaboration, R. Aaij et al., *Measurement of CP asymmetries in the decays $B^0 \rightarrow K^{*0} \mu^+ \mu^-$ and $B^+ \rightarrow K^+ \mu^+ \mu^-$* , *JHEP* **1409** (2014) 177, [[arXiv:1408.0978](#)].
- [51] **LHCb** Collaboration, R. Aaij et al., *Measurement of the $B^0 \rightarrow K^{*0} e^+ e^-$ branching fraction at low dilepton mass*, *JHEP* **05** (2013) 159, [[arXiv:1304.3035](#)].
- [52] **LHCb** Collaboration, R. Aaij et al., *Angular analysis of the $B^0 \rightarrow K^{*0} e^+ e^-$ decay in the low- q^2 region*, *JHEP* **04** (Jan, 2015) 064. 18 p.
- [53] W. Altmannshofer and D. M. Straub, *New physics in $b \rightarrow s$ transitions after LHC run 1*, [arXiv:1411.3161](#).

- [54] T. Hurth, F. Mahmoudi, and S. Neshatpour, *On the anomalies in the latest LHCb data*, arXiv:1603.00865.
- [55] **MEGA** Collaboration, M. Ahmed et al., *Search for the lepton family number nonconserving decay $\mu^+ \rightarrow e^+ \gamma$* , Phys. Rev. **D65** (2002) 112002, [hep-ex/0111030].
- [56] **SINDRUM** Collaboration, U. Bellgardt et al., *Search for the Decay $\mu^+ \rightarrow e^+ e^+ e^-$* , Nucl. Phys. **B299** (1988) 1.
- [57] **LHCb** Collaboration, R. Aaij et al., *Search for the lepton-flavour-violating decays $B_s^0 \rightarrow e^\pm \mu^\mp$ and $B^0 \rightarrow e^\pm \mu^\mp$* , Phys. Rev. Lett. **111** (2013) 141801, [arXiv:1307.4889].
- [58] **LHCb** Collaboration, R. Aaij et al., *Searches for violation of lepton flavour and baryon number in tau lepton decays at LHCb*, Phys. Lett. **B724** (2013) 36, [arXiv:1304.4518].
- [59] W. J. Marciano, T. Mori, and J. M. Roney, *Charged Lepton Flavor Violation Experiments*, Ann. Rev. Nucl. Part. Sci. **58** (2008) 315–341.
- [60] L. Evans, *The LHC machine*, PoS **EPS-HEP2009** (2009) 004.
- [61] C. Lefévre, “The CERN accelerator complex. Complexe des accélérateurs du CERN.” Dec, 2008.
- [62] **LHCb** Collaboration, A. A. Alves Jr. et al., *The LHCb detector at the LHC*, JINST **3** (2008) S08005.
- [63] **LHCb** Collaboration, R. Aaij et al., *Measurement of $\sigma(pp \rightarrow b\bar{b}X)$ at $\sqrt{s} = 7$ TeV in the forward region*, Phys. Lett. **B694** (2010) 209–216, [arXiv:1009.2731].
- [64] M. Adinolfi et al., *Performance of the LHCb RICH detector at the LHC*, Eur. Phys. J. **C73** (2013) 2431, [arXiv:1211.6759].
- [65] A. A. Alves Jr. et al., *Performance of the LHCb muon system*, JINST **8** (2013) P02022, [arXiv:1211.1346].
- [66] **LHCb** Collaboration, R. e. a. Aaij, *LHCb technical design report: Reoptimized detector design and performance*, CERN-LHCC-2003-030.
- [67] “Wikipedia.” https://en.wikipedia.org/wiki/Cherenkov_radiation. Accessed: 2016-02-26.
- [68] **LHCb** Collaboration, R. e. a. Aaij, *LHCb Detector Performance*, Int. J. Mod. Phys. A **30** (Dec, 2014) 1530022. 82 p.
- [69] M. Pivk and F. R. Le Diberder, *SPlot: A Statistical tool to unfold data distributions*, Nucl. Instrum. Meth. **A555** (2005) 356–369, [physics/0402083].

- [70] R. Aaij et al., *The LHCb trigger and its performance in 2011*, *JINST* **8** (2013) P04022, [[arXiv:1211.3055](#)].
- [71] T. Sjöstrand, S. Mrenna, and P. Skands, *PYTHIA 6.4 physics and manual*, *JHEP* **05** (2006) 026, [[hep-ph/0603175](#)].
- [72] T. Sjostrand, S. Mrenna, and P. Z. Skands, *A Brief Introduction to PYTHIA 8.1*, *Comput. Phys. Commun.* **178** (2008) 852–867, [[arXiv:0710.3820](#)].
- [73] I. Belyaev et al., *Handling of the generation of primary events in GAUSS, the LHCb simulation framework*, *Nuclear Science Symposium Conference Record (NSS/MIC)* **IEEE** (2010) 1155.
- [74] D. J. Lange, *The EvtGen particle decay simulation package*, *Nucl. Instrum. Meth.* **A462** (2001) 152–155.
- [75] P. Golonka and Z. Was, *PHOTOS Monte Carlo: a precision tool for QED corrections in Z and W decays*, *Eur.Phys.J.* **C45** (2006) 97–107, [[hep-ph/0506026](#)].
- [76] **Geant4 collaboration** Collaboration, J. Allison, K. Amako, J. Apostolakis, H. Araujo, P. Dubois, et al., *Geant4 developments and applications*, *IEEE Trans.Nucl.Sci.* **53** (2006) 270.
- [77] M. Clemencic et al., *The LHCb simulation application, GAUSS: design, evolution and experience*, *J. Phys. Conf. Ser.* **331** (2011) 032023.
- [78] R. Brun, F. Rademakers, and S. Panacek, *ROOT, an object oriented data analysis framework*, *Conf.Proc.* **C000917** (2000) 11–42.
- [79] M. Feindt and U. Kerzel, *The NeuroBayes neural network package*, *Nucl.Instrum.Meth.* **A559** (2006) 190–194.
- [80] M. Feindt, *A Neural Bayesian Estimator for Conditional Probability Densities*, [physics/0402093](#).
- [81] W. D. Hulsbergen, *Decay chain fitting with a Kalman filter*, *Nucl.Instrum.Meth.* **A552** (2005) 566–575, [[physics/0503191](#)].
- [82] H. W. Bertini, *Low-Energy Intranuclear Cascade Calculation*, *Phys. Rev.* **131** (1963) 1801–1821.
- [83] B. Andersson, G. Gustafson, and H. Pi, *The FRITIOF model for very high-energy hadronic collisions*, *Z. Phys.* **C57** (1993) 485–494.
- [84] **COMPASS** Collaboration, P. Abbon et al., *The COMPASS experiment at CERN*, *Nucl. Instrum. Meth.* **A577** (2007) 455–518, [[hep-ex/0703049](#)].
- [85] G. Hiller, M. Knecht, F. Legger, and T. Schietinger, *Photon polarization from helicity suppression in radiative decays of polarized Lambda(b) to spin-3/2 baryons*, *Phys.Lett.* **B649** (2007) 152–158, [[hep-ph/0702191](#)].

- [86] T. Mannel and S. Recksiegel, *Flavor changing neutral current decays of heavy baryons: The Case $\Lambda_b^0 \rightarrow \Lambda \gamma$* , *J.Phys.* **G24** (1998) 979–990, [hep-ph/9701399].
- [87] M. J. Aslam, Y.-M. Wang, and C.-D. Lu, *Exclusive semileptonic decays of $\Lambda_b^0 \rightarrow \Lambda l^+l^-$ in supersymmetric theories*, *Phys.Rev.* **D78** (2008) 114032, [arXiv:0808.2113].
- [88] Y.-m. Wang, Y. Li, and C.-D. Lu, *Rare Decays of $\Lambda_b^0 \rightarrow \Lambda \gamma$ and $\Lambda_b^0 \rightarrow \Lambda l^+l^-$ in the Light-cone Sum Rules*, *Eur.Phys.J.* **C59** (2009) 861–882, [arXiv:0804.0648].
- [89] C.-S. Huang and H.-G. Yan, *Exclusive rare decays of heavy baryons to light baryons: $\Lambda_b^0 \rightarrow \Lambda \gamma$ and $\Lambda_b^0 \rightarrow \Lambda l^+l^-$* , *Phys.Rev.* **D59** (1999) 114022, [hep-ph/9811303].
- [90] C.-H. Chen and C. Geng, *Rare $\Lambda_b^0 \rightarrow \Lambda l^+l^-$ decays with polarized lambda*, *Phys.Rev.* **D63** (2001) 114024, [hep-ph/0101171].
- [91] C.-H. Chen and C. Geng, *Baryonic rare decays of $\Lambda_b^0 \rightarrow \Lambda l^+l^-$* , *Phys.Rev.* **D64** (2001) 074001, [hep-ph/0106193].
- [92] C.-H. Chen and C. Geng, *Lepton asymmetries in heavy baryon decays of $\Lambda_b^0 \rightarrow \Lambda l^+l^-$* , *Phys.Lett.* **B516** (2001) 327–336, [hep-ph/0101201].
- [93] F. Zolfagharpour and V. Bashiry, *Double Lepton Polarization in $\Lambda_b^0 \rightarrow \Lambda l^+l^-$ Decay in the Standard Model with Fourth Generations Scenario*, *Nucl.Phys.* **B796** (2008) 294–319, [arXiv:0707.4337].
- [94] L. Mott and W. Roberts, *Rare dileptonic decays of Λ_b^0 in a quark model*, *Int.J.Mod.Phys.* **A27** (2012) 1250016, [arXiv:1108.6129].
- [95] T. Aliev, K. Azizi, and M. Savci, *Analysis of the $\Lambda_b^0 \rightarrow \Lambda l^+l^-$ decay in QCD*, *Phys.Rev.* **D81** (2010) 056006, [arXiv:1001.0227].
- [96] R. Mohanta and A. Giri, *Fourth generation effect on Λ_b decays*, *Phys.Rev.* **D82** (2010) 094022, [arXiv:1010.1152].
- [97] S. Sahoo, C. Das, and L. Maharana, *Effect of both Z and Z'-mediated flavor-changing neutral currents on the baryonic rare decay $\Lambda_b^0 \rightarrow \Lambda l^+l^-$* , *Int.J.Mod.Phys.* **A24** (2009) 6223–6235, [arXiv:1112.4563].
- [98] **CDF Collaboration** Collaboration, T. Aaltonen et al., *Observation of the Baryonic Flavor-Changing Neutral Current Decay $\Lambda_b \rightarrow \Lambda \mu^+ \mu^-$* , *Phys.Rev.Lett.* **107** (2011) 201802, [arXiv:1107.3753].
- [99] **CDF** Collaboration, S. Behari, *CDF results on $b \rightarrow s \mu \mu$ decays*, arXiv:1301.2244.

- 3028 [100] **LHCb** Collaboration, R. Aaij et al., *Measurement of the differential*
 3029 *branching fraction of the decay $\Lambda_b^0 \rightarrow \Lambda\mu^+\mu^-$* , *Phys. Lett.* **B725** (2013) 25,
 3030 [[arXiv:1306.2577](#)].
- 3031 [101] T. Gutsche, M. A. Ivanov, J. G. Korner, V. E. Lyubovitskij, and
 3032 P. Santorelli, *Rare baryon decays $\Lambda_b \rightarrow \Lambda l^+l^- (l = e, \mu, \tau)$ and $\Lambda_b \rightarrow \Lambda\gamma$:
 3033 differential and total rates, lepton- and hadron-side forward-backward
 3034 asymmetries*, *Phys. Rev.* **D87** (2013) 074031, [[arXiv:1301.3737](#)].
- 3035 [102] **LHCb** Collaboration, R. Aaij et al., *Measurements of the $\Lambda_b^0 \rightarrow J/\psi\Lambda$ decay
 3036 amplitudes and the Λ_b^0 polarisation in pp collisions at $\sqrt{s} = 7$ TeV*,
 3037 [*Phys. Lett.* **B724** (2013) 27, [[arXiv:1302.5578](#)]].
- 3038 [103] G. Punzi, *Sensitivity of searches for new signals and its optimization*, in
 3039 *Statistical Problems in Particle Physics, Astrophysics, and Cosmology*
 3040 (L. Lyons, R. Mount, and R. Reitmeyer, eds.), p. 79, 2003.
 3041 [[physics/0308063](#)].
- 3042 [104] T. Skwarnicki, *A study of the radiative cascade transitions between the
 3043 Upsilon-prime and Upsilon resonances*. PhD thesis, Institute of Nuclear
 3044 Physics, Krakow, 1986. DESY-F31-86-02.
- 3045 [105] W. Detmold, C.-J. D. Lin, S. Meinel, and M. Wingate, *$\Lambda_b^0 \rightarrow \Lambda\mu^+\mu^-$ form
 3046 factors and differential branching fraction from lattice QCD*, *Phys. Rev.* **D87**
 3047 (2013), no. 7 074502, [[arXiv:1212.4827](#)].
- 3048 [106] **LHCb** Collaboration, R. Aaij et al., *Precision measurement of the Λ_b^0 baryon
 3049 lifetime*, *Phys. Rev. Lett.* **111** (2013) 102003, [[arXiv:1307.2476](#)].
- 3050 [107] T. Blake, S. Coquereau, M. Chrzaszcz, S. Cunliffe, C. Parkinson, K. Petridis,
 3051 and M. Tresch, *The $B_0 \rightarrow K_0^*\mu\mu$ selection using $3fb^{-1}$ of LHCb data*, Tech.
 3052 Rep. LHCb-INT-2013-058. CERN-LHCb-INT-2013-058, CERN, Geneva,
 3053 Nov, 2013.
- 3054 [108] F. James and M. Roos, *Minuit: A System for Function Minimization and
 3055 Analysis of the Parameter Errors and Correlations*, *Comput. Phys.
 3056 Commun.* **10** (1975) 343–367.
- 3057 [109] **LHCb** Collaboration, R. Aaij et al., *Measurements of the $\Lambda_b^0 \rightarrow J/\psi\Lambda$ decay
 3058 amplitudes and the Λ_b^0 polarisation in pp collisions at $\sqrt{s} = 7$ TeV*, *Phys.
 3059 Lett.* **B724** (2013) 27, [[arXiv:1302.5578](#)].
- 3060 [110] G. J. Feldman and R. D. Cousins, *A Unified approach to the classical
 3061 statistical analysis of small signals*, *Phys. Rev.* **D57** (1998) 3873–3889,
 3062 [[physics/9711021](#)].
- 3063 [111] T. M. Karbach, *Feldman-Cousins Confidence Levels - Toy MC Method*,
 3064 [[arXiv:1109.0714](#)].

- 3065 [112] S. Meinel, *Flavor physics with Λ_b baryons*, *PoS LATTICE2013* (2014) 024,
3066 [arXiv:1401.2685].
- 3067 [113] G. Hiller and F. Kruger, *More model independent analysis of $b \rightarrow s$*
3068 *processes*, *Phys.Rev.* **D69** (2004) 074020, [hep-ph/0310219].
- 3069 [114] G. Hiller and M. Schmaltz, *Diagnosing lepton-nonuniversality in $b \rightarrow s\ell\ell$* ,
3070 *JHEP* **1502** (2015) 055, [arXiv:1411.4773].
- 3071 [115] **BaBar Collaboration** Collaboration, J. Lees et al., *Measurement of*
3072 *Branching Fractions and Rate Asymmetries in the Rare Decays*
3073 $B \rightarrow K^{(*)}l^+l^-$, *Phys.Rev.* **D86** (2012) 032012, [arXiv:1204.3933].
- 3074 [116] **BELLE Collaboration** Collaboration, J.-T. Wei et al., *Measurement of the*
3075 *Differential Branching Fraction and Forward-Backword Asymmetry for*
3076 $B \rightarrow K^{(*)}l^+l^-$, *Phys.Rev.Lett.* **103** (2009) 171801, [arXiv:0904.0770].
- 3077 [117] **LHCb Collaboration**, R. Aaij et al., *Test of lepton universality using*
3078 $B^+ \rightarrow K^+\ell^+\ell^-$ *decays*, *Phys. Rev. Lett.* **113** (2014) 151601,
3079 [arXiv:1406.6482].
- 3080 [118] **LHCb Collaboration**, R. Aaij et al., *Measurement of the ratio of branching*
3081 *fractions $\mathcal{B}(\bar{B}^0 \rightarrow D^{*+}\tau^-\bar{\nu}_\tau)/\mathcal{B}(\bar{B}^0 \rightarrow D^{*+}\mu^-\bar{\nu}_\mu)$* , *Phys. Rev. Lett.* **115**
3082 (2015), no. 11 111803, [arXiv:1506.08614]. [Addendum: *Phys. Rev.*
3083 *Lett.*115,no.15,159901(2015)].
- 3084 [119] “Lhc b loki twiki.”
3085 <https://twiki.cern.ch/twiki/bin/view/LHCb/LoKiHybridFilters>.
3086 Accessed: 2015-09-30.
- 3087 [120] “Probnn presentation at ppts meeting.” <https://indico.cern.ch/event/226062/contribution/1/material/slides/0.pdf>. Accessed: 2015-09-30.
- 3089 [121] W. Verkerke and D. P. Kirkby, *The RooFit toolkit for data modeling*, *eConf C0303241* (2003) MOLT007, [physics/0306116].
- 3091 [122] P. Ball and R. Zwicky, *New results on $B \rightarrow \pi, K, \eta$ decay form factors from*
3092 *light-cone sum rules*, *Phys. Rev.* **D71** (2005) 014015, [hep-ph/0406232].
- 3093 [123] D. Melikhov and B. Stech, *Weak form-factors for heavy meson decays: An*
3094 *Update*, *Phys. Rev.* **D62** (2000) 014006, [hep-ph/0001113].
- 3095 [124] A. Ali, P. Ball, L. T. Handoko, and G. Hiller, *A Comparative study of the*
3096 *decays $B \rightarrow (K, K^*)\ell^+\ell^-$ in standard model and supersymmetric theories*,
3097 *Phys. Rev.* **D61** (2000) 074024, [hep-ph/9910221].
- 3098 [125] J. Hrivnac, R. Lednicky, and M. Smizanska, *Feasibility of beauty baryon*
3099 *polarization measurement in $\Lambda^0 J/\psi$ decay channel by ATLAS LHC*,
3100 *J.Phys.G* **G21** (1995) 629–638, [hep-ph/9405231].

- 3101 [126] W. Detmold and S. Meinel, $\Lambda_b \rightarrow \Lambda \ell^+ \ell^-$ form factors, differential branching
3102 fraction, and angular observables from lattice QCD with relativistic b quarks,
3103 arXiv:1602.01399.

3104

APPENDIX A

3105

3106

Decay models

3107

A.1 $\Lambda_b^0 \rightarrow \Lambda \mu^+ \mu^-$ distribution

The q^2 and angular dependancies of the $\Lambda_b^0 \rightarrow \Lambda \mu^+ \mu^-$ decays are modelled based on Ref. [101], where the angular distribution for unpolarised Λ_b^0 production is defined as

$$\begin{aligned} W(\theta_\ell, \theta_B, \chi) &\propto \sum_{\lambda_1, \lambda_2, \lambda_j, \lambda'_j, J, J', m, m', \lambda_\Lambda, \lambda'_\Lambda, \lambda_p} h_{\lambda_1 \lambda_2}^m(J) h_{\lambda_1 \lambda_2}^{m'}(J') e^{i(\lambda_j - \lambda'_j)\chi} \\ &\times \delta_{\lambda_j - \lambda_\Lambda, \lambda'_j - \lambda'_\Lambda} \delta_{J, J'} d_{\lambda_j, \lambda_1 - \lambda_2}^J(\theta_\ell) d_{\lambda'_j, \lambda_1 - \lambda_2}^{J'}(\theta_\ell) H_{\lambda_\Lambda \lambda_j}^m(J) H_{\lambda'_\Lambda \lambda'_j}^{m'\dagger}(J') \\ &\times d_{\lambda_\Lambda \lambda_p}^{1/2}(\theta_B) d_{\lambda'_\Lambda \lambda_p}^{1/2}(\theta_B) h_{\lambda_p 0}^B h_{\lambda_p 0}^{B\dagger}. \end{aligned} \quad (\text{A.1})$$

In this formula θ_ℓ and θ_B correspond to the lepton and proton helicity angles, χ is angle between dimuon and Λ decay planes (for unpolarised production we are sensitive only to difference in azimuthal angles), $d_{i,j}^J$ are Wigner d-functions and h , h^B and H are helicity amplitudes for virtual dimuon, Λ and Λ_b^0 decays. The sum runs over all possible helicities with the dimuon being allowed in spin 0 and 1 states (J and J'). The m and m' indices run over the vector and axial-vector current contributions.

The production polarisation is introduced by removing $e^{i(\lambda_j - \lambda'_j)\chi}$ from the expression, swapping small Wigner d-functions $d_{i,j}^J$ to the corresponding capital ones $D_{i,j}^J$ which are related as

$$D_{i,j}^J(\theta, \phi) = d_{i,j}^J(\theta) e^{i\phi(i-j)} \quad (\text{A.2})$$

and substitute spin density matrix for $\delta_{\lambda_j - \lambda_\Lambda, \lambda'_j - \lambda'_\Lambda} \delta_{JJ'}$. The spin density matrix itself is given by

$$\rho_{\lambda_j - \lambda_\Lambda, \lambda'_j - \lambda'_\Lambda} = \frac{1}{2} \begin{pmatrix} 1 + P_b \cos \theta & P_b \sin \theta \\ P_b \sin \theta & 1 - P_b \cos \theta \end{pmatrix}. \quad (\text{A.3})$$

Those changes lead to the formula

$$\begin{aligned} W(\theta\ell, \theta_B, \chi) &\propto \sum_{\lambda_1, \lambda_2, \lambda_j, \lambda'_j, J, J', m, m', \lambda_\Lambda, \lambda'_\Lambda, \lambda_p} h_{\lambda_1 \lambda_2}^m(J) h_{\lambda_1 \lambda_2}^{m'}(J') \\ &\times \rho_{\lambda_j - \lambda_\Lambda, \lambda'_j - \lambda'_\Lambda} D_{\lambda_j, \lambda_1 - \lambda_2}^J(\theta\ell, \phi_L) D_{\lambda'_j, \lambda_1 - \lambda_2}^{J'}(\theta\ell, \phi_L) H_{\lambda_\Lambda \lambda_j}^m(J) H_{\lambda'_\Lambda \lambda'_j}^{m'\dagger}(J') \\ &\times D_{\lambda_\Lambda \lambda_p}^{1/2}(\theta_B, \phi_B) D_{\lambda'_\Lambda \lambda_p}^{1/2}(\theta_B, \phi_B) h_{\lambda_p 0}^B h_{\lambda_p 0}^{B\dagger}. \end{aligned} \quad (\text{A.4})$$

The lepton amplitudes come directly from Ref. [101], eq. 3. The Λ decay amplitudes are related to the Λ decay asymmetry parameter as

$$\alpha_\Lambda = \frac{|h_{\frac{1}{2}0}^B|^2 - |h_{-\frac{1}{2}0}^B|^2}{|h_{\frac{1}{2}0}^B|^2 + |h_{-\frac{1}{2}0}^B|^2}. \quad (\text{A.5})$$

Finally, the Λ_b^0 decay amplitudes receive contributions from vector and axial-vector currents and can be written as

$$H_{\lambda_2, \lambda_j}^m = H_{\lambda_2, \lambda_j}^{Vm} - H_{\lambda_2, \lambda_j}^{Am}. \quad (\text{A.6})$$

Finally, the remaining amplitudes are expressed in terms of form factors (Ref. [101], eq. C6) as

$$\begin{aligned} H_{\frac{1}{2}t}^{Vm} &= \sqrt{\frac{Q_+}{q^2}} \left(M_- F_1^{Vm} + \frac{q^2}{M_1} F_3^{Vm} \right), \\ H_{\frac{1}{2}1}^{Vm} &= \sqrt{2Q_-} \left(F_1^{Vm} + \frac{M_+}{M_1} F_2^{Vm} \right), \\ H_{\frac{1}{2}0}^{Vm} &= \sqrt{\frac{Q_-}{q^2}} \left(M_+ F_1^{Vm} + \frac{q^2}{M_1} F_2^{Vm} \right), \\ H_{\frac{1}{2}t}^{Am} &= \sqrt{\frac{Q_-}{q^2}} \left(M_+ F_1^{Am} - \frac{q^2}{M_1} F_3^{Am} \right), \\ H_{\frac{1}{2}1}^{Am} &= \sqrt{2Q_+} \left(F_1^{Am} - \frac{M_-}{M_1} F_2^{Am} \right), \\ H_{\frac{1}{2}0}^{Am} &= \sqrt{\frac{Q_+}{q^2}} \left(M_- F_1^{Am} - \frac{q^2}{M_1} F_2^{Am} \right), \end{aligned} \quad (\text{A.7})$$

where $M_\pm = M_1 \pm M_2$, $Q_\pm = M_\pm^2 - q^2$. The form factors F are expressed in

3130 terms of dimensionless quantities in eqs. C8 and C9 in Ref. [101]. In our actual
3131 implementation form factors calculated in the covariant quark model [101] are used
3132 and for the numerical values of the Wilson coefficients Ref. [101] is used.

To assess effect of different form factors on efficiency calculations, an alternative set of form factors is implemented, based on the LQCD calculation from Ref. [105]. The form factors relations are found by comparing eqs. 66 and 68 in Ref. [101] to eq. 51 in Ref. [105]. Denoting LQCD form factors by F_i^L and dimensionless covariant quark model ones by f_i^{XX} we have

$$\begin{aligned} f_1^V &= c_\gamma(F_1^L + F_2^L), \\ f_2^V &= -2c_\gamma F_2^L, \\ f_3^V &= c_v(F_1^L + F_2^L), \\ f_1^A &= c_\gamma(F_1^L - F_2^L), \\ f_2^A &= -2c_\gamma F_2^L, \\ f_3^A &= -c_v(F_1^L - F_2^L), \\ f_1^{TV} &= c_\sigma F_2^L, \\ f_2^{TV} &= -c_\sigma F_1^L, \\ f_1^{TA} &= c_\sigma F_2^L, \\ f_2^{TA} &= -c_\sigma F_1^L, \end{aligned}$$

where

$$\begin{aligned} c_\gamma &= 1 - \frac{\alpha_s(\mu^2)}{\pi} \left[\frac{4}{3} + \ln\left(\frac{\mu}{m_b}\right) \right], \\ c_v &= \frac{2}{3} \frac{\alpha_s(\mu^2)}{\pi}, \\ c_\sigma &= 1 - \frac{\alpha_s(\mu^2)}{\pi} \left[\frac{4}{3} + \frac{5}{3} \ln\left(\frac{\mu}{m_b}\right) \right]. \end{aligned} \quad (\text{A.8})$$

3133 In the calculations $\mu = m_b$ is used. For the strong coupling constant, we start
3134 from the world average value at the Z mass, $\alpha_s(m_Z^2) = 0.1185 \pm 0.0006$ [2], and we
3135 translate it to the scale m_b^2 by

$$\alpha_s(\mu^2) = \frac{\alpha_s(m_Z^2)}{1 + \frac{\alpha_s(m_Z^2)}{12\pi} (33 - 2n_f) \ln\left(\frac{\mu^2}{m_Z^2}\right)}, \quad (\text{A.9})$$

3136 where $n_f = 5$. The LQCD form factors F_1^L and F_2^L can be then taken directly from
3137 Ref. [105] and plugged into the code implementing the calculation from Ref. [101].

3138 A.2 Two-dimensional angular distribution parameters

3139 Expectations values for parameters in the two-dimensional angular distribution for
 3140 the $\Lambda_b^0 \rightarrow \Lambda \mu^+ \mu^-$ decay calculated using form factors and numerical inputs from
 3141 Ref. [101].

$q^2 [GeV^2/c^2]$	A_{FB}^ℓ	P_z^Λ	f_L	O_P	O_{Lp}	O_{UVA}
0.1 – 2.0	0.082	-0.9998	0.537	-0.463	-0.537	0.055
2.0 – 4.0	-0.032	-0.9996	0.858	-0.142	-0.857	-0.021
4.0 – 6.0	-0.153	-0.9991	0.752	-0.247	-0.752	-0.102
V.0 – VA.5	-0.348	-0.9834	0.508	-0.478	-0.505	-0.239
15.0 – 16.0	-0.384	-0.9374	0.428	-0.524	-0.413	-0.280
16.0 – 18.0	-0.377	-0.8807	0.399	-0.513	-0.368	-0.294
18.0 – 20.0	-0.297	-0.6640	0.361	-0.404	-0.260	-0.314
1.0 – 6.0	-0.040	-0.9994	0.830	-0.170	-0.830	-0.027
15.0 – 20.0	-0.339	-0.7830	0.385	-0.461	-0.3A	-0.302

Table A.1: Prediction for angular observables entering two-dimensional angular distributions. Prediction is based on covariant quark model form factors from Ref. [101].

3142 A.3 $\Lambda_b^0 \rightarrow J/\psi \Lambda$ distribution

3143 The angular distribution of the $\Lambda_b^0 \rightarrow J/\psi \Lambda$ decay is modelled using Ref. [125]. The
 3144 differential rate is written as

$$w(\Omega, \Omega_1, \Omega_2) = \frac{1}{(4\pi)} \sum_{i=0}^{3} \sum_{i=1}^{19} f_{1i} f_{2i}(P_b, \alpha_\Lambda) F_i(\theta, \theta_1, \theta_2, \phi_1, \phi_2), \quad (\text{A.10})$$

3145 The expression uses four observables (angles) and depends on four complex amplitudes
 3146 a_+, a_-, b_+, b_- and two real valued parameters for the production polarisation,
 3147 P_b , and the Λ decay asymmetry, α_Λ . The angle θ is the angle of the Λ momentum
 3148 in Λ_b^0 rest frame with respect to the vector $\vec{n} = \frac{\vec{p}_{inc} \times \vec{p}_{\Lambda_b^0}}{|\vec{p}_{inc} \times \vec{p}_{\Lambda_b^0}|}$, where \vec{p}_{inc} and $\vec{p}_{\Lambda_b^0}$ are the
 3149 momenta of incident proton and Λ_b^0 in the center of mass system. The angles θ_1 and
 3150 ϕ_1 are polar and azimuthal angle of the proton coming from the Λ decay in the Λ
 3151 rest frame with axis defined as $z_1 \uparrow\uparrow \vec{p}_\Lambda$, $y_1 \uparrow\uparrow \vec{n} \times \vec{p}_\Lambda$. Finally, the angles θ_2 and ϕ_2
 3152 are the angles of the momenta of the muons in J/ψ rest frame with axes defined as
 3153 $z_2 \uparrow\uparrow \vec{p}_{J/\psi}$, $y_2 \uparrow\uparrow \vec{n} \times \vec{p}_{J/\psi}$.

3154 The distribution depends on the Λ decay asymmetry parameter, α_Λ , the production
 3155 polarisation P_b and four complex amplitudes. The α_Λ is measured to be 0.642 ± 0.013
 3156 for Λ . The production polarisation P_b and magnitudes of a_+, a_-, b_+ and b_- are

³¹⁵⁷ measured in Ref. [109]. Phases are not measured therefore, as default all phases are
³¹⁵⁸ set to zero and then they are randomly varied to calculate the systematic uncertainty.

3159

APPENDIX B

3160

3161

Data-simulation comparison

3162

This appendix reports a comparison between distributions in data and simulated $\Lambda_b^0 \rightarrow J/\psi \Lambda$ events. In the plots what is labeled as “Data” is real data in a 20 MeV interval around the Λ_b^0 mass, where a sideband subtraction technique to remove background. “Side” is real data for masses above 6 GeV containing mostly combinatorial background. These can be compared to the previous sample to see which variables differ the most. “MC” corresponds to Pythia8 $\Lambda_b^0 \rightarrow J/\psi \Lambda$ simulated events. Finally, the label “MC fully W” refers to the same simulated sample but weighted for the Λ_b^0 and Λ kinematics (Sec. 3.3.2) and the decay model (Sec. 3.3.1). Distributions are shown separately for long and downstream events.

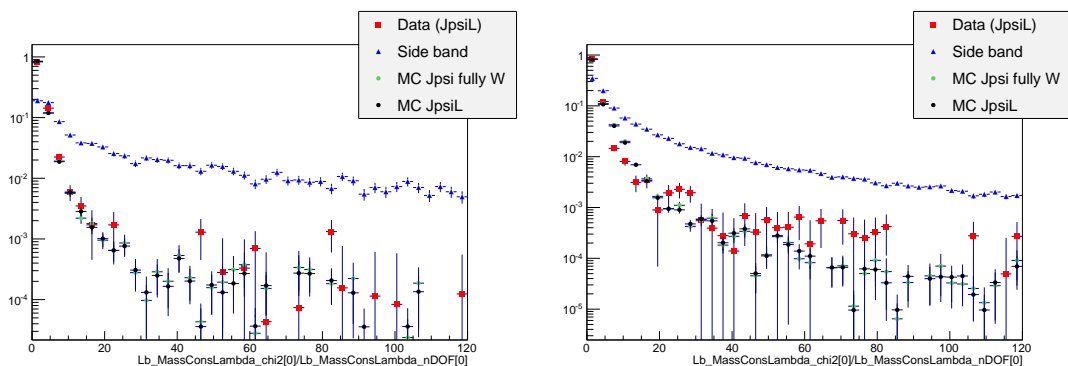


Figure B.1: Distributions of χ^2/NdF of the kinematic fit in data and simulation for LL (left) and DD (right) events.

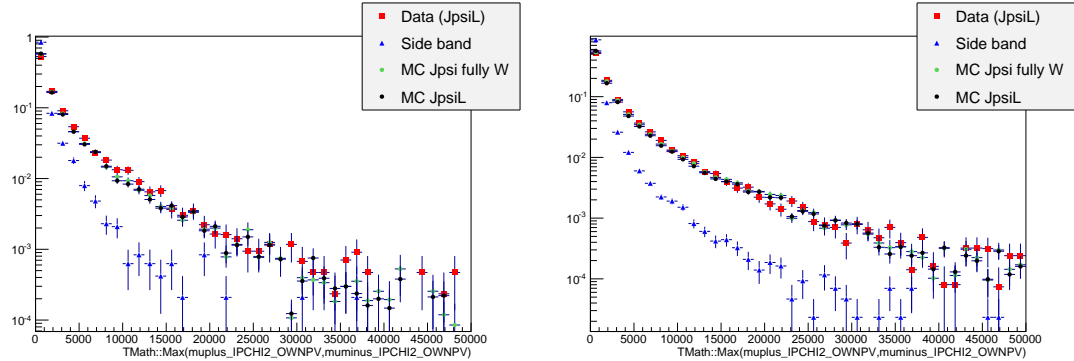


Figure B.2: Distributions of maximum muon $IP\chi^2$ variable in data and simulation for LL (left) and DD (right) events.

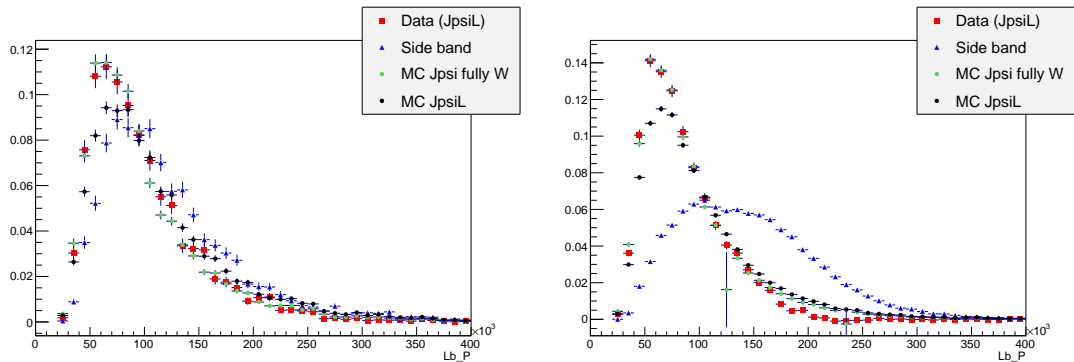


Figure B.3: Distributions of Λ_b^0 momentum variable in data and simulation for LL (left) and DD (right) events.

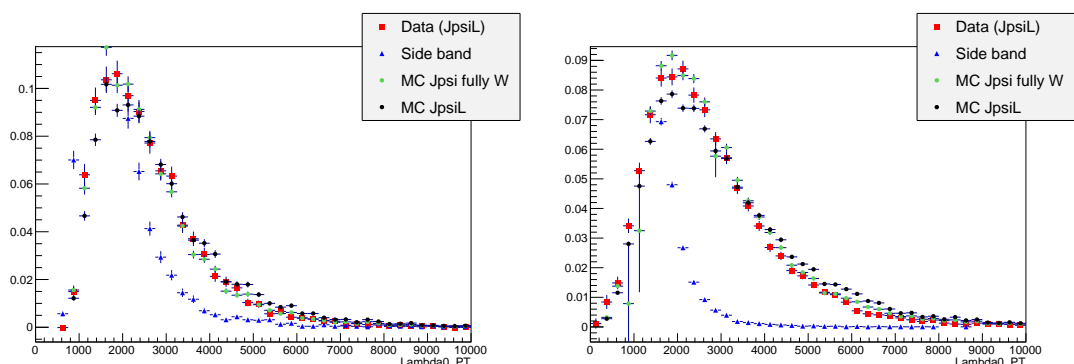


Figure B.4: Distributions of Λ transverse momentum variable in MC, data signal and data background for LL (left) and DD (right) events.

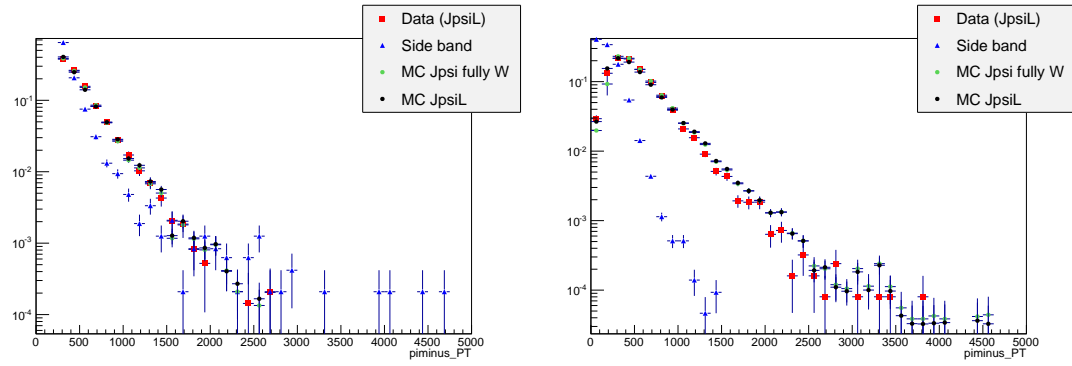


Figure B.5: Distributions of pion transverse momentum variable in data and simulation for LL (left) and DD (right) events.

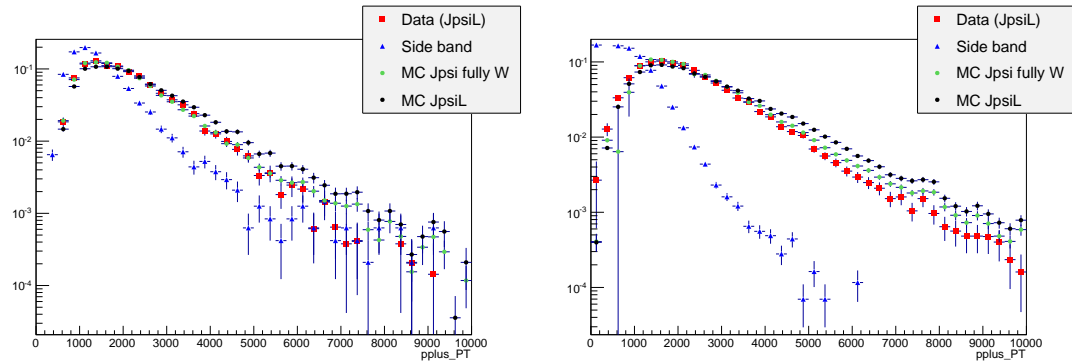


Figure B.6: Distributions of proton transverse momentum variable in data and simulation for LL (left) and DD (right) events.

3172

APPENDIX C

3173

**3174 Systematic uncertainties on the efficiency calculation for the
 3175 $\Lambda_b^0 \rightarrow \Lambda \mu^+ \mu^-$ branching fraction analysis.**

3176

3177 This appendix reports systematic uncertainties on absolute and relative efficiencies
3178 for the $\Lambda_b^0 \rightarrow \Lambda \mu^+ \mu^-$ branching fraction analysis.

q^2 [GeV $^2/c^4$]	Lifetime	Decay Model	Polarisation
0.1-2.0	0.003%	0.059%	0.145%
2.0-4.0	0.007%	0.156%	0.145%
4.0-6.0	0.002%	0.156%	0.144%
6.0-8.0	0.003%	0.080%	0.144%
11.0-12.5	0.012%	0.101%	0.144%
15.0-16.0	0.007%	0.050%	0.144%
16.0-18.0	0.002%	0.059%	0.145%
18.0-20.0	0.009%	0.016%	0.145%
1.1-6.0	0.005%	0.651%	0.144%
15.0-20.0	0.007%	0.088%	0.144%

Table C.1: Absolute values of systematic uncertainties on relative geometric efficiency.

q^2 [GeV $^2/c^4$]	Lifetime	Decay Model	Polarisation
0.1-2.0	0.007%	0.004%	0.008%
2.0-4.0	0.006%	0.001%	0.009%
4.0-6.0	0.009%	0.003%	0.008%
6.0-8.0	0.008%	0.005%	0.008%
11.0-12.5	0.010%	0.005%	0.009%
15.0-16.0	0.004%	0.006%	0.008%
16.0-18.0	0.003%	0.010%	0.010%
18.0-20.0	0.004%	0.011%	0.008%
1.1-6.0	0.009%	0.043%	0.010%
15.0-20.0	0.005%	0.072%	0.009%

Table C.2: Absolute values of systematic uncertainties on relative detection efficiency.

q^2 [GeV $^2/c^4$]	Downstream			Long		
	Lifetime	Model	Polarisation	Lifetime	Model	Polarisation
0.1-2.0	0.350%	0.234%	0.463%	0.066%	0.264%	1.081%
2.0-4.0	0.170%	0.640%	0.488%	0.005%	0.953%	1.088%
4.0-6.0	0.073%	0.514%	0.465%	0.052%	1.607%	1.087%
6.0-8.0	0.054%	0.298%	0.458%	0.011%	1.517%	1.075%
11.0-12.5	0.043%	0.030%	0.469%	0.025%	0.187%	1.080%
15.0-16.0	0.078%	0.499%	0.462%	0.030%	0.110%	1.082%
16.0-18.0	0.100%	0.215%	0.477%	0.021%	0.412%	1.078%
18.0-20.0	0.130%	0.044%	0.471%	0.034%	0.216%	1.079%
1.1-6.0	0.137%	0.279%	0.460%	0.025%	0.656%	1.078%
15.0-20.0	0.107%	0.511%	0.460%	0.016%	0.742%	1.077%

Table C.3: Absolute values of systematic uncertainties on relative reconstruction efficiency for long and downstream candidates.

q^2 [GeV $^2/c^4$]	Downstream			Long		
	Lifetime	Model	Polarisation	Lifetime	Model	Polarisation
0.1-2.0	0.038%	0.226%	0.070%	0.003%	0.061%	0.117%
2.0-4.0	0.009%	0.091%	0.034%	0.020%	0.072%	0.076%
4.0-6.0	0.028%	0.162%	0.058%	0.018%	0.165%	0.040%
6.0-8.0	0.005%	0.080%	0.075%	0.041%	0.035%	0.053%
11.0-12.5	0.002%	0.207%	0.079%	0.002%	0.148%	0.076%
15.0-16.0	0.036%	0.094%	0.035%	0.022%	0.021%	0.089%
16.0-18.0	0.023%	0.027%	0.029%	0.023%	0.003%	0.031%
18.0-20.0	0.017%	0.145%	0.034%	0.008%	0.199%	0.063%
1.1-6.0	0.024%	0.215%	0.029%	0.012%	0.733%	0.051%
15.0-20.0	0.025%	0.220%	0.031%	0.004%	0.108%	0.029%

Table C.4: Absolute values of systematic uncertainties on relative trigger efficiency for long and downstream candidates.

q^2 [GeV $^2/c^4$]	Downstream			Long		
	Lifetime	Model	Polarisation	Lifetime	Model	Polarisation
0.1-2.0	0.022%	0.019%	0.025%	0.060%	0.106%	0.072%
2.0-4.0	0.127%	0.267%	0.017%	0.095%	0.002%	0.031%
4.0-6.0	0.116%	0.106%	0.045%	0.081%	0.139%	0.119%
6.0-8.0	0.111%	0.186%	0.020%	0.085%	0.387%	0.047%
11.0-12.5	0.008%	0.056%	0.017%	0.057%	0.030%	0.027%
15.0-16.0	0.002%	0.004%	0.066%	0.070%	0.124%	0.023%
16.0-18.0	0.024%	0.088%	0.027%	0.068%	0.105%	0.023%
18.0-20.0	0.031%	0.050%	0.027%	0.180%	0.506%	0.077%
1.1-6.0	0.118%	0.164%	0.037%	0.080%	0.183%	0.058%
15.0-20.0	0.001%	0.125%	0.037%	0.102%	0.541%	0.034%

Table C.5: Absolute values of systematic uncertainties on relative MVA efficiency for long and downstream candidates.

q^2 [GeV $^2/c^4$]	Reconstruction	Trigger	MVA
0.1-2.0	0.612%	0.250%	0.173%
2.0-4.0	0.515%	0.246%	0.223%
4.0-6.0	0.408%	0.180%	0.272%
6.0-8.0	0.412%	0.090%	0.218%
11.0-12.5	0.175%	0.047%	0.103%
15.0-16.0	0.962%	0.010%	0.141%
16.0-18.0	1.173%	0.037%	0.103%
18.0-20.0	1.557%	0.050%	0.122%
1.1-6.0	0.475%	0.220%	0.246%
15.0-20.0	1.254%	0.040%	0.083%

Table C.6: Values of DD vertexing systematic uncertainties on relative reconstruction, trigger and MVA efficiencies for downstream candidates.

APPENDIX D

3181 Improved predictions for $\Lambda_b^0 \rightarrow \Lambda \mu^+ \mu^-$ observables.

3183 The publication of the results included in this thesis triggered interest in the theory
 3184 community, which produced improved lattice calculations and predictions [126].
 3185 This section reports the measured quantities with the new predictions overlaid as
 3186 reported in Ref. [126].

	Prediction	Measurement
$\langle d\mathcal{B}/dq^2 \rangle_{[15, 20]}$	0.756 ± 0.070	1.20 ± 0.27
$\langle F_L \rangle_{[15, 20]}$	0.409 ± 0.013	$0.61^{+0.11}_{-0.14}$
$\langle A_{\text{FB}}^\ell \rangle_{[15, 20]}$	-0.350 ± 0.013	-0.05 ± 0.09
$\langle A_{\text{FB}}^\Lambda \rangle_{[15, 20]}$	-0.2710 ± 0.0092	-0.29 ± 0.08

Table D.1: Comparison of predictions for the $\Lambda_b^0 \rightarrow \Lambda \mu^+ \mu^-$ observables with the LHCb data presented in this thesis in the interval $[15, 20]$ GeV^2/c^4 , where the measurement is most precise.

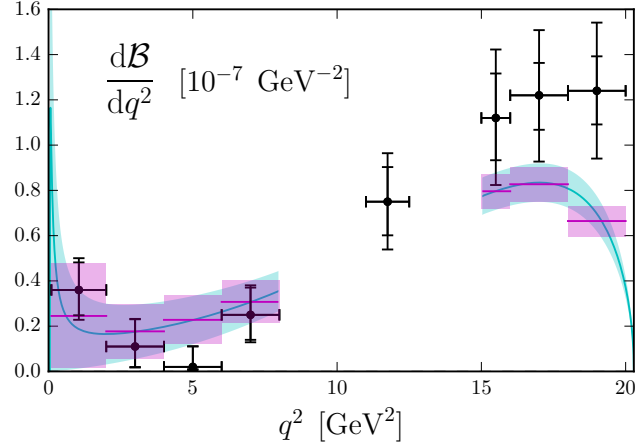


Figure D.1: Measurement of the differential branching fraction of the $\Lambda_b^0 \rightarrow \Lambda \mu^+ \mu^-$ decay as a function of q^2 already presented in Ch. 3 with improved Standard Model predictions from Ref. [126] overlaid.

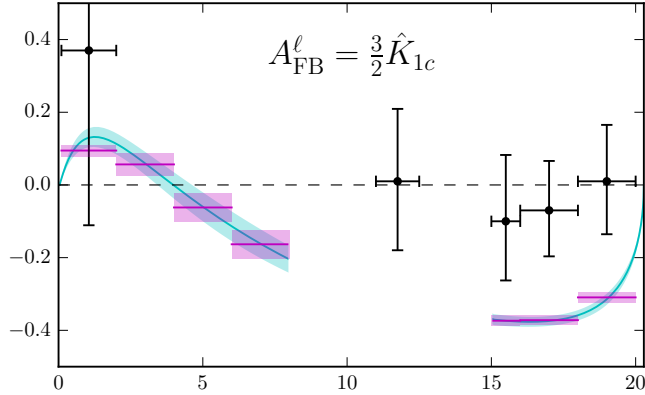


Figure D.2: Measurement of the lepton side forward-backward asymmetry, A_{FB}^ℓ , as a function of q^2 already presented in Ch. 4 with improved Standard Model predictions from Ref. [126] overlaid.

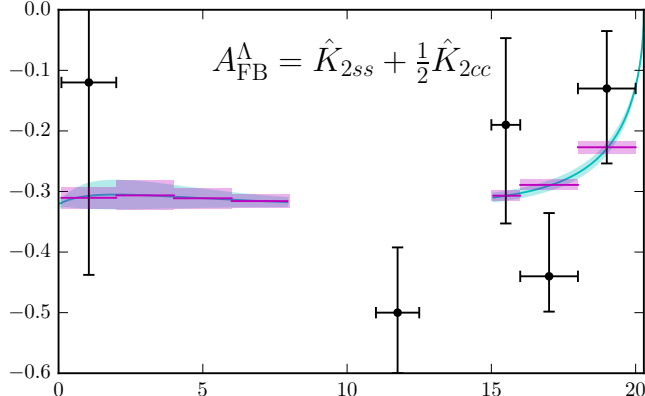


Figure D.3: Measurement of the hadron side forward-backward asymmetry, A_{FB}^h , as a function of q^2 already presented in Ch. 4 with improved Standard Model predictions from Ref. [126] overlaid.

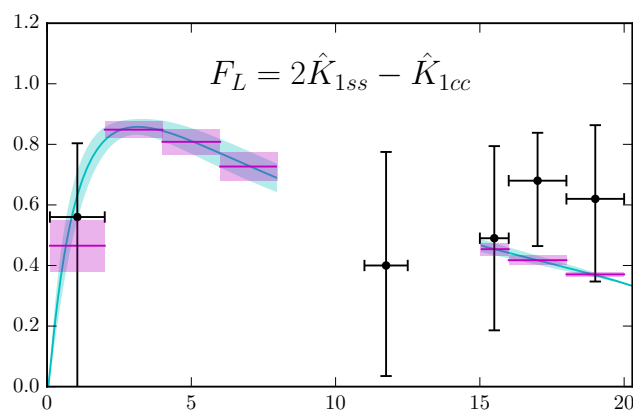


Figure D.4: Measurement of the fraction of longitudinally polarised dimuons, f_L , as a function of q^2 already presented in Ch. 4 with improved Standard Model predictions from Ref. [126] overlaid.

3187

APPENDIX E

3188

3189 **Invariant mass fits to $B^0 \rightarrow K^{*0}\ell^+\ell^-$ simulated candidates**

3190

3191 This appendix contains fits to the $m(K\pi\mu\mu)$ and $m(K\pi ee)$ invariant mass of $B^0 \rightarrow$
3192 $K^{*0}\ell^+\ell^-$ simulated candidates used to constrain parameters in the fit to data.

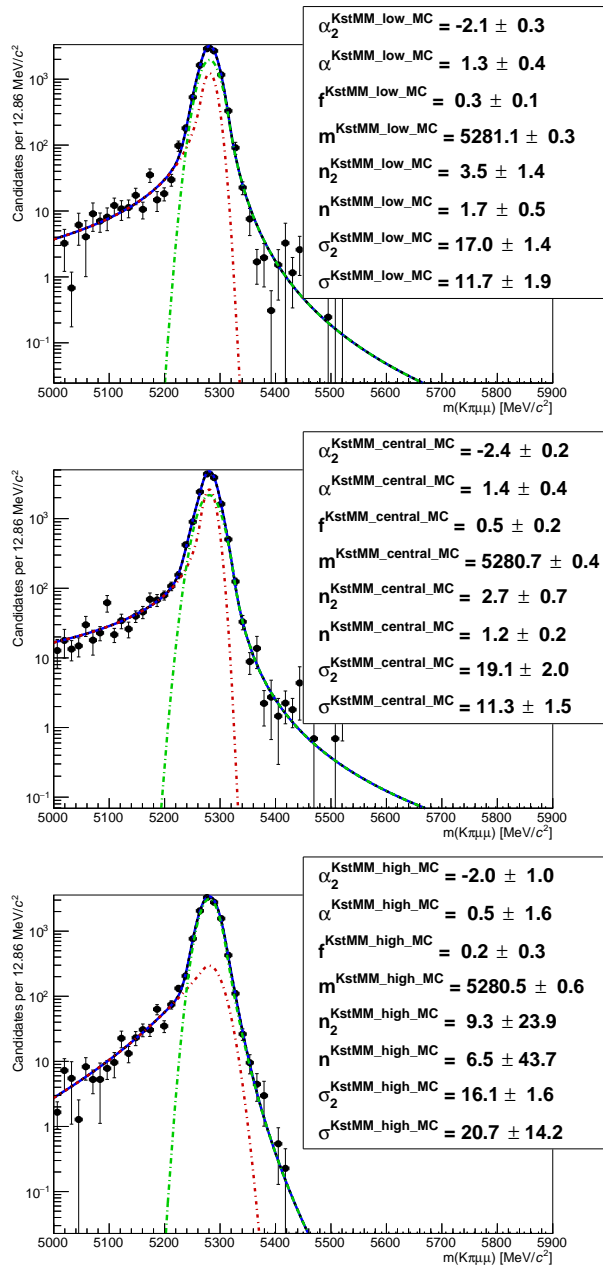


Figure E.1: Fitted $m(K\pi\mu\mu)$ mass spectrum for simulated events in the low (top), central (medium) and high (bottom) q^2 intervals.

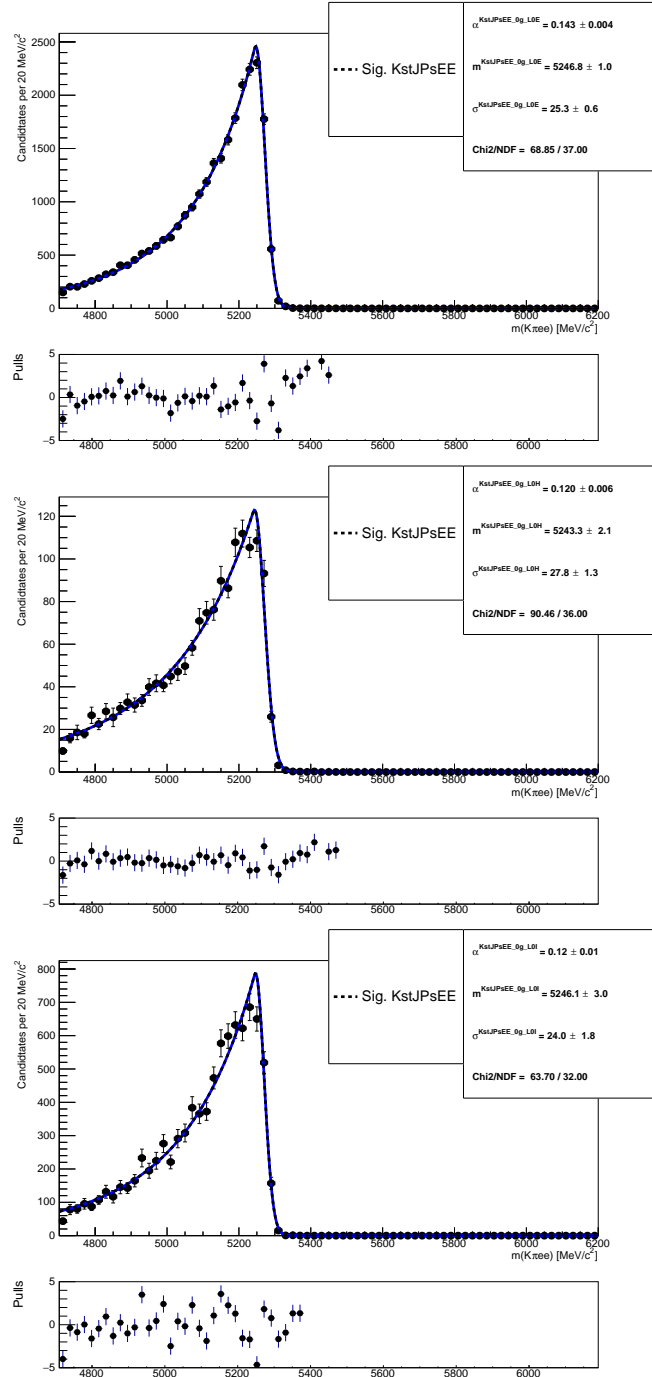


Figure E.2: Fitted $m(K\pi ee)$ mass spectrum of $B^0 \rightarrow K^{*0} J/\psi (J/\psi \rightarrow ee)$ simulated events in the three trigger categories and no photon emitted.

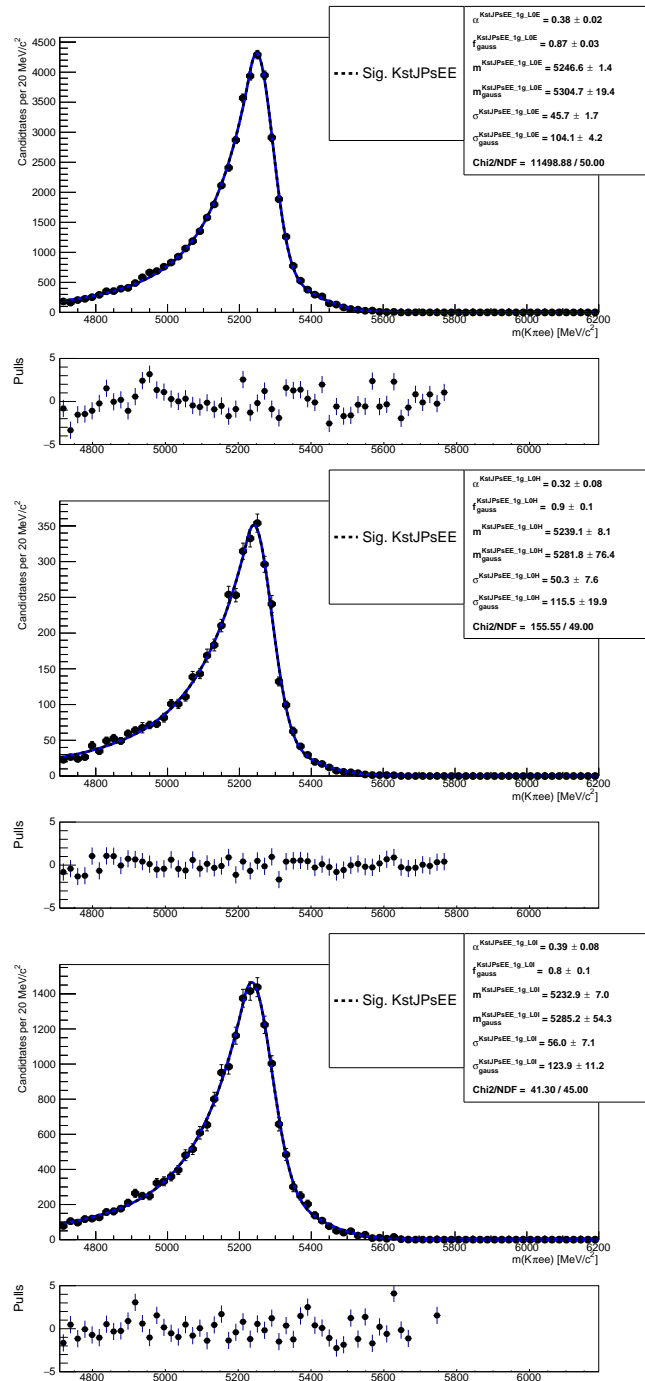


Figure E.3: Fitted $m(K\pi ee)$ mass spectrum of $B^0 \rightarrow K^{*0} J/\psi (J/\psi \rightarrow ee)$ simulated events in the three trigger categories and one photon emitted.

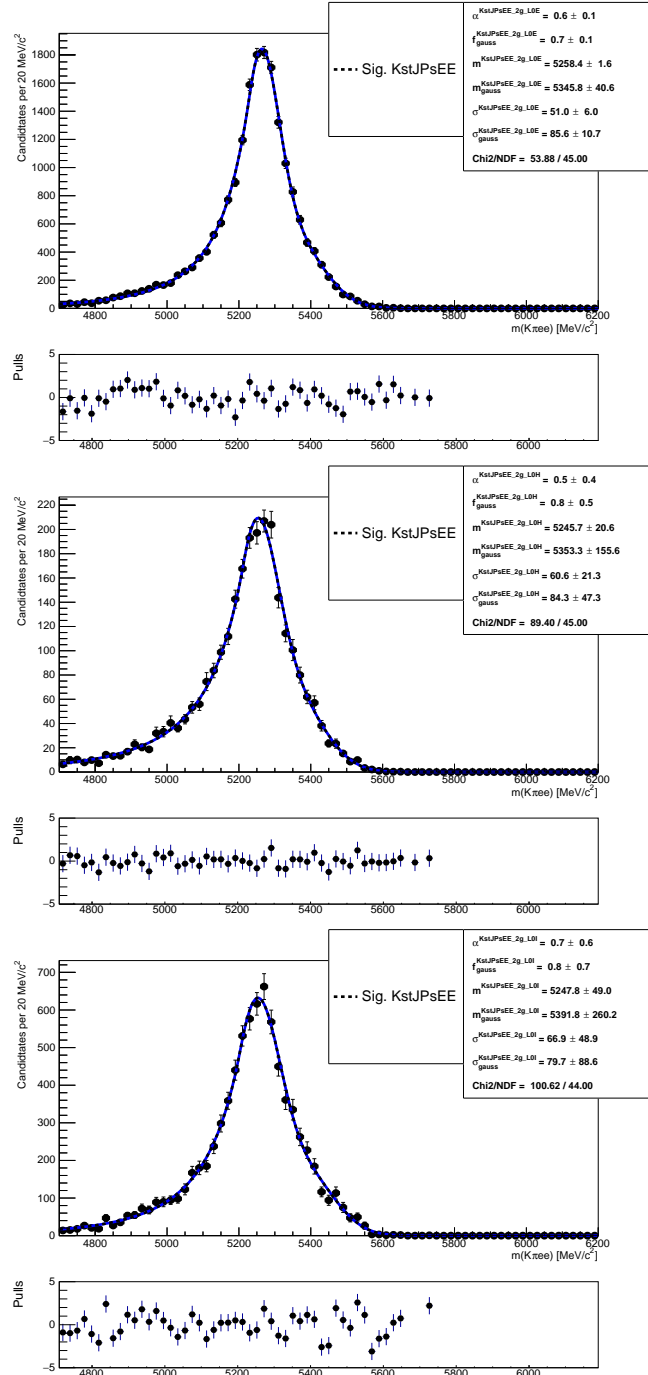


Figure E.4: Fitted $m(K\pi ee)$ mass spectrum of $B^0 \rightarrow K^{*0} J/\psi (J/\psi \rightarrow ee)$ simulated events in the three trigger categories and two photons emitted.

APPENDIX F

3194

³¹⁹⁵ Invariant mass fits to $B^0 \rightarrow K^{*0} e^+ e^-$ candidates divided in ³¹⁹⁶ trigger categories

3197

This appendix contains fits to the $m(K\pi ee)$ invariant mass of rare and control channel candidates separately in the tree trigger categories. Each trigger category is always fit with its own PDF but in the main text only their sum is shown for simplicity.

213 APPENDIX F. INVARIANT MASS FITS TO $B^0 \rightarrow K^{*0} E^+ E^-$ CANDIDATES DIVIDED IN TRIGGER CATEGORIES

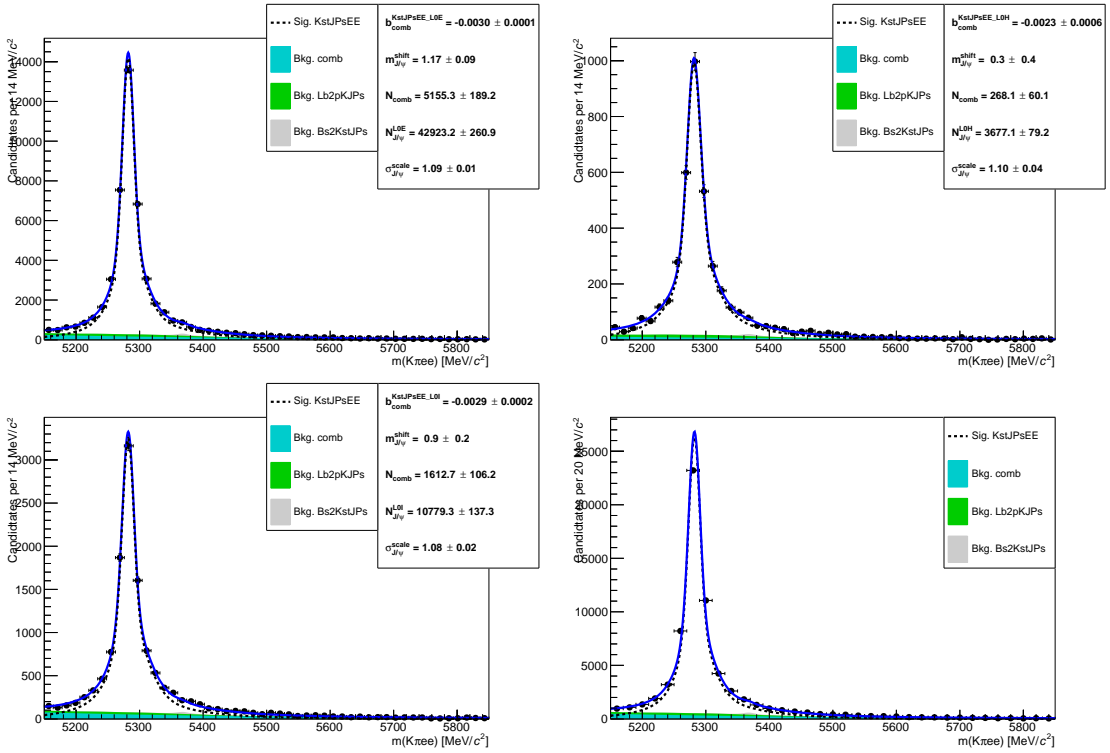


Figure F.1: Fit to the $m(K\pi ee)$ invariant mass of $B^0 \rightarrow K^{*0}(J/\psi \rightarrow e^+ e^-)$ candidates in the three trigger categories (L0E, L0H and L0I) separately, and (bottom right) combined. The dashed black line (shaded shapes) represents the signal (background) PDF.

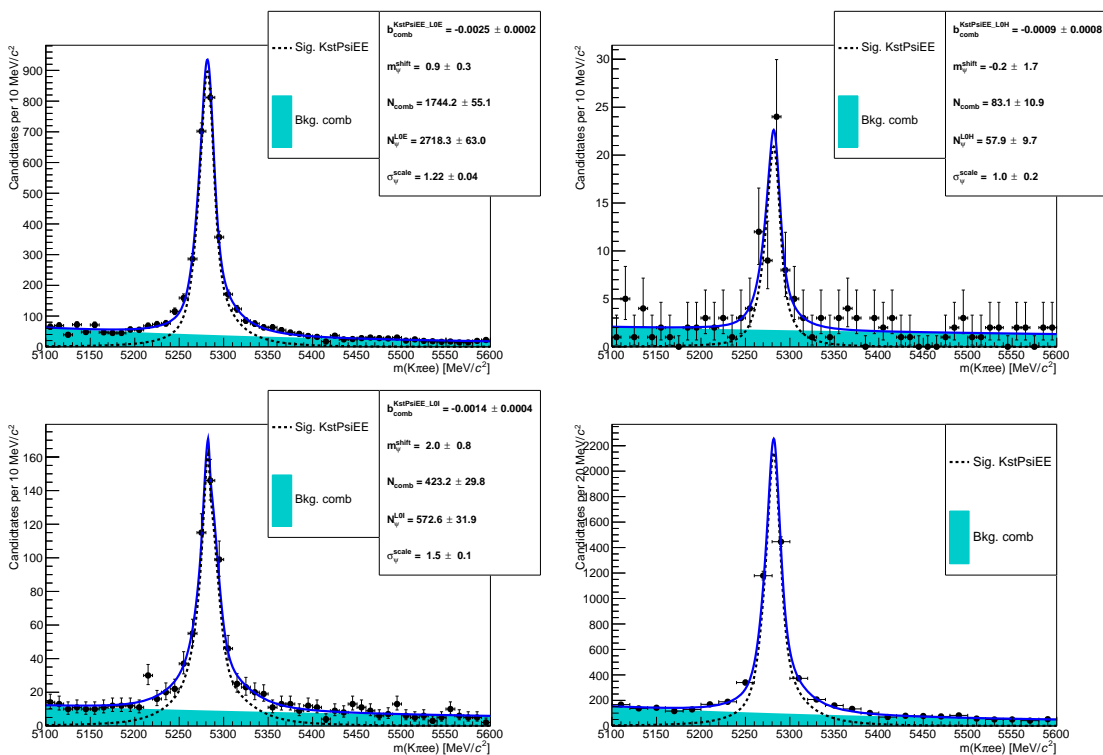


Figure F.2: Fit to the $m(K\pi ee)$ invariant mass of $B^0 \rightarrow K^{*0}(\psi(2S) \rightarrow e^+e^-)$ candidates in the three trigger categories (L0E, L0H and L0I) separately, and (bottom right) combined. The dashed black line (shaded shapes) represents the signal (background) PDF.

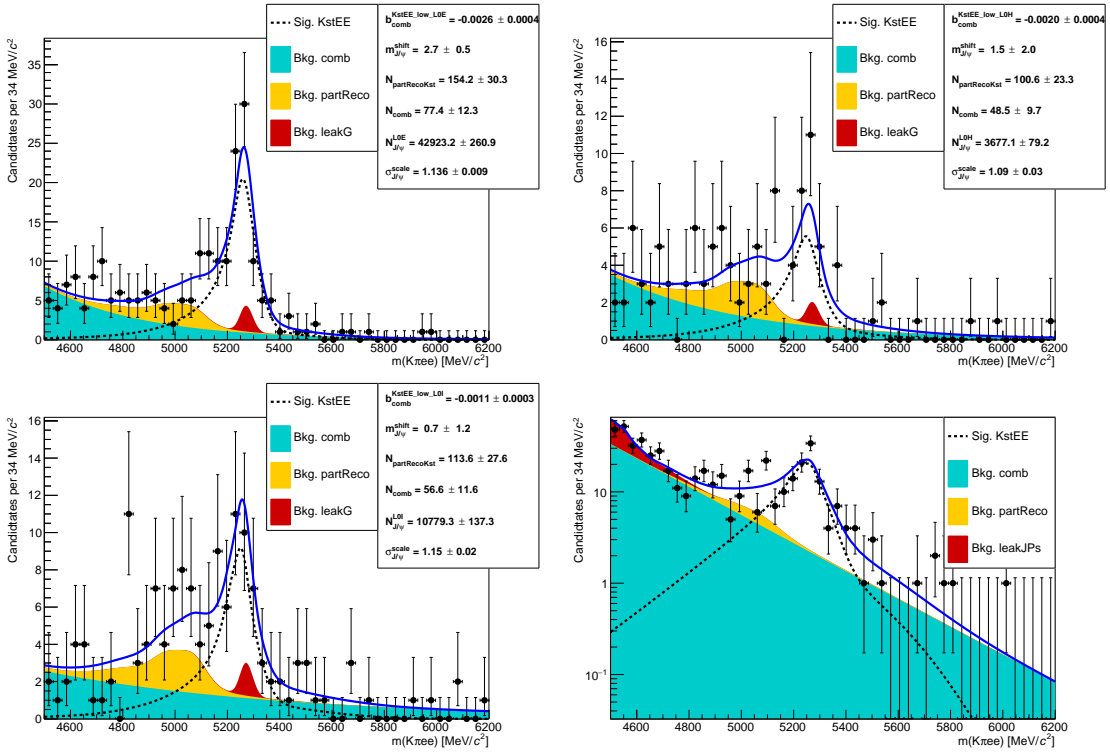


Figure F.3: Fit to the $m(K\pi ee)$ invariant mass of $B^0 \rightarrow K^{*0} e^+ e^-$ candidates at low- q^2 in the three trigger categories (L0E, L0H and L0I) separately, and (bottom right) combined. The dashed black line (shaded shapes) represents the signal (background) PDF.

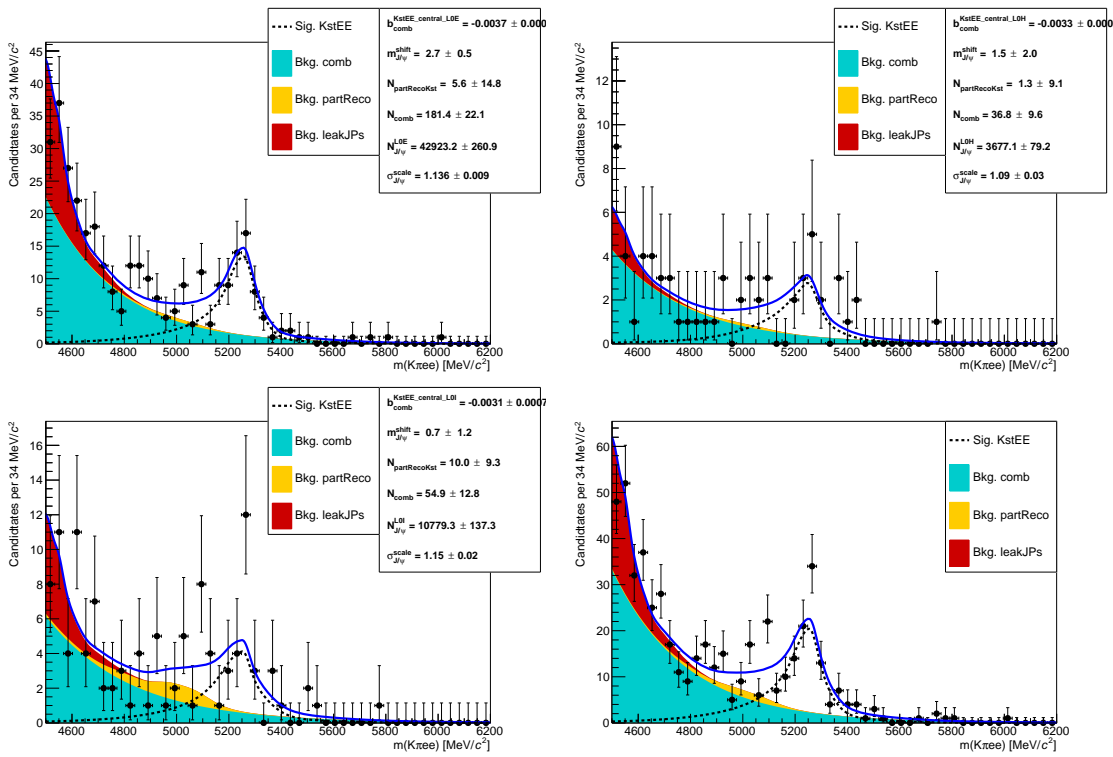


Figure F.4: Fit to the $m(K\pi ee)$ invariant mass of $B^0 \rightarrow K^{*0}e^+e^-$ candidates at central- q^2 in the three trigger categories (L0E, L0H and L0I) separately, and (bottom right) combined. The dashed black line (shaded shapes) represents the signal (background) PDF.

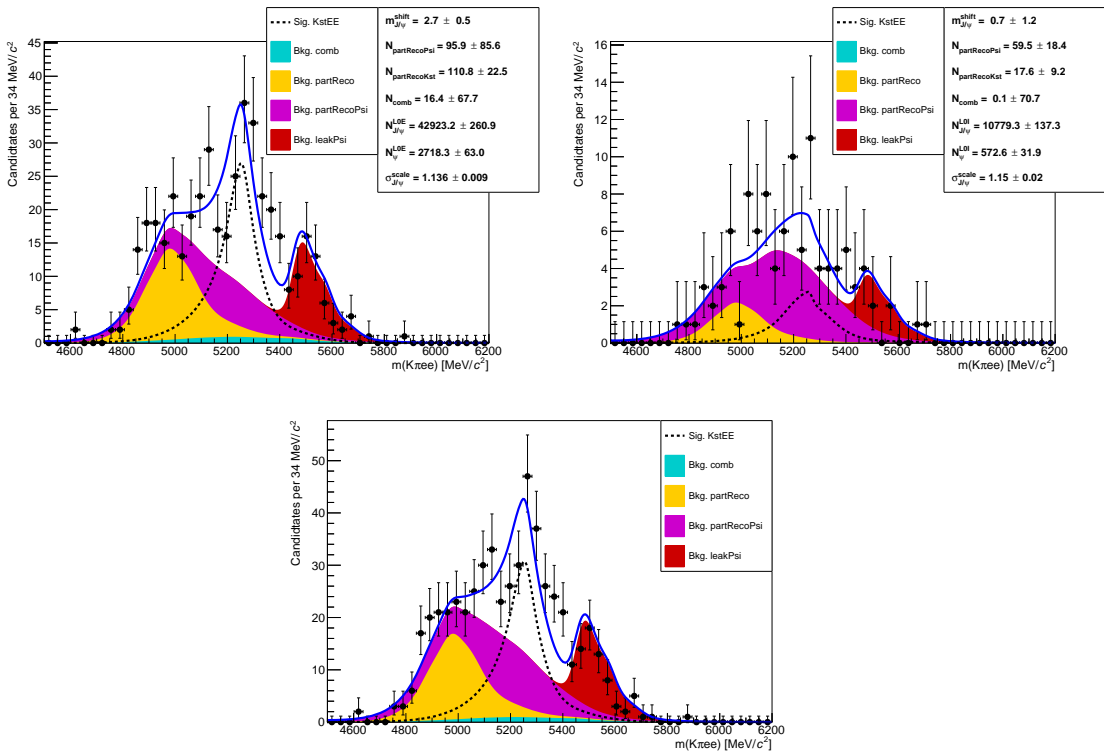


Figure F.5: Fit to the $m(K\pi ee)$ invariant mass of $B^0 \rightarrow K^{*0} e^+ e^-$ candidates at high- q^2 in the L0E and L0I trigger categories (top) separately, and (bottom) combined. The dashed black line (shaded shapes) represents the signal (background) PDF.